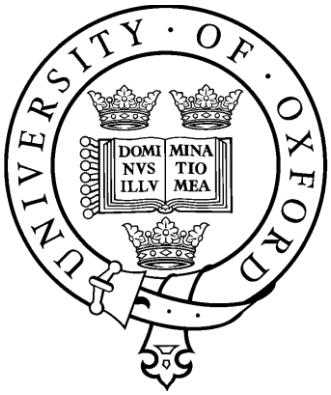
Fabrication of High Temperature Superconducting Composites for Microwave Applications



Juliana M Janurudin
St. Catherine's College
University of Oxford

A thesis submitted for the degree of
Award (Doctor of Philosophy)
Hillary Term 2016

Fabrication of High Temperature Superconducting Composites for Microwave Applications

Juliana M Janurudin
St. Catherine's College

A thesis submitted for the degree of Doctor of Philosophy in the University of Oxford
Hillary Term 2016

ABSTRACT. This thesis describes the fabrication of high temperature superconducting (HTS) composites synthesised by casting and 3-D printing techniques for a variety of potential applications such as microwave devices and metamaterials. The fabrication of metamaterials, where electromagnetic (EM) waves are manipulated by varying the effective dielectric constant (ε_{eff}) and static magnetic permeability (μ_{eff}) in 3-dimensions, is a major area of research worldwide. One approach to synthesising HTS composites with a controllable spatial distribution of electromagnetic properties is the synthesis of polymer composites comprising of multiple volume fractions of superconducting particles, which results in temperature-dependent composite materials.

$YBa_2Cu_3O_7$ (YBCO-123) superconducting powder was used as filler in the HTS composites. The effect of particle sizes and the non-superconducting $Y_2BaCu_2O_5$ (YBCO-211) phase on the magnetisation properties of the YBCO filler have been analysed using a SQUID magnetometer. The magnetisation analyses on two types of YBCO fillers proved that YBCO powder ground from top seeded melt growth (TSMG) YBCO bulks with median particle size, $d_{50} = 59\ \mu m$ possesses stronger diamagnetic properties at 77 K compared to commercially available YBCO powder with a size of $d_{50} = 5\ \mu m$. The melt-grown YBCO powder also possesses an irreversible component to the magnetisation owing to flux trapping by the YBCO-211 phase.

A custom-made polytetrafluoroethylene (PTFE) mould was designed and fabricated for the purpose of synthesising HTS composites via casting. The EM properties of the cast HTS composites were measured at room temperature and 77 K using a Vector Network Analyzer. The EM properties of these HTS composites are correlated with the homogeneity and density of YBCO particle distributions in the polymer matrix measured using scanning electron microscopy (SEM). It has been shown that the ε_{eff} values of the HTS composites were enhanced with increasing volume fraction of YBCO filler at both temperatures. A large drop of μ_{eff} values with volume fraction is observed at 77 K, owing to the diamagnetic response of the superconducting particles. Thus the refractive index of the composites could be controlled by both the volume fraction of YBCO filler and temperature.

In order to realise spatial variations in EM properties, a process has been developed for the fabrication of HTS composites via 3-D printing. The extrusion process was optimised to produce 20% YBCO loaded acrylonitrile butadiene styrene (ABS) feedstock filaments. Finer YBCO filler ($d_{50} = 20\ \mu m$) was used to print more intricate 3-D structures such as an anisotropic material and split-ring resonators, but the EM properties were suppressed, suggesting a particle size limitation of the 3-D printing. By contrast, YBCO/ABS composites have been printed with good control of YBCO volume fraction, and good agreement with the cast HTS composites at similar volume fraction of $\varepsilon_{eff} = 5.1$ and $\mu_{eff,77K}$ = 0.82 at 77 K achieved.

PREFACE

This thesis is an account of work carried out by the author in the Department of Materials, University of Oxford, under the supervision of Professor S. C. Speller and Professor C.R.M. Grovenor.

No part of this work has been previously submitted for a degree at this or any other university. The work of other authors has been freely drawn upon and is duly acknowledged in the text. A list of references has been given at the end of each chapter.

Some of the work described in this thesis has been published in the following journals and presented at conferences:

- ***Microwave Dielectric Characterisation of 3D-printed $BaTiO_3$/ABS polymer composites,*** F. Castles, D. Isakov, A. Lui, Q. Lei, C. E. J. Dancer, Y. Wang, **J. M. Janurudin**, S. C. Speller, C. R. M. Grovenor, and P. S. Grant, Scientific Reports, 6, 22714, (2016).
- ***Manufacture of Electrical and Magnetic Graded and Anisotropic Materials for Novel Manipulations of Microwaves***, P.S. Grant, F. Castles, Q. Lei, Y. Wang, **J. M. Janurudin**, D. Isakov, S.C. Speller, C.E.J. Dancer, and C. R. M. Grovenor, Philosophical Transactions of the Royal Society of London A: Mathematical, Physical and Engineering Sciences, 373, 2049, (2015).
- ***The Fabrication Approach of Superconducting/Polymer Composites***, **J. M. Janurudin**, F. Castles, C. Stevens, C. R. M.Grovenor, S. Speller, presented at the Royal Society Scientific Meeting, London, (2015).
- ***The Fabrication of Superconducting/Polymer Composites for Microwave Applications***, **J. M. Janurudin**, F. Castles, D. Isakov, C. Stevens, C. R. M. Grovenor, S. Speller, presented at the 2015 9th International Congress on Metamaterials Conference, Oxford, (2015), 2015 MRS Spring Meeting and Exhibit, San Francisco, (2015), and IOP Superconductivity Meeting, Bath, (2014).

This thesis is approximately 40, 000 words.

ACKNOWLEDGEMENTS

I would like to express my deepest gratitude to my supervisors, Prof. C.R.M. Grovenor and Prof. S. C. Speller for their provision of laboratory facilities, excellent academic supervisions and proof reading this thesis, alongside guidance and unwavering support throughout my studies. I had a truly remarkable and diverse research experience in the HTS group, and I could not have wished for a better education and place to be. I am grateful to both Chris and Susie for their guidance, continual encouragement, prompting me to think outside the box, and guiding me to think critically towards my work and data analyses. I hope that I can share this valuable knowledge and experience with others in the near future.

I would like to thank Prof. C.J. Stevens for his support and advices, especially on VNA measurements, and allowing me to use the microwave facilities in the engineering laboratory. I would also like to thank Prof. P. Grant for providing me with the opportunity to be a part of 'The Quest for Ultimate Electromagnetics using Spatial Transformations' (QUEST) Group. Via the group, I had the pleasure to work with Dr. I. Dmitry, Dr. F. Castles, Dr. E. Edwards and Dr. Y. Wang, and would like to acknowledge their contribution to this work via instrument trainings, scientific discussions, and continual support and encouragement. A special thank also goes to Dr. P. Dharmalingam in the Clarendon Laboratory for training, advising, and assisting with SQUID measurements. A special mention goes to Mrs. Gabriella Chapman, Mr. Greg Cook, and Mr. Graham Wyatt for training, advising, and assisting with the scanning electron microscopes, both at Begbroke and the city centre. I would also like to thank Dr. K. Jurkschat for training and advising me on the intricacies of the Mastersizer measurements.

I am grateful for having had the opportunity to work with all the members of the CRMG Group, both past and present, particularly Haibo Jiang, Tayebeh Mousavi, and Greg Brittles, all of whom have been great sources of knowledge and good friends throughout the years. A shout out goes to Hanis Ayuni for always being a good listener and her abundance of kind words, comfort, and a shoulder to cry on.

Most important of all, I would like to thank my family and friends for their unconditional love and support. My family (Sareah Yaacob and Mohd Janurudin) have been my greatest supporters and a boundless source of motivation and encouragement. Last, but certainly not least, I would like to thank my husband, Syed Mohd Nooh, for being here and whose love and support was essential in the final months leading to the completion of this thesis.

Glossary

SRR	Split-ring resonator
HTS	High temperature superconductor
YBCO-123	$YBa_2Cu_3O_7$
YBCO-211	Y_2BaCuO_5
YBCO	Y-Ba-Cu-O, any of the above two materials
T_c	Superconducting transition temperature
K	Kelvin
BSCCO-2223	$Bi_2Sr_2Ca_2Cu_3O_{10}$
BSCCO-2212	$Bi_2Sr_2Ca_1Cu_2O_8$
BSCCO	Bi-Sr-Ca-Cu-O, any of the above two materials
ε	Dielectric constant
ε_r	Relative dielectric constant
μ	Permeability
μ_r	Relative magnetic permeability
μ_{eff}	Effective magnetic permeability
ε_{eff}	Effective dielectric constant
n	Refractive index
η	Wave impedance
N	Complex refractive index
c	Speed of light in vacuum
v	Phase velocity of light in a medium
$BaTiO_3$	Barium Titanate
k	Loss effects in the media
ε_r'	Real dielectric constant
μ_r'	Real magnetic permeability
ε_r''	Dielectric loss
μ_r''	Magnetic loss
δ	Phase difference between the dielectric loss and the dielectric constant
LTS	Low temperature superconductors
MRI	Magnetic resonance imaging
d.c.	Direct current

J_c	Critical current density
H_c	Critical magnetic field
χ_m	Magnetic susceptibility
H	External magnetic field
ZFC	Zero-field cooled
μ_0	Magnetic permeability of vacuum
FC	Field-cooled
H_{c1}	Lower critical field
H_{c2}	Upper critical field
n_n	Density of normal electron
n_s	Density of superconducting electron
a.c	Alternating current
BCS	Bardeen- Cooper and-Schrieffer theory
f_{gap}	Gap frequency
h	Planck's constant
κ_B	Boltzmann's constant
B	Magnetic flux
λ	Penetration depth
λ_L	London penetration depth
e	Carrier charge of superconducting electrons
m	Mass of superconducting electrons
r	Size of the powder particles in radius
Z_s	Surface impedance
R_S	Real part of surface impedance, surface resistance
X_S	Imaginary part of surface impedance, surface reactance
ω	Angular frequency
σ	Conductivity
ABS	Acrylonitrile Butadine Styrene
RF	Radio frequency
Nb	Niobium
SR	Spiral resonator
PMMA	Poly(methyl methacrylate)
TSMG	Top seeded melt growth
AM	Additive manufacturing
SLS	Selective Laser Sintering

FDM	Fused deposition modelling
PVB	Polyvinylbutyral
PDMS	Polydimethylsiloxane
BBNT	Bi-Ba-Nd-TiO_3
PVDF	Polyvinylidene fluoride
VNA	Vector network analyser
DUT	Device-under-test
MUT	Material-under-test
S_{11}	Scattering parameters, return loss
S_{21}	Scattering parameters, insertion loss
NRW	Nicolson-Ross-Weir equation
TRL	Through, reflect and line calibration
MPMS	Magnetic properties measurement system
SQUID	Superconducting quantum interference device
XRD	X-ray diffraction
SEM	Scanning electron microscopy
EDS	Energy dispersive detector
EDX	Energy dispersive X-ray analysis
PTFE	Polytetrafluoroethylene, Teflon
RSD	Relative standard deviation
SE	Secondary electron
BSE	Back-scattered electron
STL	Standard tessellation language
CAD	Computer-aided design
PCB	Printed circuit board
f_c	Critical volume fraction
ϕ	Diameter

CONTENTS

Chapter 1: Introduction

1 Introduction 1

Chapter 2: Introduction to Metamaterials

2.1 A Brief History of Metamaterials 5
2.2 The Concept of Metamaterials 7
2.2.1 Effective Medium Approach 7
2.2.2 Split-Ring Resonator (SRR) 8
2.2.3 Characterisation of Metamaterials 9
2.3 Composite Media 10
2.4 Characterisation of Composite Media 12
2.5 Summary 13
References 14

Chapter 3: Superconducting Materials

3.1 A Brief Introduction to Superconducting Materials 16
3.1.1 Low Temperature Superconductors (LTS) 17
3.1.2 High Temperature Superconductors (HTS) 17
3.2 Theories of Superconductivity 18
3.2.1 Critical Parameters 18
3.2.2 The Meissner Effect 19
3.2.3 Magnetic Behaviour of Type II Superconductors 20
3.2.4 The Two-Fluid Model 22
3.2.5 The BCS Theory 23
3.2.6 Penetration Depth 24
3.2.7 Microwave Properties of Superconductors 25
References 27

Chapter 4: Superconducting Metamaterials for Microwave Applications

4.1 The Advantages of Superconductors in Metamaterials 30

4.1.1 Devices Containing Superconductors 30

4.2 Superconducting Composites 31

4.2.1 High Frequency Response of HTS Loaded Composites 32

4.3 Materials Selection for Superconducting Composites 40

4.3.1 Selection of HTS Materials 40

4.3.2 Introduction to YBCO and BSCCO 41

4.4 Factors Affecting the Superconducting Properties of HTS Powders 43

4.4.1 Factors Affecting $\boldsymbol{Tc}$ 43

4.4.2 Effect of Oxygen Stoichiometry 43

4.4.3 The Important of Microstructure 45

4.4.4 Factors Affecting Magnetic Susceptibility 45

4.4.5 Bulk HTS Processing 47

4.5 Materials Selection for the Polymer Matrix 50

4.5.1 Epoxy Resins 51

4.5.2 Acrylonitrile Butadine Styrene (ABS) 53

References 55

Chapter 5: Fabrication of Superconducting Composites

5.1 Polymer Composite Fabrication 62

5.1.1 Casting 63

5.1.2 Extrusion 64

5.1.3 Additive Manufacturing (3-D Printing) 67

5.2 Factors Affecting Fabrication of Superconducting Composites 70

5.2.1 Fillers 70

5.2.2 Environmental Effects 71

5.3 Factors Affecting Electromagnetic Properties of Superconducting Composites 71

5.3.1 Homogenisation 74

5.3.2 Application of Mixing Rules 75

5.4 Summary 79

References 80

Chapter 6: Experimental methods

6.1 Preparation of HTS Filler Powders 84

6.1.1 Melt-Grown $YBa_2Cu_3O_7$ 85

6.2 HTS Composite Fabrication 87

6.2.1 Casting Process 87

6.2.2 Preparation of HTS/ABS Powder 88

6.2.3 Extruding HTS/ABS Filaments 88

6.3 Electromagnetic Properties 89

6.3.1 Measurement of Scattering Parameters 90

6.3.2 Waveguide Measurements 91

6.3.3 Permittivity and Permeability Measurements 92

6.4 Characterization of Superconducting Properties 97

6.4.1 Transition Temperature 98

6.4.2 Magnetic Hysteresis 99

6.5 Microstructural Characterisation Techniques 99

6.5.1 X-ray Diffraction 99

6.5.2 Mastersizer 101

6.5.3 Scanning Electron Microscopy 103

References 107

Chapter 7: Processing and Characterization of Superconducting Powder

7.1 Types of Superconducting Powder 110

7.2 BSCCO Powder 110

7.2.1 Characterisation of Precursor BSCCO Powder 111

7.3 YBCO Powder 116

7.3.1 Characterisation of commercial YBCO Powder 117

7.3.2 Top Seeded Melt Growth (TSMG) YBCO bulk 123

7.3.3 Characterisation of Melt-Grown YBCO Powder 124

7.3.4 Comparison of Magnetisation Properties of YBCO Powder 128

7.4 Effect of Particle Sizes on Magnetisation Properties 131

7.4.1 Characterisation and Classification of YBCO Particles 132

7.5 Discussion and Conclusions 136

7.5.1 Selection Process for Melt-Grown YBCO Bulks 136

7.5.2 Effect of Ball milling, Grinding and Sieving Processes on The Magnetisation Properties of YBCO Powder 137
7.5.3 Conclusions 139
References 140

Chapter 8: Fabrication of HTS Composites by Casting

8.1 Making HTS Composites 144
8.1.1 Mixing 144
8.1.2 Fabricating a Mould 146
8.2 Distribution of Particles in HTS Composites 148
8.2.1 Dispersion Patterns 149
8.2.2 Effect of Powder Concentration 152
8.3 Effect of Filler 154
8.3.1 Microstructure Studies 155
8.3.2 Magnetic Levitation Tests 160
8.3.3 Static Magnetisation Measurements 161
8.3.4 Microwave Properties 164
8.4 Effect of Volume Loading 169
8.4.1 Microstructure Studies on HTS Composites 171
8.4.2 Quantitative Analysis of Particle Distribution in the HTS Composites . 178
8.4.3 Microwave Properties of HTS Composites 181
8.4.4 Magnetisation Properties 195
8.4.5 Susceptibility of the HTS Composites 198
8.5 Discussion and Conclusions 205
8.5.1 Influence of Sizes and Volume Fraction of YBCO fillers on Microwave Properties of the HTS composites 206
8.5.2 Effect of Casting Technique on Microstructure of HTS Composites 207
8.5.3 Conclusions 208
References 210

Chapter 9: Fabrication of HTS Composites by 3-D Printing

9.1 Making YBCO/ABS Composites 214
9.2 Extrusion of YBCO/ABS Filaments 215

9.2.1 Optimising Extrusion for YBCO Loaded ABS Filaments 216
9.2.2 Distribution of YBCO Particles in The ABS filament 219
9.2.3 Effect of Particle Size on The Extrusion Process 223
9.2.4 Magnetisation Properties of YBCO Loaded ABS Filaments 226
9.2.5 Magnetic Susceptibilities and Permeability of YBCO Loaded ABS Filaments 229
9.3 3-D Printing Process 230
9.3.1 Optimising 3-D Printing Parameters 230
9.4 Characterisation of 3-D Printed YBCO/ABS Composites 234
9.4.1 Single Printed Material 235
9.4.2 Graded Materials 246
9.4.3 3-D Printed Split-Ring Resonator Structures (SRRs) 254
9.5 Discussion and Conclusions 260
References 262

Chapter 10: Conclusions and Suggestions for Further Work 265

Appendix

1 Introduction

Metamaterials are artificially designed media with the ability to exhibit electromagnetic properties that cannot be found in nature. The earliest concept of metamaterials is as "Left-Handed Substances" with the electromagnetic properties of negative permittivity and permeability, and was first introduced by Veselago in 1968[1], and later forgotten due to the difficulty of finding materials with these specific electromagnetic properties. The discovery of *effective media* consisting of array structures in which the size of the unit cell is small compared to the desired operation wavelengths by Pendry in 1999[2] caused great attention amongst the scientific community, and raised the possibility of manufacturing and designing metamaterials that could control the propagation of waves by their electromagnetic properties.

In order for the metamaterials phenomenon to occur, the size of unit cells must be smaller than the desired operation wavelength and arranged in periodic arrays. The electromagnetic waves that pass through the material will interact with the arrays of unit cells as a homogeneous and continuous medium, and be affected by the electromagnetic properties of this medium as a whole[3].

Most work on metamaterials has concentrated on microwave and optical wavelengths, and has focussed on developing media with negative refractive index behaviour[4,5]. This can be done by combining unit cells of conducting wire grids and split-ring resonators (SRR) to provide both a negative permittivity and permeability[6]. These unit cells are arranged in periodic lattices with both size and separation considerably smaller than the wavelength, in order to exhibit a macroscopic response from a structure that behaves like a single homogenous material; the effective medium approach.

Due to the macroscopic response of an effective medium, electromagnetic properties can also be tailored using randomly distributed inclusions in a host matrix. The electromagnetic properties of this type of effective media are controlled by a combination of the properties of both discrete inclusions and host matrix. The electromagnetic properties of these composite materials can be modelled using established mixing rules[7]. These dispersive characteristics depend on the size of inclusions and volume fractions of both inclusions and matrix, leading to non-resonant effective dielectric and magnetic properties with potential broadband metamaterials applications[8].

The discovery of high temperature superconductors (HTS) in 1986 by Bednorz and Muller[9], has opened many possible applications for superconductivity above the temperature of liquid nitrogen. Despite their unique superconducting properties, as ceramic materials these superconductors are inherently brittle and therefore difficult to shape and fabricate into devices and products. Nies *et al.* introduced the first superconducting composites by mixing $YBa_2Cu_3O_7$ powder with a glass matrix[10]. These HTS composites demonstrated superconducting properties (such as a strong Meissner effect below the transition temperature (T_c)) and good electromagnetic properties, with potential applications such as levitating or electromagnetic devices[10,11]. However, the widespread implementation of HTS composites has been delayed due to intractable material science issues in fabricating structures with the required electromagnetic properties. In fact, large scale manufacturing for all HTS composites with controllable electromagnetic properties is one of many issues limiting HTS composite development.

The first metamaterials using superconductors were introduced in 2005 by Ricci[12], demonstrating potential applications for switching devices. The unique properties of superconductors, with transition temperature (T_c) and Meissner effect ($\mu = 0$) in low

fields and at low temperature, can be exploited in many applications from switching to electronic and magnetic devices. HTS materials may be preferable in these applications due to their higher transition temperatures (mostly above 77 K) compared to conventional superconductors, thus greatly reducing cooling costs and allowing for easy commercial application.

Strong diamagnetic response of an HTS powder with high transition temperature is required for any HTS composites application. High T_c values can be achieved in cuprate-based superconductors such as $YBa_2Cu_3O_7$ (YBCO-123), but the $Bi_2Sr_2Ca_2Cu_3O_x$ (BSCCO-2223) HTS superconductor has the advantage of significantly higher T_c. Both materials were investigated in the work reported in this thesis. HTS phases tend to be brittle in nature and are relatively difficult to fabricate into superconducting metamaterials devices, and this has limited the number of researchers working on superconductors. Therefore, a reliable and reproducible fabrication technique is required for metamaterials applications. The processability of HTS composites for metamaterials applications will be discussed in Chapters 4 and 5.

Chapter 2 and Chapter 3 describe the concept of metamaterials and use of superconductors for microwave applications. For further details on metamaterials, the reader is referred to "Theory and Phenomena of Metamaterials" by F. Capolino, and for an introduction to superconducting applications "Foundation of Applied Superconductivity" by T. P. Orlando is highly recommended. The following chapters aim to provide a background and critical overview of the materials considerations in the processing of superconducting metamaterials for potential microwave device applications.

References

1 Veselago, V. G. The electrodynamics of substances with simultaneously negative values of ε and μ. *Sov. Phys. Usp.* **10**, 509-514 (1968).

2 Pendry, J. B., Holden, A. J., Robbins, D. J. & Stewart, W. J. Magnetism from conductors and enhanced nonlinear phenomena. *Microwave Theory and Techniques, IEEE Transactions on* **47**, 2075-2084 (1999).

3 Solymar, L. & Shamonina, E. *Waves in metamaterials*. pp. 35-74 (Oxford University Press, 2009).

4 Smith, D. R., Pendry, J. B. & Wiltshire, M. C. K. Metamaterials and Negative Refractive Index. *Science* **305**, 788-792 (2004).

5 Smith, D. R. & Kroll, N. Negative refractive index in left-handed materials. *Physical Review Letters* **85**, 2933 (2000).

6 Shelby, R. A., Smith, D. R., Nemat-Nasser, S. C. & Schultz, S. Microwave transmission through a two-dimensional, isotropic, left-handed metamaterial. *Applied Physics Letters* **78**, 489-491 (2001).

7 Sihvola, A. H. *Electromagnetic mixing formulas and applications*. pp. 20-200 (Institution of Electrical Engineers, 1999).

8 Sihvola, A. H. Metamaterials in electromagnetics. *Metamaterials* **1**, 2-11 (2007).

9 Bednorz, J. G. & Müller, K. A. Possible high T_c superconductivity in the Ba−La−Cu−O system. *Zeitschrift für Physik B Condensed Matter* **64**, 189-193 (1986).

10 Nies, C. W. *et al.* Glass-bonded composites containing superconducting $YBa_2Cu_3O_{9-y}$ for levitation and magnetic shielding applications. *Materials Research Bulletin* **23**, 623-630 (1988).

11 Golosovsky, M., Tsindlekht, M. & Davidov, D. Microwave propagation through superconductor-polymer composites. *Physical Review B* **46**, 11439-11444 (1992).

12 Ricci, M., Orloff, N. & Anlage, S. M. Superconducting metamaterials. *Applied Physics Letters* **87**, 034102 (2005).

2 Introduction to Metamaterials

2.1 A Brief History of Metamaterials 5
2.2 The Concept of Metamaterials 7
2.2.1 Effective Medium Approach 7
2.2.2 Split-Ring Resonator (SRR) 8
2.2.3 Characterisation of Metamaterials 9
2.3 Composite Media 10
2.4 Characterisation of Composite Media 12
2.5 Summary 13
References 14

Metamaterials are artificial materials which are engineered to produce electromagnetic properties that cannot be found in nature[1]. In this chapter, the concept of metamaterials and the effective medium approach are discussed, with particular emphasis on composite media of spherical particles randomly scattered in a polymer matrix.

2.1 A Brief History of Metamaterials

In his attempt to find materials with negative refractive index properties, Veselago introduced a diagram to classify isotropic materials based on their dielectric constant (ε) and permeability (μ) values (Figure 2.1). Veselago theoretically predicted that the negative refractive index properties could be achieved in a material with $\varepsilon < 0$ and $\mu < 0$, which later became known as "Left-Handed Metamaterials", or "Double Negative Metamaterials"[1-5].

At that time the physical properties of the Left-Handed Metamaterials were beyond realisation, and the subject lay dormant for several decades until Pendry *et al.*[6] introduced an artificial structure made from non-magnetic sheets of conducting

materials with the potential to exhibit effective magnetic permeability (μ_r) values far from unity.

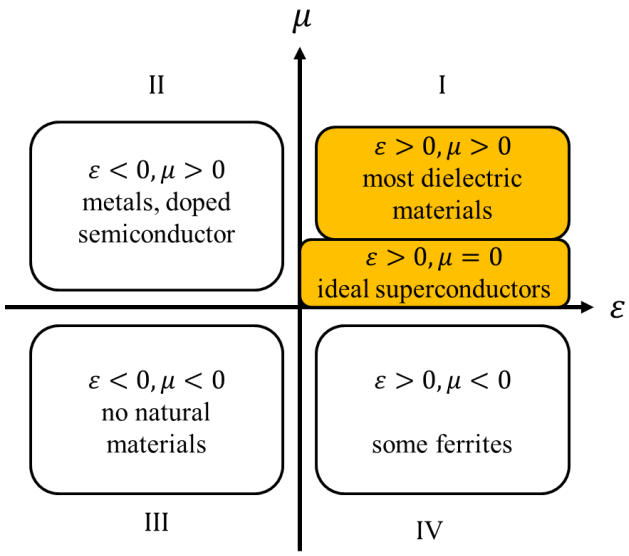


Figure 2.1 μ − ε diagram. Superconductors are categorised in group I with $\varepsilon > 0$ and $\mu > 0$ above its transition temperature. However, below the transition temperature, ideal superconductors are diamagnetic with $\mu = 0$ (Magnetic susceptibility, $\chi = -1$)[7]. The dielectric constants of superconductors are above 0 ($\varepsilon > 0$) below the transition temperature[8,9]. Figure adapted from Liu *et al.*[5], with permission of The Royal Society of Chemistry.

These artificial structures, like the Swiss Roll (Figure 2.2 (right image)) and Split-Ring Resonators (SRR) (Figure 2.2 (left image)) structures, responded to specific electromagnetic wavelengths and the μ_r values could be tuned by varying the types, structures and sizes of the artificial structures[10-12]. This led to a major breakthrough in the concept of the effective magnetic permeability, and sparked a great deal of interest in the field of metamaterials.

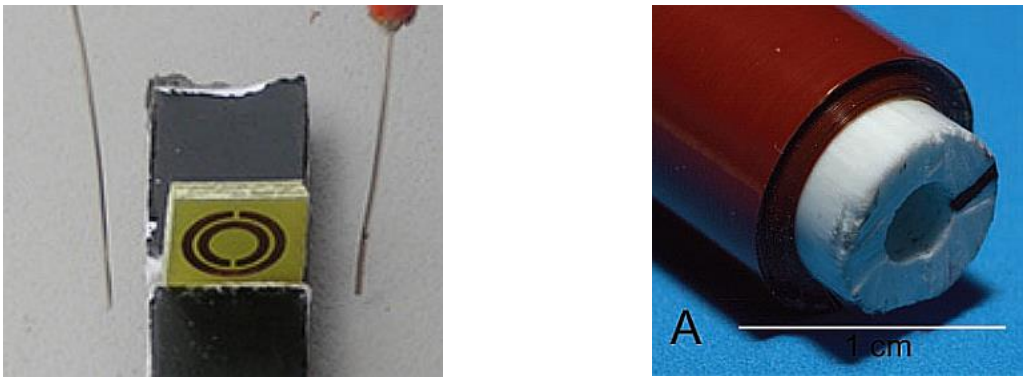


Figure 2.2 An SRR unit cell structure (left image) reprinted from Aydin *et al.*[12]. A Swiss Roll unit cell structure (right image) reprinted after Wiltshire *et al.*[10], with permission from AAAS.

2.2 The Concept of Metamaterials

Metamaterials are artificial materials in which the electromagnetic properties can be controlled using tailored permittivity and permeability values created by arranging periodic arrays of metallic resonant elements or unit cell structures[13]. In metamaterials, instead of the nature and arrangement of the atoms governing the permittivity and permeability of the material, resonant elements are arranged into arrays or lattices. These structures will act as effective media, with the dimensions, arrangement and material choice in the individual elements of the array acting as control parameters to achieve homogeneity in electromagnetic properties.

2.2.1 Effective Medium Approach

Metamaterial behaviour can be described using both microscopic and macroscopic approaches. In the microscopic response, the artificial media consists of individual elements (unit cells) which are arranged in arrays into a periodic lattice[14] (Figure 2.3). These ensembles are similar to those in natural materials except for having a larger scale.

Each unit cell has their own resonant frequency, and couple to neighbouring elements to produce characteristic waves at the desired operational wavelengths[14]. In addition, materials, shape, density, arrangement and alignment of these unit cells in this artificial media also determine the macroscopic response of the artificial structure and control the electromagnetic properties (isotropic or anisotropic).

In the macroscopic view, the size of the unit cells and the lattice spacing must be less than the desired wavelengths in order to achieve an effective homogeneity of properties in the artificial media. As a homogeneous effective medium, the details of the unit cell materials are ‘invisible’ to the propagating waves, and the medium can be characterised

by electromagnetic constants of effective dielectric constant (ε_{eff}) and magnetic permeability (μ_{eff}).

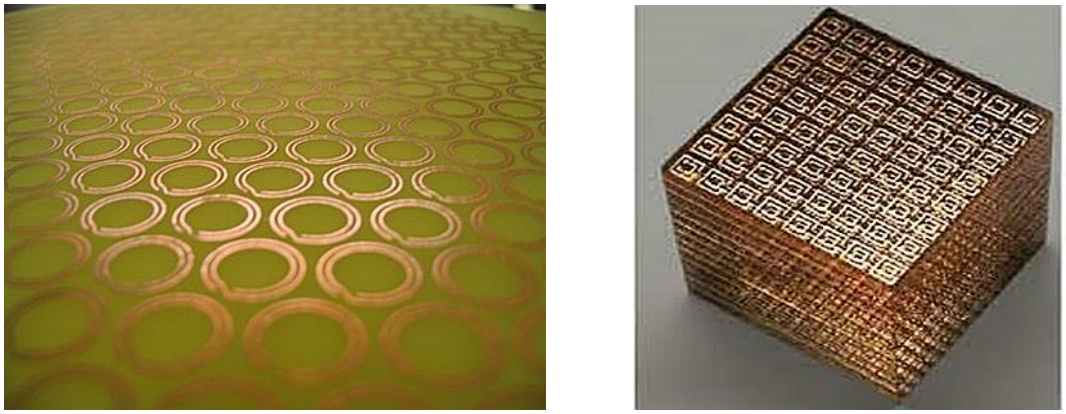


Figure 2.3 The arrangement of unit cells into arrays courtesy of Professor C. J. Stevens, University of Oxford (left image) in a hexagonal metamaterials lens plate, and a periodic 3-D lattice (right image) of 'The Boeing cube' for metamaterial devices in the GHz range. Figure reproduced from Pendry *et al.*[15], with permission of the American Institute of Physics.

2.2.2 Split-Ring Resonator (SRR)

In his mission to find materials with effective negative permeabilities, Veselago proposed several anisotropic and gyrotropic materials such as pure ferromagnetic elements and semiconductors that can exhibit negative μ_r values due to how their permeability tensor responds to electromagnetic plane waves[2]. A few decades later, Pendry *et al.* demonstrated that μ_{eff} behaviour that can be achieved using conducting shaped resonator structures, which can be controlled by tuning the size, shape, conducting material and arrangement of the unit cells[6]. Since then, a lot of papers on the theories, simulations and even fabrication of artificial magnets have been published based on these resonator structures[16-19].

A split-ring resonator (SRR) is a structure in which responds strongly to an incident magnetic field, and can be developed from a conductive loops with a small gap removed to form a "C" shape. SRR structures normally have two conductive loops arranged concentrically, Figure 2.4 (left image). These loops are considered as a unit cell of the

artificial magnetic material. Pendry demonstrated that SRRs can produce magnetic resonances at GHz frequencies, giving a practical scalable structure for an effective magnetic medium at microwave frequencies[6]. Swiss Rolls are another type of resonator reported to operate efficiently at frequencies as low as 5 MHz[10] (Figure 2.4 (right image)). Swiss Rolls are resonators with several turns of metal/dielectric laminate onto a cylindrical form, which looks like a spiral at the cross section[20]. The magnetic amplitude and frequency bandwidth of the magnetic response can be improved by assembling unit cells into a bulk structure[6,14].

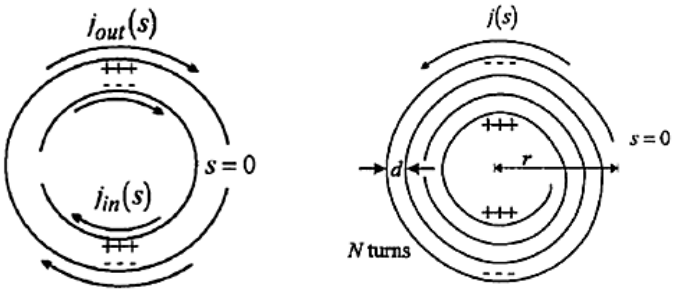


Figure 2.4 A schematic design of SRR (left image) and Swiss Roll (right image) unit cells. Figures reproduced from Pendry *et al.*[6] with permission. Copyright © 1999, IEEE.

2.2.3 Characterisation of Metamaterials

Artificial media structures can be described by their ε_{eff} and μ_{eff} values, which determine the macroscopic response of electromagnetic waves propagating in homogenously structured metamaterial. The macroscopic response can be the refractive index (n) which is given by,

$$n = \frac{c}{v} = \sqrt{\varepsilon_{eff}\mu_{eff}} \tag{2.1}$$

where $c = 3 \times 10^8$ m/s is the velocity of propagation of electromagnetic waves in free space and v is the velocity of propagation in a material. In the simplest case of wave propagation in a uniform medium, the relation of refractive index and the electromagnetic properties of a metamaterial can be written as,

$$n = \pm\sqrt{\varepsilon_{eff}\mu_{eff}} \tag{2.2}$$

The ± symbol indicates that either positive and negative refractive index values can be achieved in a medium, with positive n values if both ε_{eff} and μ_{eff} are positive, and negative n values if both ε_r and μ_r are negative. The sign will also determine the direction of wave propagation in the media. The metamaterials can also be characterised using the wave impedance (η) which is given by,

$$\eta = \pm\sqrt{\mu_{eff}/\varepsilon_{eff}}. \tag{2.3}$$

From above equations, key metamaterial properties can be defined using the four parameters ε_{eff}, μ_{eff}, n and η, where both ε_{eff} and μ_{eff} can be measured using readily available techniques such as rectangular waveguide and split post dielectric resonator methods[21].

2.3 Composite Media

In order to avoid the fabrication of complex 3-D metamaterials structures, effective media can be synthesised as composite media by mixing various types of inclusions in a host matrix[14,22]. The calculation of the ε_{eff} and μ_{eff} values of composite mixtures with periodically arranged spherical particle inclusions was done by Lewin[23] and Holloway *et al.*[24] in an early investigation of a homogenous matrix with embedded spherical particles (Figure 2.5 (left image)). However, randomly scattered particle inclusions also provide unusual properties in composite media[22,25] (Figure 2.5 (right image)). These composite materials can be conveniently tailored to achieve both desired ε_{eff} and μ_{eff} values based on their individual component properties and fractions[26]. The efficiency and accuracy of this technique in developing new composite materials can be predicted with known effective medium theories such as Maxwell-Garnett[27] or Bruggeman[28].

The electromagnetic properties of the composite media depend strongly on the type of particle inclusions selected. Grant *et al.* in a recent paper to which I contributed reported that the electromagnetic properties of this kind of polymer-based composite can be categorised into three groups based on the filler properties, dielectric, magnetic and superconducting[29]. In these polymer composite media, electromagnetic waves interact with randomly scattered inclusions, inducing electric and magnetic moments, that affect the electromagnetic properties of the bulk composite "medium"[30].

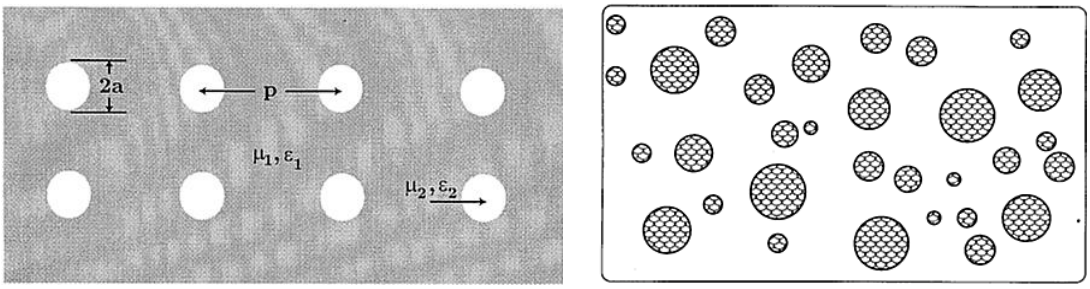


Figure 2.5 A schematic drawing of periodically arranged spherical inclusions in a host matrix (left image) after Holloway *et al.*[24]. Copyright © 2003, IEEE. Randomly scattered spherical particle inclusions embedded homogeneously in a host matrix (right image) after Sihvola[25]. Reprinted with permission of Springer Nature. ε_1 and μ_1 are electromagnetic properties of the host matrix and ε_2 and μ_2 for the particle inclusions.

For a random and well-dispersed particle distribution, the composite medium exhibits a non-resonant response to generate effective medium properties that can be characterised by ε_{eff} and μ_{eff} values often over wide frequency ranges[29]. These effective electromagnetic properties can be controlled by the volume fraction of particles, which is often limited by the degrading mechanical properties of the composite thus reducing "processability".

Fabricating metamaterials using composite materials was reported to be less complex than shaped-conducting structures, and importantly non-resonant broadband electromagnetic response can be obtained[24]. The ease of fabrication of composite materials has attracted several groups to produce and manufacture these composite materials with desired ε_{eff} and μ_{eff} properties for potential microwave applications.

For example, graded dielectric structures of $BaTiO_3$/epoxy composites were developed for a metamaterials lens design, with ε_{eff} values ranging from approximately 5 up to 17 by controlling the volume fraction of $BaTiO_3$ particles[29]. Wang *et al.* fabricated ferrite/epoxy composites for impedance-matching antenna applications by achieving both ε_{eff} and μ_{eff} values of 6 using $Ni_{0.4}Zn_{0.6}Fe_2O_4$ ferrite particle for operation over the frequency range 5-100 MHz[31].

2.4 Characterisation of Composite Media

Dilute inclusions in a polymer media can be easily measured for their dielectric constant (ε_r) and magnetic permeability (μ_r)[32]. If the particle size of the dielectric, magnetic or superconducting in the medium is small compared to the operating wavelength, the scattering of waves is negligible and wave propagation behaves like a macroscopic response in a continuous media. The wave propagation can then be described by its complex refractive index, N, which is determined from electromagnetic components ε_r and μ_r as given in equation (2.4), where n is the real refractive index and k describes loss effects in the media[33].

$$N = n + ik = \sqrt{\varepsilon_r \mu_r} \tag{2.4}$$

Both ε_r and μ_r values can then be compared with the effective medium models by considering the sizes and shapes of well-dispersed particles in a composite media. Complex ε_r and μ_r values can be written as[34],

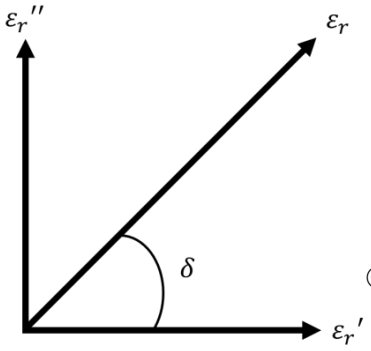
$$\varepsilon_r = \varepsilon_r' - j\varepsilon_r'' \tag{2.5}$$

$$\mu_r = \mu_r' - j\mu_r'' \tag{2.6}$$

where ε_r' and μ_r' are the real and the imaginary parts respectively, ε_r'' is the dielectric loss factor, and μ_r'' is the magnetic loss. The loss tangent measurement can be obtained by calculation of $\tan\delta$ in equation 2.7,

$$\tan\delta = \frac{\varepsilon_r''}{\varepsilon_r'} \tag{2.7}$$

where δ is the phase difference between the dielectric loss and the dielectric constant (Figure 2.6)[35].



© Keysight Technologies, Inc

Figure 2.6 A sketch of complex dielectric constant (ε_r) and loss tangent ($\tan\delta$) vector diagram. $\delta = 90°$ if there is no loss in the dielectric, and δ < 90º with loss. Figure adapted with permission, Courtesy of Keysight Technologies, *Keysight Basics of Measuring the Dielectric Properties of Materials Application note, 2012*[36].

2.5 Summary

The electromagnetic properties of metamaterials can be defined by their ε_{eff} and μ_{eff} values, and depend strongly on the size, shape and arrangement of the constitutional elements in a lattice or random structure.

In order for metamaterials to behave as an effective media with respect to electromagnetic waves propagation, the size of unit cells or resonators must be smaller than the operational wavelength. This means that for operation in the microwave frequency range, the size and separation of resonators must be at the mm scale. A combination of discrete filler particles in a polymer based matrix can exhibit macroscopic effective medium response. This type of polymer based composite is easier to fabricate than the conventional wire grids and SRR structures to produce effective media for microwave applications, and the electromagnetic properties of these composite media can be controlled by tuning the particle size and volume fractions of selected fillers. The experimental work described in this thesis concerns the preparation

and measurement of the properties of superconductor/polymer composites for operation in the microwave frequency range.

References

1 Sihvola, A. H. Metamaterials in electromagnetics. *Metamaterials* **1**, 2-11 (2007).

2 Veselago, V. G. The electrodynamics of substances with simultaneously negative values of ε and μ. *Sov. Phys. Usp.* **10**, 509-514 (1968).

3 Smith, D. R., Pendry, J. B. & Wiltshire, M. C. K. Metamaterials and Negative Refractive Index. *Science* **305**, 788-792 (2004).

4 Smith, D. R. & Kroll, N. Negative refractive index in left-handed materials. *Physical Review Letters* **85**, 2933 (2000).

5 Liu, Y. & Zhang, X. Metamaterials: a new frontier of science and technology. *Chemical Society Reviews* **40**, 2494-2507 (2011).

6 Pendry, J. B., Holden, A. J., Robbins, D. J. & Stewart, W. J. Magnetism from conductors and enhanced nonlinear phenomena. *Microwave Theory and Techniques, IEEE Transactions on* **47**, 2075-2084 (1999).

7 Campbell, A., Blunt, F., Johnson, J. & Freeman, P. Quantitative determination of percentage superconductor in a new compound. *Cryogenics* **31**, 732-737 (1991).

8 Schwan, C. *et al.* Preparation, Characterisation and Dielectric Properties of $YBa_2Cu_3O_{7-\delta}$/Insulator-Heterostructures. *Le Journal de Physique IV* **6**, pp. 321-325 (1996).

9 Nakajima, K., Yokota, K., Myoren, H., Chen, J. & Yamashita, T. Field effects on the dielectric property of YBCO bicrystal grain boundary junctions. *IEEE Transactions on Applied Superconductivity* **5**, 2861-2864 (1995).

10 Wiltshire, M. C. *et al.* Microstructured magnetic materials for RF flux guides in magnetic resonance imaging. *Science* **291**, 849-851 (2001).

11 Freire, M. J., Marques, R. & Jelinek, L. Experimental demonstration of a mu=-1 metamaterial lens for magnetic resonance imaging. *Applied Physics Letters* **93**, 231108 (2008).

12 Aydin, K. *et al.* Investigation of magnetic resonances for different split-ring resonator parameters and designs. *New Journal of Physics* **7**, 168 (2005).

13 Solymar, L. & Shamonina, E. *Waves in metamaterials*. pp. 35-74 (Oxford University Press, 2009).

14 Capolino, F. & Wiltshire, M. C. K. *Theory and Phenomena of Metamaterials: RF Metamaterials*. pp. 14-1 to 14-7 (CRC Press, 2009).

15 Pendry, J. B. & Smith, D. R. Reversing light with negative refraction. *Physics today* **57**, 37-43 (2004).

16 Shamonina, E. & Solymar, L. Properties of magnetically coupled metamaterial elements. *Journal of Magnetism and Magnetic Materials* **300**, 38-43 (2006).

17 Shamonina, E., Kalinin, V. A., Ringhofer, K. H. & Solymar, L. Magnetoinductive waves in one, two, and three dimensions. *Journal of Applied Physics* **92**, 6252-6261 (2002).

18 Gorkunov, M., Lapine, M., Shamonina, E. & Ringhofer, K. H. Effective magnetic properties of a composite material with circular conductive elements. *Eur. Phys. J. B* **28**, 263-269 (2002).

19 Belov, P. A. & Simovski, C. R. Homogenization of electromagnetic crystals formed by uniaxial resonant scatterers. *Physical Review E* **72**, 026615 (2005).

20 Wiltshire, M. C. K. Tuning Swiss roll metamaterials. *Journal of Physics D: Applied Physics* **42**, 205001 (2009).

21 Barry, W. A Broad-Band, Automated, Stripline Technique for the Simultaneous Measurement of Complex Permittivity and Permeability. *IEEE Transactions on Microwave Theory and Techniques* **34**, 80-84 (1986).

22 Sihvola, A. H. *Electromagnetic mixing formulas and applications*. pp. 20-200 (Institution of Electrical Engineers, 1999).

23 Lewin, L. The Electrical Constants of a Material Loaded with Spherical Particles. *Journal of the Institution of Electrical Engineers - Part III: Radio and Communication Engineering* **94**, 65-68 (1947).

24 Holloway, C. L., Kuester, E. F., Baker-Jarvis, J. & Kabos, P. A double negative (DNG) composite medium composed of magnetodielectric spherical particles embedded in a matrix. *IEEE Transactions on Antennas and Propagation* **51**, 2596-2603 (2003).

25 Sihvola, A. Mixing rules with complex dielectric coefficients. *Subsurface Sensing Technologies and Applications* **1**, 393-415 (2000).

26 Zhao, X., Hinchliffe, C., Johnston, C., Dobson, P. J. & Grant, P. S. Spray deposition of polymer nanocomposite films for dielectric applications. *Materials Science and Engineering: B* **151**, 140-145 (2008).

27 Levy, O. & Stroud, D. Maxwell Garnett theory for mixtures of anisotropic inclusions: Application to conducting polymers. *Physical Review B* **56**, 8035-8046 (1997).

28 Bruggeman, D. Dielectric constant and conductivity of mixtures of isotropic materials. *Ann Phys (Leipzig)* **24**, 636-679 (1935).

29 Grant, P. S. *et al.* Manufacture of electrical and magnetic graded and anisotropic materials for novel manipulations of microwaves. *Phil. Trans. R. Soc. A* **373**, 20140353 (2015).

30 Engheta, N. & Ziolkowski, R. W. *Metamaterials: Physics and Engineering Explorations: Introduction, History, And Selected Topics in Fundamental Theories of Metamaterials*. pp. 5-9 (John Wiley & Sons, 2006).

31 Wang, Y., Edwards, E., Hooper, I., Clow, N. & Grant, P. Scalable polymer-based ferrite composites with matching permeability and permittivity for high-frequency applications. *Applied Physics A* **120**, 609-614 (2015).

32 Akhtar, M. J., Feher, L. & Thumm, M. Measurement of dielectric constant and loss tangent of epoxy resins using a waveguide approach. *IEEE Antennas and Propagation Society International Symposium*, pp. 3179-3182 (2006).

33 Golosovsky, M., Tsindlekht, M., Davidov, D. & Sarychev, A. Effective-medium approach to the microwave properties of the high-T_c superconductor-insulator composites. *Physica C: Superconductivity* **209**, 337-340 (1993).

34 Grant, I. S. & Phillips, W. R. *Electromagnetism*. (John Wiley & Sons, 2013).

35 Nelson, S. O. Fundamentals of dielectric properties measurements and agricultural applications. *Journal of Microwave power and electromagnetic energy* **44**, 98-113 (2010).

36 Keysight Technologies, Inc., *Keysight Basics of Measuring the Dielectric Properties of Materials Application Note*, < http://literature.cdn.keysight.com/litweb/pdf/5989-2589EN.pdf > 2017 .

3 Superconducting Materials

3.1 A Brief Introduction to Superconducting Materials 16
3.1.1 Low Temperature Superconductors (LTS) 17
3.1.2 High Temperature Superconductors (HTS) 17
3.2 Theories of Superconductivity 18
3.2.1 Critical Parameters 18
3.2.2 The Meissner Effect 19
3.2.3 Magnetic Behaviour of Type II Superconductors 20
3.2.4 The Two-Fluid Model 22
3.2.5 The BCS Theory 23
3.2.6 Penetration Depth 24
3.2.7 Microwave Properties of Superconductors 25
References 27

3.1 A Brief Introduction to Superconducting Materials

A superconductor is a perfectly conducting material with zero electrical resistance and perfect diamagnetism when cooled below its critical temperature. Superconducting materials mostly find applications in large, high field magnets for health care[1] and scientific instruments[2,3].

Low temperature superconductors (LTS) have been used commercially in applications that require large magnetic fields such as energy storage[3], MRI devices[4,5], and magnetic shielding devices in electric machines[6]. The high critical temperature and trapped field properties of high temperature superconductors (HTS) are attractive for many potential applications that require large magnetic fields[7], levitation in maglev systems[8-10] and for electronic devices operating at 77 K[11,12].

The practical application of superconducting materials depends on the development of reliable fabrication processes, cryogenic cooling systems, reducing the cost of materials

and improving their performance[13-15]. The field trapping ability in bulk HTS materials to produce high magnetic fields has generated an interest in designing controlled fabrication processes for bulk superconductors in the form of large single grains with very high volume magnetisations[16-18]. Some of these materials have provided starting materials for my experiments, and the way they are prepared will be described in section 4.4.5.

3.1.1 Low Temperature Superconductors (LTS)

The first superconducting properties were discovered by Onnes in 1911, when he observed a sudden drop of resistance in mercury to "practically zero" below 4 K[19]. The zero resistance condition in mercury is known as the superconducting state, and the temperature at which the resistance disappears is known as the critical temperature (T_c). In the 60 years after this discovery, more elements, compounds and alloys were discovered to exhibit superconductivity, but the highest T_c measured was only 23 K. Among the elements, niobium has the highest T_c of 9.2 K, and Nb_3Ge the highest T_c found in a compound of 23 K[20]. The alloy Nb-Ti and the compound Nb_3Sn are used as the superconducting wires in high field magnets[21]. However, the breakthrough of the discovery of the first high temperature superconductor in 1986 by Bednorz and Mueller[22], attracted much interest, and a large family of superconductors with transition temperatures above the boiling temperature of liquid nitrogen have subsequently been discovered.

3.1.2 High Temperature Superconductors (HTS)

The first high temperature superconductor (HTS) discovered was a ceramic compound $La_{1.8}Ba_{0.15}CuO_4$ with T_c around 35 K[20]. A major breakthrough was made by Wu *et al.*, who discovered $YBa_2Cu_3O_7$ (YBCO-123) with a transition temperature of 93 K[23],

above the boiling temperature of liquid nitrogen at 77 K. This has sparked a huge worldwide research activity in the commercialization of HTS materials to take advantage of liquid nitrogen as a cheap cryogen. Other cuprate-based HTS superconducting families based on bismuth[24] and thallium[25] were subsequently discovered, with a higher transition temperatures of 110 K and 120 K respectively.

3.2 Theories of Superconductivity

3.2.1 Critical Parameters

Superconducting materials can be characterised by their critical parameters. A perfect superconductor exhibits zero d.c. resistivity below its characteristic critical temperature (T_c). Below this temperature, a superconductor can carry a resistanceless d.c. current, up to another critical value known as the critical current density (J_c). Thus, a superconductor loop with induced current below J_c in the superconducting state will carry a persistent current indefinitely[26].

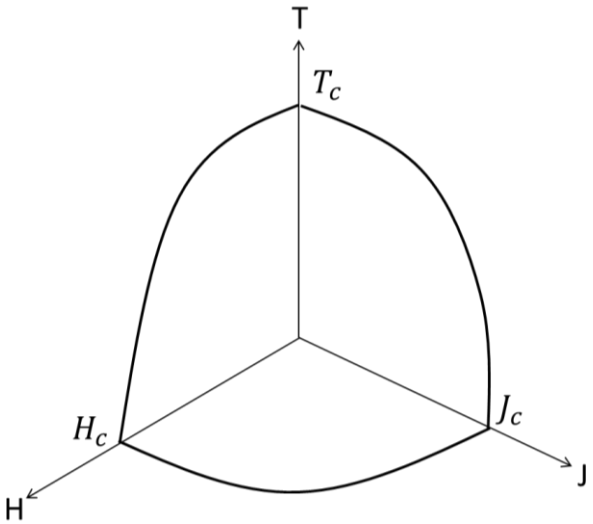


Figure 3.1 Schematic diagram showing the phase space defining the superconducting state. Figure adapted after Orlando *et al.*[20].

The superconducting state is also limited by a thermodynamic critical field parameter, where superconductivity can be destroyed when a superconductor is exposed to a critical magnetic field (H_c)[20]. These critical parameters are interdependent, as shown in

the illustrated phase space diagram in Figure 3.1, so that the critical field depends on both the sample temperature and on the current flowing. The volume bounded by these three critical parameters indicates the conditions under which the superconducting state can exist. Outside this critical region, the material is said to be in the normal state. Both H_c and J_c increase with decreasing temperature below T_c. T_c and $\mathrm{H_c}$ are both intrinsic parameters of a superconducting material, but J_c strongly depends on the physical and metallurgical properties, and especially on the microstructure[26].

3.2.2 The Meissner Effect

As mentioned above, superconductors show diamagnetic properties. A perfect diamagnetic material has a magnetic susceptibility $\chi_\mathrm{m} = -1$ below T_c, indicating that if an external magnetic field ($H < H_c$) is applied to a superconductor, the magnetic field lines are excluded from the material. Due to this diamagnetic property, superconductors tend to minimise the magnetic flux density inside a bulk sample by two processes; *flux exclusion* and *flux expulsion*[27].

Flux exclusion occurs when a superconductor in the normal state is *zero field cooled* (ZFC) cooled without an externally applied magnetic field, and subsequently exposed to an applied magnetic field. Under these conditions, a magnetic field less than H_c is excluded from the superconductor. Flux expulsion occurs when the superconductor in the normal state is placed in an applied magnetic field. The magnetic flux penetrates the superconductor because the μ value of normal material is close to the free space value, μ_0. When the superconductor is field-cooled (FC) with an applied magnetic field to a temperature below T_c, the magnetic flux lines are expelled from the superconductor. This flux expulsion behaviour is a unique property of superconductors, and is called the Meissner effect.

All superconductors exhibit the Meissner effect in the superconducting state. However, only certain elements, alloy and compound superconductors can form a mixed state, which classifies superconductors into type I and type II materials. Type I superconductors, including almost pure elementary superconductors, can only exhibit Meissner states and show perfect diamagnetism below H_c. Type II superconductors can exhibit both Meissner and mixed states, with two critical field values which are the lower critical field, H_{c1} and the upper critical field, H_{c2}. Most commercially important superconducting materials are type II.

3.2.3 Magnetic Behaviour of Type II Superconductors

Type II superconductors are the most useful superconductors. When an applied magnetic field is applied to an ideal type II superconductor, the magnetic characteristic is reversible as shown in Figure 3.2.

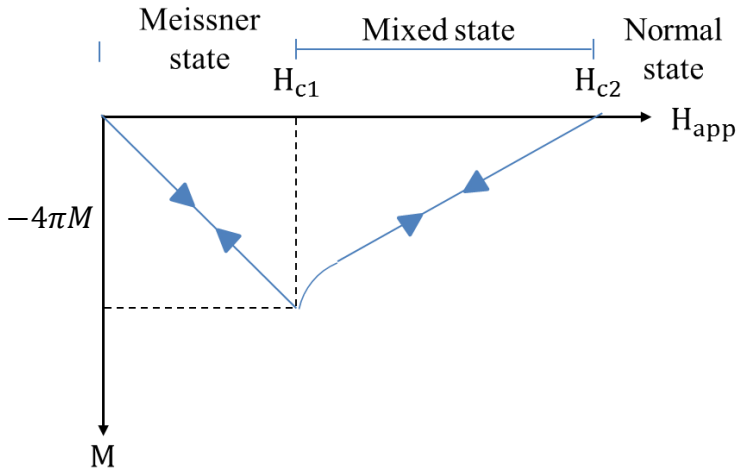


Figure 3.2 A schematic drawing of the reversible magnetisation (indicated by arrows) of a pristine type II superconductor. Figure adapted after McElfresh[28]. Copyright © 2018, Quantum Design, Inc. All rights reserved.

Perfect diamagnetism can be achieved below H_{c1}, where all the applied magnetic field is expelled due to the Meissner effect, similar to a type I superconductor. Above H_{c1}, the superconductor displays a mixed state containing both superconducting and normal regions, where flux begins to penetrate the normal material as quantised flux lines. As

the field is increased further, more flux lines penetrate the material, until H_{c2} where the flux lines completely penetrate the material and the superconducting state is destroyed. Perfect type II superconductors show reversible magnetisation behaviour.

However, type II superconductors often display an irreversible magnetisation characteristic, depending on the magnitude of the applied magnetic field. This magnetisation behaviour can be observed from the classic hysteresis loop as shown in Figure 3.3, where for this sample H_{c1} is at 53 mT and H_{c2} is 4 T[29,30].

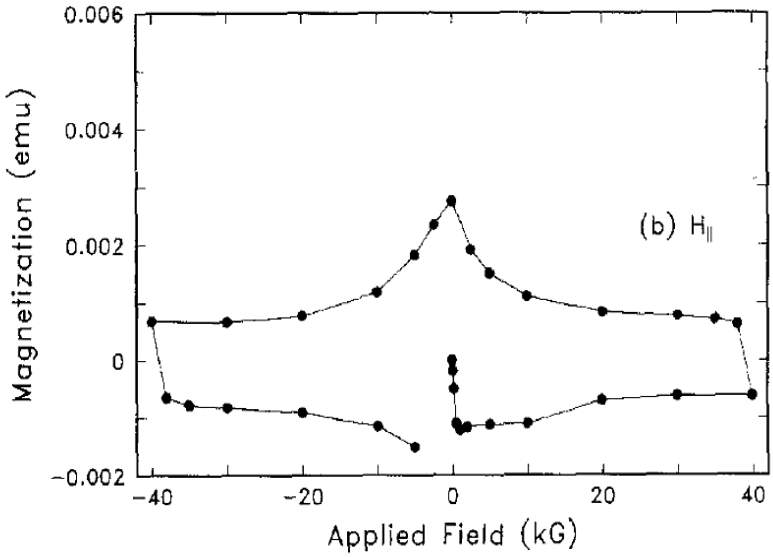


Figure 3.3 A typical magnetic hysteresis loop of single crystal YBCO at 4.5 K. Unit conversions for the applied field, 10 kG = 1 Tesla. Figure adapted from Gallagher *et al.* [30] with permission from Elsevier.

The source for the hysteretic behaviour is flux pinning at the sites of defects such as dislocations, grain boundaries and second phase precipitate. Flux is preferentially pinned in order to optimise the practical critical current of the materials. In the mixed state, flux lines penetrating a superconductor sample carrying a current experience a Lorentz force, and if they can move will result in dissipation and loss of the resistless state. As long as the Lorentz force does not exceed the pinning force, the flux lines remain pinned at the site. Increasing the density of structural defects will increase the

pinning sites, leading to an increase in J_c above that seen in perfect superconductors by orders of magnitude[31].

3.2.4 The Two-Fluid Model

The two fluid model by Gorter and Casimir in 1935[32], is one of the earliest models to successfully describe the microscopic thermodynamic phenomena controlling superconducting properties. The model postulates that there are two types of electrons in the superconductor; a fluid of normal electrons (n_n) and a fluid of superconducting electrons (n_s). Normal electrons behave like electrons in conventional metallic conductors and are responsible for the currents that flow in superconductors in the normal state, and obey Ohm's Law. Superconducting electrons are responsible for currents without resistance in the superconducting state. The densities of both normal (n_n) and superconducting (n_s) electrons are temperature dependent, and can be described by equation (3.1), where, $n = n_n + n_s$ is the total density of conduction electrons.

$$n_n = n\left(\frac{T}{T_c}\right)^4 \tag{3.1}$$

In the normal state ($T > T_c$), $n_s = 0$ and unpaired electrons are carriers of the current. In the superconducting state ($T < T_c$), both carriers exist simultaneously and contribute to the total current density with $n_n \to 0$ as $T \to 0$.

Under d.c. conditions, the current is only carried by the superconducting electrons because they "short out" the normal electrons, and do not dissipate energy, resulting in lossless current transportation. However, the superconducting electrons have a finite momentum and exhibit inertia in an alternating field. The inertia effect from the superconducting electrons and conventional losses from the normal electrons result in a.c. resistivity at higher frequencies.

In this work, the two-fluid model is useful in explaining the behaviour of HTS properties in composite materials. Furthermore, the existence of both normal and superconducting electrons in superconductors near T_c can be used to describe the loss properties of my HTS composites.

3.2.5 The BCS Theory

The BCS theory was proposed by Bardeen, Cooper and Schrieffer (BCS) in 1957[33] to explain the microscopic theory of the superconducting phenomenon. The theory was based on the pairing of normal state electrons in the superconducting state. These electron pairs are known as *Cooper pairs* and carry lossless supercurrent below T_c. The BCS theory also explained that electron pairing is limited to a gap frequency, f_{gap}, which is set by an energy gap between the normal and superconducting state, 2Δ, given by,

$$2\Delta = 3.52\kappa_B T_c = hf_{gap} \tag{3.2}$$

where h is Plancks constant, f_{gap} is a gap frequency, κ_B is Boltzmann's constant and T_c is the superconducting transition temperature[26]. f_{gap} is the frequency required to break Cooper pairs into two quasiparticles, destroying the superconducting properties. The gap frequency of YBCO-123 at $T_c = 90\,K$ is 6.6 THz, well above the range of frequencies required for microwave device applications[34]. In general, the higher the T_c value, the higher the gap frequency[34].

The energy gaps of most practical superconductors are in the range 100-1000 GHz[20]. Therefore, the microwave frequency range explored in my work will not affect the superconducting properties of these materials, and any change in electromagnetic properties below T_c in my microwave experiments, can be confidently connected to the onset of superconductivity.

3.2.6 Penetration Depth

If the superconductor is exposed to a magnetic field ($H < H_c$) at a temperature below its T_c value, the superconductor generates a shielding current on the surface, causing the Meissner effect and cancelling the interior magnetic flux to maintain a $B = 0$ condition within the material[35]. This screening current is induced within a surface layer of superconductor to a depth characterised by the penetration depth (λ). Over the penetration depth, the magnetic flux penetrates the material over a thin surface layer of a bulk superconductor. For a superconductor bulk of radius r, the magnetic flux drops exponentially from the applied magnetic field value on the surface to zero at a depth λ inside the superconducting bulk[35]. This distance can be characterised by the London penetration depth, λ_L, which is given by

$$\lambda_L = \sqrt{\frac{m}{n_s e^2 \mu_0}} \tag{3.3}$$

where e, m and n_s are the carrier charge, mass and the density of superconducting electrons respectively[36]. The charge e is negative for electron carriers in LTS materials and positive for hole carriers in most HTS materials. Since n_s for superconductors is temperature dependent, the London penetration depth is also temperature dependent[20]. The value of penetration depth defines the volume of material over which the magnetic field is excluded (or expelled) from the surface of superconductor. Typical values for the penetration depth in HTS materials are of the order of 0.1 μm depending on the material[20]. For example, the penetration depth of $YBa_2Cu_3O_7$ along the ab-planes are $\lambda_{ab} = 0.15\,\mu m$ and along the c-axis $\lambda_c = 0.6\,\mu m$, and in $Bi_2Sr_2Ca_2Cu_3O_8$ are $\lambda_{ab} = 0.20\,\mu m$ and $\lambda_c = 1.0\,\mu m$ [36]. The importance of the penetration depth is that in order to gain a strong diamagnetic effect in a superconducting powder the size of the powder particles, r, need to be considerably larger than the penetration depth ($\lambda < r$)[37].

3.2.7 Microwave Properties of Superconductors

Superconductors exhibit zero resistivity only for d.c. currents and have non-zero loss when a.c. currents are applied[38]. This can be explained by the simultaneous existence of normal and superconducting electrons in superconductors as described in Section 3.2.4. These normal and superconducting electrons respond differently under the influence of a.c. electromagnetic fields, resulting in a surface impedance (Z_s) which is a function of the electrical conductivity of materials, as given in equation (3.4) where R_S is the energy dissipation and X_S is the rate of energy stored within the skin depth in a normal metal or the penetration depth in a superconductor[39].

For microwave applications, R_S is the most important parameter of HTS materials, and determines the conductor loss that can affect the performance of HTS microwave devices[39,40].

$$Z_S = R_S + iX_s = \sqrt{\frac{i\omega\mu\mu_0}{\sigma}} \tag{3.4}$$

ω and σ in equation (3.4) are respectively the angular frequency of the incident wave and the complex conductivity, $\sigma = \sigma_1 - i\sigma_2$[40]. For normal metals, or superconductors in the normal state, σ_2 is almost negligible, hence $\sigma = \sigma_1$[40], and therefore

$$R_S = X_S = \left[\frac{\mu\mu_0\omega}{2\sigma}\right]^{1/2} \tag{3.5}$$

For a superconductor, $\sigma_1 \ll \sigma_2$ due to the pairing mechanism of Cooper pairs for $T < T_c$, resulting in a high value of n_S[39]. Hence,

$$R_S = \frac{1}{2}\omega^2\mu_0^2\lambda^3\sigma_1 \tag{3.6}$$

From equations (3.5) and (3.6) we can see that R_S scales with $\omega^{1/2}$ for normal metals and ω^2 for superconductors, indicating that the surface resistance will be lower in superconductors than in normal metals up to a critical frequency, which is promising for

the low loss operation required for microwave applications[41,42]. This can be seen from the date reported by Holsten *et al.* who compared the surface resistance values of copper and HTS films and found that the surface resistance of the HTS is 1 order of magnitude lower than copper at 10 GHz (Figure 3.4)[43], resulting in high quality factors in resonator structures operating at high frequencies. The quality factor (Q-factor) is a measurement of the efficiency of a resonator, and is also the reciprocal of the loss tangent[44] discussed in Chapter 2, which can be defined as,

$$Q \approx \frac{stored\ energy}{dissipated\ energy} \tag{3.7}$$

At the same frequency, the surface impedance YBCO films can be < 0.8 mΩ at 77 K, almost 2 orders of magnitude lower than copper, resulting in much higher Q values[36]. Since the performance of a microwave device is strongly dependent on low losses, materials with high Q-factor values are desirable for almost all applications.

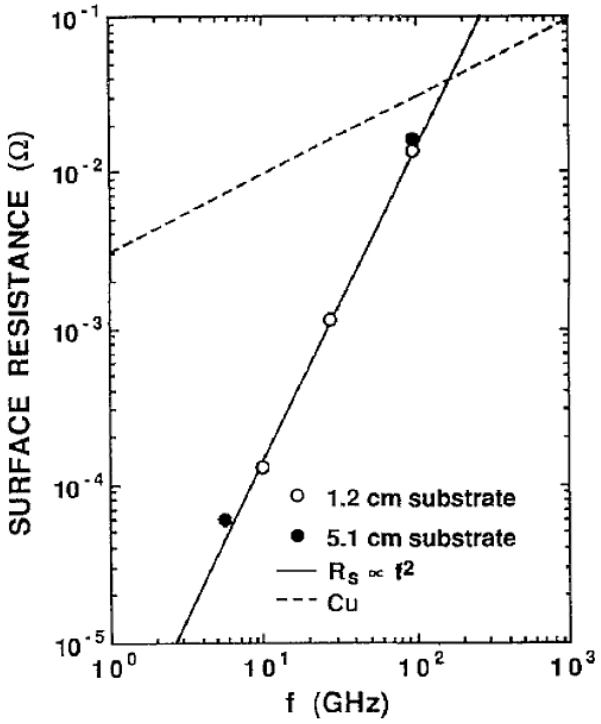


Figure 3.4 Surface resistance of Cu and High Temperature Superconductor (HTS) $Tl_2Ba_2CaCu_2O_8$ thin films. Figure reproduced after Holstein *et al.*[43]. Reprinted with permission from Springer Nature.

References

1 Cosmus, T. C. & Parizh, M. Advances in whole-body MRI magnets. *Applied Superconductivity, IEEE Transactions on* **21**, 2104-2109 (2011).

2 Scanlan, R. M., Malozemoff, A. P. & Larbalestier, D. C. Superconducting materials for large scale applications. *Proceedings of the IEEE* **92**, 1639-1654 (2004).

3 Laquer, H. L. Superconducting magnetic energy storage. *Cryogenics* **15**, 73-78 (1975).

4 Damadian, R., Goldsmith, M. & Minkoff, L. NMR in cancer: XVI. FONAR image of the live human body. *Physiol Chem Phys* **9**, 97-100, 108 (1977).

5 Williams, J. E. Superconducting magnets for MRI. *IEEE Trans. Nucl. Sci.* **NS-31:4**, 994-1005 (1984).

6 Ishiyama, A. & Hirooka, H. Magnetic shielding for MRI superconducting magnets. *Magnetics, IEEE Transactions on* **27**, 1692-1695 (1991).

7 Tomita, M. & Murakami, M. High-temperature superconductor bulk magnets that can trap magnetic fields of over 17 tesla at 29K. *Nature* **421**, 517-520 (2003).

8 Hyung-Woo, L., Ki-Chan, K. & Ju, L. Review of maglev train technologies. *IEEE Transactions on Magnetics* **42**, 1917-1925 (2006).

9 Wang, J. *et al.* The first man-loading high temperature superconducting Maglev test vehicle in the world. *Physica C: Superconductivity* **378**, 809-814 (2002).

10 Wang, S. Y. *et al.* High temperature superconducting Maglev equipment on vehicle. *Physica C: Superconductivity* **386**, 531-535 (2003).

11 Chrisey, D. B. & Inam, A. Pulsed Laser Deposition of High Tc Superconducting Thin Films for Electronic Device Applications. *MRS Bulletin* **17**, 37-43 (1992).

12 Lee, L. P., Char, K., Colclough, M. S. & Zaharchuk, G. Monolithic 77 K dc SQUID magnetometer. *Applied Physics Letters* **59**, 3051-3053 (1991).

13 John, R. H. Applications of high-temperature superconductors in power technology. *Reports on Progress in Physics* **66**, 1865 (2003).

14 Morrow, G. Progress in MRI magnets. *IEEE Transactions on Applied Superconductivity* **10**, 744-751 (2000).

15 Ono, M., Koga, S. & Ohtsuki, H. Japan's superconducting Maglev train. *Instrumentation & Measurement Magazine, IEEE* **5**, 9-15 (2002).

16 Chen, I. G. & Weinstein, R. Improvement of persistent magnetic field trapping in bulk Y-Ba-Cu-O superconductors. *IEEE Transactions on Applied Superconductivity* **3**, 1041-1044 (1993).

17 Kiyoshi, S. *et al.* High Magnetic Flux Trapping by Melt-Grown YBaCuO Superconductors. *Japanese Journal of Applied Physics* **30**, pp. L1157-L1159 (1991).

18 Babu, N. H. *et al.* Growth of large sized $YBa_2Cu_3O_7$ single crystals using the top seeded melt growth process. *Superconductor Science and Technology* **25**, 075012 (2012).

19 Onnes, H. K. The superconductivity of mercury. *Comm. Phys. Lab. Univ. Leiden* **122**, 124 (1911).

20 Orlando, T. P. & Delin, K. A. *Foundations of applied superconductivity*. Vol. 224 pp. 2-6 (Addison-Wesley Reading, MA, 1991).

21 Krauth, H. in *Handbook of applied superconductivity* (ed Bernd Seeber) pp. 397-141 (Institute of Physics, 1998).

22 Bednorz, J. G. & Müller, K. A. Possible high T_c superconductivity in the Ba−La−Cu−O system. *Zeitschrift für Physik B Condensed Matter* **64**, 189-193 (1986).

23 Wu, M. K. *et al.* Superconductivity at 93 K in a new mixed-phase Y-Ba-Cu-O compound system at ambient pressure. *Physical Review Letters* **58**, 908-910 (1987).

24 Maeda, H., Tanaka, Y., Fukutomi, M. & Asano, T. A new high-T_c oxide superconductor without a rare earth element. *Japanese Journal of Applied Physics* **27**, L209-L210 (1988).

25 Sheng, Z. Z. & Hermann, A. M. Bulk superconductivity at 120 K in the Tl-Ca/Ba-Cu-O system. *Nature* **332**, 138-139 (1988).

26 Nisenoff, M. Microwave superconductivity part 1: History, properties and early applications. *2011 IEEE MTT-S International Microwave Symposium, IMS 2011*, pp. 1-4 (2011).

27 Eatough, M. O., Ginley, D. S., Morosin, B. & Venturini, E. L. Orthorhombic-tetragonal phase transition in high-temperature superconductor $YBa_2Cu_3O_7$. *Applied Physics Letters* **51**, 367-368 (1987).

28 McElfresh, M. *Fundamentals of Magnetism and Magnetic Measurements, Featuring Quantum Design's Magnetic Property Measurement System*. pp. 28 (Quantum Design, 1994).

29 Dinger, T. R., Worthington, T. K., Gallagher, W. J. & Sandstrom, R. L. Direct observation of electronic anisotropy in single-crystal $Y_1Ba_2Cu_3O_{7-x}$. *Physical Review Letters* **58**, 2687-2690 (1987).

30 Gallagher, W. J. *et al.* Anisotropy in the magnetic properties of single-crystal $Y_1Ba_2Cu_3O_{7-x}$. *Physica B+C* **148**, 228-232 (1987).

31 Mendelssohn, K. On Different Types of Superconductivity. *Reviews of Modern Physics* **36**, 50-51 (1964).

32 Gorter, C. J. & Casimir, H. in *On supraconductivity I* pp. 1-15 (Springer Netherlands, 1935).

33 Bardeen, J., Cooper, L. N. & Schrieffer, J. R. Theory of superconductivity. *Physical Review* **108**, 1175 (1957).

34 Miiller, G. Microwave Properties of High-T, Oxide Superconductors. *Proceedings of the Fourth Workshop on RF Superconductivity*, pp. 267 (1989).

35 Poole, C. P., Farach, H. A. & Creswick, R. J. *Superconductivity 2nd Edition*. Vol. 2nd Edition pp. 141-415, (Academic Press, 2007).

36 Cyrot, M. *Introduction to superconductivity and high-Tc materials*. 52, 205, 218 (World Scientific, 1992).

37 Campbell, A., Blunt, F., Johnson, J. & Freeman, P. Quantitative determination of percentage superconductor in a new compound. *Cryogenics* **31**, 732-737 (1991).

38 Anlage, S. M. The physics and applications of superconducting metamaterials. *Journal of Optics* **13**, 024001 (2011).

39 John, G. Microwave applications of high-temperature superconductors. *Superconductor Science and Technology* **10**, A120 - A141 (1997).

40 Hinken, J. H. *Superconductor electronics : fundamentals and microwave applications*. pp. 20 (Springer-Verlag, 1989).

41 Speller, S. C. Thallium based high temperature superconductors for microwave device applications. *Materials Science and Technology* **19**, 269-282 (2003).

42 Ralston, R. W. Microwave applications of superconducting electronics. *Superconductor Science and Technology* **4**, 386 (1991).

43 Holstein, W. L. *et al.* Surface resistance of large-area $Tl_2Ba_2CaCu_2O_8$ thin films at microwave and millimeter wave frequencies measured by three noncavity techniques. *J Supercond* **6**, 191-200 (1993).

44 Dussin, W. J. *Electricity and magnetism*. (McGraw-Hill Publishing Company, 1990).

4 Superconducting Metamaterials for Microwave Applications

4.1 The Advantages of Superconductors in Metamaterials 30
4.1.1 Devices Containing Superconductors 30
4.2 Superconducting Composites 31
4.2.1 High Frequency Response of HTS Loaded Composites 32
4.3 Materials Selection for Superconducting Composites 40
4.3.1 Selection of HTS Materials 40
4.3.2 Introduction to YBCO and BSCCO 41
4.4 Factors Affecting the Superconducting Properties of HTS Powders 43
4.4.1 Factors Affecting $\boldsymbol{Tc}$ 43
4.4.2 Effect of Oxygen Stoichiometry 43
4.4.3 The Important of Microstructure 45
4.4.4 Factors Affecting Magnetic Susceptibility 45
4.4.5 Bulk HTS Processing 47
4.5 Materials Selection for the Polymer Matrix 50
4.5.1 Epoxy Resins 51
4.5.2 Acrylonitrile Butadine Styrene (ABS) 53
References 55

As has been discussed in Chapter 2, both the effective dielectric constant (ε_{eff}) and magnetic permeability (μ_{eff}) values of metamaterials depend on the dimensions, shapes, thicknesses and materials of unit cells[1,2]. The choice of materials for metamaterial unit cell fabrication is critical, as conventional materials such as copper or aluminium tend to introduce some resistance in the current carrying components. In this chapter, the potential application of low loss superconductors is discussed for metamaterials and microwave devices fabrication.

4.1 The Advantages of Superconductors in Metamaterials

The unique properties of superconductors such as zero d.c. resistivity and very low surface resistance at high frequencies (Figure 3.4) can be very useful for metamaterials applications. The gap frequency of superconductors ranges from the RF to low terahertz range (6.6 THz), indicating that the unique properties of superconductors can be utilised in the microwave frequency range.

4.1.1 Devices Containing Superconductors

Superconductors have been implemented in the fabrication of SRR and wire arrays for both metamaterials and non-metamaterials applications[3-5]. Ricci *et al.* demonstrated a reduction of dielectric loss of one order of magnitude upon entering the superconducting state using miniaturised Nb wires and Nb/quartz SRRs[5]. The reduction of loss in the superconducting structure is due to the lower loss. Yogi demonstrated surface resistance of 8.8 μΩ for Nb films at 4.2 K and 8.86 GHz[6] which is two order of magnitude lower than copper at 4 K and 10 GHz[7]. A combination of both Nb wires and SRRs could be used to generate ε_{eff} and μ_{eff} values less than zero below T_c, indicating a potential application in a negative refractive index device such as a perfect lens.

Another potential application of superconducting metamaterials with $\mu_{eff} < 0$ is for active devices. The resonant frequencies of spiral resonators (SR) made from Nb/quartz films can be tuned as a function of temperature and magnetic field, which can be important for MRI applications[8]. The quality factor of this type of SR is 35 times higher below its T_c (Q-factor=5044) than can be achieved with the normal metal SR, and gives improved transmission images in MRI.

4.2 Superconducting Composites

Superconducting composites can be realised using the dielectric inclusion technique by incorporating superconducting powder in a polymer-based matrix. Research on superconducting powder-loaded polymer composites dates back to 1990 when Weinberger *et al.* investigated the Meissner levitation of high temperature superconductors suspended in a paraffin wax composite using YBCO-123 as a filler[9]. It was observed that the magnetic levitation properties of the superconducting inclusions are maintained in the YBCO-123/paraffin composite. Since then superconducting composites have been investigated with different matrices, processing techniques and potential applications in various fields.

In polymers, the diamagnetic properties of superconducting composites have been studied for their levitation properties, with potential for use in magnetic bearings and as magnetic shielding, where superconducting grain coupling is not required[10,11]. The polymer-based matrix provides flexibility in shaping to achieve any desired physical properties as well as to improve the mechanical properties caused by the brittle superconductor[11]. The matrix layers also provide a shield for the superconductor from environmental exposure, because YBCO degrades severely on reaction with moisture[12].

In electronic applications, superconducting composites have been studied for high frequency operation as capacitors[13]. Composites have been demonstrated with dielectric properties that depend on the superconductor volume fraction, showing the capacitance increases with increasing density of superconducting particles[13,14]. This would enable control over the capacitance values in production. Furthermore, the use of a polystyrene matrix in the composites has provided flexibility and greater processability in the fabrication process.

4.2.1 High Frequency Response of HTS Loaded Composites

As described in Chapter 2 (Section 2.3 on page 10) the electromagnetic properties of polymer-based composites are determined by their constituent phases and volume fraction of the fillers. Efros et al. reported that a transition from insulating to conducting behaviour occurs in polymer-based composites with increasing volume fraction of conducting fillers[15]. This transition is known as the percolation threshold. At low loadings below the percolation threshold, the filler particles are isolated from each other so the polymer composites behave like insulators[15]. At the percolation threshold a conducting network develops throughout the material, and the composite behaves as a conductor[16].

The degree of connectivity of conductive fillers in the polymer matrix depends on the distribution and morphology of the filler particles as well as their volume fraction. The schematic drawing in Figure 4.1 by Dang *et al*. shows the formation of conducting networks with increasing filler concentrations for a homogeneous distribution of randomly shaped particles[17].

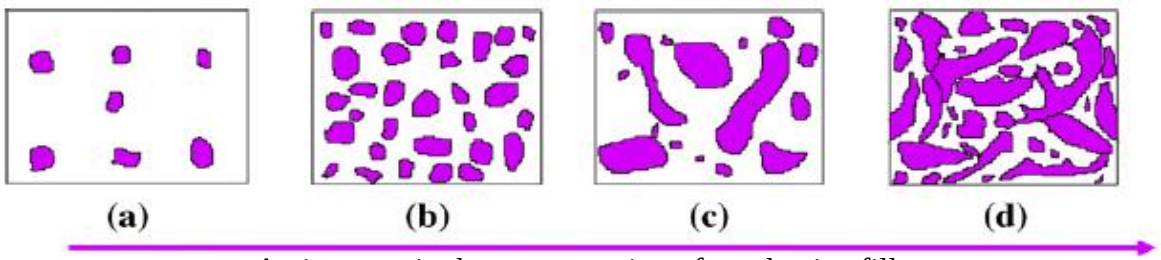


Figure 4.1 Schematic drawing of the development of conductive networks with increasing conducting filler concentrations, reproduced from Dang *et al.*[17] with permission from Elsevier.

Figure 4.1 (a) and (b) show homogeneously distributed particles in matrix at low concentrations. Each conducting particle can be observed separated by thin layers of matrix. With increasing filler concentrations, thicknesses of matrix layers between fillers decreases and clusters of particles are formed (Figure 4.1 (c)). At critical volume

fractions, these clusters form three-dimensional conducting paths through the matrix, which lead to the percolation threshold (Figure 4.1 (d)).

The percolation threshold in conducting fillers/polymer composites is characterised by a jump in electrical conductivity and a divergence in the real part of dielectric constant. The critical volume fractions, f_c of conducting filler/polymer can be estimated by percolation theory, which can describe the behaviour of the conducting filler/polymer composites near the percolation threshold using power law equations (4.1) and (4.2)[18]. The behaviour for electrical conductivity,

$$\sigma_{eff} \propto (f - f_c)^t \quad \text{for } f > f_c \tag{4.1}$$

and behaviour for dielectric permittivity,

$$\varepsilon_{eff} \propto (f - f_c)^{-s} \text{ for } f < f_c \tag{4.2}$$

where, f is the volume fraction of filler, t is the critical exponent in the conducting region, and s is the critical exponent in the insulating region.

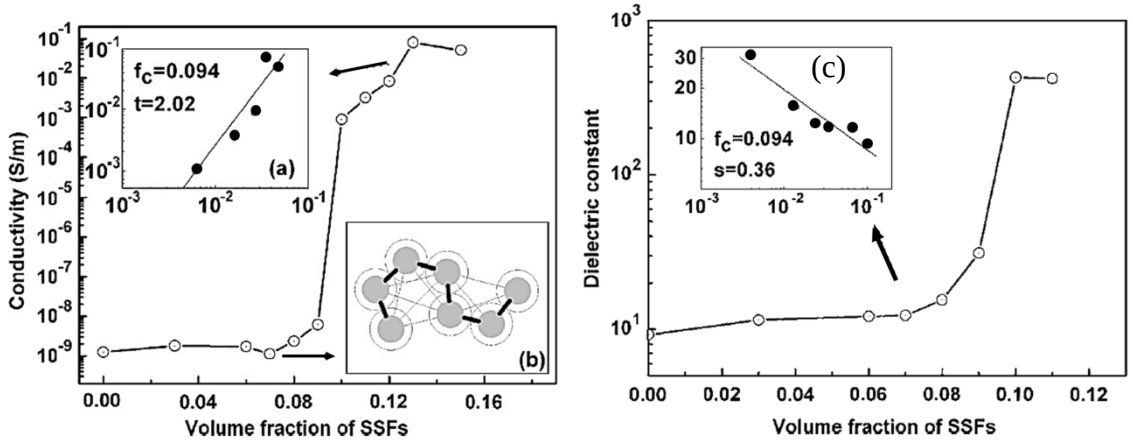


Figure 4.2 Effective conductivity (Left image) and dielectric constant (Right image) of stainless steel fiber (SSF/poly(vinylidene fluoride) measured at 50 Hz and room temperature. Inset (a) and (c) show the best fit of conductivity and dielectric constant by percolation theory. Inset (b) Schematic image shows possible conductivity path occur inter-particles. Figures reproduced from Yun Jia *et al.*[19] with permission of AIP Publishing.

For instance, Yun Jia *et al*. observed a jump in electrical conductivity from ~10^{-9}[S/m] to ~10^{-3}[S/m] and dielectric constant from 10 to 30 of stainless steel fibre/poly(vinylidene fluoride) composites within 9-10 vol%, where f_c is estimated at 9.4 vol% by fitting in equation 4.1 and 4.2 (Figure 4.2)[19] .

The development of these conducting paths and f_c of conducting fillers/composites depends on diameter, shape and distribution pattern of fillers in matrix. For example, Yang *et al*. simulated that ZnO/silicone rubber composites reached percolation threshold at f_c=33 vol% using spherical 60-80 μm ZnO fillers, and reached percolation threshold at f_c =31 vol% using spherical 125-150 μm ZnO fillers, estimating that larger size fillers have potential to form conducting path at lower critical volume fractions[20].

The percolation theories have been developed on the properties of filler particles such as microstructural shapes[21,22] and volume fractions[23] to predict the f_c of percolation threshold in composite materials. Garboczi *et al.* studied the effect of geometrical properties of randomly distributed filler particles on the percolation threshold development in a matrix[21]. These geometrical of filler particles are ellipsoids ranged from the extreme oblate limit such as plate-like particles to the extreme prolate limit of needle-like particles. The aspect ratio of these ellipsoids a/b, (a is the length of the symmetry axis and b is the length of each axis perpendicular to the symmetry axis) is plotted against the reciprocal threshold $\frac{1}{p_c}$ where $p_c = f_c$ is a critical volume fractions of randomly oriented particles with the same geometrical ellipsoid properties overlapping in a matrix (Figure 4.3). It has been found that the reciprocal threshold to scale linearly with the ratio of the larger ellipsoid dimensions to the smaller dimensions in the extreme ellipsoid limits[21]. In the extreme cases of oblate (plate-like) and prolate (needle-like) shaped filler particles, the value of p_c goes to zero and p_c value for sphere shaped filler particles (a/b=1) is 29%[21]. The result is demonstrated for the simple case of

overlapping identical ellipsoidal particles in a matrix to form geometrically connected conductivity phase.

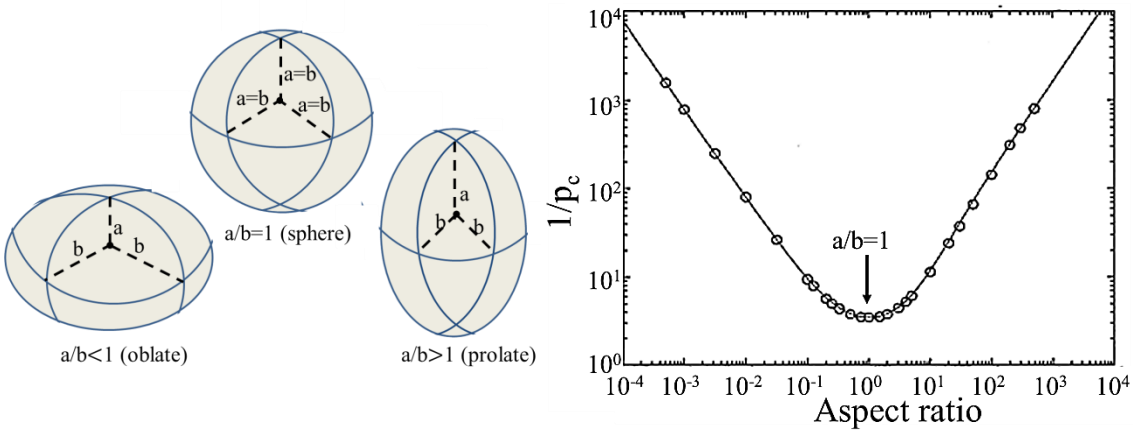


Figure 4.3 Range of ellipsoids with aspect ratio a/b (left image). Inverse of the critical volume fraction ($1/p_c$) for percolation plotted against aspect ratio of ellipsoids particles (right image). Figure on the right has been adapted from Garboczi *et al.*[21] with permission. Copyright © 1995 by The American Physical Society.

Studies and theories on percolation threshold development can be found mostly for spherical filler particles distributed in a matrix[21,22]. One model used to predict the percolation threshold for spherical particles of diameter, d consists of an impermeable hard core of diameter, $d - 2\delta$ and a permeable soft shell of thickness, δ (Figure 4.4 (left)[22]. In a real composite system, the impermeable hard core is viewed as an inclusion and the permeable soft shell is an insulation layer of polymer matrix. If the soft shell layer is thin enough, electrons can be transported between particles through the layer, reducing the resistivity of composites[22]. This can be seen from the resistivity of nickel/polyethylene composite in Figure 4.4 (right image)[22]. An aggregated structure of nickel fillers has lower resistivity than those randomly (homogenously) distributed nickel in polyethylene matrix. This is due to close contact of fillers in aggregate structure develop higher efficiency of networking and at the same time reducing the critical volume fractions[22].

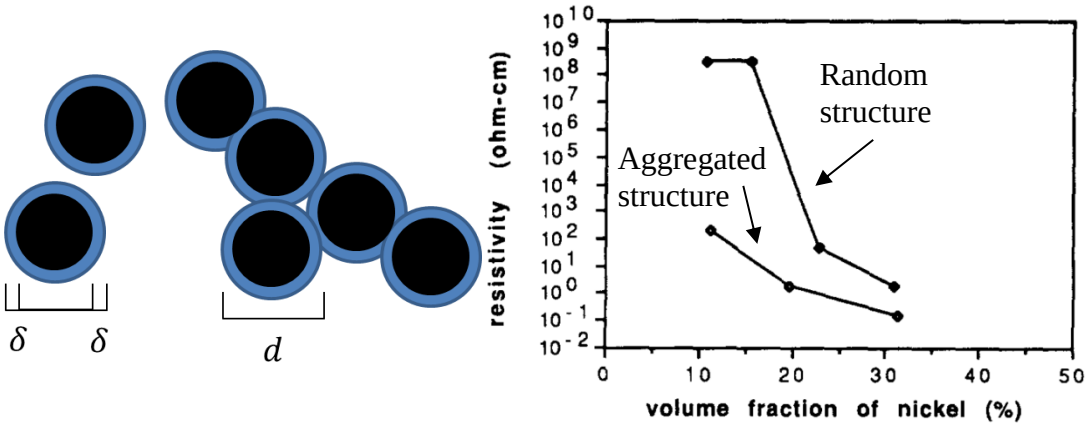


Figure 4.4 Schematic image of the spherical model consists of a hard core with diameter, $d - 2\delta$, and a soft shell of thickness, δ with an overall diameter, d (left image). Comparison of resistivity values of random and aggregated structures of nickel fillers loaded polyethylene composites (the diameter of nickel filler is 2.9 μm and the experimental f_c of nickel/polyethylene composite is 10%). Figures adapted from Wang *et al.*[22] with permission from Elsevier.

The conducting path can be developed at lower volume fractions using fillers with high aspect (length or diameter) ratio, such as fiber-like-particles[24], graphite[25] and carbon nanotubes (CNTs)[16]. This is because fillers with a high aspect ratio have higher contact probability of forming the conducting network, which can lead to a percolation threshold development at lower concentrations[25]. Celzard *et al.* reported that graphite flake (thin discs shape) loaded in epoxy and polyurethane have critical concentrations 2% lower than that of spherical fillers (see table Table 4.1)[24]. In Table 4.1, graphite-flake like fillers (FMG2-Polyurethane) with higher aspect ratio (diameter/thickness) has lower critical concentrations, resulting from the high contact probability in the matrix.

Table 4.1 Critical concentrations of graphite flake (FMG-Flat micron graphite) loaded polymers. Table adapted from Celzard *et al.*[24] with permission. Copyright © 1996 by The American Physical Society.

Composite	Aspect ratio of filler	Critical concentration, f_c [vol%]
FMG1-Polyurethane	100	1.7
FMG2-Polyurethane	200	0.7

Fillers with shapes like thin disc (graphite flake)[24] and elongated cylinder (carbon black)[26] are anisotropic, and the orientations of these fillers in matrix significantly affect

the critical concentrations of fillers. The critical concentrations of these types of fillers were studied by Celzard *et al*. who conducted a numerical study to estimate critical volume fractions of carbon fibres (diameter=8.5 μm and length=1 mm) in polymers (the calculation method can be referred to Celzard *et al.*[24]), and found that the critical volume fractions for parallel arranged elongated carbon fibres, is estimated $16.05 \leq f_c \leq 29.53$, and a randomly arranged carbon fibre is $0.58 \leq f_c \leq 1.15$[24]. This is because randomly arranged fillers decrease the barrier and increases the connectedness between fillers in the matrix than the oriented fillers[22].

Bergman *et al*. described that above the percolation threshold, d.c. conductivity of conducting filler/polymer composite is non-zero and increases with volume fractions[27]. Below the percolation threshold, there is a frequency-dependent a.c. conductivity, which increases with increasing volume fractions of fillers approaching critical concentration at the threshold. This is due to the development of "pure conductive channels" connected at length between grains in the composite system only to be blocked off by barriers of insulating layers up to a critical concentration, which made the whole system behave like a large capacitor[27].

The effect of critical volume fractions on the behaviour of the polymer-based materials with superconducting fillers also can be seen from the YBCO powder loaded polymethylmetacrilate (PMMA) composites at low frequency (d.c.) conductivity by Golosovsky *et al*. who reported that the percolation threshold was estimated to occur at $f_c = 0.2$ based on the jump of conductivity by 4 orders of magnitude at 300 K and 100 Hz (Figure 4.5)[28]. The highest concentration of YBCO filler (f=0.48) is observed to have conductivity ~10^{-3} Ω^{-1} cm^{-1} which is reported to be relatively lower than YBCO single crystals, which is 10^3 to 10^4 Ω^{-1} cm^{-1} at 300 K[28]. Since the microwave losses, $2nk$ is directly related to the conductivity, $\sigma(\omega)$ by $2nk = 4\pi\sigma(\omega)/\omega$, Gosolovsky *et al.*[28]

investigated the effect of the percolation effect on the microwave losses of YBCO loaded polymer at 10 GHz and 97 K (Figure 4.5 indicated by a small arrow to the right scale). The d.c. percolation threshold at $f_c \sim 0.2$ is not visible as an abrupt change in the microwave properties (n and k), suggesting that capacitive coupling of the grains dominates over resistive coupling at high frequency. This suggests that it is unlikely that the percolation threshold can be observed in the microwave measurements of HTS composites at high frequencies (above 10 GHz). The discussion of dielectric properties of my microwave measurements will be discussed in Chapter 8.

Overall, the percolation threshold or conductivity jump of the YBCO/PMMA composites can be seen only at low frequencies and there are no dramatic changes in conductivity at high microwave frequencies (10 GHz) for all volume fractions. This indicates fully dielectric behaviour of superconducting composites at high frequencies (10 GHz) and 97 K.

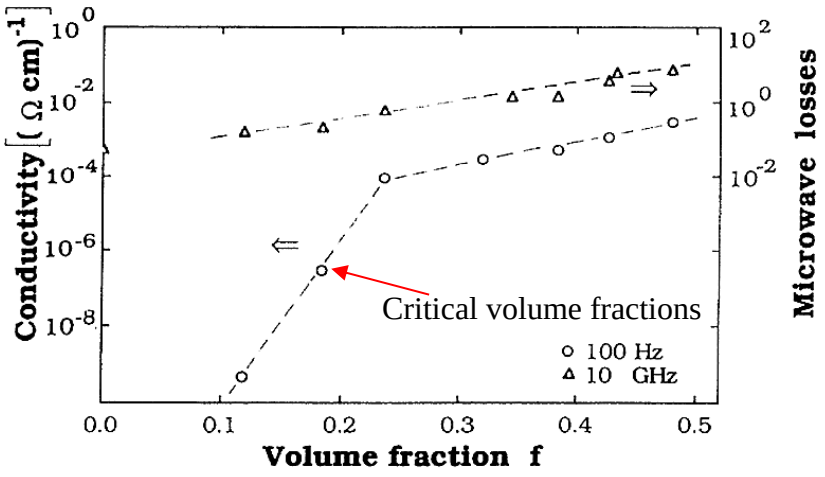


Figure 4.5 Conductivity of YBCO loaded polymer as a function of HTS volume fraction at low frequency (100 Hz) and 300 K, and microwave losses of HTS loaded polymer as a function of HTS volume fraction at high frequency (10 GHz) and 97 K. Figure reproduced from Golosovsky *et al.*[28] with permission. Copyright © 1992 by The American Physical Society.

The electromagnetic properties of superconductor composites depend strongly on the T_c of the superconductor filler. The electromagnetic waves propagation in the

superconducting composites is, as expected, reported to show less loss in the superconducting state than the normal state due to the lower R_s value in the superconducting state[29]. This has sparked research interests in superconducting composites for application in far-infrared[30,31] and microwave transmission[28,32-34]. Golosovsky demonstrated that the electromagnetic properties of superconducting composites depend not just on the μ_{eff} but also on the ε_{eff}, which can be tuned by adjusting the volume fraction and size of the superconducting filler[28,35].

The control of ε_{eff} and μ_{eff} of superconducting properties can be utilised in metamaterials applications. Although superconducting powder has rather anisotropic properties as described below, they are randomly averaged and so basically isotropic in the matrix. In addition the flexibility of a polymeric matrix can be designed to suit any shape of metamaterial. The superconducting composites can be moulded using conventional polymer processing techniques such as casting, spray deposition, extrusion and additive manufacturing[36-38].

Table 4.2 HTS composites in a variety of polymer matrices and their applications

Polymer	**HTS filler**	**Processing method**	**Application**	**Ref**
Polystyrene	YBCO-123	Compression molding	Capacitors	13,39
PMMA	YBCO-123	Cast	Electromagnetic studies	28,35
High density polyethylene	YBCO-123 BSCCO-2223	Hydraulic press	Electrical studies	40
Paraffin	Tin-lead	Baker's method	Diamagnetic studies	41
Unknown plastic	YBCO-123 BSCCO-2223	Extrusion	Microwave devices	38
Liner low density polyethylene	YBCO-123	Melt mixing and extrusion	Magnetic shielding Levitation device	10,42
Polyfluorocarbon	YBCO-123	Plasma coating	Surface protection	43
Polyvinylchloride	YBCO-123	Rolling and compression	Processibility	44

Even though there is as yet no clear implementation in practical metamaterials, other potential applications of superconducting composites have been well established, as summarised in Table 4.2. However, there are several technical issues in fabrication of superconducting composite that need to be overcome in order to enhance and widen the application of superconducting composites for various applications. This is a major focus of the work reported in this thesis.

4.3 Materials Selection for Superconducting Composites

4.3.1 Selection of HTS Materials

Several kinds of HTS superconducting powder have been used as the filler in superconducting composites. This is mainly due to their transition temperature above 77 K. The properties of these HTS filler particles depends largely on the source of bulk superconductor. Since all the critical parameters of a superconductor depend on the T_c, the higher the T_c, the larger the J_c and H_c values, at a given operating temperature[45].

BSCCO-2223 is HTS material with the T_c value ~ 108 K[46,47]. As explained below, single phase BSCCO-2223 bulk materials can be difficult to synthesise, requiring a complex and lengthy sintering process. In addition, there is no guarantee that phase uniformity can be achieved in BSCCO bulks or powders. However, a mixture of BSCCO phases might still have T_c > 77 K because T_c for the lower temperature BSCCO-2212 is still 86 K[47]. Thus, BSCCO powder is considered for use as a superconducting filler.

YBCO-123 has become the most frequently chosen HTS material in superconducting composite applications as shown in Table 4.2. YBCO has a relatively lower T_c (T_c = 93 K) than BSCCO-2223 and also can be severely degraded by reaction with atmospheric moisture[48], although this effect might not be critical when the powders are coated with a

polymer layer[49]. The fact that bulk YBCO made by the TSMG process described below can have large magnetisation values made YBCO-123 a suitable HTS material for me to study.

4.3.2 Introduction to YBCO and BSCCO

YBCO and BSCCO are both high temperature oxide superconductors, with structures consisting of active planes where the superconducting properties originate and inactive insulating layers[50]. The active layers contain CuO_2 planes and the inactive layers are formed of BaO, BiO and SrO[51]. The YBCO-123 compound has a unit cell of the perovskite structure, with Cu ions at the centre of cubic cells surrounded by octahedra of O^{2-} ions and cornered by either Ba or Y ions. The unit cell of YBCO is composed of a perovskite-like stacking consisting of six planes in the sequence Cu-O_2, Ba-O, Cu-O_2, Y, Cu-O_2, Ba-O (Figure 4.6)[50,52]. The YBCO-123 phase crystallizes with a tetragonal structure at high temperatures, but converts to an orthorhombic unit cell due to oxygen uptake and ordering upon cooling[51].

$YBa_2Cu_3O_6$ where the two Cu planes of top and bottom of the unit cell have lost one oxygen atom is an antiferromagnetic insulator, but $YBa_2Cu_3O_7$ is a superconductor when these planes are fully saturated with oxygen by annealing in an oxygen-containing atmosphere[51]. The supercurrent is carried by the Cu-O layers of the structure, which lie perpendicular to the c-axis of the unit cell, and the resulting J_C values are much higher in the a/b direction than in the c direction[53,54]. Hence, it is important to align YBCO crystals with their c-axis perpendicular to the required direction of maximum current flow.

The BSCCO family contains three superconducting phases that can be described as "a homologous series of the form $Bi_2Sr_2Ca_{n-1}Cu_nO_{6+n}$(n=1, 2, 3)"[47]. $Bi_2Sr_2Ca_2Cu_3O_9$

(BSCCO-2223) is the one with the highest T_C ($T_C = 110K$). The Cu-O layers are separated by Ca layers and spaced by Sr-O and double Bi-O layers (Figure 4.7)[47,51].

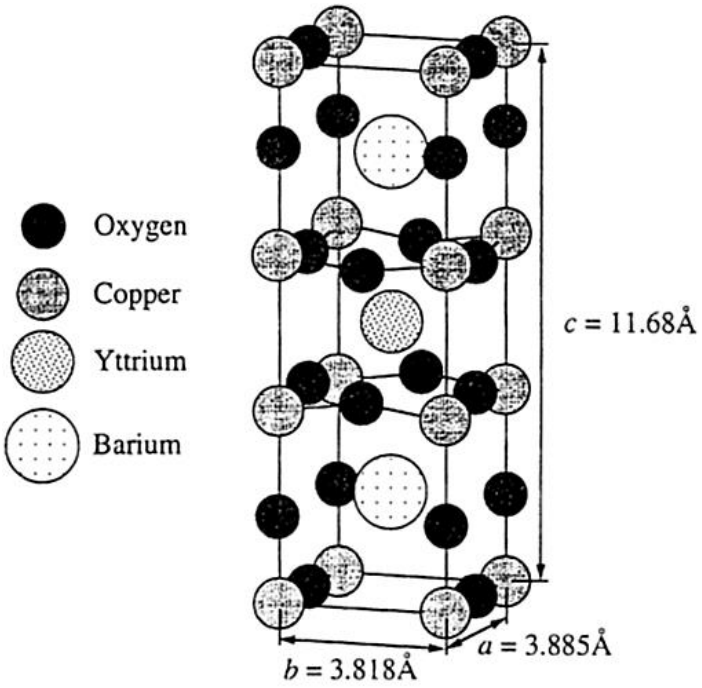


Figure 4.6 A schematic diagram of $YBa_2Cu_3O_{7-\delta}$ unit cell. Figure reproduced from Chrisey *et al.*[52] with permission of Springer Nature.

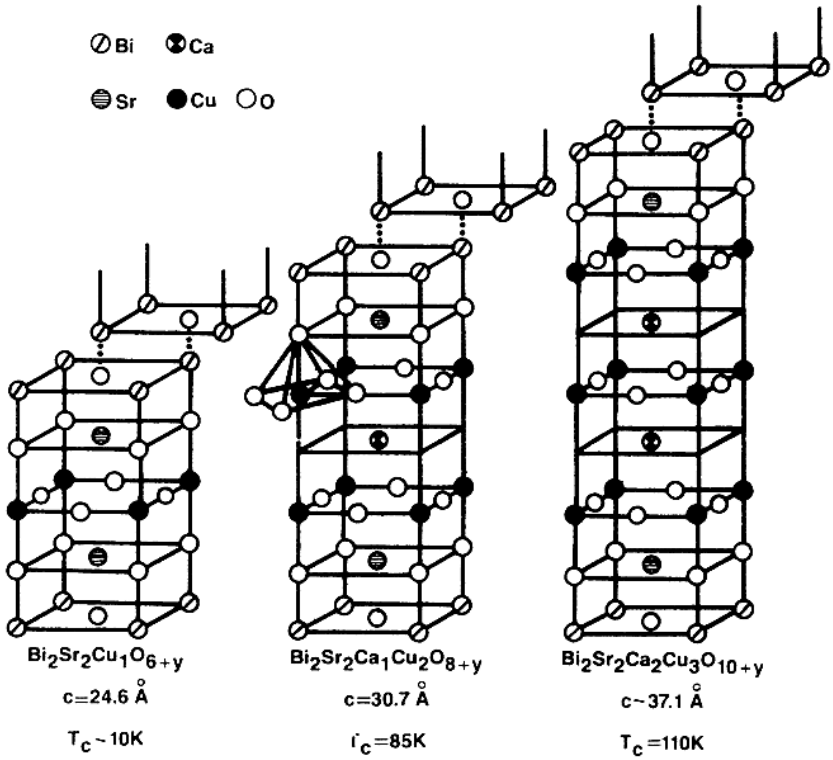


Figure 4.7 Schematic illustrations of $Bi_2Sr_2Ca_{n-1}Cu_nO_{6+n}$ (n=1, 2, 3) crystal structure. Figure reproduced from Tarascon *et al.*[47] with permission. Copyright © 1988 by The American Physical Society.

4.4 Factors Affecting the Superconducting Properties of HTS Powders

The superconducting properties of HTS powders are strongly dependent on oxygen content, chemical composition, impurity phases and microstructure. Factors affecting the superconducting properties of HTS powders are discussed below.

4.4.1 Factors Affecting T_c

The correlation of material properties and T_c has been extensively studied in the YBCO and BSCCO systems[47,55,56]. All cuprate superconductors contain two dimensional Cu-O sheets and, in addition, RE-123 compounds contain one dimensional Cu-O chains. T_c generally increases with increasing number of CuO_2 layers, and decreases with the length of the Cu-O bond[57]. Increasing the density of Cu-O sheets in the YBCO perovskite can be due to the increase in oxygen discussed above. It has also been shown that as the number of CuO_2 planes increases in the BSCCO materials both the lattice parameter along the a-axis and the Cu-O bond length along the c-axis become shorter[58]. Cava demonstrated that an increase in c-axis lattice parameter due to increasing oxygen deficiency leads to the destruction of superconductivity[55].

4.4.2 Effect of Oxygen Stoichiometry

The effect of oxygen stoichiometry on the superconducting transition temperature of YBCO-123 has been investigated by many groups[59-61] by post-annealing superconductor samples at different temperatures and atmospheres. Oxygen stoichiometry changes in the superconducting $YBa_2Cu_3O_x$ leads to changes in transition temperature as a result of the transformation of the YBCO crystal structure from orthorhombic at x=7.0 to tetragonal at x=6.0 (Figure 4.8)[59].

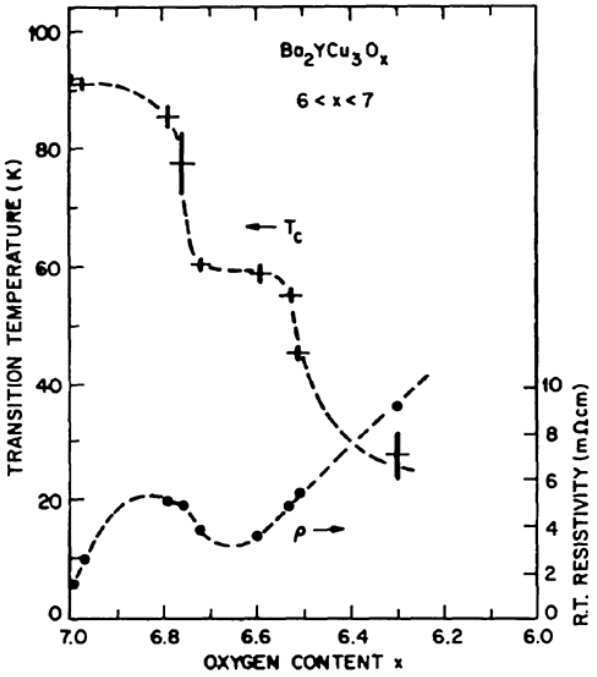


Figure 4.8 The change of transition temperature with oxygen stoichiometry of $YBa_2Cu_3O_x$. Figure reproduced from Cava *et al.*[59] with permission by the Cambridge University Press.

This can be achieved by oxygenation at 400-500 °C. x is close to 7.0 when oxygenation is done in O_2 gas and 6.9 when done in air (Figure 4.9) [61]. Annealing between 400 and 500 °C in O_2 is the optimal treatment to achieve the highest O_2 content, and YBCO in its orthorhombic structure shows the sharpest superconducting transition at T_c.

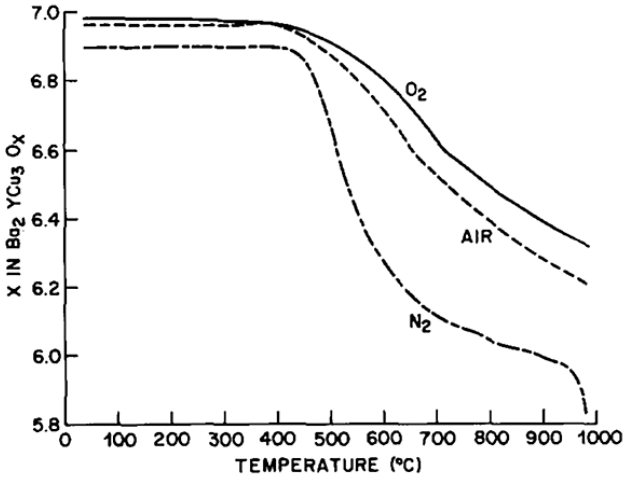


Figure 4.9 The change of x in $YBa_2Cu_3O_x$ with temperature in various atmospheres. Figure reproduced after Gallagher *et al.*[61] with permission from Elsevier.

4.4.3 The Important of Microstructure

The physical properties of HTS superconductors depend strongly on the microstructure, such as the density of twin and grain boundaries, second phases and intergrowth defects[51]. Most of these micro defects occur during synthesis, particularly with respect to the quantity and distribution of non-superconducting second phases, but also in relation to the control of intergrowths and the quality of the grain interconnections[62,63]. One of the most severe defects that can be found in superconducting powders are grain boundaries. Grain boundaries in the superconducting powder is a region of structural distortion that acts as a "weak-link", leading to much lower critical current densities and can significantly affect R_s values in a magnetic field[64].

Since the critical current density is not the primary concern in this work, the effect of the superconducting powder on the magnetisation properties are discussed as a function of particle size, defect and impurity layer as described below.

4.4.4 Factors Affecting Magnetic Susceptibility

The quality of a superconductor sample can be easily defined by measuring the susceptibility of the materials (χ_m), in practice by measuring the magnetic moments[65,66]. The χ_m value of a superconductor can be affected by the sizes and volume fractions of superconducting phases in particles[67], geometrical constants (shapes of samples)[68] and penetration depth[69,70].

χ_m will be -1 for an ideal superconductor in its Meissner state (low fields) with particle size larger than the penetration depth[71]. However the current flow, J_C in a superconductor depends on the microstructure, and can vary across the sample[72]. As described in previous sections, in the superconducting state, lossless supercurrents flow on the surface of the superconducting materials, to a depth defined by the London

penetration depth (λ_L), which is inversely proportional to the density of superconducting carriers. In HTS materials, this carrier density is relatively small, so λ_L tends to be large. For a bulk superconductor, the effect of λ_L can be considered to be negligible because the sample size is large compared to λ_L[70]. However, for superconducting particles with radius of the same order as the penetration depth, the magnetisation properties can be severely reduced. Clem *et al.*[69] demonstrated the magnetisation effect of spherical particles as a function of temperature and ratio of their radius to penetration depth ($\frac{r}{\lambda}$), and found that the magnetisation of particles increases with increasing ratio of $\frac{r}{\lambda}$ at low temperature. Campbell *et al.*[70] and Hibbs *et al.*[73] conducted measurements on a wide range of 100% pure YBCO particles with controlled particle size and penetration depth, and plotted susceptibility values normalised to the largest particle size. The susceptibility values decreased with decreasing particle size (Figure 4.10). The information on penetration depth effects on particles is important for my work where I have used superconducting powders in my composites.

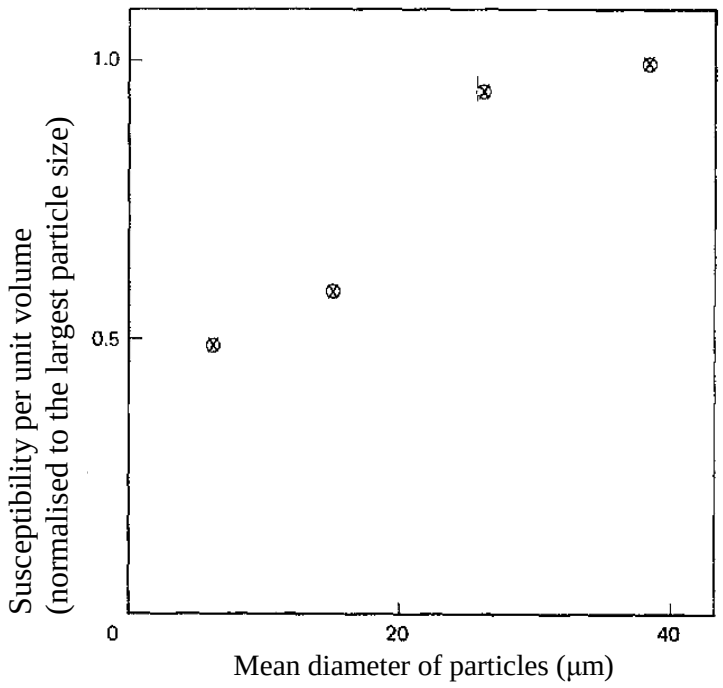


Figure 4.10 Susceptibility per unit volume of YBCO particles with well-defined parameters. Figure reproduced from Campbell *et al.*[70] with permission from Elsevier.

Porch *et al.*[74] also observed an increase in penetration depth in cobalt doped YBCO compounds. The diamagnetic screening current flows within the ab-planes (λ_{ab}) and along the c-axis (λ_c) from $\lambda_{ab} = 140\,\text{nm}$ and $\lambda_c = 1040$ nm (non-doped YBCO) to $\lambda_{ab} = 200\,\text{nm}$ and $\lambda_c = 2000$ nm (cobalt doped YBCO), which reducing the susceptibility values of the doped YBCO compounds[74]. This shows that non-superconducting layers or impurities can enhance penetration depths in HTS particles, leading to smaller susceptibility values in YBCO powders of a particular size.

4.4.5 Bulk HTS Processing

An appropriate processing technique is required to produce a large single grain bulk superconductor sample with optimized magnetic properties[75]. One of the keys to gain samples with high magnetic and critical current densities is to control the grain size and distribution of the non-superconducting phases (YBCO-211) as flux pinning sites in the bulk of superconducting matrix (YBCO-123)[76,77].

4.4.5.1 Melt Processing Techniques

Melt processing techniques have been widely used to produce large grains of HTS bulk superconductor with good diamagnetic properties at 77 K[78]. It is important to enhance the flux-pinning properties and align the crystals to a preferred orientation in individual large single grains[79]. In the fabrication of $YBa_2Cu_2Cu_3O_{6.28}$ (YBCO-123) bulk samples, flux pinning can be achieved by homogenously distributing the non-superconducting YBCO-211 inclusions in the YBCO-123 matrix[80].

The preferred fabrication technique is based on a peritectic reaction in which solid YBCO-211 particles react with a liquid phase Ba-Cu-O and oxygen gas at a characteristic peritectic temperature ($1000°C < T_p < 1080°C$), to form YBCO-123[81].

The target YBCO-123 phases are formed by slow cooling through T_p according to the reaction:

$$Y_2BaCuO_5 + Ba_3Cu_5O_{6.72} + 0.42\ O_2 \rightarrow 2(YBa_2Cu_2Cu_3O_{6.28})^{82}$$

4.4.5.2 Top Seeded Melt Growth Technique (TSMG)

In order to produce large single grain YBCO crystals with controlled nucleation and homogenously distributed fine YBCO-211 inclusions, the top seeded melt growth (TSMG) technique is used[83], where the use of seed crystals such as Sm-123[84] or Nd-123[85] allows the preferred orientation of the grain growth along the ab-planes to take place[86] (Figure 4.11). This technique has been reported to produce YBCO superconductor with high trapped magnetic fields over a wide range of temperatures, 3.1 T at 77 K and 10.1 T at 42 K[81].

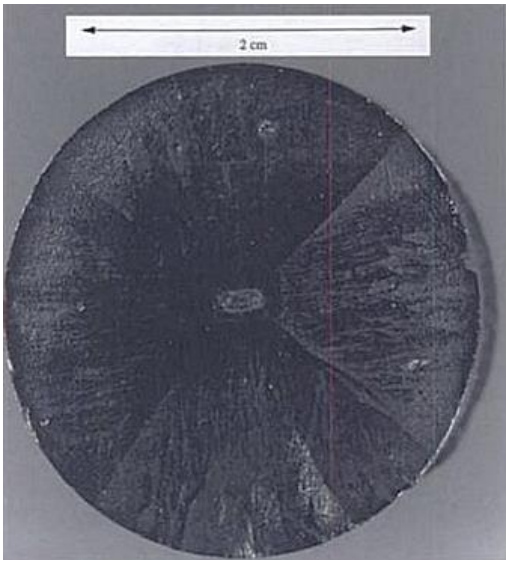


Figure 4.11 A single large crystal YBCO fabricated by the TSMG process seeded by SmBCO. Figure reproduced from Cardwell *et al.*[81] with permission from Elsevier.

4.4.5.3 Sintering techniques for other superconductors

The solid-state route is the classic sintering technique for producing powders of HTS superconductors. The technique involves cycles of mixing and grinding, and prolonged heat-treatment[87].

The technique has been widely used in producing both YBCO and BSCCO superconductors, using precursor powders such as commercially available metal oxide or carbonate compounds. In producing YBCO-123, the starting powders of Y_2O_3, $BaCO_3$ and CuO are mixed in the 1:2:3 stoichiometric ratio by repeated grinding and sintering, followed by calcination around 920 °C to 950 °C[88] and subsequent annealing[89]. The mixtures are usually pressed in pellets and calcined in either air or controlled oxygen to produce the intended bulk composition. YBCO-123 prepared by this sintering route tends to be poorly sintered, both porous and friable and with disorientated grain alignment across boundaries also resulting in low critical current densities[90].

In contrast to YBCO, the solid-state reaction route is the most common method of preparing the $Bi_2Sr_2Ca_{n-1}Cu_nO_{2n+4}$ (n=1, 2 and 3) compounds[91]. The calcination temperature (< 950 °C) is slightly lower than for YBCO powders but other steps are mostly the same. In this work, consideration is given to the fabrication of $Bi_2Sr_2Ca_2Cu_3O_{10}$ (BSCCO-2223) with a high $T_c = 110\ K$. However, difficulties have been reported in the production of BSCCO as a single phase material[46,92]. This is due to the similarities in structures, lattice dimensions (apart from c-axis parameter), and formation kinetics of all the related BSCCO phases[55,93].

In order to produce a significant volume fraction of BSCCO-2223 with T_c higher than 100 K, precise control over the sintering temperature is important as it is reported that this phase can only be formed between 827 and 856 °C, and is thermodynamically unstable above 856 °C[94]. Chen *et al.* also reported that long heat-treatment times are also necessary, 50-100 hours[94]. Even after a lengthy heat treatment the existence of both phases of BSCCO-2212 and BSCCO-2223 is unavoidable, which leads to a degradation of superconducting properties in bulk BSCCO superconductors[95].

4.5 Materials Selection for the Polymer Matrix

Polymers have been used as dielectric substrates for many applications in the microelectronic industry[96-98] due to their strong chemical stability, low density and good adhesion to semiconductors and metals[99]. A combination of polymers and materials with good electromagnetic properties can produce polymer matrix composites for electromagnetic applications. In order to produce useful HTS composites, a significant volume fraction of HTS powder must be mixed with a polymer that satisfies several criteria:

1. Chemical compatibility with the HTS powder is essential as it reacts easily on contact with moisture leading to a degradation of superconducting properties.

2. Low temperature resistance to avoid severe thermal contraction and cracks during operation at low temperature (T=77 K).

3. A non-magnetic material is required and a low loss tangent ($\tan\delta < 10^{-4}$) at the frequency of operation is needed to reduce overall lossy effects in the HTS composite.

4. The availability of precursor materials and cost of fabrication is important for realisation in large scale manufacturing. The polymer must be suitable for processing using simple polymerisation techniques.

5. A minimum water permeability to avoid degradation of the HTS properties in service.

In general, materials for the polymer matrix can be classified into *thermosetting* and *thermoplastic composites*[100]. Thermosetting are strengthened by applying heat to encourage a cross-linking reaction, but the process is irreversible after the initial heat-treatment[101]. Such polymers are epoxy resin, vinyl ester, polyester and polyimides. Thermoplastics can be softened by applying heat and hardened upon cooling, and

include polypropylene, polystyrene and acrylonitrile butadine styrene[102]. Thermoplastics can be recycled as they can be cooled and heated several times, only limited by thermal aging[103].

The following sections describe two materials that have been considered as the polymer matrix for HTS composites in this study, based on their availability, requirements for the processing route and final device specifications, focussing on the electromagnetic properties of the chosen polymers. Examples of other types of polymers used in other work on superconducting composites are summarised in Table 4.2.

4.5.1 Epoxy Resins

Epoxy resins are one of the most versatile thermosetting polymers and can be formulated with many attractive properties such as high specific stiffness and strength, cured dimensional stability, adequate electrical properties and excellent corrosion and chemical resistance with low absorption of moisture[104]. The ease of processing makes them attractive for diverse applications such as metal coating, electronic devices, electrical insulators, instrument shielding and matrices for fiber-reinforced plastic and composite materials[105]. The use of epoxy resins as the matrix in fiber-reinforced plastics have provided structural support and adhesives for magnetic shielding in superconducting magnets[106] and vacuum tight joints for cryogenic application[107].

Epoxy resins are reported to show brittle behaviour at low temperatures, which can lead to fracture of composite matrix, especially at cryogenic temperatures[108]. The fracture toughness decreases with decreasing flexibility of the resins[109]. Usami *et al.* reported that the working strain of the epoxy decreases with decreasing temperature[110]. This is due to the internal stresses in the epoxy matrix caused by thermal contraction when the temperature is decreased[105]. The ultimate tensile strain of epoxy is given as 2% at 4.2

K[108]. Fast cooling from room temperature to cryogenic temperature can also cause thermal shock and compressive stresses in the epoxy matrix (Figure 4.12)[105].

These are due to the thermal contraction mismatch between filler and matrix, which may result in the weakening of the filler-matrix interface and/or micro cracking in the epoxy matrix[111]. The thermal stress of the epoxy matrix, however, can be reduced by slow cooling from room temperature[105]. The fracture toughness of epoxy is temperature dependent[110] and can be improved by choosing the appropriate hardener or mixer for the epoxy. Ueki *et al.* reported that a mixture of phenoxy and epoxy can enhance fracture toughness at cryogenic temperatures[112].

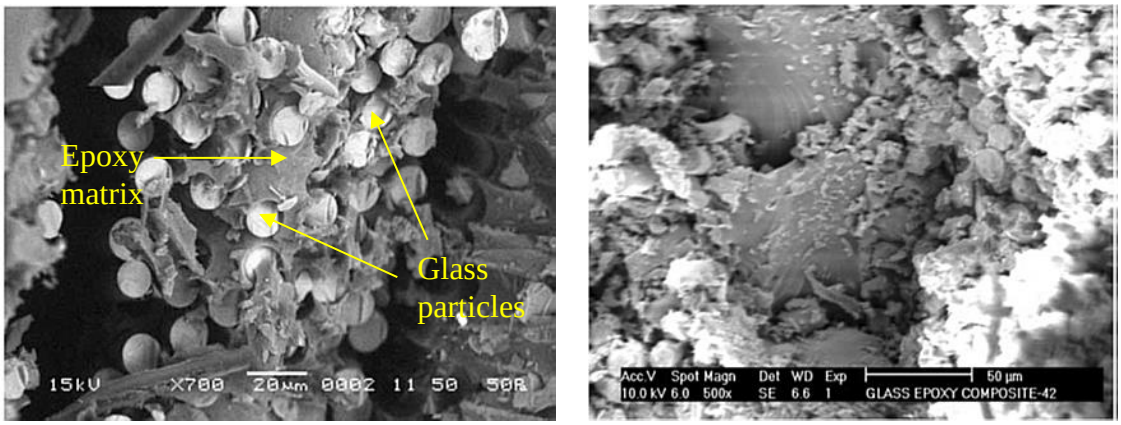


Figure 4.12 SEM images of glass fibre loaded epoxy before (left image) and after (right image) cryogenic test. Right image shows epoxy matrix condition after thermal contraction. Figures adapted from Kumar *et al.*[105] with permission. Copyright © 2008, © SAGE Publications.

Like most thermosetting polymers, a curing agent is used with epoxy resins to form a network upon curing[113]. A combination of epoxy and aliphatic amines develops the highest exothermic temperatures during the curing reaction and produces resin that cures at room temperature in a relatively short time, and so is very convenient especially for use with air sensitive HTS fillers[101]. The physical and electrical properties of epoxy resins cured with aliphatic amines tend to provide fairly good flexibility, an increase in chemical resistance and improved electrical properties, with 0.004-0.005% water

absorption and < 0.01 moisture absorption[113]. Epoxies cured with aliphatic amines find their greatest usefulness when room-temperature curing is desirable, and where the operating temperature is below 100°C. A number of studies into the mixing of magnetic fillers[114,115] and $BaTiO_3$[18,116] using epoxy resins have been reported for the measurement of electromagnetic properties at microwave frequencies.

4.5.2 Acrylonitrile Butadine Styrene (ABS)

Acrylonitrile butadiene styrene (ABS) is a common thermoplastic polymer, made of 15-35% acrylonitrile, 5-30% butadiene and 40-60% styrene[117] with the chemical formula $(C_8H_8)_x(C_4H_6)_y(C_3H_3N)_z$. ABS shows hardness, rigidity, chemical and heat resistance and a good colour range from the acrylonitrile and styrene, toughness from butadiene, and strength and flexibility in processing from the rubbery polymer butadiene[104]. This combination makes ABS the most versatile polymer in the plastics industry[118]. The glass temperature of ABS is 105 °C, which is convenient for use at high temperatures, with an ideal operating temperature between -20 °C to 80 °C[101]. Thermoplastics are ductile in their behaviour at low temperatures and have a higher ultimate tensile strain of 4-6% at 4.2 K[108], suggesting the suitability of ABS for low temperature application.

ABS can be obtained in the form of powder, beads and pellets, depending on the subsequent polymerisation and processing route[36,118]. These intermediate forms of ABS can be mixed with other additives or materials to enhance the properties for applications such as pigments, colorants, plasticizers and fillers before undergo a homogenising and compounding process[119]. The compounding process requires devices such as extruders or 3-D printers to melt and shape the ABS into a desired product.

Since there is no aqueous media involved in the polymerisation process, ABS is a good choice for mixing with reactive HTS fillers such as YBCO powders[120]. Depending on

the grade of materials, ABS has <1% water absorptivity and moisture absorption between 0.3-0.6%, which requires drying for applications such as injection moulding and plating to prevent voids[121]. ABS polymers are inert to aqueous acids and alkalis due to the strong polarity of acrylonitrile[119]. At high acrylonitrile levels, ABS can maintain its mechanical properties and at the same time form an effective diffusion barrier for oxygen and carbon dioxide[101], which can both react with YBCO. In addition, the electrical and electromagnetic properties of ABS are fairly constant over a wide range of frequencies making it more attractive for electronic and electromagnetic device applications. For example the dielectric constant for ABS is 2.4 to 3.0 over frequency range from MHz to GHz[122-124], while the dielectric loss tangent and relative magnetic permeability values are 0.01 and 1 respectively[36]. However, these electronic properties are slightly affected by exposure to high temperatures and atmospheric humidity, limiting the application of the devices in some environments[101]. Riddle *et al.* reported with increasing temperature from -151.51 ºC to 83.85 ºC the dielectric constant of the ABS decreased by ~3% and the loss tangent increased by approximately one order of magnitude at ~ 11 GHz[122]. The change in dielectric constant and lost tangent may affects reflection loss and frequency dispersion, which are issues for microwave circuits and broadband applications[124]. Iannuzzi *et al.* reported that ABS is subjected to oxidative degradation when exposed to heat and UV-light for 1500 hour at 75 °C and 50% relative humidity (accelerated weather test), resulting in discoloration of ABS, limiting its application for electrical appliances[125].

Moulart el. al. investigated $BaTiO_3$ and carbon powder loaded ABS polymer composites, and found reasonable dielectric constant values for $BaTiO_3$ composites suitable for electromagnetic shielding applications[123]. Since then, several publications on carbon loaded ABS composites have been presented, not just for improving electrical

conductivity but also for electromagnetic shielding applications[126,127]. A combination of nickel carbon coated filler and ABS composite was reported to have good shielding effects at frequencies up to 1 GHz[128].

References

1 Aydin, K. *et al.* Investigation of magnetic resonances for different split-ring resonator parameters and designs. *New Journal of Physics* **7**, 168 (2005).

2 Saha, C., Siddiqui, J. Y. & Antar, Y. M. M. Square split ring resonator backed coplanar waveguide for filter applications. *General Assembly and Scientific Symposium, 2011 XXXth URSI*, pp. 1-4 (2011).

3 Ricci, M. C. *et al.* Tunability of Superconducting Metamaterials. *IEEE Transactions on Applied Superconductivity* **17**, 918-921 (2007).

4 Ricci, M. C. & Anlage, S. M. Single superconducting split-ring resonator electrodynamics. *Applied Physics Letters* **88**, 264102 (2006).

5 Ricci, M., Orloff, N. & Anlage, S. M. Superconducting metamaterials. *Applied Physics Letters* **87**, 034102 (2005).

6 Yogi, T. & Mercereau, J. Microwave surface resistance of Nb films. *Magnetics, IEEE Transactions on* **17**, 931-934 (1981).

7 Nisenoff, M. Superconducting electronics: current status and future prospects. *Cryogenics* **28**, 47-56 (1988).

8 Kurter, C., Abrahams, J. & Anlage, S. M. Miniaturized superconducting metamaterials for radio frequencies. *Applied Physics Letters* **96**, 253504 (2010).

9 Weinberger, B. R., Lynds, L. & Hull, J. R. Magnetic bearings using high-temperature superconductors: some practical considerations. *Superconductor Science and Technology* **3**, 381 (1990).

10 Bhadrakumari, S. & Predeep, P. Preparation and Characterization of $YBa_2Cu_3O_{7-x}$/Linear Low Density Polyethylene (LLDPE) Composites. *Journal of Reinforced Plastics and Composites* **29**, 518-523 (2010).

11 Bhadrakumari, S., Predeep, P. & Sheela, A. Magnetic levitation force measurement on HTSC ceramic/thermoplastic polymer composites. *Composites Science and Technology* **68**, 3230-3233 (2008).

12 Horowitz, H. S., Bordia, R. K., Flippen, R., Johnson, R. & Chowdhry, U. Degradation of sinterability and superconducting properties of fine particle $YBa_2Cu_3O_{7-y}$ by exposure to moisture. *Materials research bulletin* **23**, 821-830 (1988).

13 Abraham, R., Kuryan, S., Isac, J., Zacharia, A. K. & Thomas, S. Yttrium barium copper oxide-filled polystyrene as a dielectric material. *Journal of applied polymer science* **120**, 2233-2241 (2011).

14 Abrahams, S. Structure relationship to dielectric, elastic and chiral properties. *Acta Crystallographica Section A* **50**, 658-685 (1994).

15 Efros, A. L. & Shklovskii, B. I. Critical Behaviour of Conductivity and Dielectric Constant near the Metal-Non-Metal Transition Threshold. *physica status solidi (b)* **76**, 475-485 (1976).

16 Pan, Y. *et al.* Percolation threshold and electrical conductivity of a two-phase composite containing randomly oriented ellipsoidal inclusions. *Journal of Applied Physics* **110**, 123715 (2011).

17 Dang, Z. M. *et al.* Fundamentals, processes and applications of high-permittivity polymer–matrix composites. *Progress in Materials Science* **57**, 660-723 (2012).

18 Dang, Z. M., Yu, Y. F., Xu, H. P. & Bai, J. Study on microstructure and dielectric property of the $BaTiO_3$/epoxy resin composites. *Composites Science and Technology* **68**, 171-177 (2008).

19 Li, Y. J., Xu, M., Feng, J. Q. & Dang, Z. M. Dielectric behavior of a metal-polymer composite with low percolation threshold. *Applied Physics Letters* **89**, 072902 (2006).

20 Yang, X., Hu, J., Chen, S. & He, J. Understanding the Percolation Characteristics of Nonlinear Composite Dielectrics. *Scientific Reports* **6**, 30597 (2016).

21 Garboczi, E. J., Snyder, K. A., Douglas, J. F. & Thorpe, M. F. Geometrical percolation threshold of overlapping ellipsoids. *Physical Review E* **52**, 819-828 (1995).

22 Wang, S. F. & Ogale, A. A. Continuum space simulation and experimental characterization of electrical percolation behavior of particulate composites. *Composites Science and Technology* **46**, 93-103 (1993).

23 Holm, E. A. & Cima, M. J. Two-Dimensional Whisker Percolation in Ceramic Matrix–Ceramic Whisker Composites. *Journal of the American Ceramic Society* **72**, 303-305 (1989).

24 Celzard, A. *et al.* Critical concentration in percolating systems containing a high-aspect-ratio filler. *Physical Review B* **53**, 6209-6214 (1996).

25 Zheng, W., Wong, S. C. & Sue, H. J. Transport behavior of PMMA/expanded graphite nanocomposites. *Polymer* **43**, 6767-6773 (2002).

26 Carmona, F., Prudhon, P. & Barreau, F. Percolation in short fibres epoxy resin composites: Conductivity behavior and finite size effects near threshold. *Solid State Communications* **51**, 255-257 (1984).

27 Bergman, D. J. & Imry, Y. Critical Behavior of the Complex Dielectric Constant near the Percolation Threshold of a Heterogeneous Material. *Physical Review Letters* **39**, 1222-1225 (1977).

28 Golosovsky, M., Tsindlekht, M. & Davidov, D. Microwave propagation through superconductor-polymer composites. *Physical Review B* **46**, 11439-11444 (1992).

29 Jung, P., Ustinov, A. V. & Anlage, S. M. Progress in superconducting metamaterials. *Superconductor Science and Technology* **27**, 073001 (2014).

30 Kilibarda-Dalafave, S. & Ng, H. Far-infrared transmission spectra of granular free-standing thin films of $YBa_2Cu_3O_x$ near the percolation threshold. *Physical Review B* **46**, 1107 (1992).

31 Garner, J. & Stroud, D. Theory of far-infrared absorption in superconducting composites. *Physical Review B* **28**, 2447-2451 (1983).

32 Cheah, H., Porch, A. & Waldram, J. Microwave conductivity of powdered unaligned $YBa_2Cu_3O_{7-\delta}$. *Physica B: Condensed Matter* **165**, 1195-1196 (1990).

33 Owens, F. J. Resonant and non-resonant microwave absorption in the high-temperature superconductors. *Synthetic Metals* **33**, 225-242 (1989).

34 Owens, F. J. Theory of line shape of nonresonant microwave absorption in granular composites of copper oxide superconductors. *Physica C: Superconductivity* **171**, 25-30 (1990).

35 Golosovsky, M., Tsindlekht, M., Davidov, D. & Sarychev, A. Effective-medium approach to the microwave properties of the high-T_c superconductor-insulator composites. *Physica C: Superconductivity* **209**, 337-340 (1993).

36 Grant, P. S. *et al.* Manufacture of electrical and magnetic graded and anisotropic materials for novel manipulations of microwaves. *Phil. Trans. R. Soc. A* **373**, 20140353 (2015).

37 Abraham, R. *et al.* Mechanical properties of ceramic-polymer nanocomposites. *polymer* **8**, 12 (2009).

38 Alford, N. M., Button, T. & Birchall, J. Processing, properties and devices in high-Tc superconductors. *Superconductor Science and Technology* **3**, 1 (1990).

39 Abraham, R. *et al.* Structural and mechanical properties of YBCO-polystyrene composites. *Journal of Applied Polymer Science* **118**, 1027-1041 (2010).

40 Sarkar, A. K. & Peterson, T. L. Fabrication and electrical properties of ceramic superconductor/polymer composites. *Polymer Engineering & Science* **32**, 305-309 (1992).

41 Mettout, B., Dumas, P., Waysand, G. & Chardin, G. in *Volume 5 of European Materials Research Society Symposia Proceedings* pp. 201-206 (Elsevier Science, 2012).

42 Bhadrakumari, S. & Predeep, P. High-Tc superconductor/linear low density polyethylene (LLDPE) composite materials for diamagnetic applications. *Superconductor Science and Technology* **19**, 808 (2006).

43 Sato, K., Omae, S., Kojima, K., Hashimoto, T. & Koinuma, H. Stabilization of $Ba_2YCu_3O_{7-\delta}$ by Surface Coating with Plasma Polymerized Fluorocarbon Film. *Japanese journal of applied physics* **27**, L2088-L2090 (1988).

44 Unsworth, J., Du, J., Crosby, B. J. & Bryant, P. $YBa_2Cu_3O_{7-x}$ superconducting ceramic/thermoplastic 0–3 composites. *Materials Research Bulletin* **26**, 1041-1050 (1991).

45 Nisenoff, M. Microwave superconductivity part 1: History, properties and early applications. *2011 IEEE MTT-S International Microwave Symposium, IMS 2011*, pp. 1-4 (2011).

46 Maeda, H., Tanaka, Y., Fukutomi, M. & Asano, T. A new high-T_c oxide superconductor without a rare earth element. *Japanese Journal of Applied Physics* **27**, L209-L210 (1988).

47 Tarascon, J. M. *et al.* Preparation, structure, and properties of the superconducting compound series $Bi_2Sr_2Ca_{n-1}Cu_nO_y$ with n=1,2, and 3. *Physical Review B* **38**, 8885-8892 (1988).

48 Yan, M. F. *et al.* Water interaction with the superconducting $YBa_2Cu_3O_7$ phase. *Applied Physics Letters* **51**, 532-534 (1987).

49 Barns, R. L. & Laudise, R. A. Stability of superconducting $YBa_2Cu_3O_7$ in the presence of water. *Applied Physics Letters* **51**, 1373-1375 (1987).

50 Goodenough, J. B. & Manthiram, A. Crystal chemistry and superconductivity of the copper oxides. *Journal of Solid State Chemistry* **88**, 115-139 (1990).

51 Portis, A. M. *Electrodynamics of high-temperature superconductors*. Vol. 48 pp. 1-64 (World Scientific, 1993).

52 Chrisey, D. B. Progress in the first ten years of HTS film growth. *JOM* **49**, 28-32 (1997).

53 Dinger, T. R., Worthington, T. K., Gallagher, W. J. & Sandstrom, R. L. Direct observation of electronic anisotropy in single-crystal $Y_1Ba_2Cu_3O_{7-x}$. *Physical Review Letters* **58**, 2687-2690 (1987).

54 Gallagher, W. J. *et al.* Anisotropy in the magnetic properties of single-crystal $Y_1Ba_2Cu_3O_{7-x}$. *Physica B+C* **148**, 228-232 (1987).

55 Cava, R. J. *et al.* Studies of oxygen-deficient $Ba_2YCu_3O_{7-\delta}$ and superconductivity Bi(Pb)SrCaCuO. *Physica C: Superconductivity* **153**, 560-565 (1988).

56 Tarascon, J.-M. *et al.* Oxygen and rare-earth doping of the 90-K superconducting perovskite $YBa_2Cu_3O_{7-x}$. *Physical Review B* **36**, 226 (1987).

57 Subramanian, M. *et al.* A New High-Temperature Superconductor: Bi_2Sr_{3-x} Ca_x Cu_2O_{8+y}. *Science* **239**, 1015-1017 (1988).

58 Sleight, A. W. Chemistry of High-Temperature Superconductors. *Science* **242**, 1519-1527 (1988).

59 Cava, R. J. *et al.* $Ba_2YCu_3O_{7-\sigma}$; Effect of Oxygen Stoichiometry. *MRS Proceedings* **99**, 19-26 (1987).

60 Cava, R. *et al.* Oxygen stoichiometry, superconductivity and normal-state properties of $YBa_2Cu_3O_{7-\delta}$. *Nature* **329**, 423-425 (1987).

61 Gallagher, P. K., O'Bryan, H. M., Sunshine, S. A. & Murphy, D. W. Oxygen stoichiometry in $Ba_2YCu_3O_x$. *Materials Research Bulletin* **22**, 995-1006 (1987).

62 Jin, S. & Graebner, J. E. Processing and fabrication techniques for bulk High-Tc superconductors: A critical review. *Materials Science and Engineering: B* **7**, 243-260 (1991).

63 Murakami, M. *et al.* Flux pinning and critical currents in melt processed YBaCuO superconductors. *Superconductor Science and Technology* **4**, S43-50 (1991).

64 Koblischka, M. & Wijngaarden, R. Magneto-optical investigations of superconductors. *Superconductor Science and Technology* **8**, 199-213 (1995).

65 Fedor, G. Characterization of high-temperature superconductors by AC susceptibility measurements. *Superconductor Science and Technology* **10**, 523 (1997).

66 Nikolo, M. Superconductivity: A guide to alternating current susceptibility measurements and alternating current susceptometer design. *American Journal of Physics* **63**, 57-65 (1995).

67 Chen, D. X., Sanchez, A., Puig, T., Martinez, L. M. & Muñoz, J. S. AC susceptibility of grains and matrix for high-Tc superconductors. *Physica C: Superconductivity* **168**, 652-667 (1990).

68 Lévy, L.-P. *Magnetism and superconductivity*. pp. 7-11 (Springer, 2000).

69 Clem, J. R. & Kogan, V. G. Theory of the Magnetization of Granular Superconductors: Application to High-Tc Superconductors. *Japanese Journal of Applied Physics* **26**, 1161 (1987).

70 Campbell, A., Blunt, F., Johnson, J. & Freeman, P. Quantitative determination of percentage superconductor in a new compound. *Cryogenics* **31**, 732-737 (1991).

71 Poole, C. P., Farach, H. A. & Creswick, R. J. *Superconductivity 2nd Edition*. Vol. 2nd Edition pp. 141-415, (Academic Press, 2007).

72 Iida, K., Babu, N. H., Reddy, E. S., Shi, Y. H. & Cardwell, D. A. The effect of nano-size ZrO 2 powder addition on the microstructure and superconducting properties of single-domain Y–Ba–Cu–O bulk superconductors. *Superconductor Science and Technology* **18**, 249 (2005).

73 Hibbs, A., Eberhardt, F., Campbell, A. & Male, S. Effect of particle size on the magnetization of high T_c powders. *Cryogenics* **28**, 678-680 (1988).

74 Porch, A. *et al.* Temperature dependent magnetic penetration depth of Co and Zn doped $YBa_2Cu_3O_7$ obtained from the AC susceptibility of magnetically aligned powders. *Physica C: Superconductivity* **214**, 350-358 (1993).

75 Miiller, G. Microwave Properties of High-T, Oxide Superconductors. *Proceedings of the Fourth Workshop on RF Superconductivity*, pp. 267 (1989).

76 Masato, M. *et al.* Large Levitation Force due to Flux Pinning in YBaCuO Superconductors Fabricated by Melt-Powder-Melt-Growth Process. *Japanese Journal of Applied Physics* **29**, L1991 (1990).

77 Lee, D. F., Selvamanickam, V. & Salama, K. Influences of Y2BaCuO5 particle size and content on the transport critical current density of YBa2Cu3Ox superconductor. *Physica C: Superconductivity* **202**, 83-96 (1992).

78 Murakami, M. Processing of bulk YBaCuO. *Superconductor Science and Technology* **5**, 185 (1992).

79 Balachandran, U., Zhong, W., Youngdahl, C. A. & Poeppel, R. B. Microstructure and associated properties of YBCO superconductors prepared by melt-processing techniques. *Journal of Elec Materi* **22**, 1285-1288 (1993).

80 Fujimoto, H., Taguchi, T., Murakami, M., Nakamura, N. & Koshizuka, N. Microstructures and critical currents in melt-processed YBCO. *Cryogenics* **32**, 954-958 (1992).

81 Cardwell, D. A. Processing and properties of large grain (RE)BCO. *Materials Science and Engineering: B* **53**, 1-10 (1998).

82 Lo, W., Cardwell, D. A., Dewhurst, C. D. & Dung, S.-L. Fabrication of large grain YBCO by seeded peritectic solidification. *Journal of Materials Research* **11**, 786-794 (1996).

83 Babu, N. H. *et al.* Growth of large sized $YBa_2Cu_3O_7$ single crystals using the top seeded melt growth process. *Superconductor Science and Technology* **25**, 075012 (2012).

84 Morita, M. *et al.* Quench and Melt Growth (QMC) Process for Large Bulk Superconductor Fabrication. *Advances in Superconductivity III*, pp. 733-736 (1991).

85 Meng, R. L. *et al.* Growth and possible size limitation of quality single-grain YBa2Cu3O7. *Physica C: Superconductivity* **232**, 337-346 (1994).

86 Babu, N. H., Iida, K., Shi, Y. & Cardwell, D. A. Fabrication of high performance light rare earth based single-grain superconductors in air. *Applied Physics Letters* **87**, 202506 (2005).

87 Beruto, D., Giordani, M. & Botter, R. Effect of the atmosphere on the formation of cuprate superconductor powders from highly reactive $RE_2O_3/BaO_2/CuO$ mixtures. *Materials Letters* **10**, 17-22 (1990).

88 Cava, R. J. *et al.* Bulk superconductivity at 91 K in single-phase oxygen-deficient perovskite $Ba_2YCu_3O_{9-b}$. *Physical Review Letters* **58**, 1676-1679 (1987).

89 Cava, R. J. *et al.* Single-phase 60-K bulk superconductor in annealed $Ba_2YCu_3O_{7-\delta}$ ($0.3< \delta< 0.4$) with correlated oxygen vacancies in the Cu-O chains. *Physical Review B* **36**, 5719-5722 (1987).

90 Clarke, D. R., Shaw, T. M. & Dimos, D. Issues in the processing of cuprate ceramic superconductors. *Journal of the American Ceramic Society* **72**, 1103-1113 (1989).

91 Cloots, R., Cardwell, D. A. & Ginley, D. S. *Handbook of Superconducting Materials: Powder processing techniques*. Chapter B2.1, pp. 223-242 (CRC Press, 2003).

92 Tarascon, J. M. *et al.* Crystal substructure and physical properties of the superconducting phase $Bi_4(Sr,Ca)_6Cu_4O_{16+x}$. *Physical Review B* **37**, 9382-9389 (1988).

93 Green, S. M. *et al.* Effects of compositional variations on the properties of superconducting $(Bi,Pb)_2Sr_2Ca_2Cu_3O_\delta$. *Journal of Applied Physics* **66**, 728-734 (1989).

94 Chen, Y. L. & Stevens, R. 2223 Phase Formation in Bi (Pb)─ Sr─ C─ a─ Cu─ O: II, The Role of Temperature—Reaction Mechanism. *Journal of the American Ceramic Society* **75**, 1150-1159 (1992).

95 Halim, S. A., Khawaldeh, S. A., Mohamed, S. B. & Azhan, H. Superconducting properties of $Bi_{2-x}Pb_xSr_2Ca_2Cu_3Oy$ system derived via sol–gel and solid state routes. *Materials Chemistry and Physics* **61**, 251-259 (1999).

96 Masashi, K. in *Polymeric Materials for Microelectronic Applications* Vol. 579 *ACS Symposium Series* Ch. 17, pp. 220-233 (American Chemical Society, 1995).

97 Feger, C. *et al.* in *Polymeric Materials for Microelectronic Applications* Vol. 579 *ACS Symposium Series* Ch. 21, pp. 272-282 (American Chemical Society, 1995).

98 Johnen, N. A., Kim, H. K. & Ober, C. K. in *Polymeric Materials for Microelectronic Applications* Vol. 579 *ACS Symposium Series* Ch. 23, pp. 298-315 (American Chemical Society, 1995).

99 Sroog, C. E. Polyimides. *Journal of Polymer Science: Macromolecular Reviews* **11**, 161-208 (1976).

100 Ratna, D. *Epoxy Composites : Impact Resistance and Flame Retardancy*. Vol. 16 pp. 5-7 (Smithers Rapra, 2005).

101 Harper, C. A. *Handbook of plastics, elastomers, and composites Third Edition*. (McGraw-Hill, 1996).

102 Biron, M. *Thermoplastics and thermoplastic composites : technical information for plastics users*. pp. 623 (Elsevier, 2007).

103 Akovali, G. N. & Kaynak, C. *Handbook of composite fabrication*. pp. 22 (Rapra Technology, 2001).

104 Murphy, J. *The reinforced plastics handbook*. pp. 4-14 (Elsevier Advanced Technology, 1994).

105 Kumar, S. M., Sharma, N. & Ray, B. C. Mechanical Behavior of Glass/Epoxy Composites at Liquid Nitrogen Temperature. *Journal of Reinforced Plastics and Composites* **27**, 937-944 (2008).

106 Rey, J. M., Gallet, B., Kircher, F. & Lottin, J. C. Epoxy resin developments for large superconducting magnets impregnation. *Cryogenics* **38**, 19-23 (1998).

107 Anashkin, O. P., Keilin, V. E. & Patrikeev, V. M. Cryogenic vacuum tight adhesive. *Cryogenics* **39**, 795-798 (1999).

108 Hartwig, G. & Knaak, S. Fibre-epoxy composites at low temperatures. *Cryogenics* **24**, 639-647 (1984).

109 Sawa, F., Nishijima, S. & Okada, T. Molecular design of an epoxy for cryogenic temperatures. *Cryogenics* **35**, 767-769 (1995).

110 Usami, S., Suzuki, T., Ejima, H. & Asano, K. Thermo-mechanical properties of epoxy GFRPs used in superconducting magnet winding. *Cryogenics* **39**, 905-914 (1999).

111 Ray, B. C. Effects of Thermal and Cryogenic Conditionings on Mechanical Behavior of Thermally Shocked Glass Fiber-Epoxy Composites. *Journal of Reinforced Plastics and Composites* **24**, 713-717 (2005).

112 Ueki, T., Nishijima, S. & Izumi, Y. Designing of epoxy resin systems for cryogenic use. *Cryogenics* **45**, 141-148 (2005).

113 Lee, H. *Epoxy resins : their applications and technology*. pp. 30-61 (McGraw-Hill, 1957).

114 Wang, B., Wei, J., Yang, Y., Wang, T. & Li, F. Investigation on peak frequency of the microwave absorption for carbonyl iron/epoxy resin composite. *Journal of Magnetism and Magnetic Materials* **323**, 1101-1103 (2011).

115 Wang, Y. & Grant, P. NiZn ferrite/Fe hybrid epoxy-based composites: extending magnetic properties to high frequency. *Applied Physics A* **117**, 477-483 (2014).

116 Yang, W. *et al.* A systematic study on electrical properties of the $BaTiO_3$–epoxy composite with different sized $BaTiO_3$ as fillers. *Journal of Alloys and Compounds* **620**, 315-323 (2015).

117 McKeen, L. W. *Film Properties of Plastics and Elastomers*. 3rd edn, pp. 10-81 (William Andrew, 2012).

118 Olabisi, O. & Adewale, K. *Handbook of Thermoplastics*. (Taylor & Francis, 1997).

119 Basdekis, C. H. *ABS plastics*. Vol. 28 pp. 46-47 (Reinhold, Chapman & Hall, 1964).

120 Alford, N. M. *et al.* Physical and mechanical properties of $YBa_2Cu_3O_{7-\delta}$ superconductors. *Journal of Materials Science* **23**, 761-768 (1988).

121 Friedrich, K., Zhang, Z. & Schlarb, A. K. Effects of various fillers on the sliding wear of polymer composites. *Composites Science and Technology* **65**, 2329-2343 (2005).

122 Riddle, B., Baker-Jarvis, J. & Krupka, J. Complex permittivity measurements of common plastics over variable temperatures. *Microwave Theory and Techniques, IEEE Transactions on* **51**, 727-733 (2003).

123 Moulart, A., Marrett, C. & Colton, J. Polymeric composites for use in electronic and microwave devices. *Polymer Engineering & Science* **44**, 588-597 (2004).

124 Deffenbaugh, P. I., Rumpf, R. C. & Church, K. H. Broadband Microwave Frequency Characterization of 3-D Printed Materials. *Components, Packaging and Manufacturing Technology, IEEE Transactions on* **3**, 2147-2155 (2013).

125 Iannuzzi, G., Mattsson, B. & Rigdahl, M. Color changes due to thermal ageing and artificial weathering of pigmented and textured ABS. *Polymer Engineering & Science* **53**, 1687-1695 (2013).

126 Liang, X., Ling, L., Lu, C. & Liu, L. Resistivity of carbon fibers/ABS resin composites. *Materials Letters* **43**, 144-147 (2000).

127 Chiang, W. Y. & Cheng, K. Y. Processing conditions for electromagnetic interference shielding effectiveness and mechanical properties of acrylonitrile-butadiene-styrene based composites. *Polymer Composites* **18**, 748-756 (1997).

128 Lu, G., Li, X. & Jiang, H. Electrical and shielding properties of ABS resin filled with nickel-coated carbon fibers. *Composites Science and Technology* **56**, 193-200 (1996).

5 Fabrication of Superconducting Composites

5.1 Polymer Composite Fabrication 62
5.1.1 Casting 63
5.1.2 Extrusion 64
5.1.3 Additive Manufacturing (3-D Printing) 67
5.2 Factors Affecting Fabrication of Superconducting Composites 70
5.2.1 Fillers 70
5.2.2 Environmental Effects 71
5.3 Factors Affecting Electromagnetic Properties of Superconducting Composites 71
5.3.1 Homogenisation 74
5.3.2 Application of Mixing Rules 75
5.4 Summary 79
References 80

The processing routes for superconducting composites depend mainly on the choice of polymer material for the matrix. This chapter will introduce the methods that have been explored for superconducting composites.

5.1 Polymer Composite Fabrication

The fabrication of superconducting composites is similar to conventional polymer processing techniques, with an additional step of mixing filler into the polymer matrices before polymerisation. The details of the mixing process, however, differ by the choice of polymer, while the design or shape of the polymer composites depends on the processing methods selected to make the part.

5.1.1 Casting

Casting is a straightforward, inexpensive and widespread manufacturing technique commonly used to fabricate a wide range of polymer composites for electromagnetic applications using epoxy resin as the matrix[1-3].

Hojo *et al.* fabricated epoxy resin composites by mixing epoxy, curing agent and fillers and pouring them into a pre-heated mould under vacuum[4]. The mixture of well-dispersed composite filler is then poured into a simple mould and cured at room temperature, usually for 24 hours[5,6] depending on the type of resin and curing agent used for the polymerisation process.

The casting technique only requires a low cost mould to produce large and relatively simple shaped samples, and is most suitable for low filler volume fractions[6]. However, Wang *et al.* demonstrated that a wide range of mould designs can be used for multi ferrite fillers with loading high as 60 vol%[7]. Another successful casting fabrication process is the "step-graded all dielectric structures" made from $BaTiO_3$/epoxy composites for a surface wave splitter application[5]. The device was fabricated using a specially designed set of moulds with discrete increases in size to control the shape of $BaTiO_3$ layers with various loading volume fractions.

Golosovsky *et al.* applied this simple casting technique to fabricate YBCO/PMMA composites for studies of electromagnetic properties[8]. Unlike the conventional casting method, 20 μm YBCO powder was mixed into dry polymethylmetacrylate powder and fast cured (10 minutes) by adding a soluble curing agent. The YBCO/PMMA mixture was then cast into rectangular bars to fit into a waveguide holder for electromagnetic measurements. A convenience of casting techniques is that the thickness of cured YBCO composites can be easily varied from 0.5 to 2.0 cm. However, this simple

method of fabrication was reported to have a limitation on the filler volume fraction of a maximum of 50 vol%.

5.1.2 Extrusion

Polymer composites can be produced in the form of continuous filaments by extrusion[9,10]. A number of dielectric and conductive polymer composites loaded with $BaTiO_3$, alumina or carbon have been produced using this technique to produce feedstocks for electromagnetic applications[11,12]. It has been reported recently that polymer extrusion can be used to produce the feedstock filament for additive manufacturing[13,14].

In the extrusion process, a granular mixture is converted to a high viscosity paste by heat and pressure[15]. The extrusion process basically involves loading the starting mixture into the barrel of an extruder through the hopper, and forcing the heated and melted thermoplastic polymer composite through a die that has an opening shaped to allow the formation of filaments, films, sheets and other useful cross sections[16] (Figure 5.1).

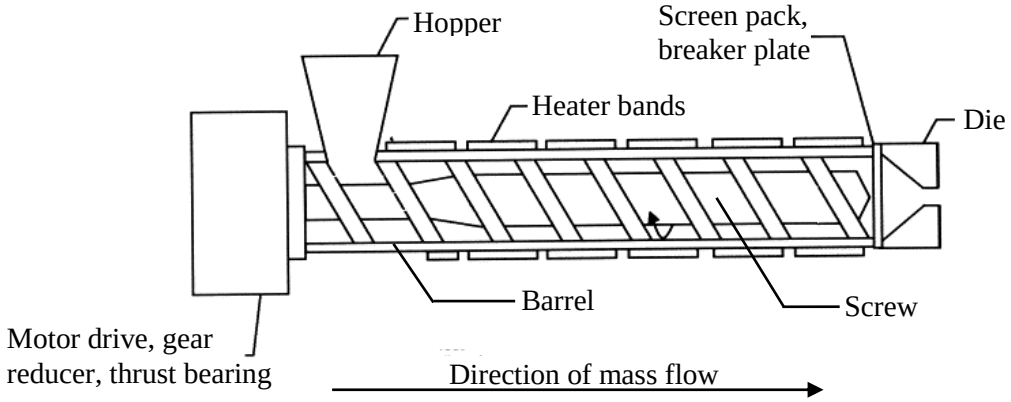


Figure 5.1 A schematic diagram of a typical single screw extruder with continuous melt flow. Figure adapted after Breitenbach[17] with permission from Elsevier.

In order to produce composite filaments with a good uniform thickness and tensile strength, the viscosity of the melted composite must be consistent up to the die entrance,

which can be controlled by adjusting on the content of fillers and the melt temperature of the composites[18]. Filler loaded in the polymer can improve the tensile strength of the extruded filament. For example, Shenawar *et al.* demonstrated that the extruded 10 wt% carbon black loaded ABS composites has ~22% higher tensile strength than the ABS filament[19]. Bakar *et al.* also reported the talc/kaolin powder loaded polypropylene composites have 60% higher tensile strength than the unloaded polypropylene[20]. It should be noted that the tensile strength (stress) may improve for the extruded filaments, but the tensile strain does not.

A good temperature control is important to achieve constant polymer melt temperature and pressure at the die, in order to produce extruded filaments with uniform cross section dimensions[16]. Inconsistent viscosity of the melted polymer flow can cause changes of extruded filament dimensions[21]. Polymer viscosity and flow can be controlled by adjusting the melt temperature. Wells *et al.* reported that the melt temperature has a significant influence on melt pressure of the melted polymer composites, with melt pressure decreasing with increasing melt temperature[22]. This indicates that decreases in the melt temperature result in higher viscosity of the melted polymer, which increases resistance to flow of the melted polymer, requiring increased melt pressure and resulting in faster output. This suggests that, the melt temperature needs to be carefully optimised based on the filler and materials used for extrusion to produce extruded filament with uniform and consistent filament dimensions.

Die swell is another common factor that can affect extruded filament dimensions, and occurs when a high flow rate of melt polymer is compressed into a die, followed by subsequent die shape and volume of the polymer recovery upon exiting the die. Die swell is controlled by die dimensions, melt viscosity and temperature, where die swell decreases with increasing melt temperature and longer die dimensions[23]. Longer die

dimensions and lower viscosity of melt polymer provide ample time for the melted polymer to relax and gain its shape from the die upon extrusion[24].

The precursor composite materials are prepared prior to extrusion, and two preparation methods have been proposed, which can be categorised as *direct* and *indirect*. The direct process is more convenient, and involves mixing fillers into the melted polymer as it is extruded as a filament[11]. The indirect process is preferred to obtain well-dispersed filler fractions in the polymer. This requires mixing fillers into a dissolved polymer solution, and evaporating the solvent to have a solidified mixture, which can later be loaded into the extruder for filament extrusion[25]. Since the moisture guidelines for the extrusion process are < 0.02%[21], the solidified mixture needs to be properly dried in air or in an oven. Improper drying of the solidified mixture leads to air bubbles and void formation in the extruded filaments (Figure 5.2)[25]. Huang *et al.* suggested vacuum treatment on the solidifying mixture during the sample mixing process to remove air bubbles efficiently[26].

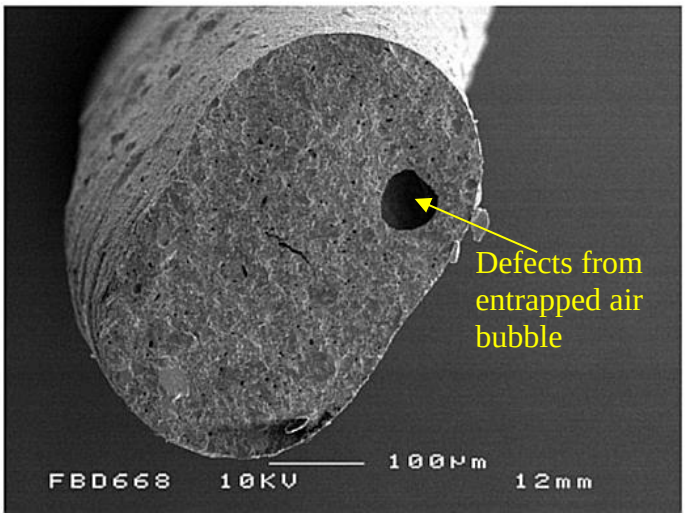


Figure 5.2 Entrapped air bubbles causing defects in the extruded Al_2O_3 loaded PVB composite filament. Air bubbles were developed during the composite mixture preparation. Figure reproduced from Lu *et al.*[25] with permission from Elsevier.

5.1.3 Additive Manufacturing (3-D Printing)

Additive manufacturing (AM), also known as 3-D printing[27], was developed in the 1990's as a rapid prototyping technique[28]. Selective Laser Sintering is one of the AM techniques that uses a laser to sinter powdered material by scanning cross-sections on the surface of a powder bed, using a computer-controlled laser beam, followed by several sequences of sintering on fresh powder layers piled on top of the old one until a three dimensional structure was developed[29]. Agarwala *et al.* were the first to report the fabrication of three dimensional Ag-YBCO structures using the AM technique of Selective Laser Sintering[30].

Fused deposition modelling (FDM) is another type of AM process that can be used for producing 3-D composites. In this process, a feedstock filament of polymer based materials is fed into a printer head and melted in a heater and pushed through a print nozzle by a pinch roller mechanism (Figure 5.3)[28]. The 3-D printing process starts when melted beads are extruded from the print nozzle and printed on a building stage. The movement of the print nozzle is controlled in the horizontal x-y plane as the material is deposited on the build stage, and builds up in the vertical z direction to produce 3-D objects[31]. Layers are bonded through thermal heating from the printing head[29]. Unlike conventional polymer fabrication techniques, no post curing is required for FDM printed structures[29], which reduces the process time for fabrication. X, y and z movements are programmed using built-in or externally designed software integrated with commercial 3-D printers[31].

Thermoplastics have been commonly used as a feedstock polymer in the FDM process[11]. Composite materials based on ABS, polyvinylbutyral (PVB) and polydimethylsiloxane (PDMS) have been developed using the FDM process for many device applications using fillers such as ceramics, ferrites, superconductors, alumina

and Bi-Ba-Nd-TiO_3 (BBNT) to produce feedstock filament by extrusion and then printed into 3-D structures for potential electromagnetic devices applications[5,32,33].

Since commercial 3-D printers were initially designed to print ABS, re-optimisation of the printing parameters such as nozzle temperature, feed rate and traverse speed of the printer head are required for polymer composite applications[5]. The printing resolution depends on the size of the print nozzle, and typical nozzle sizes for ABS printing are about 100-500 μm[28]. Taking into account the loaded filament, the nozzle sizes for printing composite ABS might have to be larger depending on the size of the fillers. Reducing the nozzle size should improve the printing resolution, improving the precision of electromagnetic properties but increasing the printing time.

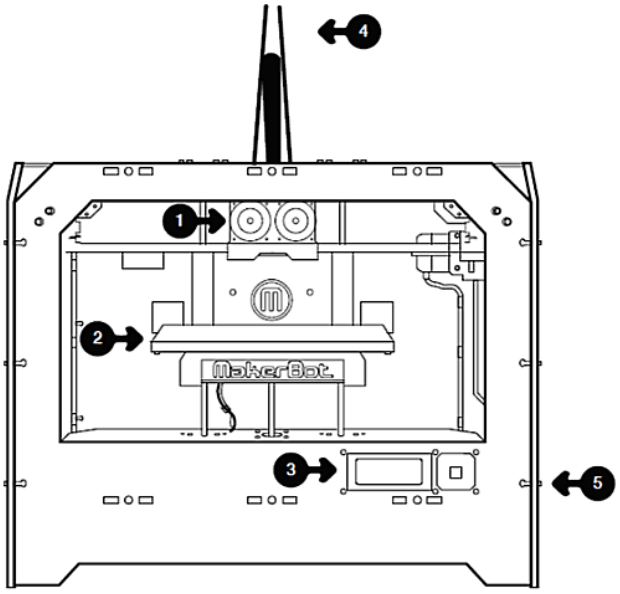


Figure 5.3 A diagram of 3-D printer by MakerBot; 1. Printer head with a pinch roller mechanism, 2. Build platform, 3. Interface panel, 4. Feedstock filament guide tubes and 5. SD Card slot panel. Figure reproduced from *MakerBot The Replicator™ Set up Guide*[34] with permission. Copyright © 2012 MakerBot Industries LLC.

The printing resolution might also have an impact on the development of air gaps between printing layers. The space between the printed layers may contain air gaps that have the potential to affect the electromagnetic properties of devices. This has been

observed by Koulouridis *et al.* who reported the shift of resonant frequencies from the simulated frequency at 6.4 GHz due to air bubbles encapsulated in the printed Bi-Ba-N-TiO_3/PDMS microwave filters[33]. Entrapped air in printed ABS composite samples can originate from the porosity of feedstock filaments, the extrusion process in the printer head, and the air gap parameter set up in the 3-D printer[35].

In order to reduce air gaps in feedstock material, high quality feedstock material needs to be used and stored in air tight storage to avoid moisture absorption. Another method to reduce the air gap in printed samples is by adjusting the distance between beads of FDM materials using air gap parameter setting, which can be set in the 3-D printing software. The air gap parameter is used to increase the structure density and reduce the porosity of printed samples.

The size and properties of the feedstock filament is another factor limiting the types of material that can be printed. Grant *et al.* demonstrated that the maximum loading of $BaTiO_3$ in ABS filament that can be loaded and printed using a 3-D printer is ~ 75 wt% (equivalent to ~35 vol%) before the filament becomes too brittle and fragile to handle[5]. However, Bandyopadhyay *et al.* suggested that the addition of surfactants or plasticizers may improve the printable performance of high volume fraction filaments[36].

The AM technique also provides considerable design freedom for 3-D structures of HTS composites, which convenient for building electromagnetic devices with designs based on the spatial transformation approach. This includes the anisotropic devices discussed in Chapter 9 fabricated by printing both filled and unfilled composite layers oriented in specific orientations to the electric and magnetic fields directions of incident electromagnetic waves.

5.2 Factors Affecting Fabrication of Superconducting Composites

5.2.1 Fillers

The major obstacle in fabricating practical polymer composites is avoiding the poor mechanical properties of fillers, while maintaining their electrical or magnetic properties. Ceramic powders such as superconductors and $BaTiO_3$ are inherently brittle in nature and tend to cause a problem during casting or moulding, even for the simplest shapes[37]. Problems occur in mixing when the size and volume fraction of fillers are large compared to the polymer matrix. A high density of filler can cause non-uniform dispersion across large volumes of composite materials during processing, and a large size filler might affecting the mechanical strength of the polymer composites[4,5,38,39]. A well-dispersed particle distribution is important in order to achieve homogeneous properties. Several methods such as mechanical mixing using high shear rates, mechanical stirring or sonication in a ultrasonic bath[40] have been used to improve the mixing process.

High filler content and fine size filler particles also tend to agglomerate in the polymer and this can also affect the mechanical properties of the printed composite[41]. Agglomerates often trap moisture, which can lead to porosity, reducing the tensile strength of the composite[42]. The application of dispersing liquids have been reported with moderate success to break agglomerates without breaking individual particle as compared to using mechanical mixing or stirring for several hours[43].

There are several ways for achieving homogeneous mixing depending on the polymer matrix and the processing route. Epoxy and ABS polymers require different techniques for homogenisation depending on their source polymer. In epoxy resin, particles can be typically dispersed using sonication or a mechanical stirrer. Alford *et al.* proposed mechanical mixing at high shear rates to break down powder agglomeration[44]. Re-

extrusion of composite filaments has been proven to improve mixing, and produce a high quality polymer composite filament[45]. However, re-extrusion needs to be done carefully to avoid thermal ageing which can severely degrade the properties of extruded composite polymers.

5.2.2 Environmental Effects

Epoxy resins tend to absorb moisture when exposed to high humidity, leading to a degradation of resin properties. Letteri *et al.* reported that the mechanical properties of epoxy can be affected by exposure to 75% humidity, leading to the reduction in the stiffness of the epoxy[46]. This suggests that the physical properties and curing behaviour of HTS composites can be affected by the environment. For example, a longer curing time may be required to produce a fully cured HTS composite in the summer or rainy season due to high humidity. The curing process, however, can be speeded up using a heat-treatment below 60 ℃[47].

5.3 Factors Affecting Electromagnetic Properties of Superconducting Composites

Hale has described that the physical properties of polymer composites are controlled by two sets of parameters; the properties of the constituent phases, their volume fractions, and the composite geometry, and structural factors such as the arrangement of fillers and dimensions of the particles[48].

Golosovsky *et al.* explained how the electromagnetic wave propagation behaviour in a composite of diluted HTS particles in polymer can be described using the refractive index (n) and loss coefficient (k) as in equation (2.4) in both normal and superconducting states[2]. In their measurements $n >> k$, characteristic of the insulating polymer matrix, rather than showing metallic $(n \approx k)$ or superconducting $(n < 0)$ properties. This allowed them to analyse the superconductor particles as a dielectric

material, where the dielectric constant and relative magnetic permeability in both normal and superconducting states are measured.

Figure 5.4 shows that the n and k values extracted for their HTS composites depend on volume fractions and T_c of the superconducting filler, showing that the electromagnetic properties of HTS composites can be controlled by tuning the volume fraction of the HTS filler[8]. They reported that the increase in n values in the normal and superconducting states is due to the increase in volume fraction of HTS filler. The decrease in n value in the superconducting state is due to the change of relative magnetic permeability ($\mu_r < 1$) of the superconducting particles. The increase in amplitude of Δn from the normal to the superconducting state with volume fraction also suggests that there is an expected μ_r dependence on the volume fraction of HTS filler.

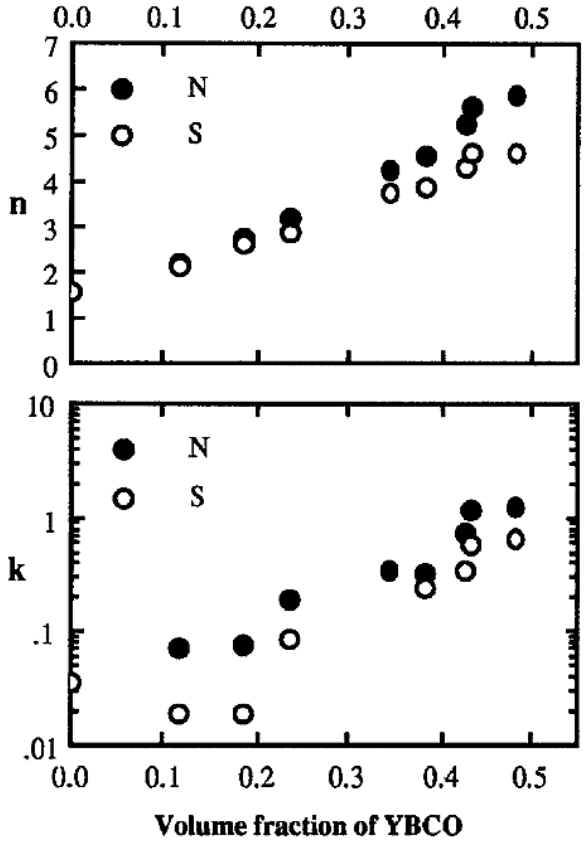


Figure 5.4 The complex refractive index of YBCO/PMMA composites in the normal state (N) and superconducting state (S). Figure reproduced from Golosovsky *et al.*[2] with permission from Elsevier.

The change of dielectric constant of HTS composites in the normal and superconducting states can be explained using several models. Pomerantz[49] proposed the calculation of the dielectric constant of HTS composites using a combination of the effective medium theory and the London penetration (λ_L) depth at T=0, given as

$$\frac{\varepsilon_{SC}}{\varepsilon_N} = 1 - \frac{fr^2}{(1+3f)(10\lambda_p^2)} \tag{5.1}$$

where $\varepsilon_N = \varepsilon_0(1+3f)$ and f and r are the volume fraction and size of the HTS filler respectively. Equation 5.1 also suggests that that the dielectric constant is frequency independent, *i.e.* that there is no significant difference of ε_r values in the superconducting state and normal state at all frequencies[2]. Golosovsky *et al.* suggested that the change of refractive index of the HTS particles is due to the change of effective magnetic permeability in the superconducting state[8].

The effective magnetic permeability of HTS composites with $f \ll 1$ can be given as[8],

$$\mu = 1 + \frac{3\alpha f}{r^3} \tag{5.2}$$

where α is the magnetic polarizability. $\alpha = 0$ for a poorly conducting metal such as a ceramic superconductor in the normal state and $\alpha = -r^3/2$ for superconducting particle with $\lambda_L < r$. This suggests that a good quality HTS filler is required in order to observe a significant change of the relative magnetic permeability in the superconducting state. A good quality HTS powder will have a small penetration depth due to the large number of superconducting electrons as explained in section 3.2.7, and the particle size will have to be chosen so that $r \gg \lambda_L$. λ_L values for anisotropic HTS filler such as $YBa_2Cu_3O_7$ (YBCO-123) and $Bi_2Sr_2Ca_2Cu_3O_{10}$ (BSCCO-2223) depend on the direction of applied field along ab planes and c-axis. Typical λ_p values for single crystal YBCO-123 are $\lambda_{ab} = 0.03 - 0.13\ \mu m$[50,51] and $\lambda_c = 0.12 - 0.80\ \mu m$[50,52,53], and in BSCCO-2223 are $\lambda_{ab} = 0.2\ \mu m$[54] and $\lambda_c = 1.0\ \mu m$[54].

5.3.1 Homogenisation

Homogeneous composite materials are required to achieve good control over electromagnetic wave propagation. The particles must be well-dispersed in order for the wave to propagate through a uniform effective medium.

The distribution of fillers into a polymer matrix can be achieved by the mixing processes explained in section 5.2.1. However, problems can occur when a high density of filler is required. Golosovsky *et al.* reported agglomerations of YBCO particles of sizes from 5 to 20 μm in their YBCO/PMMA composites[8]. However, the agglomeration of YBCO particles may not affect the electromagnetic properties of YBCO/PMMA composites even at the highest loadings, volume fraction 48 vol%, where the refractive index in the normal and superconducting states are 6 and 5 respectively as can be seen in Figure 5.4. The superconducting powders in the HTS composites were reported to be weakly capacitively coupled due to poor grain-to grain connectivity[55], suggesting that no supercurrent can flow between isolated grains even if they are in the superconducting state. Abraham *et al.* stated that the poor grain-to-grain connectivity is due to the insulating layers of polymer between YBCO particles even at high volume fractions of the HTS filler (Figure 5.5)[56].

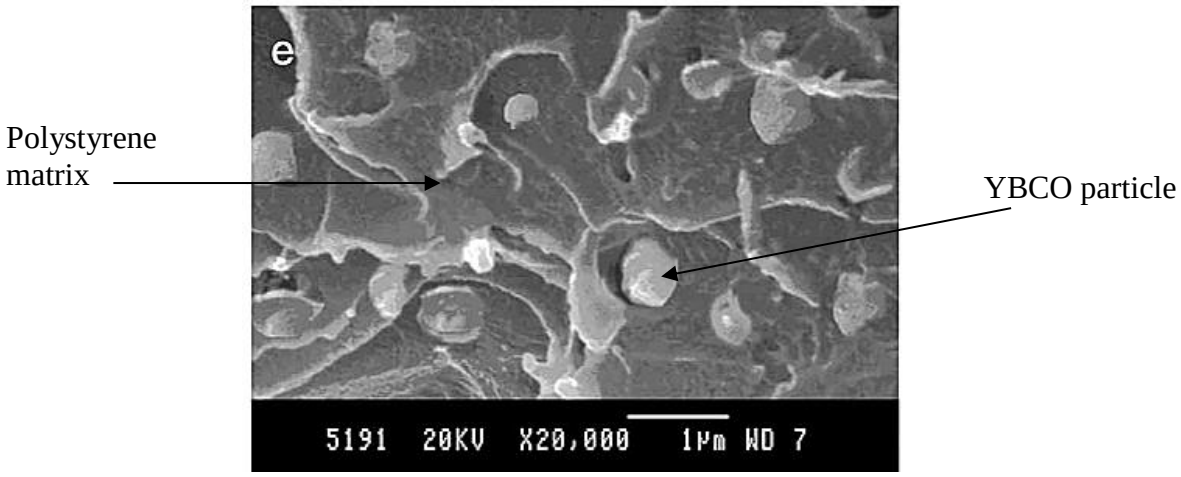


Figure 5.5 SEM image of 40 vol% YBCO filler loaded in polystyrene. Figure reproduced from Abraham *et al.*[56] with permission by John Wiley and Sons, Inc.

5.3.2 Application of Mixing Rules

Mixing laws are often used to understand the dielectric constant and magnetic permeability of effective medium HTS composites. These mixing laws can be used in two ways; 1) to predict electromagnetic properties of constituent phases in a composite and 2) to observe the effects of filler agglomeration and uneven distribution in the polymer matrix which may result in deviations from the predicted values for the ideal effective medium.

In general, mixing laws predict the dielectric properties of composite materials by considering the volume fractions of homogeneously distributed spherical fillers (with permittivity ε_i) in a polymer matrix (with permittivity ε_m) (Figure 5.6). These mixing rules are only accurate at high frequencies where the size of the particles is smaller than the wavelengths of interest.

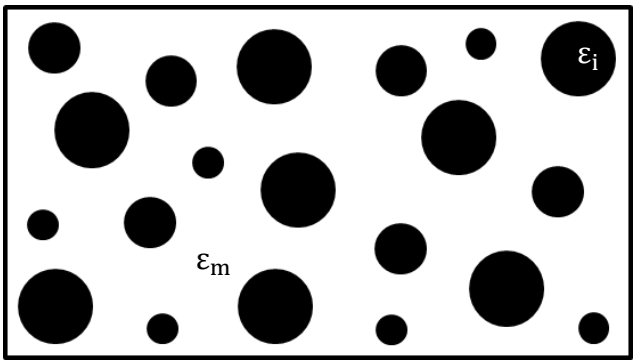


Figure 5.6 A schematic drawing of a simple composite polymer with spherical particle fillers ε_i embedded homogeneously in polymer matrix ε_m. Figure adapted after Sihvola[57] with permission of Springer Nature.

5.3.2.1 Maxwell-Garnett Mixing Rule

The Maxwell-Garnett is the most basic mixing rule used to calculate ε_{eff} values of polymer composites by considering the volume fractions of heterogeneous components, and has been widely used in various fields[58]. The Maxwell-Garnett formula for two components can be given as[59]

$$\varepsilon_{eff} = \varepsilon_m + 3f\varepsilon_m \frac{\varepsilon_i - \varepsilon_m}{\varepsilon_i + 2\varepsilon_m - f(\varepsilon_i - \varepsilon_m)} \quad (5.3)$$

where f is the volume fraction of the inclusions in the mixture. The ε_{eff} values are linearly dependent on f at low volume fractions, but progressively become more non-linear at large volume fractions. This formula was developed for spherical particles only, which were assumed to be isolated, and assuming no interaction with neighbouring particles in an insulated matrix material. However, at higher volume fraction, these interactions between particles cannot be neglected and might affect the predicted ε_{eff} values[60]. This can be seen from the predicted ε_{eff} values of $BaTiO_3$ nano-size particle-loaded polyvinylidene fluoride (PVDF) nanocomposites, where the Maxwell-Garnett fits only at low volume fractions of $BaTiO_3$ particles (Figure 5.7)[61].

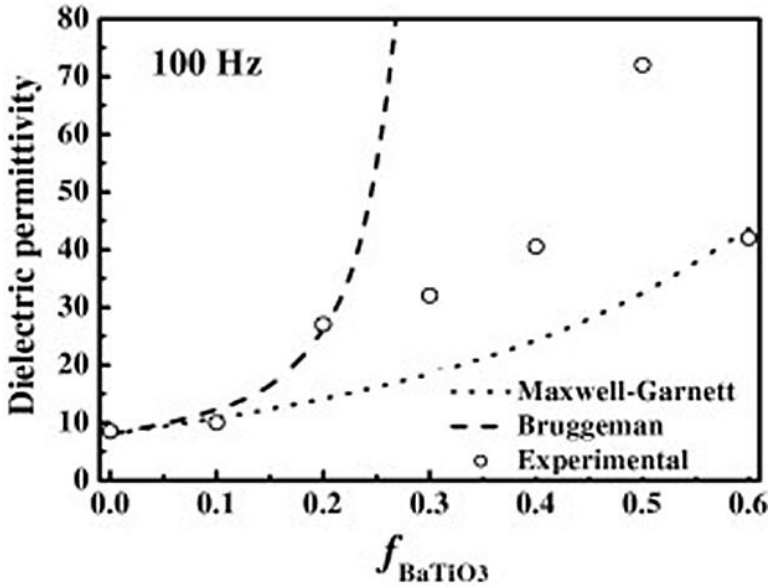


Figure 5.7 The experimental and predicted ε_{eff} values of $BaTiO_3$/PVDF composites. Figure reproduced from Dang *et al.*[61] with permission from Elsevier.

5.3.2.2 Bruggeman formula

The Bruggeman formula, also known as the effective-medium model, has been widely used to approximate the electromagnetic properties of composites, where it considers the volume fractions of both inclusions (*f*) and matrix (*1-f*)[62]. The Bruggeman formula can be given as

$$(1-f)\frac{\varepsilon_m-\varepsilon_{eff}}{\varepsilon_e+2\varepsilon_{eff}}+f\frac{\varepsilon_i-\varepsilon_{eff}}{\varepsilon_i+2\varepsilon_{eff}}=0 \quad (5.4)$$

usually approximates well to measured composite properties for minority filler additions by assuming that the particles are well-isolated and well-dispersed in the insulating matrix[5]. The Bruggeman formula has been used to assess composite media at relatively high loading filler up to 50 vol% as long as a percolation path is not established[61]. Mettout *et al.* reported a good fit of the measured dielectric constant of metal/paraffin composites using tin and tin/lead as fillers with the Bruggeman formula, but deviations at large concentrations of fillers ($f > 40$ vol%) that might be due to aggregates[63].

The image originally presented here cannot be made freely available via ORA because of copyright. The image was sourced at:

Mettout, B., Dumas, P., Waysand, G. & Chardin, G. in *Volume 5 of European Materials Research Society Symposia Proceedings*, pp. 201-206, **Fig. 2 on page 204** (Elsevier Science, 2012).

Figure 5.8 Dielectric constant of tin and tin-lead loaded in paraffin composites. ε is the dielectric constant of tin or tin-lead and ε_1 is the dielectric constant of paraffin. B.A is a Bruggeman formula, M.G is a Mazur-Geigenmuller formula and C.M is a Clausius-Mossotti formula. Figure has been reproduced from Mettout *et al.*[63]

5.3.2.3 Lichtenecker formula

Lichtenecker formula originated from the 'power-law' model and has been used to evaluate the effective permittivity of composite media. The formula has been frequently used to consider topology of components in a composite[64]. The general equation for two-component mixture is,

$$\varepsilon_{eff}^{\alpha} = f_i \varepsilon_i^{\alpha} + (1 - f)\varepsilon_m^{\alpha} \quad (5.5)$$

where $\propto$ varies from -1 for to 1 depending on shape and orientation of particles in the composite, where -1 is a mixture of components alternately arranged perpendicular to the electric field and 1 is a mixture of components alternately arranged parallel to the electric field[64]. Goncharenko et al. reported that in the extreme cases of Lichtenecker equation $\propto = 1$ refers to composite with disc shaped layers arranged parallel to the field, and $\propto = -1$ refers to composite made of parallel needle shaped particles arranged perpendicularly to the field[64]. In the case of two-phase mixture with randomly distributed spherical shaped fillers, $\propto \rightarrow 0$, the Lichtenecker formula can be written as equation 5.6[65],

$$\log \varepsilon_{eff} = f_i \log \varepsilon_i + (1 - f_i) \log \varepsilon_m \quad (5.6)$$

The Lichtenecker formula is considered as semi-empirical in nature[66], where equation (5.6) can be modified into equation (5.7)[67].

$$\log \varepsilon_{eff} = \log \varepsilon_m + f_{filler}(1 - k) \log \left(\frac{\varepsilon_i}{\varepsilon_m}\right) \quad (5.7)$$

where k is an empirical parameter describing interaction between fillers and polymer matrix. It was reported that for most well-dispersed polymer-ceramic composites $k \sim 0.3$[67]. Abraham et al. has used the Lichtenecker formula to describe the reproducibility of YBCO-123 loaded polystyrene at various range of YBCO loadings in polystyrene[68].

5.4 Summary

There are many applications areas where HTS composite devices could have beneficial electromagnetic properties. For optimising performance, high temperature superconducting (HTS) powder is often chosen due to its high T_c and large magnetisation properties compared to low temperature superconductors (LTS). In order for high performance microwave media to be fabricated, a good quality of HTS powder with particle size less than the microwave wavelength must be used, distributed evenly in polymer matrices. Epoxy resin and ABS have been discussed for use in composites because these polymers have good mechanical properties and tolerance to temperature excursions and humidity suitable in both room and liquid nitrogen applications.

The fabrication of HTS composites with a well-dispersed, uniform distribution of HTS powder in a polymer matrix is challenging, requiring the preparation of optimised HTS powder, followed by polymerisation into the polymer composite. The casting process, which is the simplest fabrication method, requires an HTS powder mixed into epoxy precursor, followed by curing in moulds, while the versatile 3-D printing process requires HTS composite feedstock prepared in advance by extrusion. Controls over the melt temperature and pressure of the extruder are required to produce HTS composite filament with a good enough tensile strength and flexibility for 3-D printing.

The electromagnetic properties of cast HTS composites have been previously studied by a few groups and proved to have temperature and frequency dependence of refractive index that can be tuning by changing the HTS volume fraction[8]. These unique properties of HTS composites might have potential applications as metamaterials. In order to achieve the local variation in electromagnetic properties measured by designs predicted by the spatial transformation methodology, 3-D printing is needed to fabricate HTS composites with complex structures. Since the 3-D printing performance of most

commercial printers has been set for pure ABS filament, optimisation studies on HTS composite filaments and print parameters are necessary.

References

1 Subodh, G., Deepu, V., Mohanan, P. & Sebastian, M. Dielectric response of high permittivity polymer ceramic composite with low loss tangent. *Applied Physics Letters* **95**, 62903 (2009).

2 Golosovsky, M., Tsindlekht, M., Davidov, D. & Sarychev, A. Effective-medium approach to the microwave properties of the high-T_c superconductor-insulator composites. *Physica C: Superconductivity* **209**, 337-340 (1993).

3 MacKinnon, A. J., Jenkins, S. D., McGrail, P. T. & Pethrick, R. A. A dielectric, mechanical, rheological and electron microscopy study of cure and properties of a thermoplastic-modified epoxy resin. *Macromolecules* **25**, 3492-3499 (1992).

4 Hojo, H., Toyoshima, W., Tamura, M. & Kawamura, N. Short- and long-term strength characteristics of particulate-filled cast epoxy resin. *Polymer Engineering & Science* **14**, 604-609 (1974).

5 Grant, P. S. *et al.* Manufacture of electrical and magnetic graded and anisotropic materials for novel manipulations of microwaves. *Phil. Trans. R. Soc. A* **373**, 20140353 (2015).

6 Harper, C. A. *Handbook of plastics, elastomers, and composites Third Edition*. (McGraw-Hill, 1996).

7 Wang, Y., Edwards, E., Hooper, I., Clow, N. & Grant, P. Scalable polymer-based ferrite composites with matching permeability and permittivity for high-frequency applications. *Applied Physics A* **120**, 609-614 (2015).

8 Golosovsky, M., Tsindlekht, M. & Davidov, D. Microwave propagation through superconductor-polymer composites. *Physical Review B* **46**, 11439-11444 (1992).

9 Fenner, R. T. *Extruder screw design : solutions to polymer melt flow in extrusion equipment, including wire-coating dies.* pp. 1-6 (Iliffe for the Plastics Institute, 1970).

10 Powell, P. C. & Housz, A. J. I. *Engineering with Polymers, 2nd Edition*. pp. 52-55 (Taylor & Francis, 1998).

11 Moulart, A., Marrett, C. & Colton, J. Polymeric composites for use in electronic and microwave devices. *Polymer Engineering & Science* **44**, 588-597 (2004).

12 Lu, X. *et al.* Fabrication of electromagnetic crystals by extrusion freeforming. *Metamaterials* **2**, 36-44 (2008).

13 Masood, S. H. & Song, W. Q. Development of new metal/polymer materials for rapid tooling using Fused deposition modelling. *Materials & Design* **25**, 587-594 (2004).

14 Nikzad, M., Masood, S. & Sbarski, I. Thermo-mechanical properties of a highly filled polymeric composites for fused deposition modeling. *Materials & Design* **32**, 3448-3456 (2011).

15 Akovali, G. N. & Kaynak, C. *Handbook of composite fabrication*. pp. 22 (Rapra Technology, 2001).

16 Rauwendaal, C. *Polymer extrusion*. (Carl Hanser Verlag GmbH Co KG, 2014).

17 Breitenbach, J. Melt extrusion: from process to drug delivery technology. *European Journal of Pharmaceutics and Biopharmaceutics* **54**, 107-117 (2002).

18 Ariffin, A. & Ahmad, M. S. B. Review: Single Screw Extruder in Particulate Filler Composite. *Polymer-Plastics Technology and Engineering* **50**, 395-403 (2011).

19 Shenavar, A., Abbasi, F., Aghjeh, M. K. R. & Zamani, A. Flow and Mechanical Properties of Carbon Black Filled Acrylonitrile-Butadiene-Styrene (ABS). *Journal of Thermoplastic Composite Materials* **22**, 753-766 (2009).

20 Bakar, M., Leong, Y., Ariffin, A. & Ishak, Z. Mechanical, flow, and morphological properties of talc-and kaolin-filled polypropylene hybrid composites. *Journal of applied polymer science* **104**, 434-441 (2007).

21 Giles, H. F., Mount, E. M. & Wagner, J. R. *Extrusion: The Definitive Processing Guide and Handbook*. pp. 197 (Elsevier Science, 2004).

22 Wells, L. J., Nightingale, S. A. & Spinks, G. The effect of temperature on the extrusion behavior of a polymer/ceramic refractory paste. *Journal of Materials Science* **40**, 315-321 (2005).

23 Majumdar, A., Das, A., Alagirusamy, R. & Kothari, V. K. *Process Control in Textile Manufacturing*. pp. 114-116 (Elsevier Science, 2012).

24 Hiemenz, P. C. & Lodge, T. P. *Polymer Chemistry*. 2nd edn, (CRC Press, 2007).

25 Lu, X. *et al.* Fine lattice structures fabricated by extrusion freeforming: Process variables. *Journal of Materials Processing Technology* **209**, 4654-4661 (2009).

26 Huang, T., Hilmas, G. E., Fahrenholtz, W. G. & Leu, M. C. Dispersion of Zirconium Diboride in an Aqueous, High-Solids Paste. *International Journal of Applied Ceramic Technology* **4**, 470-479 (2007).

27 Campbell, I., Bourell, D. & Gibson, I. Additive manufacturing: rapid prototyping comes of age. *Rapid Prototyping Journal* **18**, 255-258 (2012).

28 Turner, B. N. & Gold, S. A. A review of melt extrusion additive manufacturing processes: II. Materials, dimensional accuracy, and surface roughness. *Rapid Prototyping Journal* **21**, 250-261 (2015).

29 Yan, X. & Gu, P. A review of rapid prototyping technologies and systems. *Computer-Aided Design* **28**, 307-318 (1996).

30 Agarwala, M., Bourell, D., Beaman, J., Marcus, H. & Barlow, J. Synthesis, selective laser sintering and infiltration of high Tc, dual phase Ag-$YBa_2Cu_3O_{7-x}$ superconductor composites. *Proc. SFF Symp., Austin*, pp. 339-349 (1993).

31 Sood, A. K., Ohdar, R. K. & Mahapatra, S. S. Parametric appraisal of mechanical property of fused deposition modelling processed parts. *Materials & Design* **31**, 287-295 (2010).

32 Lee, Y. *et al.* Rapid prototyping of ceramic millimeterwave metamaterials: Simulations and experiments. *Microwave and Optical Technology Letters* **49**, 2090-2093 (2007).

33 Koulouridis, S., Kiziltas, G., Yijun, Z., Hansford, D. J. & Volakis, J. L. Polymer–Ceramic Composites for Microwave Applications: Fabrication and Performance Assessment. *Microwave Theory and Techniques, IEEE Transactions on* **54**, 4202-4208 (2006).

34 Makerbot.com. *MakerBot The Replicator Setup Guide*, <https://images.makerbot.com/support/production/mt524.pdf> (2012).

35 Ahn, S. H., Montero, M., Odell, D., Roundy, S. & Wright, P. K. Anisotropic material properties of fused deposition modeling ABS. *Rapid Prototyping Journal* **8**, 248-257 (2002).

36 Bandyopadhyay, A., Das, K., Marusich, J. & Onagoruwa, S. Application of fused deposition in controlled microstructure metal-ceramic composites. *Rapid Prototyping Journal* **12**, 121-128 (2006).

37 Bhadrakumari, S., Predeep, P. & Sheela, A. Magnetic levitation force measurement on HTSC ceramic/thermoplastic polymer composites. *Composites Science and Technology* **68**, 3230-3233 (2008).

38 Skinner, S. M., Bobalek, E. G., Blum, G. W. & Ling, T. H. Reinforcement of Synthetic Elastomers -Influence of Particle Size and Type on Tensile Behavior. *Industrial & Engineering Chemistry* **48**, 2086-2094 (1956).

39 Fu, S. Y., Feng, X. Q., Lauke, B. & Mai, Y. W. Effects of particle size, particle/matrix interface adhesion and particle loading on mechanical properties of particulate–polymer composites. *Composites Part B: Engineering* **39**, 933-961 (2008).

40 García, M. G., Marchese, J. & Ochoa, N. A. Effect of the particle size and particle agglomeration on composite membrane performance. *Journal of Applied Polymer Science* **118**, 2417-2424 (2010).

41 Friedrich, K., Zhang, Z. & Schlarb, A. K. Effects of various fillers on the sliding wear of polymer composites. *Composites Science and Technology* **65**, 2329-2343 (2005).

42 Pietsch, W. *Agglomeration Processes: Phenomena, Technologies, Equipment*. (Wiley, 2008).

43 American Society for Testing Materials. *Symposium on Particle Size Measurement: Presented at the Sixty-first Annual Meeting, Boston, Mass.*, pp. 132-136 (ASTM International, 1958).

44 Alford, N. M., Button, T. & Birchall, J. Processing, properties and devices in high-Tc superconductors. *Superconductor Science and Technology* **3**, 1 (1990).

45 Marrett, C., Moulart, A., Colton, J. & Tcharkhtchi, A. Flexible polymer composite electromagnetic crystals. *Polymer engineering and science* **43**, 822 (2003).

46 Lettieri, M. & Frigione, M. Effects of humid environment on thermal and mechanical properties of a cold-curing structural epoxy adhesive. *Construction and Building Materials* **30**, 753-760 (2012).

47 Zhang, Y., Adams, R. D. & da Silva, L. F. M. Effects of Curing Cycle and Thermal History on the Glass Transition Temperature of Adhesives. *The Journal of Adhesion* **90**, 327-345 (2014).

48 Hale, D. K. The physical properties of composite materials. *Journal of Materials Science* **11**, 2105-2141 (1976).

49 Pomerantz, M. Microwave propagation through granular superconductors. *Physics Letters A* **108**, 359-361 (1985).

50 Krusin-Elbaum, L., Malozemoff, A. P., Yeshurun, Y., Cronemeyer, D. C. & Holtzberg, F. Temperature dependence of lower critical fields in Y-Ba-Cu-O crystals. *Physical Review B* **39**, 2936-2939 (1989).

51 Gallagher, W. J. *et al.* Anisotropy in the magnetic properties of single-crystal $Y_1Ba_2Cu_3O_{7-x}$. *Physica B+C* **148**, 228-232 (1987).

52 Umezawa, A. *et al.* Anisotropy of the lower critical field, magnetic penetration depth, and equilibrium shielding current in single-crystal $YBa_2Cu_3O_{7-\delta}$. *Physical Review B* **38**, 2843-2846 (1988).

53 Harshman, D. R. *et al.* Temperature dependence of the magnetic penetration depth in the high-T_c superconductor Ba2YCu3O9-δ: Evidence for conventional *s*-wave pairing. *Physical Review B* **36**, 2386-2389 (1987).

54 Cyrot, M. *Introduction to superconductivity and high-Tc materials*. 52, 205, 218 (World Scientific, 1992).

55 Sarkar, A. K. & Peterson, T. L. Fabrication and electrical properties of ceramic superconductor/polymer composites. *Polymer Engineering & Science* **32**, 305-309 (1992).

56 Abraham, R. *et al.* Structural and mechanical properties of YBCO-polystyrene composites. *Journal of Applied Polymer Science* **118**, 1027-1041 (2010).

57 Sihvola, A. Mixing rules with complex dielectric coefficients. *Subsurface Sensing Technologies and Applications* **1**, 393-415 (2000).

58 Maxwell, G. JC,"Colours in metal glasses and metal films,". *Philos. Trans. R. Soc. London, Sect. A* **3**, 385-420 (1904).

59 Sihvola, A. H. & Kong, J. A. Effective permittivity of dielectric mixtures. *Geoscience and Remote Sensing, IEEE Transactions on* **26**, 420-429 (1988).

60 Nicolais, L. & Carotenuto, G. *Metal-Polymer Nanocomposites*. pp. 194-196 (John Wiley & Sons, 2004).

61 Dang, Z. M. *et al.* Fundamentals, processes and applications of high-permittivity polymer–matrix composites. *Progress in Materials Science* **57**, 660-723 (2012).

62 Bruggeman, D. Dielectric constant and conductivity of mixtures of isotropic materials. *Ann Phys (Leipzig)* **24**, 636-679 (1935).

63 Mettout, B., Dumas, P., Waysand, G. & Chardin, G. in *Volume 5 of European Materials Research Society Symposia Proceedings* pp. 201-206 (Elsevier Science, 2012).

64 Goncharenko, A. V., Lozovski, V. Z. & Venger, E. F. Lichtenecker's equation: applicability and limitations. *Optics Communications* **174**, 19-32 (2000).

65 Unsworth, J., Du, J., Crosby, B. J. & Stevens, M. G. Complex electrical permittivity of 0–3 superconducting ceramic/polymer composites. *Materials Research Bulletin* **27**, 1161-1169 (1992).

66 Simpkin, R. Derivation of Lichtenecker's logarithmic mixture formula from Maxwell's equations. *IEEE Transactions on Microwave Theory and Techniques* **58**, 545-550 (2010).

67 Yang, R., Jianmin, Q., Marinis, T. & Wong, C. P. A precise numerical prediction of effective dielectric constant for polymer-ceramic composite based on effective-medium theory. *IEEE Transactions on Components and Packaging Technologies* **23**, 680-683 (2000).

68 Abraham, R., Kuryan, S., Isac, J., Zacharia, A. K. & Thomas, S. Yttrium barium copper oxide-filled polystyrene as a dielectric material. *Journal of applied polymer science* **120**, 2233-2241 (2011).

6 Experimental Methods

6.1 Preparation of HTS Filler Powders 84
6.1.1 Melt-Grown $YBa_2Cu_3O_7$ 85
6.2 HTS Composite Fabrication 87
6.2.1 Casting Process 87
6.2.2 Preparation of HTS/ABS Powder 88
6.2.3 Extruding HTS/ABS Filaments 88
6.3 Electromagnetic Properties 89
6.3.1 Measurement of Scattering Parameters 90
6.3.2 Waveguide Measurements 91
6.3.3 Permittivity and Permeability Measurements 92
6.4 Characterization of Superconducting Properties 97
6.4.1 Transition Temperature 98
6.4.2 Magnetic Hysteresis 99
6.5 Microstructural Characterisation Techniques 99
6.5.1 X-ray Diffraction 99
6.5.2 Mastersizer 101
6.5.3 Scanning Electron Microscopy 103
References 107

In this chapter, the main techniques used in this work are described. In the first half, the basic sample preparation methods for superconductor composites are described in detail. The latter half of the chapter concentrates on the physical and microstructural characterisation techniques most commonly employed in the testing and characterisation of these materials.

6.1 Preparation of HTS Filler Powders

HTS powders used in this work were obtained commercially or fabricated from bulk single-grain samples grown by the top-seeded melt-growth technique (TSMG). The

TSMG technique is described in Chapter 4 section 4.4.5.2. All commercial powders used in the work are described on the next chapter (Chapter 7 and Chapter 8), including $Bi_2Sr_2Ca_2Cu_3O_y$ (BSCCO) and $YBa_2Cu_3O_7$ (YBCO) powder. The following section describes how powder was processed from bulk TSMG YBCO-123.

6.1.1 Melt-Grown $YBa_2Cu_3O_7$

Single-grain YBCO bulks grown by the Bulk Superconductivity Group, University of Cambridge using the top-seeded melt grown (TSMG) technique[1] were used as a source of superconducting powder. The used of single-grain YBCO bulks were required to obtain larger (single grain) powder particles than obtainable commercially. Using this high quality source of superconducting materials was also important because, commercial YBCO-123 powder is very sensitive to reaction with moisture[2,3], and after any length of storage the surface of powder particles is no longer superconducting. The single-grain YBCO-123 bulk materials supplied from Cambridge were off-cuts of YBCO-123 bulks without seed crystals. Since these pieces were collected from the edge of TSMG bulks, their quality was rather variable, so simple magnetic levitation test was conducted to screen for the best samples. The screening process is described in Chapter 7 section 7.3.2.

All selected off-cuts from single-grain YBCO bulks were processed to produce YBCO powder using the following procedure:

1. Crush large grain YBCO bulks using a hydraulic press.
2. Crush the remaining medium size YBCO chunks by hand using a pestle and mortar to produce a fine powder.
3. Sieve powder to produce YBCO powder with desired particle sizes. Generally, sieving was performed by passing through and manually shaking YBCO powders

into sieves of sizes 38 μm, 63 μm and 125 μm-mesh, which separated them into fractions of particle size based on sieve diamaters, d_{sieve}. Table 6.1 summarised particle size fractions of YBCO powder used to produce the HTS composites, described in Chapter 7, Chapter 8 and Chapter 9.

4. Anneal at 450 ºC for 12 hours in air to improve properties of YBCO powder by trying to make sure that the oxygen stoichiometry is restored as close to $O_{6.9}$ after exposure to environment during powdering process[4] (Refer to section 4.4.2).

Table 6.1 Summary of melt-grown YBCO powder for HTS composite preparation.

Melt-grown YBCO fragments	YBCO powder fraction size, d_{sieve} (μm)	HTS samples	Characterisation	Chapters
Sample 1	$63 < d_{sieve} < 125$	Set 1 of MG HTS composites	XRD, Mastersizer, SEM, SQUID magnetometer, VNA	7, 8
Sample 2*	$63 < d_{sieve} < 125$ $53 < d_{sieve} < 63$ $38 < d_{sieve} < 53$ $d_{sieve} < 38$	-	Mastersizer, SQUID magnetometer	7
Sample 3	$d_{sieve} < 125$	35 vol% of MG HTS composite	SEM, SQUID magnetometer, VNA	8
Sample 4	$63 < d_{sieve} < 125$	Set 2 of MG HTS composites	VNA	8
Mix of samples	$63 < d_{sieve} < 125$	20% extruded HTS composites	SEM, SQUID magnetometer, VNA	9
Mix of samples	$d_{sieve} < 38$	20% extruded HTS composites	SEM, SQUID magnetometer, VNA	9

**Sample 2 is only used for powder size characterisation in Chapter 7.*

All melt-grown YBCO powders used to produce HTS composites in this work originated from off-cut fragments of single-grain YBCO bulks. In chapter 8, a set of HTS composites with various volume fractions were prepared using a single piece of bulk material. For repeatability, another set of composites with various volume fractions

was prepared using a different off-cut YBCO fragment. In chapter 9, a YBCO powder used was made from several selected off-cut fragments. These melt-grown YBCO powders were homogenously mixed by grinding and sieving process before mixing them with polymer to produce HTS composites. Table 6.1 summarised the sets of HTS composite samples prepared from melt-grown YBCO bulks for studies described in subsequent chapters.

6.2 HTS Composite Fabrication

The first stage of fabrication of HTS composites involved loading polymeric materials with HTS powder. The processing routes for HTS composites depend mainly on the choice of polymer material that has been chosen for the matrix. Epoxy resin was chosen for the casting process, and acrylonitrile butadiene styrene (ABS) is chosen for extrusion as it is one of the common industrially used polymer materials[5].

6.2.1 Casting Process

Casting is one of the most common techniques used in manufacturing of composite materials by mixing two or more components in a polymer matrix and using a mould to shape the composite mixture[6]. A typical casting procedure starts by mixing a 5:1 ratio of epoxy and hardener (as specified by the manufacturer) followed by slow mixing for 10 minutes. HTS powder was added into the epoxy solution and dispersed well using a magnetic stirrer. The HTS and epoxy mixture is then transferred into the mould and left to cure at room temperature.

The polymer matrix used in this study was two-component epoxy provided by Epo-Kwick from Buehler. The two components are Epoxy Resin (20-8136-128, Buehler Epo-Kwick Resin, Composition: 60-100 Wt/Wt% Bisphenol-A, 5-10 Wt/Wt% Alkyl glycidyl ether, 5-10 Wt/Wt% Acrylate ester, 5-10 Wt/Wt% Neopentyl glycol diglycidyl

ether) and Epoxy Hardener (20-8138-032, Epo-Kwick Harderner, Composition: 60-100 Wt/Wt% Polyamine and 5-10 Wt/Wt% Dietylenetriamine) with mix ratio of 5 parts resin to 1 part hardener by volume. The amine cured epoxy resin allows curing at room temperature[7], thus it was chosen for its ease of processing and rapid curing time (90 minutes at room temperature).

6.2.2 Preparation of HTS/ABS Powder

The *indirect* method was used to prepare the precursor powder of HTS/ABS composite materials (refer to section 5.1.2). ABS pellets (MFI-22, Styrolution, Frankfurt am Main) were used to produce filaments. The preparation procedure I have used was developed by Dr. F. Castles, Department of Materials, University of Oxford as a general method for producing HTS/ABS filament.

1. Mix HTS and ABS pellets in 200 ml acetone
2. Stir the HTS and ABS solutions with a magnetic stirrer to form a paste
3. Spread the paste on trays and leave to dry for 24 hours. This forms a good dispersion of the two materials.
4. Scrape dried paste from trays and grind to form fine HTS/ABS particles using a food blender.
5. Spread the particles on the tray and leave to dry to remove acetone residue.

6.2.3 Extruding HTS/ABS Filaments

HTS/ABS filaments were extruded using a Noztek extruder (Figure 6.1). The extruder is heated up to 180 ºC prior to extrusion. HTS/ABS particles are then loaded into the extruder through the hopper. The particles are slowly dragged from the hopper to the die by the motorised controlled screw enclosed in the heated barrel at the centre of the machine. As the particles move forward in the heated barrel, the HTS/ABS plastic is

melted and is then pushed into the die entrance via the heated band by pressure. The HTS/ABS plastic is compressed and melted by the heat from the heated barrel and generated frictional heat from the compounding and compression actions of the screw[8]. During the heating, the melted HTS/ABS is forced into the nozzle, where it is extruded into filaments with a shape defined by the die. The extruded filament is then hardened by either air or water cooling[7].

A standard extrusion process for pure ABS filaments used a 1.75 mm die to produce 1.75 ± 0.04 mm diameter filaments with recommended extrusion temperature between 180 to 200 ºC[9]. The optimisation process for HTS/ABS filament extrusions will be discussed in Chapter 9.

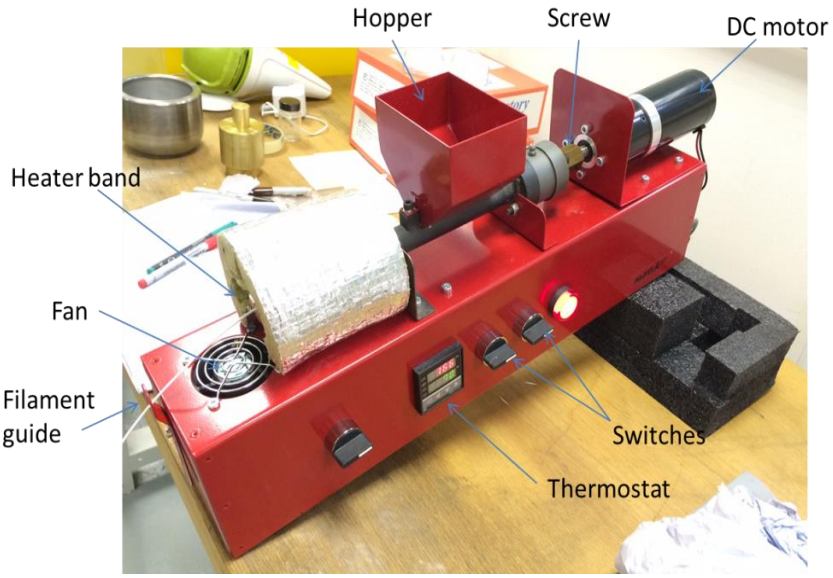


Figure 6.1 The Noztek desktop extruder used to extrude YBCO loaded ABS filament.

6.3 Electromagnetic Properties

A vector network analyser (VNA) has been used for the measurement of the electromagnetic properties of composite materials and metamaterials. These instruments measure the amplitude and phase of reflected and transmitted waves propagating through the test material, and these values are used to calculate complex scattering

parameters of a device, and hence electromagnetic parameters like dielectric constant (ε_r) and magnetic permeability (μ_r), losses and quality factors (Q-factor).

In this study, an Agilent 8510C system consisting of an 8360 series RF signal source, the device for sending the desired signal to the device-under-test (DUT) or materials-under-test (MUT), a network analyser for signal processing and peripheral devices such as a disc drive were used to measure the dielectric and magnetic properties of HTS composites. All the measurements were done using the two-port microwave system with a capability of measurement from 30 KHz to 6 GHz. Detailed information in the parameters and operation of this instrument can be found in the operating manual of the *Agilent Technologies 8510C Network Analyzer System*[10]. The basic concepts of VNA operation can be found in the *Foundations for Microwave Engineering* [11].

6.3.1 Measurement of Scattering Parameters

To perform high frequency measurements, the electromagnetic properties of the sample are characterized by measuring the response of the MUT to an input signal. In this study, a VNA with two ports is used. A port is matched when an input signal is completely transmitted and no output signal is measured at the port. However, mismatch occurs when the input signal is reflected. Since port matching is frequency dependent, most devices are designed to be matched over a small bandwidth of frequencies. The measurement of signals at each port can be carried out using the VNA.

In the VNA, the electromagnetic properties of an MUT can be characterized by identifying the relative intensity and phase of both incident and reflected waves propagating from the analyser to the MUT. The relation of these scattering waves can be defined using the scattering parameters (S-parameters). The S-parameters are

complex linear power quantities that are commonly used to measure the gain, loss, reflection and transmission coefficients of waves at high frequencies.

The number of S-parameters for a given MUT is equal to the square of the number of the VNA ports. In this case, the two port MUT used in this work arrangement will have four S-parameters. The S-parameters for a two port MUT arrangement can best be explained using the scattering matrix which relates the incident waves, a_i, and reflected waves, b_i, of the VNA at each port as in equation (6.1).

$$\begin{bmatrix} b_1 \\ b_2 \end{bmatrix} = \begin{bmatrix} S_{11} & S_{12} \\ S_{21} & S_{22} \end{bmatrix} \cdot \begin{bmatrix} a_1 \\ a_2 \end{bmatrix} \tag{6.1}$$

where the S-Parameters are used to represent the relationship between scattered waves between ports S_1 and S_2, where S_1 indicates where the waves enter and S_2 where the waves emerge from the MUT. The method calculating both reflection and transmission coefficients using S-parameters can be found in the *Fundamental of Vector Network Analysis* [12] .

In this study, both reflection and transmission coefficients were measured using the waveguide technique. Each measurement was performed using a specially designed experimental set up to increase the efficiency and reproducibility of the resulting data.

6.3.2 Waveguide Measurements

Since superconducting composites can be shaped to precisely fit in a sample holder, a rectangular waveguide was used for measuring the S-parameters. The rectangular waveguide is a common and efficient technique for measuring dielectric samples with a wide range thicknesses and cross sections at microwave frequencies[13]. Samples were shaped to entirely fill the cross-section of an enclosed rectangular waveguide without gaps at the fixture walls by polishing the sample surfaces (Figure 6.2). Smit *et al.*[14]

reported that the thickness t of the sample needs to be less than half the wavelength of the electromagnetic waves propagating inside the material, λ_m. Hence, the thickness of my samples was set to less than $\frac{\lambda_m}{2}$ to avoid resonance phenomena that will invalidate the measurement of S_{11} and S_{21} values[15].

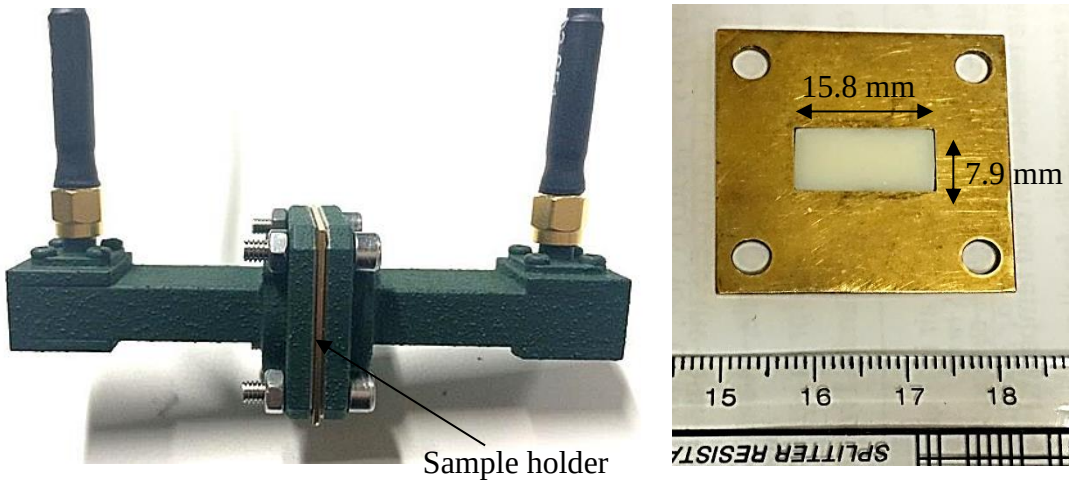


Figure 6.2 WR-62 waveguide assembly. A sample of size 15.8 mm x 7.9 mm x 1 mm is mounted in the brass holder.

The accuracy of broadband transmission measurements are largely determined by the quality of the calibration. Information on the calibration techniques for waveguide measurements can be found in the reference by M. Hiebel[12].

6.3.3 Permittivity and Permeability Measurements

The ε_r and μ_r values of the superconducting composites can be measured from the total reflected coefficient (S_{11}) and transmitted coefficient (S_{21}) of scattering waves. The measured S-parameters and materials properties are derived by measuring the multiple reflections of a unit amplitude wave incident upon the air-sample interfaces within a waveguide using the Nicolson-Ross-Weir (NRW) method[16]. The ε_r and μ_r values can be derived from S_{11} and S_{21} values from the following equations.

$$\varepsilon_r = \frac{k}{k_0}\left(\frac{1-R}{1+R}\right) \tag{6.2}$$

$$\mu_r = \frac{k}{k_0}\left(\frac{1+R}{1-R}\right) \tag{6.3}$$

where $k_0 = \omega\sqrt{\varepsilon_0\mu_0}$ is the propagation constant, $R = \frac{S_{11}}{\left(e^{-j2k_0l} - S_{21}e^{-jkt}\right)}$, l is the length of the waveguide, and $kt = \cos^{-1}\left(\frac{e^{-j4k_0l} + S_{12}^2 - S_{11}^2}{2e^{-j2k_0l}S_{12}}\right)$, where t is the thickness of sample[15]. Complex ε_r and μ_r values were calculated using a Matlab program developed by Dr. I. Hooper of the Department of Physics, University of Exeter.

6.3.3.1 Dielectric constant and magnetic permeability measurement at 77 K

Dielectric constant ($\varepsilon_{r,77}$) and magnetic permeability ($\mu_{r,77}$) measurements at 77 K were carried out by immersing both waveguide and sample in liquid nitrogen. The sample was first fixed in the section of the waveguide and sealed as tightly as possible. The waveguide is then placed in a polystyrene box, which is later filled with liquid nitrogen as in Figure 6.3.

The temperature of the sample in the waveguide was calibrated using a thermocouple. The thermocouple was set in a fixture at the centre of the sample holder using cryogenic glue to avoid liquid nitrogen leaking to the thermocouple (Figure 6.4). The cooling process started when liquid nitrogen is poured into the polystyrene box until it fully covered the waveguide. The measurement is taken when the boiling stops, indicating that the waveguide reaches equilibrium at 77 K. The actual temperature of the sample in the waveguide was found to be 81±2 K, a few degrees higher than the liquid nitrogen boiling temperature (Figure 6.4).

As a result of this temperature profiling described above, all the remaining work in this study, the $\varepsilon_{r,77}$ and $\mu_{r,77}$ values of HTS composite samples are measured 10 minutes after the liquid nitrogen stopped boiling.

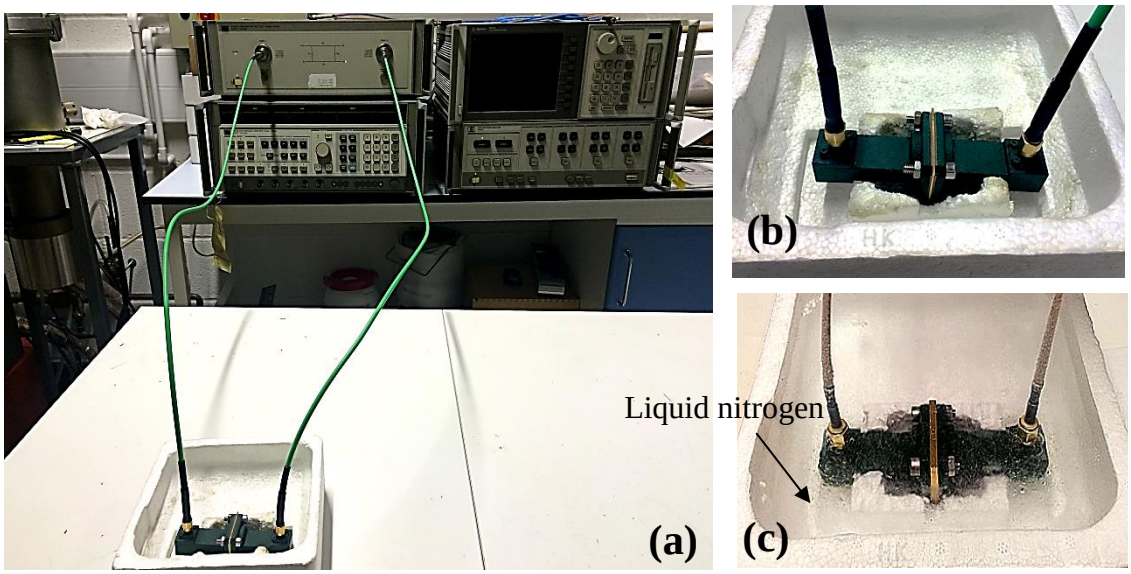


Figure 6.3 Experimental set up for the VNA measurement (a). The waveguide was fixed in the enclosed polystyrene box for the measurement at room temperature (b) and filled with liquid nitrogen for the VNA measurement at 77 K (c).

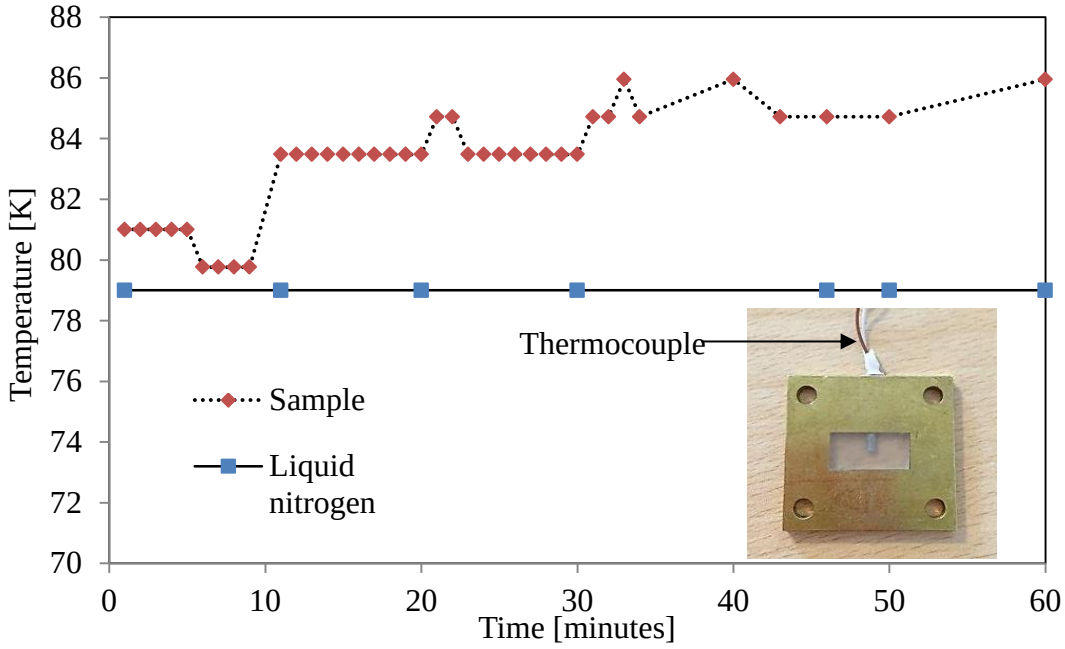


Figure 6.4 Calibration of the temperature of a sample in the waveguide as a function of time during the cooling process. Insert shows a thermocouple fixture in the sample holder for measurement at 77 K.

6.3.3.2 Measurement errors

In computing the ε_r and μ_r values, it is assumed that ideal conditions can be achieved during the S-parameter measurements. However, uncertainties of measurement can cause errors in the S_{11} and S_{21} values, which can lead to errors in calculating ε_r and μ_r.

There are two types of measurement uncertainties; random measurement errors and systematic measurement errors. Random measurement errors can be improved by operating the VNA in thermal equilibrium. This can be done by starting the VNA device 30 minutes before microwave measurement. Random measurement errors can also be improved using clean and rust free connectors and test port cables. Systematic measurement errors are reproducible errors and can be corrected using calibration. The "through, reflect and line" (TRL) calibration is suitable for transmission line measurements using a rectangular waveguide[12]. TRL calibration corrects the reference planes of the measured S_{11} and S_{21} values at the edges of the sample holder. Information on the TRL calibration method can be found in Hiebel[12], and was also conducted in the cooling tests (measurement of S_{11} and S_{21} at 77 K). The calibration is conducted 10 minutes after the liquid nitrogen boiling stops, but as quickly as possible to eliminate errors from the thermal drift shown in Figure 6.4.

During the cooling process from room temperature to 77 K, both sample and waveguide materials experience thermal contraction. The relatively high thermal contraction of the epoxy matrix of the superconducting composites ($\Delta L/L_{Epoxy} \equiv 1.03\%$)[17] compared to brass ($\Delta L/L_{Brass} \equiv 0.38\%$)[17] in the waveguide sample holder can cause errors in S_{11} and S_{21} measurements at 77 K[1]. These uncertainties arise from gaps created between the sample and the sample holder that can result in 'microwave signal leakage' during measurements. The contribution from this effect can be studied by measuring and comparing the ε_r and μ_r values of air and pure epoxy at both room temperature and 77 K, Figure 6.5.

---

[1] $\Delta L/L \equiv (L_{293K} - L_{77K})/L_{293K}$, so $\Delta L/L$ is the total linear contraction from room temperature to 77 K.

Pure epoxy sample was prepared with dimensions 15.8 mm x 7.9 mm x 1 mm to fit tightly into the section in the sample holder with thickness of 1 mm (see sample holder on Figure 6.2). The ε_r and μ_r values were taken by measuring S_{11} and S_{21} at room temperature (293 K) and 77 K at 15 GHz. The S_{11} and S_{21} measurement at 77 K was measured 10 minutes after the liquid nitrogen stop boiling based on the temperature profiling in section 6.3.3.1. The ε_r and μ_r values for pure epoxy sample (ε_{epoxy} and μ_{epoxy}) were derived from S_{11} and S_{21} using the NRW method as discussed in section 6.3.3. All measurements were repeated three times by re-centring the epoxy sample in the sample holder between each measurement.

Figure 6.5 shows the ε_{epoxy} and μ_{epoxy} values at room temperature and 77 K at 15 GHz. The measured ε_{epoxy} and μ_{epoxy} values were compared with the reported dielectric constant and relative permeability values of epoxy resin from literatures, which are $\varepsilon_{epoxy} = 2.89$[18] and $\mu_{epoxy} = 1.00$[19] at room temperature. The measured ε_{epoxy} values are 2.8 ± 0.06 and 2.78 ± 0.02 at room temperature and 77 K respectively. These values are in good agreement with the reported ε_{epoxy} values at 0.1% (room temperature) and 1.4% (77 K). The μ_{epoxy} value of epoxy resin is 0.99 ± 0.02 at room temperature, which is in good agreement with the reported μ_{epoxy} value at 1.4%. However, the μ_{epoxy}value is 0.94 ± 0.01 at 77 K, lower than the reported value by 6.0%. These errors occur due to the uncertainty of S-parameters values in the measurement at room temperature and 77 K using the VNA. The measurement errors of epoxy at 77 K are larger than those measured at room temperature. This is due to the cooling process from room temperature to 77 K, where both sample and waveguide materials experience thermal contraction, causing microwave signal leakage.

The effect of microwave signal leakage was investigated by comparing the measured ε_{epoxy} and μ_{epoxy} values at both room temperature and 77 K. At 15 GHz, the $\varepsilon_{epoxy}$and μ_{epoxy} values of the pure epoxy show less than 5.0% drop at 77 K, consistent with the reported uncertainty in S-parameters values in this kind of measurement of ±5.0%[15]. I concluded that the microwave leakage effect was not going to seriously compromise the materials parameters measured at 77 K. The measurement errors of ε_{epoxy} and μ_{epoxy} at both room temperature and 77 K will be used as a calibration of errors on the microwave measurement in the thesis.

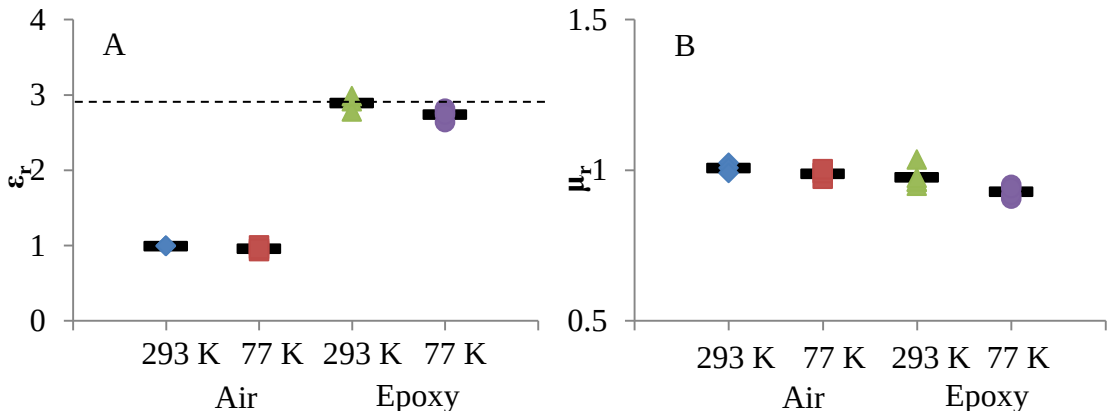


Figure 6.5 ε_r and μ_r values of air and epoxy measured at 15 GHz. A and B show ε_r and μ_r values measured using the 1 mm sample holder. Black lines are average values over three measurements. Dashed line shows average ε_r values of epoxy at room temperature, which is 2.89.

6.4 Characterization of Superconducting Properties

A quantum design SQUID magnetometer (MPMS) was used for the characterization of static superconducting properties. The MPMS determines the magnetic moment of a sample by measuring the output voltage of the SQUID detection system. Typically, a solid sample is prepared by mounting the sample with size around 2.5 x 2.5 x 2.5 mm firmly inside a plastic straw. Powder samples are encapsulated in plastic capsules with diameter 5.2 mm, which are then mounted inside a straw.

The plastic straw is then attached to the end of a probe for insertion into the centre of the magnet. A measurement is performed by moving a sample through the symmetry axis of the detection coils and magnet. The position of a sample is corrected to the centre of the detection coils to improve the accuracy of the measurement and emphasize the position independence of the magnetic moment under ideal conditions. As the sample moves through the coils, the magnetic dipole moment of the sample induces an electric current in the detection coils. Variations in the current produced in the detection coil circuits are then converted to the output voltage with corresponding variations by the SQUID electronics. The magnetic moment m is then determined by analysing the output voltage. MPMS results in this work were reported in terms of the magnetisation, M, calculated by dividing the value of the magnetic moment, m, by the volume or mass of the samples plotted against temperature or applied field, B_{app}.

In this study, all measurements of transition temperature, T_c, and magnetization, $M(H)$, of HTS composites were performed using the SQUID magnetometer in the Clarendon Laboratory Department of Physics, University of Oxford. The SQUID magnetometer is equipped with a 7 T magnet, and field strength and temperature parameters that are controlled automatically according to a desired measurement sequence set in the SQUID.

6.4.1 Transition Temperature

The zero-field-cooled/field cooled (ZFC/FC) measurement was used to determine the transition temperature, T_c, of HTS composites. Firstly the sample is cooled in zero applied field (H=0) to 7 K. After the temperature has stabilized, a small measurement field (10 Oe) is applied and the magnetic moment, m [Am^2], of the sample is measured on warming to 120 K. Then the FC measurement is performed by slowly cooling to 7 K

in the same measurement field. Results display *m* plots against temperatures (K) in the ZFC/FC measurement. T_c is defined as the temperature at which M sharply drops due to the sample becoming diamagnetic. This drop indicates a transition from the normal conductor state to the superconducting state.

6.4.2 Magnetic Hysteresis

The static magnetic properties of HTS composites were measured as a function of applied magnetic field, B_{app}, at fixed temperatures. The magnetic moments of the samples were measured by sweeping the field from 0 T to 7 T, 7 T to -7 T, and from -7 T to 7 T, obtaining a full hysteresis loop. The measured magnetic moments were divided by sample volume to give magnetisation, M. The relationship between M and the applied field can be given by,

$$\boldsymbol{B = B_{app} - nM} \tag{6.4}$$

where n is a demagnetising factor. The demagnetising factor is a correction factor of the field inside the sample, which is sample shape dependent, to the direction of applied field. n varies from 0 for a rod arranged parallel to the field to 1 for disc arranged perpendicular to the field, and for a sphere $n = 1/3$[20].

In this study, the magnetic moment is measured over the superconducting samples with an applied field range $-7T \leq B_{app} \leq 7T$ at 7 K and 77K.

6.5 Microstructural Characterisation Techniques

6.5.1 X-ray Diffraction

X-ray diffraction (XRD) has been used for phase identification for the superconducting powders. The superconducting powder was pressed and flattened into a sample holder,

then aligned parallel to the surface normal on the rotational axis of goniometer, while the detector and X-ray source move along the periphery, performing a θ-2θ scan.

In this study, the θ-2θ scans were measured with a Philips θ-2θ X-ray generator and a PW1710 control unit. Cu Kα radiation is generated using an accelerating voltage of 35 kV and a current of 50 mA. The diffraction patterns of superconducting powder were characterized over a 2θ range of 4 º to 70 º.

6.5.1.1 Principles of θ-2θ Measurement.

A θ-2θ scan is a major X-ray technique to measure and determine the diffraction patterns from powder samples. In the θ-2θ scan, the X-ray tube is fixed in position, while the sample is tilted by the angle θ with respect to the X-ray source and the detector moves in a circular arc around the sample, while recording the diffracted X-ray intensity at each 2θ angle (Figure 6.6).

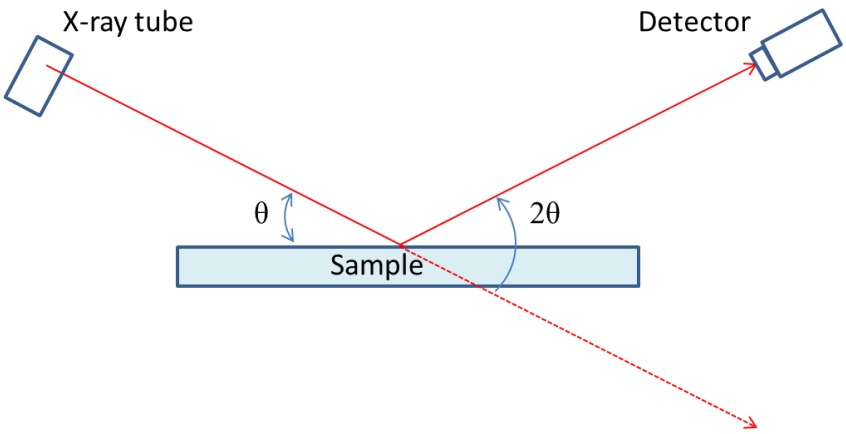


Figure 6.6 A schematic diagram of a θ-2θ XRD scan. Figure adapted from Birkholz[21] with permission by John Wiley and Sons Inc.

When a sample with lattice plane spacings d_{hkl} is irradiated with monochromatic X-rays of wavelength λ at an angle θ, elastic scattering occurs and generates a high X-ray intensity at specific Bragg angles, θ_B, for constructive interference, satisfying the Bragg condition at 2θ as defined by the Bragg equation[21].

$$2d_{hkl}sin\theta = n\lambda \quad (6.5)$$

The XRD patterns over θ-2θ scans show peaks from crystal planes (hkl) aligned parallel to the sample surface, and information on the sample can be gained from the intensity, position and shape of diffraction peaks. Each peak in intensity corresponds to the d-spacing of one set of crystal planes, and the combination of this information gives identification of the crystalline phases present[22]. Results are typically presented as a function of peak intensity I (counts) to peak position (2θ). The phase identification can be achieved by comparing the peak intensities (counts) and the peak positions (d-spacing) in the diffraction pattern with known compounds.

In order to identify precisely the crystal line phases, every peak position and intensity in the scanned XRD patterns should perfectly match the reference data. However, in this work, there are several factors contributing to difficulties in XRD pattern analysis, which are systematic peak position error due to misaligned sample height in the XRD goniometer, and texture effects in phases with powder, where grains with high aspect ratio can be preferentially aligned during sample preparation and so contribute higher intensity peaks compared to those from randomly oriented samples, which will cause peak intensities to not be in the same ratio as in the reference pattern[21].

In this study, XRD has been used to check the superconducting phase of $YBa_2Cu_3O_7$ for both starting powder and composites. The measured XRD diffraction patterns are compared with spectra from the Powder Diffraction Files (PDF) in X'pert Highscore Plus published by the International Center for Diffraction data (JCPDS-ICCD) database.

6.5.2 Mastersizer

A Malvern Mastersizer 2000 has been used for the measurement of HTS particle size using a laser diffraction technique. Powders are dispersed in a liquid and pumped

through a cell mounted in the path of the laser beam. The incident beam scatters at characteristic angles that are particle size dependent. Lenses are used to collect these scattered laser beams and focus them onto the detectors. The collected data is then sent to the computer for particle distribution analysis using dedicated program measurement. The Mie theory of light scattering is used to analyse this data and calculate the particle size distribution by assuming the measurements are made based on scattering volume of spherical particles. The characteristic angle through which incident light is scattered is proportional to the volume of particles of a particular size.

The measurement was started by pumping the dispersing liquid into the cell via polyethylene tubing, for a background reading. Then the powder was added into the dispersant liquid, while the liquid was still pumped through the cell. The powder was added until the obscuration level of the laser was reached; indicating a sufficient amount sample for measurement has been added. A predetermined obscuration between 10% to 30% level has been used in this work to ensure accuracy of measurements as suggested by Malvern[23]. 20 seconds of ultrasonic agitation was applied to break powder agglomerates and disperse particles in the dispersion liquid. Measurements are then taken of particle size distribution.

The size of HTS powder was reported as a particle distribution, where the shape of particle distribution presents the population of the measured particle diameters. The particle size distributions are plotted against the total volume of particles. The distribution of these particle sizes were defined by d_{90}, d_{50}, and d_{10}. The median diameter, d_{50}, indicates the diameter of particles where half of the population lies below this value. Similarly, 90% of the particles of the population have diameters below d_{90} and 10% of the particle population have diameters below d_{10}. The particle size was also

reported by the highest peak seen in the distribution, which represents the particle size most commonly found in the distribution.

In laser diffraction, particle diameters are calculated by assuming volume spherical particles. Therefore, the accuracy of particle size distribution can be affected by non-spherical particles, which can lead to misleading results and information. In order to understand the powder particle size distributions of HTS powder for the superconducting composites, the morphology of the powders were reported using Scanning Electron Microscopy.

6.5.3 Scanning Electron Microscopy

Scanning electron microscopy (SEM) has been used to gain information on surface morphology, grain distribution and the chemical composition of surface structures of split-ring resonators and superconducting composites. A typical SEM consists of an electron column, specimen chamber, vacuum pumping system and the electronic control and imaging system. When an energetic electron beam is focussed on a solid surface several signals can be generated, each providing useful information about the material surface. In general, there are three types of signals generated by the interaction of incident electrons with solid materials; secondary electrons, backscattered electrons and X-rays. The characteristic interaction of these signals with the solid can be described using the concept of the interaction volume (Figure 6.7). The shape and escape depth of each signal depends on accelerating voltage of the electron beam and the atomic number of the elements in the sample. The size of the interaction volume increases with increasing incident electron energy and decreasing atomic number.

In general a 20 keV primary electron beam was used to produce high-resolution images of electrically conductive materials in the SEM. However, a relatively lower electron

beam energy was used for imaging non-conducting or insulating samples to reduce the charging. This charging effect is a common problem when electron beams are applied to insulating or low conducting materials, causing distortion in scanned images. In order to improve imaging, my samples were coated with layers of gold or carbon and connected to the mounting stub with silver or carbon dag to create an electrically conductive path to ground.

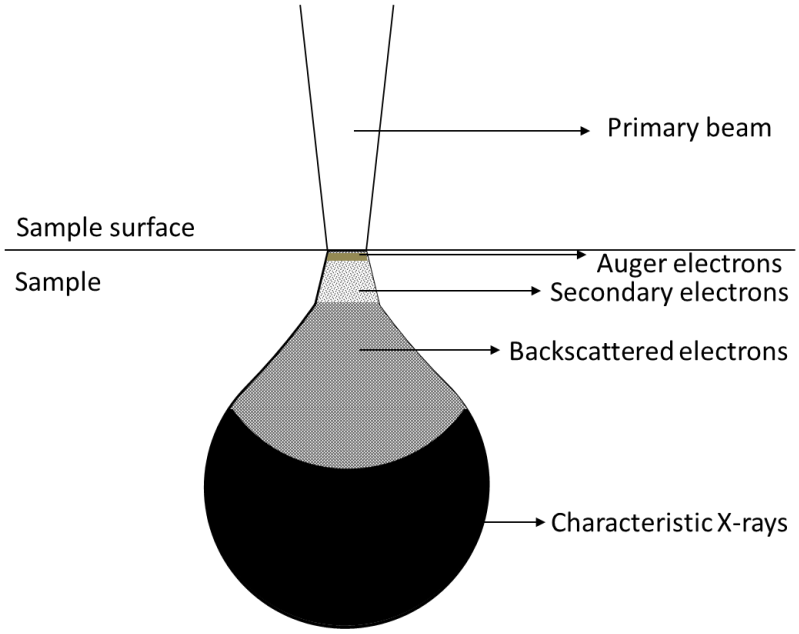


Figure 6.7 Schematic drawing of the interaction volume of incident electrons with a sample surface. The shape and size of the penetration depth of the interaction volume indicates the region from which the signals will appear to originate from the sample surface. Secondary electrons originate from the depth of about 10 nm, backscattered electrons 0.5 um and X-rays 1 um from the surface. Figure adapted from *ASM Handbook: Volume 10 Materials Characterization 9th edn (ASM International, 1986)*[24].

In this study, a number of microscopes were used for imaging and chemical analysis of superconductor composites. JEOL 840A and 840F instruments were used to analyse superconducting powder, and a JEOL 5510 was used for imaging of superconducting powder distribution in a polymer matrix. Several of these SEMs are equipped with secondary electron detectors, backscattered detectors and energy-dispersive

spectrometers for both secondary electron and backscattered imaging and chemical analysis.

6.5.3.1 Secondary electron imaging

The low energy secondary electrons generated by the primary electron beam are sensitive to surface topography. In this study, a 20 keV electron beam was used to observe the distribution of superconducting powders in a polymer matrix, and a 10 keV beam to give images of poorly conductive superconducting powders.

6.5.3.2 Backscattered electron imaging

Backscattered electrons are highly energetic signals generated by elastic scattering at depths 1 to 2 μm below the sample surface (see interaction volume in Figure 6.7). The signal strength of backscattered electrons is proportional to the local average atomic number of the sample[24]. Thus, materials with higher atomic number appear brighter than those with a lower atomic number, providing atomic composition information.

In this study, backscattered electron imaging was used to obtain images of superconducting powders in polymer matrices. The threshold intensity was set to distinguish the superconducting powder particles clearly from the background of the less dense matrix polymer, so that any signals above this value were considered superconducting powder. The area fraction of superconducting powder could then be analysed using ImageJ software[25].

6.5.3.3 Chemical analysis by Energy Dispersive X-rays

Characteristic X-rays are generated when electrons fall from a higher excited to a lower energy shell and emit energy during interaction of the incident electrons with target materials. These high energy characteristic X-rays are produced within the whole of the interaction volume (see Figure 6.7), and offer an efficient technique to qualitatively and

quantitatively measure the elemental concentrations in bulk samples. The characteristic energies of the emitted X-rays are unique for every element, depending on the specific ionization energies of electron shells involved in the transition process[24].

The characteristic X-rays can be detected by a solid state energy dispersive detector (EDS). Typically, an X-ray spectrum is displayed by X-ray count rate detected plotted against X-ray energy. The positions of X-ray peaks displayed provide qualitative information about the elements that form the sample, while the intensities of the X-ray peaks yield quantitative information that can be used to estimate the concentration of elements in materials by calculating atomic or weight percentages of specific elements. The spatial resolution and depth resolution of EDX analysis depends on the size of the interaction volume, which for 20 keV incident electrons on the order of a few micrometres.

In this study, EDX has been applied to provide phase information on the superconducting powder used in this work. This requires semi-quantitative analysis of atomic percentages of YBCO-123 and YBCO-211 composites in the YBCO powder by analysing information from the characteristic X-ray emission peaks.

References

1 Cardwell, D. A. Processing and properties of large grain (RE)BCO. *Materials Science and Engineering: B* **53**, 1-10 (1998).

2 Barns, R. L. & Laudise, R. A. Stability of superconducting $YBa_2Cu_3O_7$ in the presence of water. *Applied Physics Letters* **51**, 1373-1375 (1987).

3 Yan, M. F. *et al.* Water interaction with the superconducting $YBa_2Cu_3O_7$ phase. *Applied Physics Letters* **51**, 532-534 (1987).

4 Gallagher, P. K., O'Bryan, H. M., Sunshine, S. A. & Murphy, D. W. Oxygen stoichiometry in $Ba_2YCu_3O_x$. *Materials Research Bulletin* **22**, 995-1006 (1987).

5 Turner, B. N. & Gold, S. A. A review of melt extrusion additive manufacturing processes: II. Materials, dimensional accuracy, and surface roughness. *Rapid Prototyping Journal* **21**, 250-261 (2015).

6 Ratna, D. *Epoxy Composites : Impact Resistance and Flame Retardancy*. Vol. 16 pp. 5-7 (Smithers Rapra, 2005).

7 Harper, C. A. *Handbook of plastics, elastomers, and composites Third Edition*. pp. 1.25 (McGraw-Hill, 1996).

8 Fenner, R. T. *Extruder screw design : solutions to polymer melt flow in extrusion equipment, including wire-coating dies*. pp. 1-6 (Iliffe for the Plastics Institute, 1970).

9 Noztek.com. *Noztek Pro User Manual*, <http://www.noztek.com/wp-content/uploads/2013/11/User-manual-Nov-161.pdf> (2013).

10 Agilent Technologies, I. Agilent Technologies 8510C Network Analyzer System Operating and Programming Manual. (Agilent Technologies, USA, 2001).

11 Collin, R. E. *Foundations for Microwave Engineering*. 2nd edn, (IEEE Press Series on Electomagnetic Wave Theory, 2001).

12 Hiebel, M. *Fundamentals of Vector Network Analysis*. 6th edn, (Rohde & Schwarz GmbH & Co. Kg, 2014).

13 Abbas, Z., Pollard, R. D. & Kelsall, R. W. Further extensions to rectangular dielectric waveguide technique for dielectric measurements. *Instrumentation and Measurement Technology Conference, 1997. IMTC/97. Proceedings. Sensing, Processing, Networking., IEEE* **1**, 44-46 (1997).

14 Smit, J. *Ferrites : physical properties of ferrimagnetic oxides in relation to their technical applications*. Chapter 7, page 132-134 (Philips' Technical Library, 1959).

15 Barry, W. A Broad-Band, Automated, Stripline Technique for the Simultaneous Measurement of Complex Permittivity and Permeability. *IEEE Transactions on Microwave Theory and Techniques* **34**, 80-84 (1986).

16 Nicolson, A. M. & Ross, G. F. Measurement of the Intrinsic Properties of Materials by Time-Domain Techniques. *IEEE Transactions on Instrumentation and Measurement* **19**, 377-382 (1970).

17 Ekin, J. *Experimental Techniques for Low-Temperature Measurements: Cryostat Design, Material Properties and Superconductor Critical-Current Testing*. pp. 93 (Oxford University Press 2006).

18 Lei, Q. *All-dielectric composites for metamaterial applications*, Thesis (D.Phil.)--University of Oxford, (2016).

19 Wang, Y., Edwards, E., Hooper, I., Clow, N. & Grant, P. Scalable polymer-based ferrite composites with matching permeability and permittivity for high-frequency applications. *Applied Physics A* **120**, 609-614 (2015).

20 Huebener, R. P., Cardwell, D. A. & Ginley, D. S. *Handbook of Superconducting Materials: The Meissner-Ochsenfeld effect*. Chapter A2.2 pp. 63-66 (Institute of Physics, 2003).
21 Birkholz, M. in *Thin Film Analysis by X-Ray Scattering* pp. 1-40 (Wiley-VCH Verlag GmbH & Co. KGaA, 2006).
22 Suryanarayana, C. & Norton, M. G. *X-ray diffraction: a practical approach*. pp. 87 (Springer Science & Business Media, 2013).
23 *Malvern Instruments Ltd.: Getting Started Manual 0101 Issue 1.3* (Malvern Instruments Ltd., 1997).
24 *ASM Handbook: Volume 10 Materials Characterization* 9th edn, (ASM International, 1986).
25 Seuntjens, J. M., Clark, F. Y., Headley, T. J., Geulich, F. E. & Yang, N. Y. C. Image analysis of superconducting composites. *IEEE Transactions on Applied Superconductivity* **3**, 729-733 (1993).

7 Processing and Characterization of Superconducting Powder

7.1 Types of Superconducting Powder 110
7.2 BSCCO Powder 110
7.2.1 Characterisation of Precursor BSCCO Powder 111
7.3 YBCO Powder 116
7.3.1 Characterisation of commercial YBCO Powder 117
7.3.2 Top Seeded Melt Growth (TSMG) YBCO bulk 123
7.3.3 Characterisation of Melt-Grown YBCO Powder 124
7.3.4 Comparison of Magnetisation Properties of YBCO Powder 128
7.4 Effect of Particle Sizes on Magnetisation Properties 131
7.4.1 Characterisation and Classification of YBCO Particles 132
7.5 Discussion and Conclusions 136
7.5.1 Selection Process for Melt-Grown YBCO Bulks 136
7.5.2 Effect of Ball milling, Grinding and Sieving Processes on The Magnetisation Properties of YBCO Powder 137
7.5.3 Conclusions 139
References 140

This chapter discusses the selection of HTS materials for the superconducting filler in the fabrication of high temperature superconducting (HTS) composites. The simplest criterion, and the most industrially relevant, is the critical temperature, (T_c), of the superconductor filler. Given the convenience of working with liquid nitrogen, the T_c values of the chosen superconducting filler must be above 77 K.

In this work, the suitability of different HTS materials for HTS composite fabrication has been investigated. The processes involved in synthesizing powder for the fabrication of HTS composites will be described, where each material requires a different approach for powder processing. The microstructure and magnetisation

properties of these HTS materials have been investigated in order to establish the baseline for studying superconductor/polymer composites.

7.1 Types of Superconducting Powder

I have investigated the superconducting properties of $Bi_2Sr_2Ca_2Cu_3O_y$ (BSCCO) and $YBa_2Cu_3O_7$ (YBCO) powder by studying the size, morphology and the magnetisation properties of the particles, with an in depth study of the latter material. Factors affecting the magnetic properties of the potential superconducting filler have been investigated. In order to gain an understanding of the information that could be extracted from basic magnetic measurements, the effect of size and morphology of HTS particles on magnetisation properties were studied. This magnetic study is likely to give us an idea of the optimised magnetic properties that can be achieved using a superconducting filler in the fabrication of HTS composites.

The synthesis process for each HTS material is different, depending on the condition of the starting powders. The effect of these processing conditions on the size and morphology of superconducting particles and their magnetisation properties was studied, with the aim of selecting optimum sizes of superconducting filler with the best superconducting properties.

7.2 BSCCO Powder

One of the most extensively studied BSCCO compounds is $Bi_2Sr_2Ca_2Cu_3O_y$ (BSCCO-2223), which has T_c values above 77 K[1-3]. Because the 2223 phase is hard to synthesise[3], it is normally only commercially available as a precursor powder from which the customer can synthesise the BSCCO-2223 phase. In this project the precursor powder was readily available as provided by Merck Ltd ((Pb/Bi)SrCaCuO 2223). This precursor powder consists of a mixture of oxide compounds with the overall

stoichiometry of 2 moles of Bi to 2 moles of Sr to 2 moles of Ca to 3 moles of Cu with a small amount of added lead, which greatly aids the stabilisation of BSCCO-2223 in the high temperature phase[4]. The powder particle size distribution was measured using the Mastersizer, and the morphology of the powders were observed using SEM. A Quantum Design Magnetic Property Measurement System (MPMS) featuring a superconducting SQUID magnetometer was employed to measure the magnetic properties of BSCCO powder both before and after heat-treatment.

7.2.1 Characterisation of Precursor BSCCO Powder

Figure 7.1 shows the particle size distribution of the precursor BSCCO powder showing a peak in the distribution of particle sizes at 30 μm – 40 μm. The morphology of typical particles can be seen from Figure 7.2. It should be noted that the preparation process of dispersion in a polar liquid with ultrasonic agitation for the particle distribution measurement is likely to change the state of agglomeration in these samples and, hence change the observed particle size distributions. In addition, the non-spherical shape of particles can be clearly observed from the SEM images in Figure 7.2 will affect the accuracy of the particle size distribution. As stated in Chapter 6 (section 6.5.2), in laser diffraction experiments particle diameters are calculated assuming spherical particles, and the effect of non-spherical particles can lead to misleading results.

The image on the left (Figure 7.2) shows a distribution of clusters with size less than 50 μm, and the quantity of clusters of this size seems to be in good agreement with 5.5% volume fraction for particle size less than 40 μm in Figure 7.1. At higher magnification, each cluster appears to be an agglomerate of flat, irregular plate-shaped features. In addition, a few thin square features (indicated by arrows) can also be seen, which appear to be have similar grain morphology to the cuprate superconductors. These plate-like

features and sizes are in a good agreement with observation of $Bi_2Sr_2Ca_2Cu_3O_y$ (BSCCO-2223) particles reported previously by Jiang *et al.*[5].

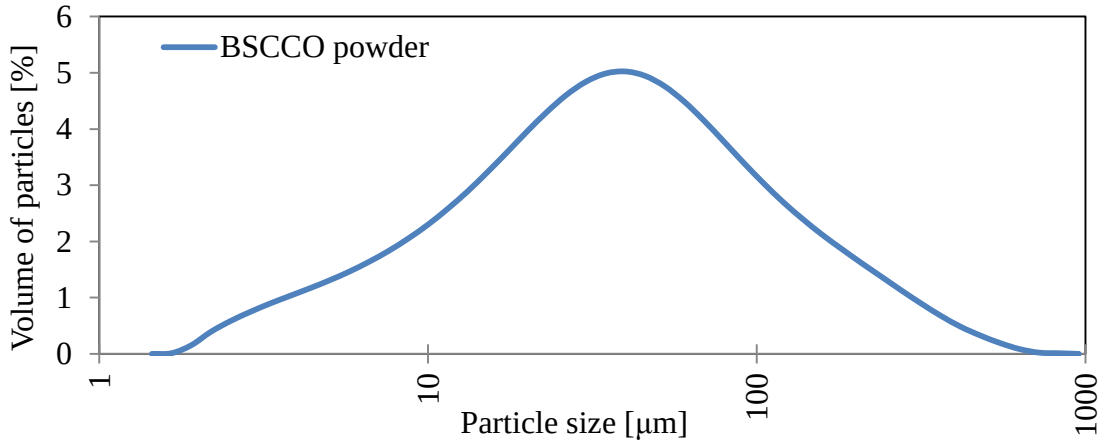


Figure 7.1 Particle size distribution of the precursor BSCCO powder. The graph shows the volume percentages of the particle size distribution with the highest volume percentage at 39.8 μm.

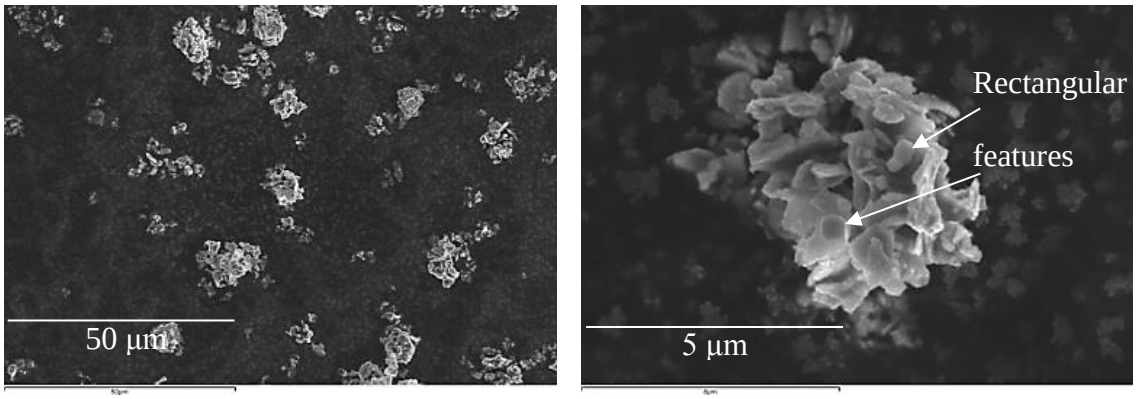


Figure 7.2 SEM images showing the surface morphology of the clusters of precursor BSCCO powder with size less than 50 μm (Left), Right: One of the clusters consists of agglomerated particles.

The magnetic properties of the precursor BSCCO powder were measured using 27 mg of powder. The sample was zero-field cooled (ZFC), exposed to a small field (H=10 Oe), warmed up in the field above T_c, and then a field-cooled (FC) measurement was made by cooling in the same field. To determine the magnetic properties of the powder, the magnetic hysteresis loop was also measured at 2 K and 77 K by sweeping the field from 0 to 7 T, 7 T to -7 T, and -7 T to 7 T. The results are shown in Figure 7.3, where the magnetisation of the precursor BSCCO powder is plotted versus temperature (left image), and the magnetic hysteresis loop is plotted at T=2 K (right image). The

magnetic hysteresis was measured at 2 K to estimate the maximum flux exclusion that can be observed from this powder. From these SQUID results, the BSCCO powder is shown to be weakly diamagnetic, with a transition temperature of 54 K. It is not surprising that the superconducting properties of this material are so poor because in the as-delivered state the precursor powder has not been converted to the high T_c BSCCO-2223 phase, as can also be seen in the XRD pattern in Figure 7.5. The XRD patterns for the precursor powder can be assigned mainly to the BSCCO-2212 phase. This can be observed from the diffraction peak of the (002) planes at 2θ=5.7° and other BSCCO-2212 peaks from (008), (113), (115), (117), (020), (0012), (119), (2010), (220), and (2012) planes at 23.0°, 24.8°, 27.4°, 30.9°, 33.1°, 34.9°, 35.1°, 44.5°, 47.5° and 48.9° respectively. The precursor BSCCO powder was also found to contain weak BSCCO-2223 peaks from (0012) and (119) planes at 28.8° and 31.9°. The existence of BSCCO-2212 and BSCCO-2223 powder in the precursor powder is likely to be common in the precursor BSCCO powder due to the sintering method used to manufacture the precursor powder[6] and similarities in structures and lattice dimensions (apart from c-axis) of the different phases BSCCO. The precursor powder needs a heat-treatment to enhance the growth of BSCCO-2223 phase.

To improve the superconducting properties, the precursor BSCCO powder was heat-treated and the magnetisation properties of the heat-treated BSCCO powder were measured. In order for the 110 K transition to be observed, Tarascon e. al. suggested heating precursor BSCCO powder near its melting point 885 ºC for a week[4,7]. In this work, the precursor powder was processed by heating the compound at 880 ºC for 168 hours. This heat-treatment process improved the superconducting characteristics of the BSCCO powder, with a stronger diamagnetic signature and the transition temperature increased to 84 K (Figure 7.4).

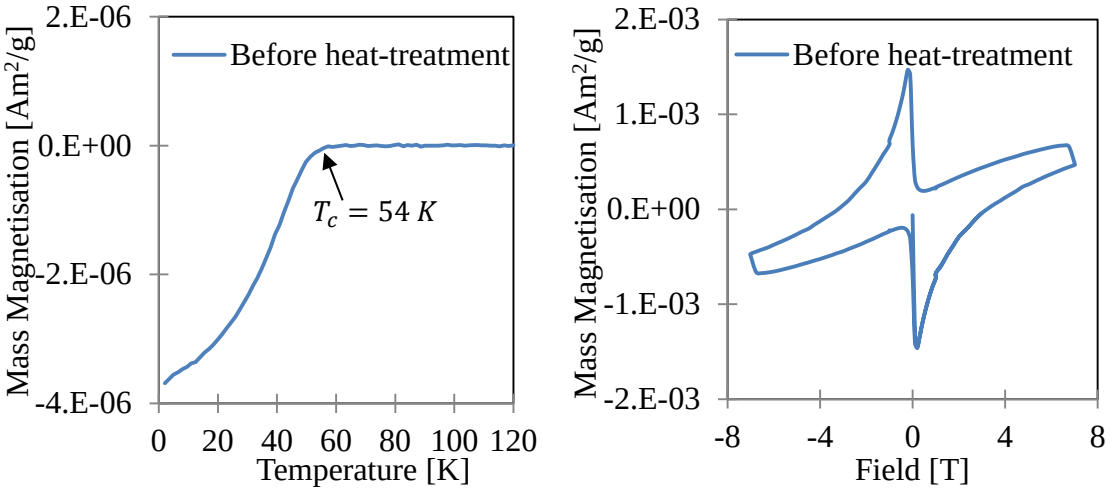


Figure 7.3 Magnetisation properties of the precursor BSCCO powder. Left: Temperature dependence of magnetic hysteresis at H=10 Oe. Right: Magnetic hysteresis of the precursor BSCCO powder at T=2 K

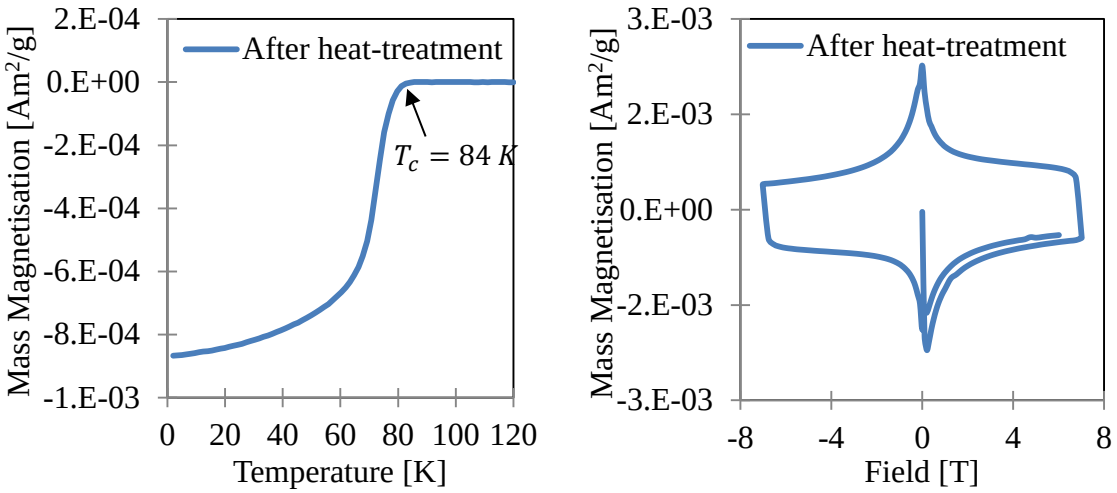


Figure 7.4 Magnetisation properties of BSCCO powder after heat-treatment at 880 ºC for 168 hours in air. Left: Temperature dependence of magnetic hysteresis at H=10 Oe. Right: Magnetic hysteresis at T=2 K.

However, the heat-treatment process was not successful in producing the pure BSCCO-2223 powder, as indicated by the the low T_c (Figure 7.4) and XRD results of the heat-treated BSCCO powder (Figure 7.6). The XRD pattern in Figure 7.6 shows a mixture of BSCCO-2212 and BSCCO-2223 phases, with major phase still being BSCCO-2212. This can be seen from the growth of BSCCO-2212 peaks from (002), (008), (108), (0012), (119) and (1113) planes at 5.7°, 23.0°, 28.3°, 34.9°, 35.1° and 45.0°. The development of the BSCCO-2223 phase can be seen from the BSCCO-2223 peaks from (115), (0012), (119) and (0018) planes at 26.2°, 28.8°, 31.9° and 43.9°. However, strong

BSCCO-2223 peaks such as (0010) and (0014) at 23.8° and 33.9° as highlighted by Tarascon *et al.*[7] are not observed in the XRD pattern. Small peaks at 17.7°, 35.9° and 45.9° might relate to the non-superconducting secondary phase of Ca_2PbO_4 (as described by Biju *et al.*[8]), which develop during the heat-treatment. An unknown peak is also observed at 21.9°, which does not match with any known secondary phase, however, based on its position, the peak might be from the (115) BSCCO-2212 peak of air-annealed $Bi_{1.6}Pb_{0.4}Ca_1Sr_2Cu_2O_y$ at 1120 K (847 °C) for 24 hour referred to by Sequeira *et al.*[9].

Figure 7.6 has shown the existence of BSCCO-2212 and BSCCO-2223 phases with non-superconducting secondary phase Ca_2PbO_4 in the heat-treated precursor BSCCO powder. Ca_2PbO_4 often occurs as a transient phase during early phase transition of BSCCO-2212 to BSCCO-2223 in the heat treatment, however, these peaks diminish together with the full growth of BSCCO-2223 peaks[10]. This suggests that a longer heat-treatment might be required to complete the BSCCO-2212 transformation to BSCCO-2223. However, as discussed in Chapter 4 (Section 4.4.5.3, page 49), even after lengthy heat-treatment, the existence of BSCCO-2212 and BSCCO-2223 phases is unavoidable due to similarities in structures and lattice dimensions (apart from c-axis)[11], leading to the the low T_c values (84 K) (Figure 7.4). This is in a good agreement with Tarascon *et al.* who postulated that the transition temperature of 84 K was observed in the BSCCO-2212 compound and that a transition temperature of 110 K was only expected if a high volume fraction of BSCCO-2223 could be achieved[7]. These results suggest that the precursor BSCCO powder is likely to have deteriorated due to long storage (more than 10 years since purchased). Fully reacted BSCCO-2223 powder is not commercially available, which made it difficult to outsource the starting materials for this work on HTS fabrication. I concluded, therefore, that BSCCO-2223 powder is not a suitable

filler for the fabrication of superconductor/polymer composites with good superconducting and microwave properties.

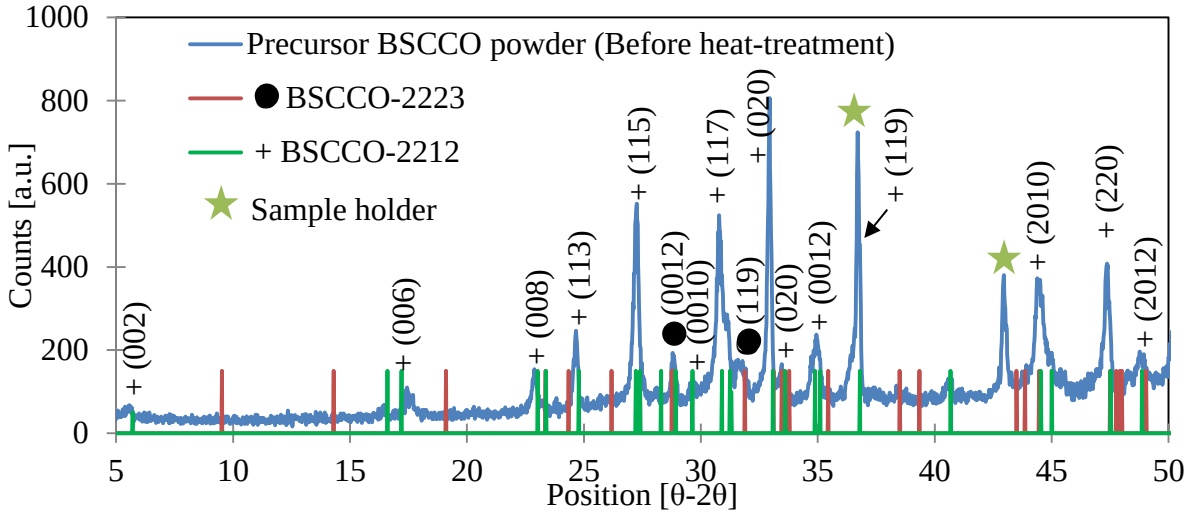


Figure 7.5 XRD pattern of the precursor BSCCO powder. All significant peaks of $Bi_2Sr_2Ca_2Cu_3O_y$ (BSCCO-2212) were indexed [Reference number from the X'pert score data base 00-041-0317]. $Bi_2Sr_2Ca_2Cu_3O_y$ (BSCCO-2223) peaks can be observed by referring to data base 00-041-0374.

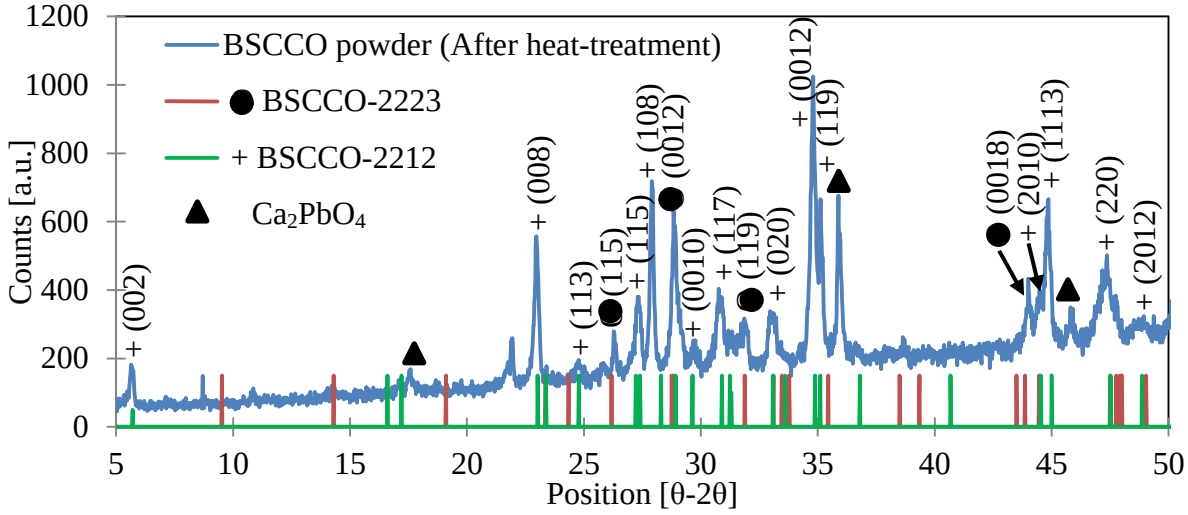


Figure 7.6 XRD pattern of BSCCO powder heat-treated at 880ºC for 168 hours. $Bi_2Sr_2Ca_2Cu_3O_y$ (BSCCO-2212) and $Bi_2Sr_2Ca_2Cu_3O_y$ (BSCCO-2223) peaks were indexed using X'pert score data base 00-041-0317 and 00-041-0374. Ca_2PbO_4 peaks were indexed by referring to data base 00-012-0780.

7.3 YBCO Powder

As has been discussed in Chapter 4, $YBa_2Cu_3O_7$ (YBCO-123) has been used in composites to experimentally study the properties of the HTS composites at microwave

frequencies[12-14]. With a T_c values of 92 K, YBCO-123 properties can be exploited using liquid nitrogen, a low cost refrigerant.

In this section, factors affecting the magnetisation properties of YBCO-123 have been investigated. Two types of YBCO-123 materials were studied; commercial YBCO powder and large grain bulk YBCO processed into powder (Table 7.1). The processing steps taken to prepare these materials for use as effective superconducting filler are described separately. YBCO powder was commercially available from Alfa Aesar with 99.5% purity and -325 mesh sizes, corresponding to a sieve diameter of around 40 μm. The magnetic properties of this commercial YBCO powder were set as a baseline value in the superconducting filler study. In order to produce YBCO powder with well-controlled particle sizes, single grain YBCO bulks fabricated by the top-seeded melt growth (TSMG) process were provided by the Bulk Superconductivity Group, University of Cambridge. The process taken to prepare the melt-grown YBCO powder will be discussed in section 7.3.2.

Table 7.1 Sample conditions for synthesizing YBCO powder

Sample powder	Category	Process
Commercial YBCO	Small particles	Ball milled for 20 hours
Melt-grown YBCO	Large particles	Mechanically ground and passed through sieves of size 63 μm and 125 μm-mesh

7.3.1 Characterisation of commercial YBCO Powder

The crystalline phases in the commercial YBCO powder were determined by reference to the $YBa_2Cu_3O_7$ (YBCO-123) phase from the X'pert score data base (Reference number 00-038-1433). All (2θº) peaks from 20º to 50º were closely matched to YBCO-123, with the major peak indexed as (103) as indicated in Figure 7.7. The XRD pattern is in good agreement with the data from commercially available YBCO powder used by Shi *et al.*[15], and no significant peaks associated with impurity phases could be detected.

As has been discussed in the previous chapter, it is difficult to establish the YBCO-123 content precisely using X-ray diffraction because the peak heights can be affected by many factors including grain size and texture[16]. In this work, XRD analysis has been used only to confirm the superconducting phase of YBCO-123 in YBCO powder. It is more relevant for this project to observe the superconducting properties of this YBCO powder and its effect on the magnetisation properties of HTS composites fabricated using the powders. As such, the size and elemental composition of the YBCO powder have been studied, in order to control and optimise the magnetisation properties of YBCO powder in the HTS composites.

The size and shape of the YBCO powder was checked using SEM. YBCO powder was lightly dusted on the carbon sticky tab before removing loose particles using compressed air. This left a suitable amount of YBCO powder for studying the morphology of individual particles. The commercial YBCO powder was observed to have clusters of agglomerated particles with size less than 9 μm, as can be seen from the SEM images in Figure 7.8. At higher magnification, these agglomerated particles are observed to consist of flat, irregular plate-shaped flake-like features ranging in size from 1 - 3 μm.

As the range of particle sizes was too wide to assess accurately from SEM observations, particle size measurements were carried out using a Malvern Mastersizer laser diffraction system. YBCO powder was added to distilled water and dispersed using an

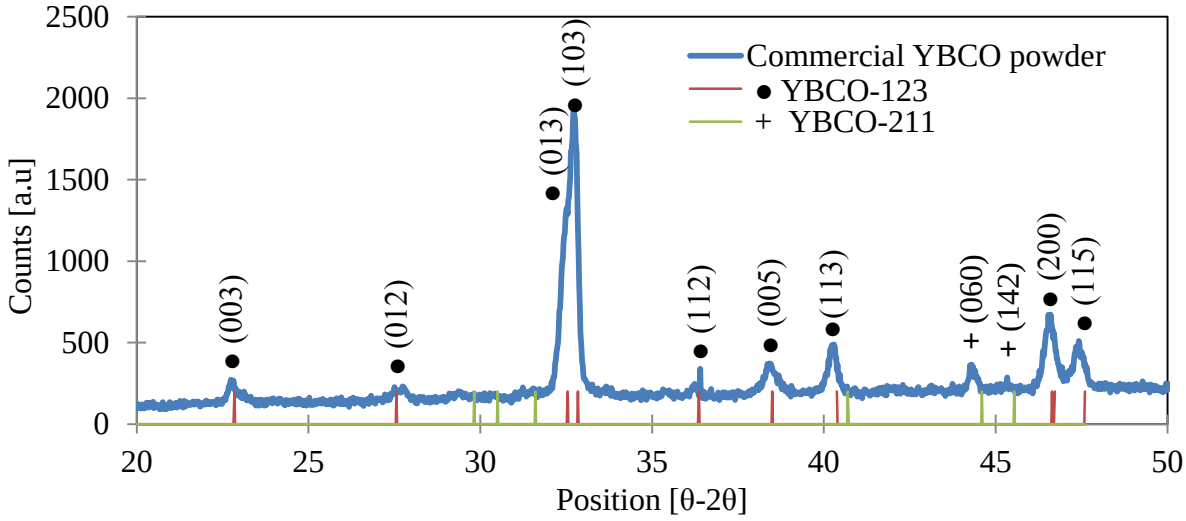


Figure 7.7 XRD pattern of the commercial YBCO powder. All significant peaks could be indexed to the 123 phase [Reference number from the X'pert score data base 00-038-1433].

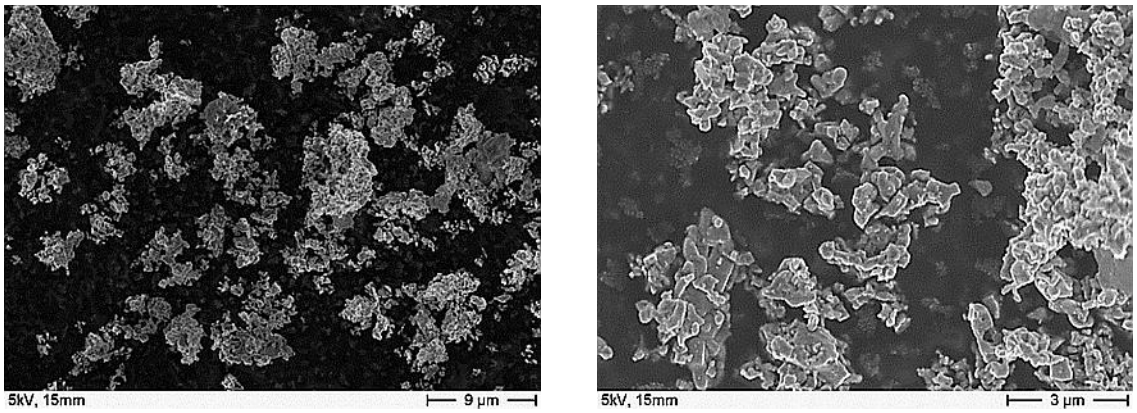


Figure 7.8 SEM images of the commercial YBCO powder.

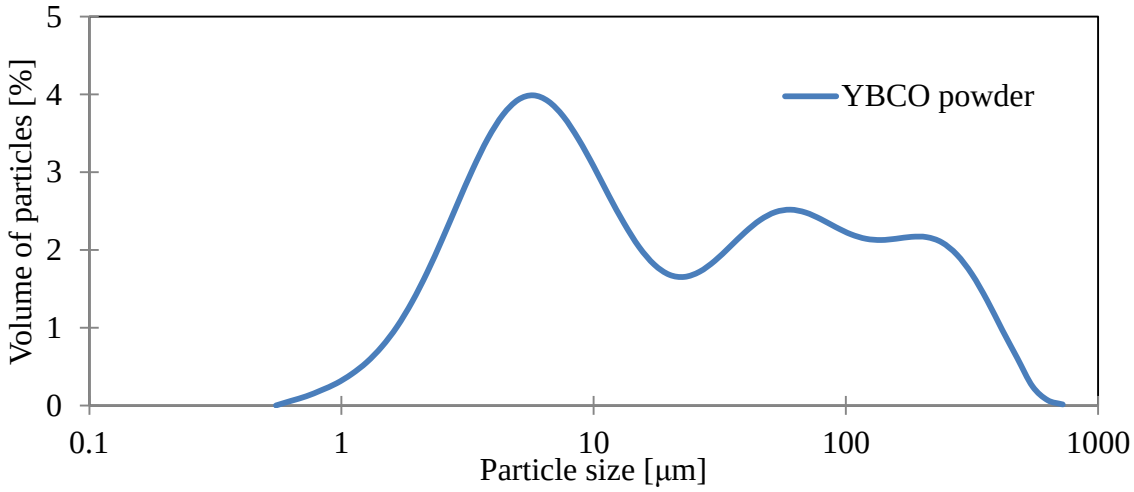


Figure 7.9 Particle distribution of commercial YBCO powder. The size of the source powder varies from 0.6 µm to 631.0 µm with the highest volume percentage at 5.8 µm.

ultrasonic bath for 20 s. The particle size distribution for the commercial YBCO powder is shown in Figure 7.9, and has a wide range of particles sizes from 0.7 μm to 631.0 μm, with the main peak at 5.8±0.4 μm. The median particle size, d_{50}, indicates that 50% of the particle distribution lies below 14.6 μm. This broad range of particle sizes is likely related to the agglomeration of YBCO particles, as can be observed in Figure 7.8, and which cannot be broken up by the ultrasonic treatment. This can be clearly seen from the plateau-like distribution of the particle size above 40 μm, indicating attachment of small particles to form agglomerates.

To further study the effect on the particle size of processing commercial YBCO powder, the powder was ball milled. Ball milling is a mechanical process that can cause reduction of particle sizes. The most common ball milling process involves preparation of a container or bottle containing the powder sample and grinding balls, which is placed on a mill and rotated. With each rotation of the container, the balls impact against the powder sample and the force of the impact on the particle surface can fracture the powder particles[17]. The rate of particle size reduction depends on the raw materials (initial powder size), size and hardness of the grinding balls, and process variables such as time and speed of milling[17]. The rate of particle size reduction is roughly exponential with time[17]. Ball milling can be conducted in a liquid medium mixed with the grinding media and powder samples in the container, which is referred as wet grinding, while without the liquid medium the process is referred as dry grinding. The wet grinding method is reported to be useful to produce finer ground particles with less agglomeration[17]. However, dry grinding is more suitable for ball milling moisture sensitive YBCO powder.

In this work, the dry grinding method was carried out on the commercial YBCO powder. 50% yttria-stabilised zirconia (YSZ) grinding media (Inframat Advanced

Materials; 3.0 mm beads) and 45 g commercial YBCO powder with 5:1 ball-to-powder weight ratio were loaded in a polypropylene bottle (500 ml). The bottle was sealed and a rubber O-ring was placed around the bottle to ensure that maximum rolling can be achieved during milling. The rotation of the bottle in the mill was controlled by the speed and time. The speed of the ball milling was based on listening to the sound made by the grinding media, and selecting the rotation speed that gave the maximum volume[18]. The bottle was placed horizontally into the mill and rotated for 20 hours at speed setting 4 (approximately 100 rpm). The milling time was chosen based on the ball milling time for magnesium diboride powder (MgB_2), which was reported to have agglomerates effectively broken down after ultrasonication[19]. This is important to ensure that homogeneous mixing can be achieved in the fabrication process for HTS composites.

Figure 7.10 shows the particle distribution of commercial YBCO powder after ball milling for 20 hours. The ball milled YBCO powder has a bi-modal size distribution, but the particle size distribution has narrowed from 0.5 μm to 91.2 μm, with the highest peak of the particle distribution at 3.0±0.3 μm. It is clear that the maximum particle size shifts from 631.0 μm (Figure 7.9) to 91.2 μm (Figure 7.10), indicating agglomerates in the starting powder were successfully broken up by the ball milling process. This can be seen in Figure 7.11, where d_{90} in the initial powder is 195.6 μm and decreased to below 33.7 μm after milling. The median size, d_{50} also decreases from 14.6 μm to 4.5 μm after ball milling. However, even in this sample, a large fraction of the particles below 30 μm can be seen from the SEM images in Figure 7.12 to be formed by agglomeration of smaller particles. This agglomeration of particles is likely to occur during extended ball milling in air. The same effect was observed by Dancer *et al.* who reported increases of

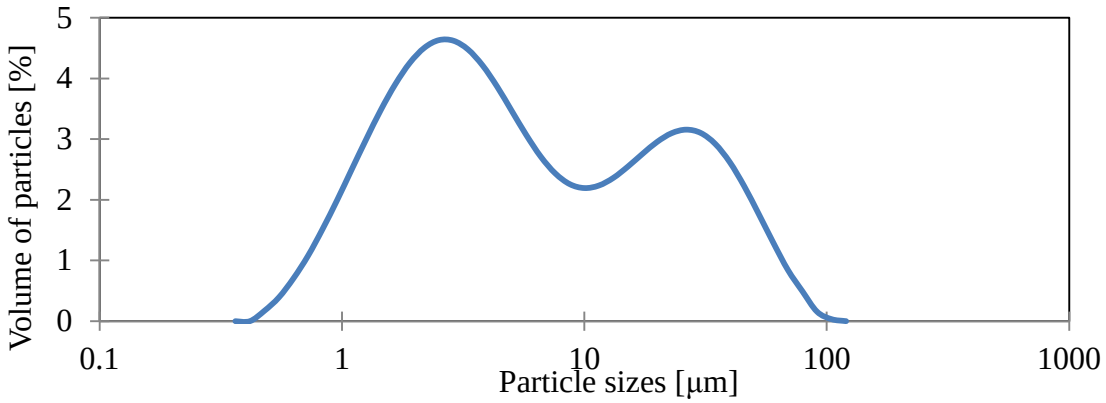


Figure 7.10 Particle distribution of commercial YBCO powder after ball milling for 20 hours. The particle size varies from 0.5 µm to 91.2 µm with large volume percentage distributed between 2.5 and 26.3 µm.

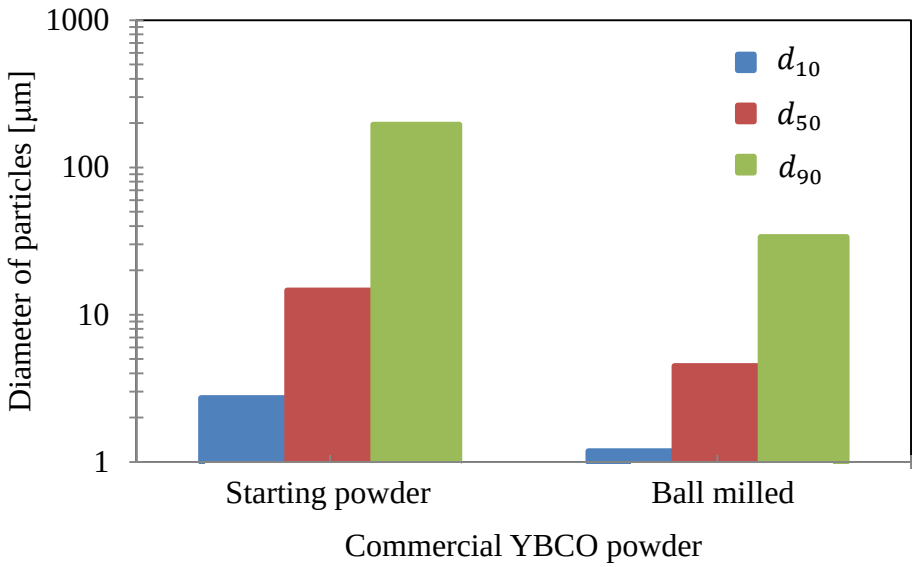


Figure 7.11 Comparison of commercial YBCO particle sizes before and after the ball milling process.

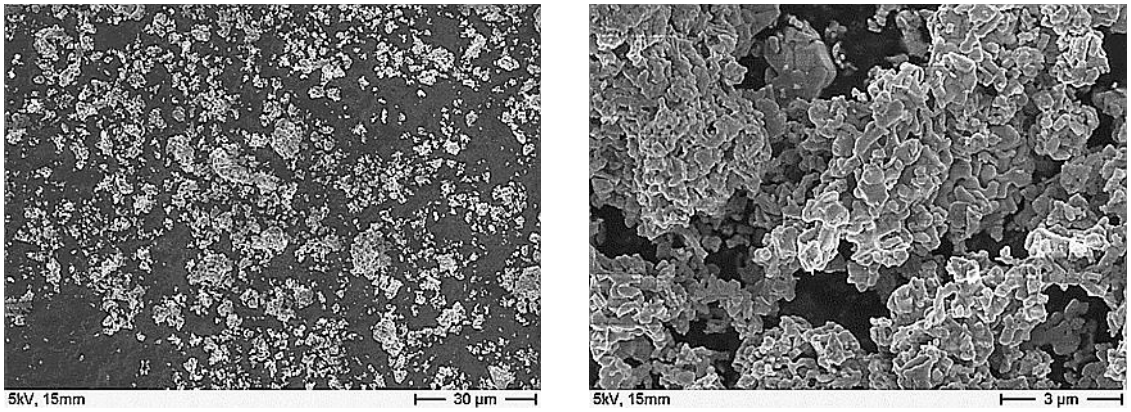


Figure 7.12 SEM image of the commercial available YBCO powder after the ball milling process.

magnesium diboride (MgB_2) particle sizes after 20 hour ball milling in air due to the effects of capillary forces and drying of the powder[19]. It can be clearly observed that the shape of commercial YBCO particles before and after ball milling process are non-spherical from the SEM images in Figure 7.8 and Figure 7.12. Since the laser diffraction particle diamaters are calculated by assuming spherical particles, it should be noted that these non-spherical shape of particles will affect the accuracy of the particle size distribution measured. It is difficult to make generalised observations on the particle morphology from SEM images, but it appeared that some particles are not as angular and sharp in the ball milled powder as those in starting powders, presumably due to the mechanical milling process.

7.3.2 Top Seeded Melt Growth (TSMG) YBCO bulk

YBCO bulks were fabricated using the TSMG technique[20] (details of fabrication technique can be found in Chapter 4). I was provided with off-cuts from the edge of TSMG bulks by the Cambridge group (Figure 7.13 (left image)).

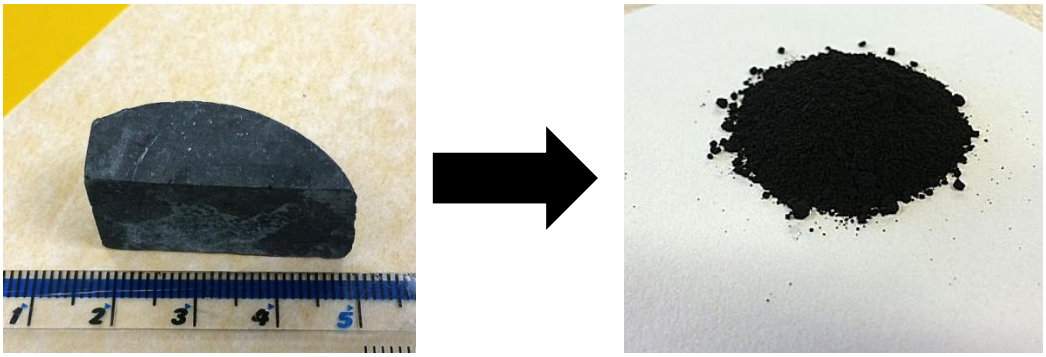


Figure 7.13 A fragment of a single-grain of YBCO bulk. The fragment was mechanically ground using 63 and 125 μm mesh size sieves.

These off-cut fragments were supplied without crystal seeds. The quality of these was rather variable, so I carried out a simple magnetic levitation test to screen for the best fragments. The bulk was immersed in liquid nitrogen, and a NdFeB permanent magnet

was placed above it. The samples for which the magnet was successfully levitated were selected as these contained a large volume fraction of superconducting phase.

In order to create a powder containing fragments of these large superconducting crystals, these YBCO bulks were mechanically ground using a pestle and mortar and filtered through 63 μm and 125 μm-mesh size sieves to produce YBCO powder with size $63 < d_{sieve} < 125\ \mu m$ (Figure 7.13 (right image)). A single-grain YBCO bulk like that shown in Figure 7.13 can produce approximately 10 g YBCO powder with fraction size $63 < d_{sieve} < 125\ \mu m$. To produce a sufficient amount of YBCO powder for HTS composite fabrication, off-cuts from several YBCO grains were used and the resulting powder mixed thoroughly.The crystal phases of the melt-grown YBCO powder were identified using XRD, and the shapes and sizes of the powder were determined using SEM and the Mastersizer. Similar to the commercial powder, the magnetic properties of YBCO powder were measured at 2 K.

In this work several off-cut melt-grown YBCO samples were used for the characterisation studies in section 7.3 and 7.4.

Table 7.2 Melt-grown YBCO samples for characterisation studies

Section	Melt-grown YBCO fragments	YBCO powder fraction size, d_{sieve} (μm)	Characterisation
7.3	Sample 1	$63 < d_{sieve} < 125$	XRD, Mastersizer, SEM, SQUID magnetometer
7.4	Sample 2	$63 < d_{sieve} < 125$ $53 < d_{sieve} < 63$ $38 < d_{sieve} < 53$ $d_{sieve} < 38$	Mastersizer, SQUID magnetometer

**Sample 1 is used for producing HTS composites in Chapter 8.*

7.3.3 Characterisation of Melt-Grown YBCO Powder

XRD measurements were carried out on both melt-grown YBCO powder and the starting bulk material. The crystalline phase of both materials were measured and compared. The XRD spectrum confirms that the main crystalline phase in the melt-

grown YBCO bulk is $YBa_2Cu_3O_7$ (YBCO-123) with all the major (00l) peaks, (003), (005) and (006) matching closely to the reference spectrum. This bulk material shows only the (001) peaks of YBCO-123 because they are single crystal. However, from the melt-grown YBCO powder the major peaks were (013) and (103) as expected from a random arrangement of powder particles, rather than the highly oriented melt-grown bulk sample. It can also be seen that the XRD peaks of the melt-grown YBCO powder are shifted to the left with respect to the database positions. The shifting of peak positions may be due to variations in sample height adjustment during XRD measurement, which contributes to a systematic shift in the XRD spectrum. It is important to highlight that a small amount of Y_2BaCuO_5 (YBCO-211) phase is detected from both the melt-grown YBCO bulk and the powder by reference to the YBCO-211 phase in the database (Reference number 00-038-1433) as indicated in Figure 7.14 and Figure 7.15 respectively. YBCO-211 is a non-superconducting phase deliberately added in the starting materials prior to the melt processing to improve the flux pinning in single grain YBCO[20].

The approximate composition of the YBCO powder was checked using the EDX method in the SEM. YBCO powder was pressed firmly onto a carbon sticky tab before dusting several times to remove loose particles using compressed air. This produced a reasonably flat and thick sample for elemental analysis. EDX was used to estimate the concentration of individual elements in YBCO by analysing information from the characteristic X-ray emission peaks. EDX spectra were taken at several points using area analysis spot mode, and the resulting Y and Ba compositions from three typical points are shown in Table 7.3. The volume fractions of YBCO-211 in the melt-grown YBCO particles were estimated by calculating the atomic percentages of cation elements, Y and Ba using equation (7.1).

$$Estimated\ volume\ fraction\ of\ YBCO-211 = 1/\left(\frac{2-\left(\frac{Y}{Ba}\right)}{2\left(\frac{Y}{Ba}\right)-1}\right) \quad (7.1)$$

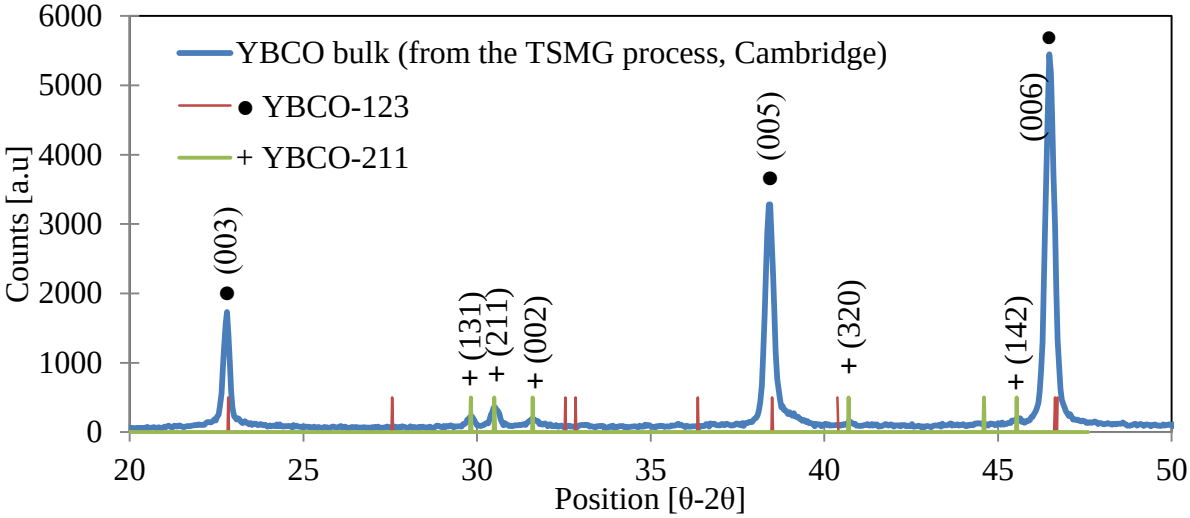


Figure 7.14 XRD pattern of the YBCO bulk from the melt-grown process. All significant peaks were indexed [Reference number from the X'pert score data base 00-038-1433]. Y_2BaCuO_5 (YBCO-211) peaks can be observed by referring to data base 00-038-1433.

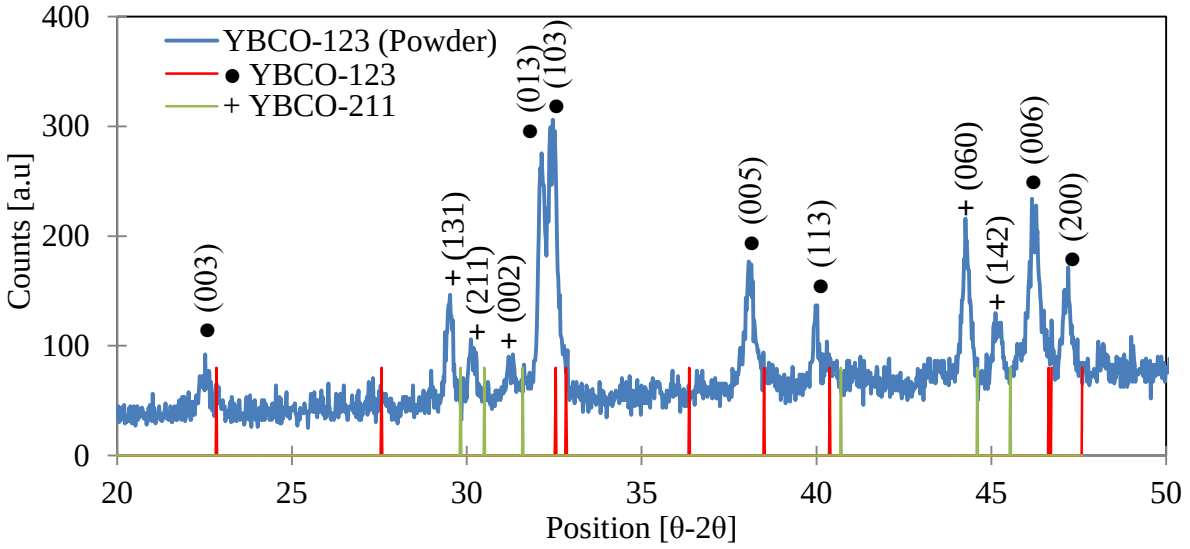


Figure 7.15 XRD pattern of the melt-grown YBCO powder.

Table 7.3 EDX analysis of the melt-grown YBCO powder

Elements	Y	Ba	Estimated volume fraction of YBCO-211 [%]
Particle 1	7.59	9.87	30
Particle 2	7.47	10.57	24
Particle 3	6.66	10.59	16

Approximately 16% of the non-superconductor 211 phase was detected in the melt-grown YBCO powder. This explains YBCO-211 peaks observed from the XRD pattern.

Figure 7.16 shows SEM images of the melt-grown process YBCO powder. We can see that the grinding process contributed to the formation of irregular-shaped grains with size less than 100 μm. Unlike the commercial YBCO powder, no agglomerated particles can be clearly seen from the SEM images of the melt-grown YBCO powder. Among these features, flat plate-like particles are observed with size less than 50 μm. This is not unexpected when grinding a brittle ceramic sample with very large crystal grain size. Embedded in the sticky carbon tab, finer particles were also observed. It was difficult to establish the average particle size or to generalise observations of particle morphology from these SEM images, but it appeared that the melt-grown YBCO powder contained a wide range of particle sizes. Since the YBCO powder was filtered using 63 μm and 125 μm mesh sieves, the particle sizes $63 < d < 125\ \mu m$ was too great to assess accurately only from SEM observations. Therefore the particle size was also measured using the Mastersizer. The particle size distribution shows a wide range from 1.0 μm to 363.2 μm with the highest peak distribution skewed to the left at 104.7 μm (Figure 7.17). Since the Mastersizer measures light scattering intensity of particles by assuming that every particle is a sphere, the volume of irregular-shaped particles will not be perfectly accurate for this YBCO powder. This can cause an overestimation of the volume percentage especially for flat plate-like particles. The same phenomenon was reported by Allen *et al.,* who reported broadening in the particle size distributions due to measurement of non-spherical particles lying at all orientations[21].

From the SEM observations, some of the particles are elongated, where the width and thickness of individual particles were less than the size of the mesh aperture, and passed through the sieve hence contributing to the distribution of particle sizes above 125 μm. The presence of small particles may also be responsible for the agglomerates. This is due to grinding and sieving errors such as the inclusion of weakly bound agglomeration

due, for example, to static charges, van-der-Waals forces, or capillary forces from moisture adsorption[18].

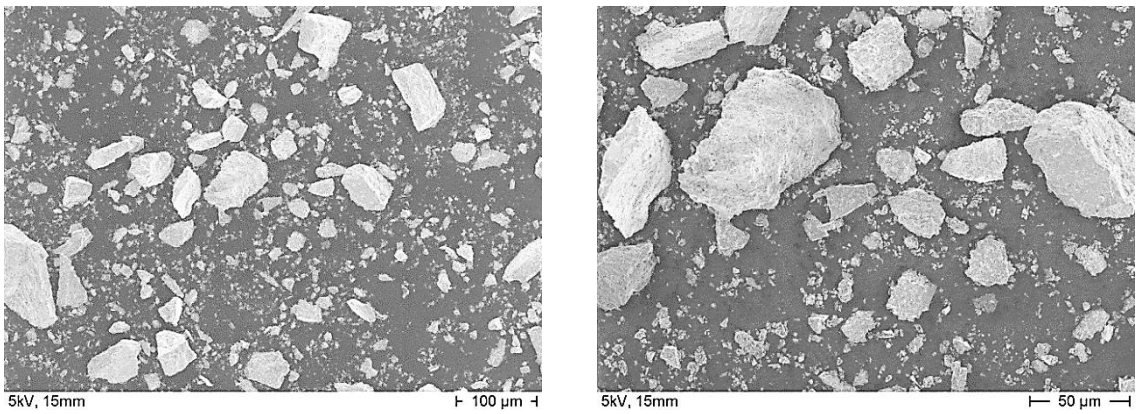


Figure 7.16 SEM images of melt-grown YBCO powder sieved through 63 and 125 µm mesh.

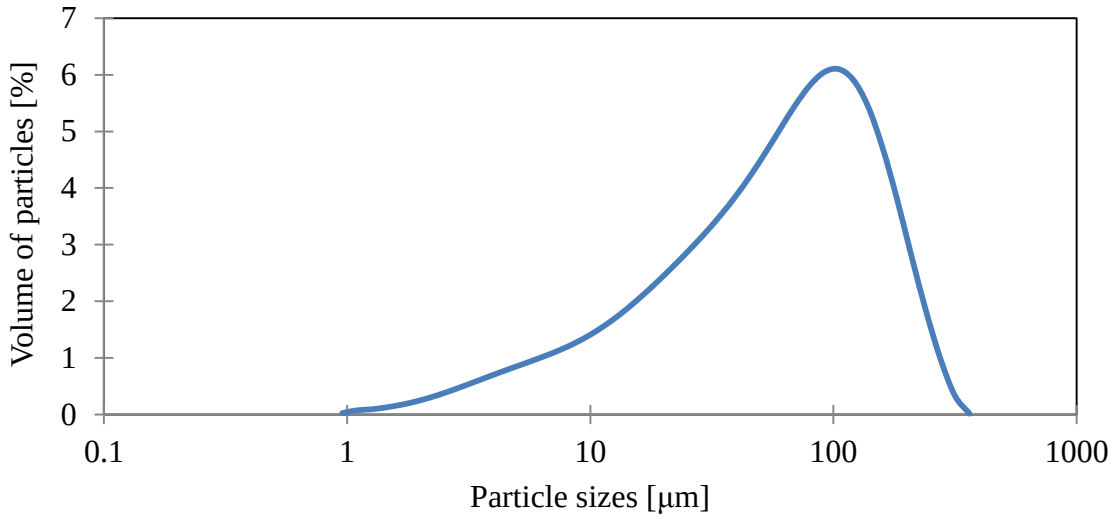


Figure 7.17 Particle distribution of the ground YBCO powder filtered through 63 and 125 µm-mesh sieves. The particle distribution is peaked at 104.7 µm.

7.3.4 Comparison of Magnetisation Properties of YBCO Powder

Figure 7.18 shows a comparison of the particle size distributions for the commercial and melt-grown YBCO powder used for the magnetic property evaluation. A large difference of particle sizes were observed from the melt-grown and commercial YBCO powder by comparing the d_{10}, d_{50} and d_{90} values. The median diameters, d_{50}, of the commercial powder are 4.5 µm and for the melt-grown powder 59.2 µm, and similarly the d_{10} and d_{90} values for the commercial powder were 1.2 and 33.7 µm, and melt-

grown powder were 9.5 μm and 157.5 μm respectively, indicating the particle sizes of the melt-grown YBCO powder are bigger than the commercial YBCO powder. In this work, the large size particles of YBCO powder are required to avoid the effect of surfaces where the superconducting properties are lost[22] and my choice of sieve sizes for the melt-grown powder was intended to result in a larger average particle size. This effect of penetration depth on YBCO particle size will be discussed in detail in Chapter 8. It is important to have a well-controlled size of YBCO powder with known magnetisation values in the following process of HTS composite fabrication.

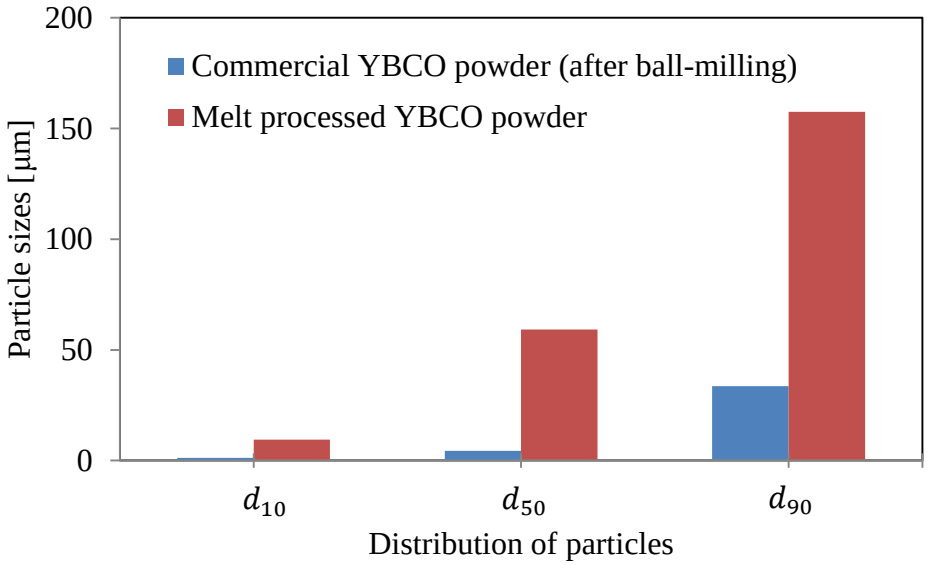


Figure 7.18 Comparison of particle size distributions for the commercial and melt-grown YBCO powder.

Magnetisation properties of both commercial and melt-grown YBCO powder from sieve fractions of $63 < d_{sieve} < 125\,\mu m$ were measured using the SQUID magnetometer. As suggested by Hibbs *et al.* all data were normalised by the sample mass to compensate for the different weight of YBCO powders[23]. The results of these measurements are shown in Figure 7.19, Figure 7.20 and Figure 7.21.

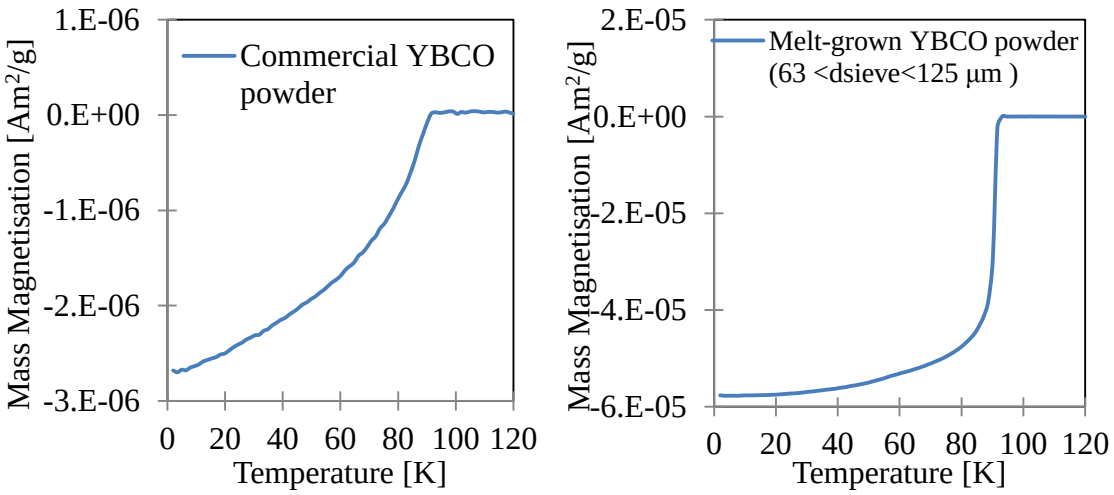


Figure 7.19 The magnetisation of YBCO powder from which the T_c value can be seen to be 93 K; commercial YBCO powder (left) and the melt-grown YBCO powder (right). Note the different vertical scale.

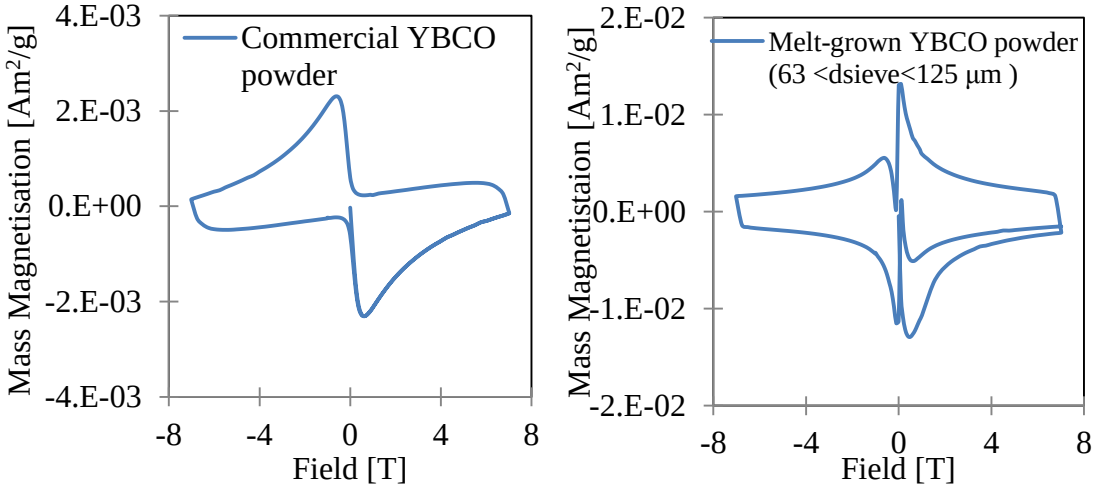


Figure 7.20 The hysteresis loops of commercial YBCO powder (left) and the melt-grown YBCO powder (right) at 2 K. Note the different vertical scale.

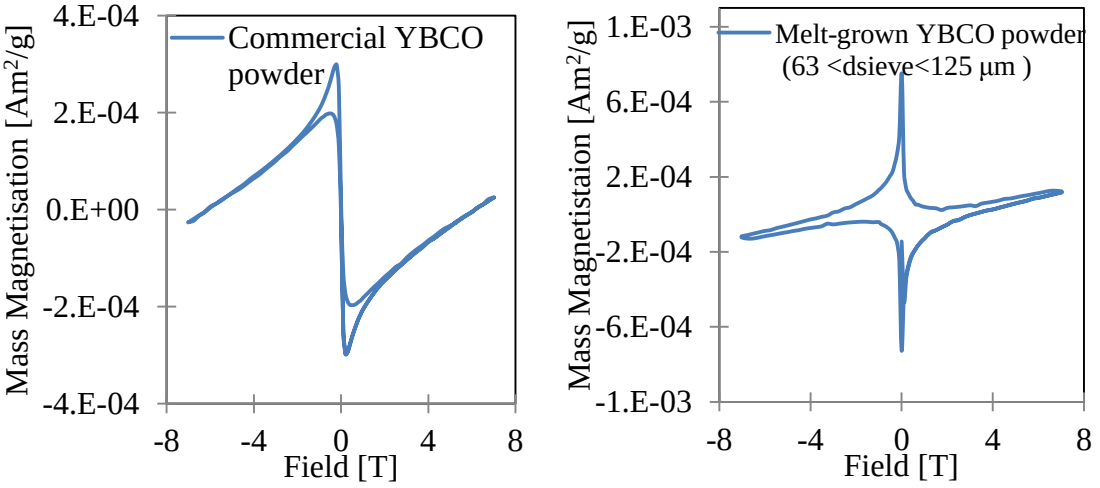


Figure 7.21 The hysteresis loops of commercial YBCO powder (left) and the melt-grown YBCO powder (right) at 77 K. Note the different vertical scale.

Both commercial and melt-grown YBCO powders showed a diamagnetic response with transition temperature of 92 K, but the transition was much sharper in the melt-grown YBCO powder, indicating uniform T_c distribution. Hysteresis loops of the melt-grown YBCO powder were observed with typical irreversibility of a strongly pinned superconductor. This can be correlated with the YBCO-211 phases found in the melt-grown YBCO powder by XRD. However, the commercial YBCO powder has a weaker hysteretic effect than the melt-grown processed YBCO at 7 K (Figure 7.21). This is due to the weaker flux pinning in the commercial YBCO than the melt-grown YBCO powder. At 77 K, the commercial YBCO powder has the hysteresis loop shape similar to a reversible superconductor, indicating no significant flux pinning. This is in agreement with the XRD results, where commercial YBCO powder is mainly composed of YBCO-123, with no 211.

Overall, the magnetisation effect of YBCO powder at 77 K is crucial to ensure significant electromagnetic change at microwave frequencies can be achieved in the HTS composites. Better quality superconducting powder with stronger diamagnetic signal should make composites with larger change in electromagnetic properties below T_c. In this case, the commercial YBCO powder was not the best choice for application in composite devices. Therefore, the melt-grown YBCO powder was used as the preferred source powder for all further work.

7.4 Effect of Particle Sizes on Magnetisation Properties

It is well-known that particle sizes can affect the magnetic properties of YBCO powder[24,25]. For this reason, the effect of the selected particle size of melt-grown YBCO powder on magnetisation properties has been investigated using various size ranges.

These data provide information about the change of magnetic properties with particle size.

In this study, only one fragment of a large YBCO bulk (Sample 2 as referred to Table 7.2) was used to generate all the powder. This is to minimise variables in the sample that can affect changes in the magnetic properties. Based on the previous levitation test, a fragment of YBCO bulk was chosen to have a good flux exclusion property with a transition temperature above 77 K. After grinding by pestle and mortar, the melt-grown YBCO powder was prepared by passing through a 125 μm mesh sieve and then separating them into several fractions of particle sizes based on their sieve diameter, d_{sieve}. The fractions produced will be referred to as follows:

- $63 < d_{sieve}$ (μm) <125, as d_{125}
- $53 < d_{sieve}$ (μm) < 63, as d_{63}
- $38 < d_{sieve}$ (μm) < 53, as d_{53}
- d_{sieve} (μm) < 38, as d_{38}

7.4.1 Characterisation and Classification of YBCO Particles

The particle size distribution measurement was carried out using the Mastersizer. The particle size distributions for each fraction are shown in Figure 7.22. In general the particle size increases with larger sieve mesh, as expected. This can be seen from the highest peak of each particle distribution, which is shifting to the right with increasing sieve mesh. The size of the peak distribution for each powder and its median particle size, d_{50}, are given in Table 7.4. The populations of particle size distributions are fairly similar for all fractions of particle sizes, except for the smallest fraction (d_{38}), which has the peak distribution skewed to the right, having lower limits of 0.6 μm. This is due to the wide distribution of particle sizes filtered through the 38 μm mesh sieve. These

small particles have high tendency to form agglomerates, which contribute to this wide particle distribution.

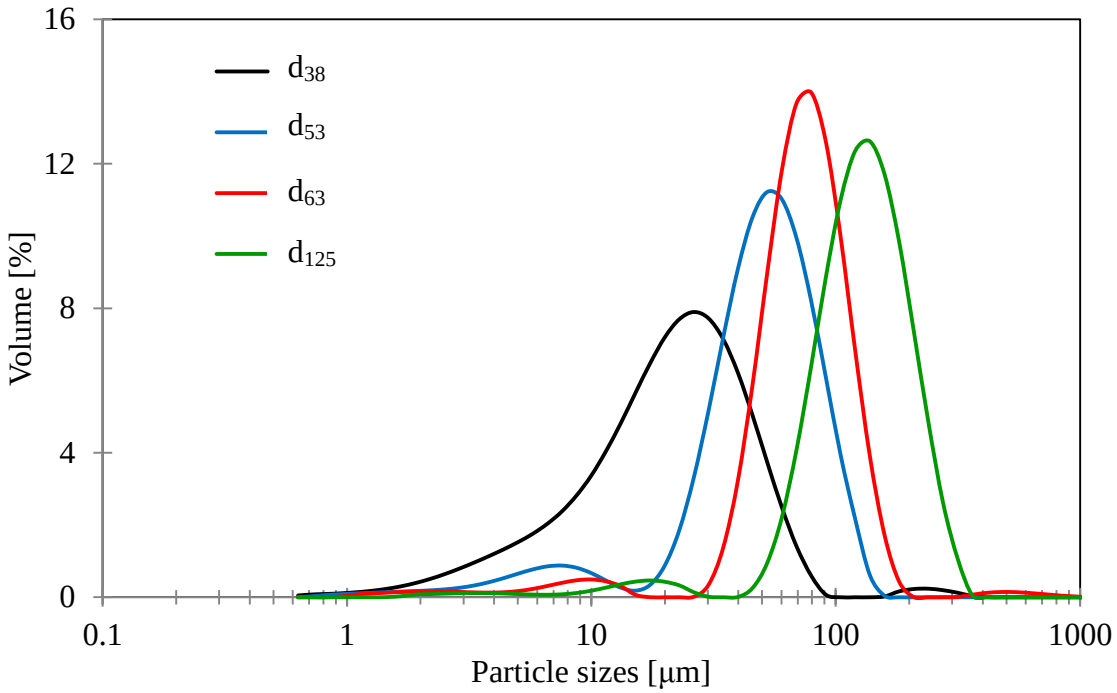


Figure 7.22 Particle size distribution of YBCO-123 powders.

Table 7.4 Particle size by laser diffraction.

Fraction of particles	Peak distribution of particle sizes [µm]	Median particle size, $d_{50,}$ [µm]	Proportion of the total mass of ground powder [%]
d_{38}	26.3	20.3	12
d_{53}	52.5	47.6	18
d_{63}	79.4	69.3	21
d_{125}	138.0	120.3	24

The magnetic properties of each powder was measured using a SQUID magnetometer. Hysteresis curves were measured at 7 K and 77 K for all powders by sweeping the applied fields from 0 to 7 T, 7 T to -7 T, and -7 T to 7 T. Figure 7.23 and Figure 7.24 shows magnetisation per gram of YBCO powder plotted against the applied fields at 7 K and 77 K respectively. The magnetisation values were normalised by weight of YBCO powder for comparison. The mass magnetisation increased with increasing particle sizes at 7 K, and the same observation can be seen at 77 K. Figure 7.23 shows the height of the hysteresis loops increases with particle sizes ($d_{53} > d_{63} > d_{125}$),

indicating the YBCO powder size has a strong effect on magnetisation properties. The values of the magnetisation of all powders at 77 K are approximately an order of magnitude lower than that measured at 7 K. The decrease is as expected from the temperature dependence of superconducting electron density, which increases with decreasing temperature (Chapter 3).

Figure 7.23 and Figure 7.24 also show that the magnetisation properties of the d_{38} and d_{53} fractions are not significantly different. This is likely due to the agglomeration of particles in both d_{38} and d_{53} fractions. Agglomeration of particles is likely to allow some weak intergranular current flow across the boundaries between grains through Josephson junctions, as well as intragranular shielding current flow within grains, as explained by Poole *et al.*[26] and Lam *et al.*[27]. In order to effectively investigate variations in the magnetisation values of YBCO with various particle sizes, the YBCO powder needs to be diluted with a non-superconducting material. This is to ensure that particles can no longer interact with each other, so that the signal per unit volume of superconductor could be measured as a function of dilution[28]. For YBCO powder particles, there will be an electrical interaction, and maybe magnetic coupling effect.

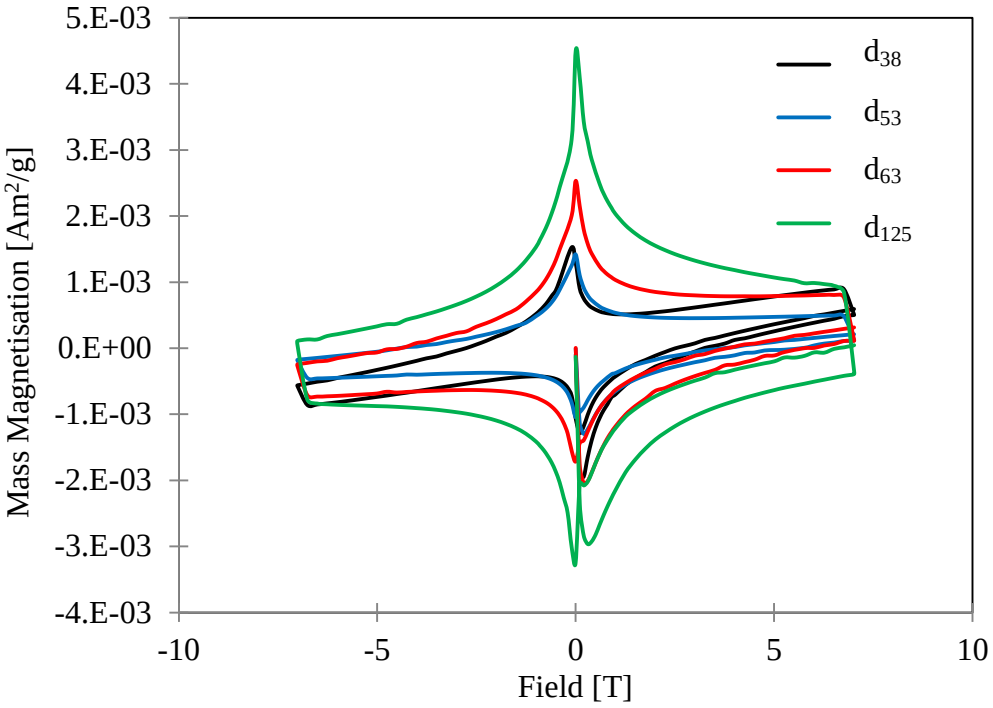


Figure 7.23 Magnetisation properties of melt-grown YBCO powder with various particle sizes at T=7 K.

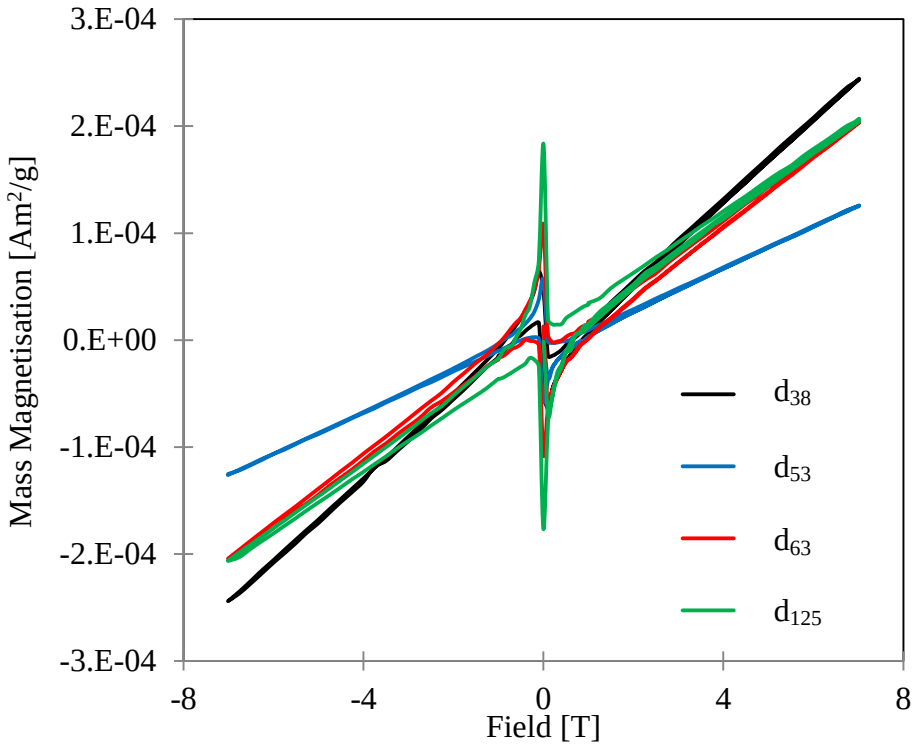


Figure 7.24 Magnetisation properties of melt-grown YBCO powder with various particle sizes at T=77 K.

7.5 Discussion and Conclusions

Since a high transition temperature is the main criterion for powder selection in the study, YBCO powder is a good candidate to be used as superconducting filler. The magnetisation measurements of YBCO powders has shown stronger diamagnetic properties than the BSCCO powder I had available. However, the amplitude of the hysteresis loops has shown that the commercial YBCO powder has considerably poorer diamagnetic properties than the melt processed YBCO powder by order of a factor of 10 (Figure 7.19, Figure 7.20 and Figure 7.21). In order to understand these variations in the magnetic properties of YBCO powders, we must consider the effect of size, morphology, crystallinity and quality of YBCO powder, all of which are affected by the synthesis process.

There are three possible ways in which the synthesis process of YBCO powder can affect the magnetisation properties. I will concentrate mostly on the powder obtained from the TSMG process as this gives the best superconducting performance.

1. Quality of superconducting bulk.

2. Mechanical grinding and ball milling.

3. Annealing.

7.5.1 Selection Process for Melt-Grown YBCO Bulks

YBCO bulks in this work have been proven to have a considerable levitation effect by conducting a simple levitation test between a permanent magnet and fragments of YBCO bulk cooled to 77 K. This indicates that fragments of YBCO bulks gathered from the TSMG process have reasonably strong flux pinning, yielding a good shielding current to expel magnetic field from the crystal. Cardwell *et al.*[20] reported a low critical current density region more than 4 mm from the seed due to growth inhomogeneity in

the YBCO crystals from the TSMG process, and this is where most of the fragments of YBCO bulks used in this study were collected from. Therefore, careful screening of the melt-grown YBCO bulks used in this study was essential for the successful fabrication of HTS composites with good electromagnetic properties.

7.5.2 Effect of Ball milling, Grinding and Sieving Processes on The Magnetisation Properties of YBCO Powder

It has been shown from the XRD analysis in Figure 7.15 that the melt-grown YBCO powder is polycrystalline YBCO-123 with small fraction of YBCO-211 as in the bulk crystal. This proves that grinding and sieving processes have no significant impact on the crystal structure when producing powder from the melt-grown YBCO bulks. It should be noted that it is difficult to qualitatively and quantitatively compare magnetisation properties of YBCO bulks and powders due to differences in sizes, orientations and demagnetisation factors of grains[29]. Nevertheless, the magnetisation properties of YBCO powders with different particle sizes can be qualitatively compared. Figure 7.19, Figure 7.20 and Figure 7.21 show a comparison of magnetisation properties between melt-grown and commercial YBCO powder.

The magnetisation properties of the melt-grown YBCO powder are stronger than the commercial powder by one order of magnitude. The difference of the magnetic properties of these 2 types of YBCO powder can be either due to size and shape or superconducting performance of individual superconducting particles. These effects can be further explained from the magnetisation properties of YBCO powders, which are both shape and size dependent[30]. As discussed previously, the penetration depth in superconducting materials will affect the volume of a particle that is superconducting. Campbell *et al.*[22] reported a consistent reduction of magnetisation of apparently 100%

superconducting YBCO particles as the size/penetration depth ratio decreased. This explains the low magnetisation values I observed from the commercial YBCO powder with particle size below 30 μm. It has been reported that above this size, the susceptibility values are closer or equal to $\mathcal{X} = -1$[22].

Irregular shapes of YBCO particles are another reason for the variation in magnetisation properties. Ball milling and grinding processes contribute to producing variations in the microscopic shapes of YBCO particles. This can be observed from the SEM images of both commercial and melt-grown YBCO in Figure 7.12 and Figure 7.16. This variation in shape has made it difficult to quantitatively compare the magnetisation properties of my YBCO powders. One might overestimate the magnetic properties of YBCO powder by assuming that all particles are spherical. In order to effectively investigate variations in the magnetisation values of YBCO with various particles sizes, the YBCO powder needs to be diluted with a non-superconducting material so that the signal per unit volume of superconductor could be measured as a function of dilution[22]. The mixing rules can then be used to consider the effect of varying size and volume fractions of these superconducting particles in HTS composite materials. This work will be discussed later in Chapter 8, with strong emphasis on melt-grown YBCO powder mixed in a polymer matrix.

Hibbs et al.[24] suggested that a layer of weakly-superconducting or non-superconducting material coating around each particle of superconductor could effect the diamagnetic properties. This layer could be developed from grinding or during storange[24]. This material coating can be in the form of an amorphous layer, and is independent of particle size. This causes the critical current to be low, hence worsening the superconducting properties at the surface of the particles, which affects the magnetisation properties of YBCO powder, especially at higher applied fields. In my

work, no such layer was observed from SEM images of YBCO particles (Figure 7.12 and Figure 7.16). This is agreement with Hibbs *et al.* who only predicted a 1 μm impurity layer coat around YBCO particles from their analysis of the magnetisation curves of YBCO samples with particles ranging from 15 μm to 250 μm, using $M = M_o\left(\frac{4}{3}\pi a^3 - 4\pi d a^2\right)/\frac{4}{3}\pi a^3 = M_o(a-3d)/a$, where M is magnetisation, M_o is applied field, a is the size of particles in radius and d is the thickness of the non-superconducting layer coating around each particle[24]. In practice, a 1 μm layer of coating material may be very difficult to detect without transmission electron microscopy analysis.

The quality of HTS powder can also be degraded by impurities due to reaction with atmospheric CO_2 H_2O and O_2[31,32]. The stability of $BaCO_3$ is a strong driving force for the reaction of YBCO with CO_2, so the effect of long storage can cause loss of the YBCO-123 phase limiting the magnetic properties of YBCO powder. This explains the weak magnetic properties observed for the commercial YBCO powder, and also BSCCO powder which has been stored for more than 10 years since original purchase. The effect of impurity on YBCO particles will be discussed in detail in Chapter 8.

7.5.3 Conclusions

Two types of HTS materials were studied, BSCCO and YBCO, selected for their transition temperatures above 77 K. A precursor BSCCO-2223 powder was sintered as suggested in the literature, but the magnetisation properties were not as good as YBCO. Two types of YBCO materials were studied; a commercial powder and a melt-grown processed YBCO bulk. The commercial YBCO powder needs to be ball-milled to de-agglomerate clusters of particles and the melt-grown YBCO bulk needs to be ground and sieved to control the size of particles. By comparing the magnetic properties, the

melt-grown YBCO powder has an order of magnitude higher magnetisation than the commercial powder.

The use of melt-grown YBCO starting material has proved essential to obtain YBCO powder with controllable particle sizes and good superconducting properties. Table 7.5 summarised the characteristics of HTS powder selected for the fabrication of HTS composites. The successful electromagnetic study of HTS composites in Chapter 8 and 9 demonstrates the importance of choosing superconducting materials with optimised magnetisation properties.

Table 7.5 Characteristic of HTS powder for HTS composites

Powder	$YBa_2Cu_3O_7$ (YBCO-123)
Origin	Melt-grown YBCO
Sieve fraction	$63 < d_{sieve} < 125$
Size of particles, d_{50}	59.2 μm

In order to minimise impurities in YBCO powder, the ball milling process was discontinued. As previously discussed, in order to achieve high magnetisation properties, the size of YBCO particles needs to be above 30 μm, which can easily be achieved by mechanical grinding using a pestle and mortar. Therefore, the ball milling technique was not applied in the powder preparation process from YBCO bulks.

References

1 Maeda, H., Tanaka, Y., Fukutomi, M. & Asano, T. A new high-T_c oxide superconductor without a rare earth element. *Japanese Journal of Applied Physics* **27**, L209-L210 (1988).

2 Larbalestier, D., Gurevich, A., Feldmann, D. M. & Polyanskii, A. High-Tc superconducting materials for electric power applications. *Nature* **414**, 368-377 (2001).

3 Cloots, R., Cardwell, D. A. & Ginley, D. S. *Handbook of Superconducting Materials: Powder processing techniques*. Chapter B2.1, pp. 223-242 (CRC Press, 2003).

4 Cava, R. J. *et al.* Studies of oxygen-deficient $Ba_2YCu_3O_{7-\delta}$ and superconductivity Bi(Pb)SrCaCuO. *Physica C: Superconductivity* **153**, 560-565 (1988).

5 Jiang, C., Yoo, J., Ko, J., Chung, H. & Qiao, G. Optimization of precursor powders for manufacturing Bi-2223/Ag tapes. *Superconductor Science and Technology* **16**, 85 (2003).

6 Hsueh, Y. W., Chang, S. C., Liu, R. S., Woodall, L. & Gerards, M. A comparison of the properties of Bi-2223 precursor powders synthesized by various methods. *Materials Research Bulletin* **36**, 1653-1658 (2001).

7 Tarascon, J. M. *et al.* Preparation, structure, and properties of the superconducting compound series $Bi_2Sr_2Ca_{n-1}Cu_nO_y$ with n=1,2, and 3. *Physical Review B* **38**, 8885-8892 (1988).

8 Biju, A., Aloysius, R. P. & Syamaprasad, U. Enhanced critical current density in Gd-added (Bi, Pb)-2212 bulk superconductor. *Superconductor Science and Technology* **18**, 1454 (2005).

9 Sequeira, A., Rajagopal, H., Sastry, P. V. P. S. S., Yakhmi, J. V. & Iyer, R. M. A neutron diffraction study of the structure of $Bi_{1.6}Pb_{0.4}Ca_1Sr_2Cu_2O_y$. *Physica C: Superconductivity* **173**, 267-273 (1991).

10 Xu, M., Finnemore, D. K., Balachandran, U. & Haldar, P. Intermediate phases produced in growth of $Bi_2Sr_2Ca_2Cu_3O_{10+\delta}$. *Journal of Applied Physics* **78**, 360-363 (1995).

11 Halim, S. A., Khawaldeh, S. A., Mohamed, S. B. & Azhan, H. Superconducting properties of $Bi_{2-x}Pb_xSr_2Ca_2Cu_3Oy$ system derived via sol–gel and solid state routes. *Materials Chemistry and Physics* **61**, 251-259 (1999).

12 Porch, A., Waldram, J. & Cohen, L. Microwave measurements of powdered $YBa_2Cu_3O_{7-\delta}$. *Journal of Physics F: Metal Physics* **18**, 1547 (1988).

13 Cheah, H., Porch, A. & Waldram, J. Microwave conductivity of powdered unaligned $YBa_2Cu_3O_{7-\delta}$. *Physica B: Condensed Matter* **165**, 1195-1196 (1990).

14 Cohen, L., Gray, I., Porch, A. & Waldram, J. Surface impedance measurements of superconducting $YBa_2Cu_3O_{6+x}$. *Journal of Physics F: Metal Physics* **17**, L179-L183 (1987).

15 Shi, Y. *et al.* Synthesis of $YBa_2Cu_3O_{7-\delta}$ and Y_2BaCuO_5 Nanocrystalline Powders for YBCO Superconductors Using Carbon Nanotube Templates. *ACS nano* **6**, 5395-5403 (2012).

16 Wong-Ng, W. *et al.* X-ray powder characterization of $Ba_2YCu_3O_{7-x}$. *Advanced Ceramic Materials; (USA)* **2:3B**, 565-576 (1987).

17 Suryanarayana, C. Mechanical alloying and milling. *Progress in Materials Science* **46**, 1-184 (2001).

18 Dancer, C. *Ceramic processing of magnesium diboride*, Thesis (D.Phil.)-University of Oxford, (2008).

19 Dancer, C., Prabhakaran, D., Crossley, A., Todd, R. & Grovenor, C. The effects of attrition and ball milling on the properties of magnesium diboride. *Superconductor Science and Technology* **23**, 065015 (2010).

20 Cardwell, D. A. Processing and properties of large grain (RE)BCO. *Materials Science and Engineering: B* **53**, 1-10 (1998).

21 Allen, T. *Powder Sampling and Particle Size Determination*. pp. 544-545 (Elsevier Science, 2003).

22 Campbell, A., Blunt, F., Johnson, J. & Freeman, P. Quantitative determination of percentage superconductor in a new compound. *Cryogenics* **31**, 732-737 (1991).

23 Hibbs, A. & Campbell, A. Size effects in the magnetisation of high T_c powders. *Magnetics, IEEE Transactions on* **25**, 2142-2145 (1989).

24 Hibbs, A., Eberhardt, F., Campbell, A. & Male, S. Effect of particle size on the magnetization of high T_c powders. *Cryogenics* **28**, 678-680 (1988).

25 Shimizu, E. & Ito, D. Critical current density obtained from particle-size dependence of magnetization in $YBa_2Cu_3O_{7-\delta}$ powders. *Physical Review B* **39**, 2921 (1989).

26 Poole, C. P., Farach, H. A. & Creswick, R. J. *Superconductivity 2nd Edition*. Vol. 2nd Edition pp. 141-415, (Academic Press, 2007).

27 Lam, Q. H., Kim, Y. & Jeffries, C. D. Nonlinear electrodynamics in granular $YBa_2Cu_3O_7$: Measurements and models of complex permeability. *Physical Review B* **42**, 4846-4849 (1990).

28 Campbell, I., Bourell, D. & Gibson, I. Additive manufacturing: rapid prototyping comes of age. *Rapid Prototyping Journal* **18**, 255-258 (2012).

29 Elschner, S. & Gauss, S. Magnetic properties of melt processed and sintered Y-Ba-Cu-O. *Superconductor Science and Technology* **5**, 300-303 (1992).

30 Edmond, I. & Firth, L. Hysteresis in a high-temperature superconductor. *Journal of Physics: Condensed Matter* **4**, 3813 (1992).

31 Lundy, D., Swartzendruber, L. & Bennett, L. Brief Review of Recent Superconductivity Research at NIST. *Journal of Research of the National Institute of Standards and Technology* **94**, 147-178 (1989).

32 Murphy, D., Johnson, D. W., Jin, S. & Howard, R. Processing techniques for the 93 K superconductor $Ba_2YCu_3O_7$. *Science* **241**, 922-930 (1988).

8 Fabrication of HTS Composites by Casting

8.1 Making HTS Composites 144
8.1.1 Mixing 144
8.1.2 Fabricating a Mould 146
8.2 Distribution of Particles in HTS Composites 148
8.2.1 Dispersion Patterns 149
8.2.2 Effect of Powder Concentration 152
8.3 Effect of Filler 154
8.3.1 Microstructure Studies 155
8.3.2 Magnetic Levitation Tests 160
8.3.3 Static Magnetisation Measurements 161
8.3.4 Microwave Properties 164
8.4 Effect of Volume Loading 169
8.4.1 Microstructure Studies on HTS Composites 171
8.4.2 Quantitative Analysis of Particle Distribution in the HTS Composites . 178
8.4.3 Microwave Properties of HTS Composites 181
8.4.4 Magnetisation Properties 195
8.4.5 Susceptibility of the HTS Composites 198
8.5 Discussion and Conclusions 205
8.5.1 Influence of Sizes and Volume Fraction of YBCO fillers on Microwave Properties of the HTS composites 206
8.5.2 Effect of Casting Technique on Microstructure of HTS Composites 207
8.5.3 Conclusions 208
References 210

The selection process for YBCO as the superconductor filler for my composite materials has been discussed in Chapter 7. I have shown that the processing and characterisation process carried out on melt-grown YBCO can produce powders with a controllable range of particle size distributions and optimised magnetisation properties. The use of melt-grown YBCO starting material has proved suitable to produce HTS composites with useful electric, magnetic and superconducting properties. Not only

does the Meissner effect can lead to a substantial negative susceptibility of HTS composites in a static magnetic field, but the electromagnetic properties also change at the onset of the superconducting state[1]. These changes in the electromagnetic properties were reported to depend on the measurement frequency, temperature and volume fraction of the superconducting filler[1].

The work reported in this chapter was to explore a new and scalable fabrication technique for HTS composites, to optimise the processing conditions, and produce HTS composites with controllable magnetic and superconducting properties. The latter half of the chapter will concentrate on the characterisation of HTS composites by analysing their microstructure and correlate these with their electromagnetic properties.

In this work, two fabrication techniques were investigated; casting and 3-D printing. Each technique requires different procedures and materials preparation. In this chapter, the fabrication of HTS composites by the casting technique will be described in detail, while the use of 3-D printing will be discussed in Chapter 9.

8.1 Making HTS Composites

In this work, there are two main stages involved in producing HTS composites; mixing and preparing appropriate stable and castable mixtures of epoxy resin and HTS powder, and designing and fabricating a mould for the casting.

8.1.1 Mixing

Epoxy resin solution was prepared based on the method discussed in section 6.2.1. HTS composites were prepared by mixing HTS powder into the epoxy resin solution and stirring mechanically until the gel phase was formed. A range of HTS composites were prepared with nominal volume fractions up to a maximum of 51 vol% HTS powder.

Beyond this loading, the mixture became too stiff for mixing into a homogeneous composite. To avoid sedimentation of the powder, the mixtures were stirred carefully until they were almost cured. The mixture was then slowly poured into a mould and left for 24 hours curing at room temperature.

In this work, the two-component epoxy solution was provided by Epo-Kwick from Buehler (refer to Chapter 6, section 6.2.1) unless otherwise stated. Melt-grown $YBa_2Cu_3O_7$ (YBCO-123) powder has been used as the filler for HTS composites, and all the melt-grown YBCO-123 powder was prepared using the method discussed in section 6.1.1 unless otherwise stated. Commercial YBCO powder from Alfa Aesar (with 99.5% purity and -325 mesh sizes) has also been used in the HTS composite fabrication studies for electromagnetic, magnetic and morphology comparison. As stated in Chapter 7, the application of BSCCO-2223 powder as a filler for HTS composite was discontinued due to difficulty in outsourcing the starting material and producing BSCCO-2223 phase with transition temperature of 110 K. However, BSCCO-2223 powder (Merck Ltd ((Pb/Bi)SrCaCuO 2223) was used in the early section of this chapter to study the effect of casting on the HTS composites, in order to gain an understanding of the parameters controlling the casting process. Table 8.1 summarises the HTS powder used in Chapter 8 for the fabrication of the HTS composites.

Table 8.1 Summary of HTS powder used in Chapter 8

HTS powder	Origin	Nominal volume fractions of HTS composite samples [vol%]	Section
BSCCO-2223	Commercial	2, 6	8.2.1
YBCO-123	Commercial	10, 28, 35, 40, 42	8.2.2, 8.3.1, 8.4
	*Melt-grown (Sample 3)	35	8.3.1
	*Melt-grown (Sample 1)	6, 10, 20, 30, 39, 42, 45, 51	8.4
	*Melt-grown (Sample 4)	5, 9, 20, 39,43	8.4

**Each sample originated from one off-cut fragment of single grain YBCO-123.*

Melt-grown HTS composites (MG HTS) from Sample 4 were prepared to check the reproducibility of HTS composites by casting. The measured microwave properties were within calibration errors of pure epoxy at 0.1% and 1.4% for ε_{eff} and 1.4% and 6.0% for μ_{eff} at room temperature and 77 K respectively, but microstructure analysis only focussed on the MG HTS composites from sample 1 in section 8.4.

8.1.2 Fabricating a Mould

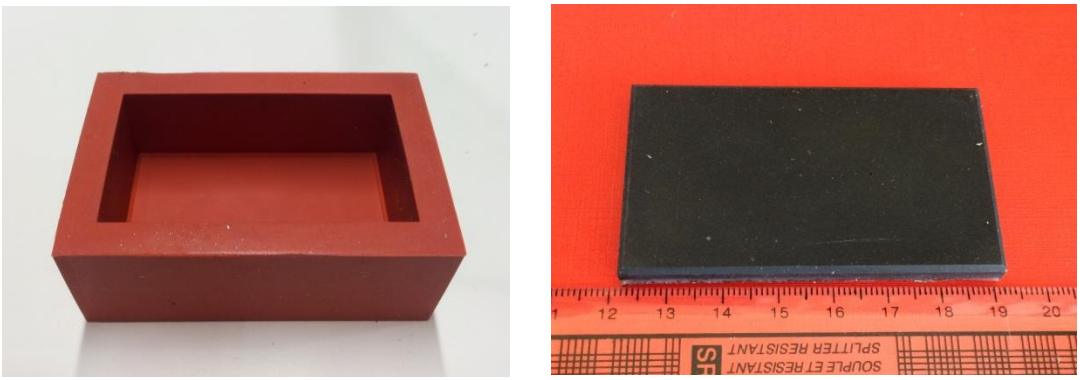
The choice of mould plays an important role in the fabrication of high quality HTS composites. A mould was chosen based on the following criteria:

1. Materials flexibility for the de-casting process.
2. Ability to form a uniform and flat surface in the HTS composites.
3. To produce HTS composites with thickness close to 1 mm to be suitable for microwave testing by the waveguide technique described below.

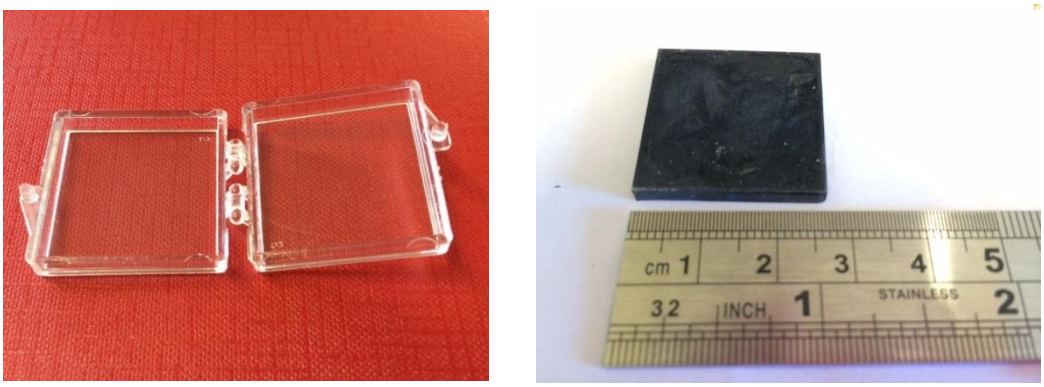
Several moulds were used in this study, purchased from a variety of suppliers. Rubber and plastic based moulds were used in my first attempt to produce HTS composites (Figure 8.1). The flexibility and elastic properties of the rubber moulds make the de-casting process of HTS composites easier, but these moulds required a large volume of YBCO powder and epoxy mixture to produce the desired thickness of HTS composites, which consumed a lot of source material. Unlike the rubber mould, a plastic mould only requires a relatively small amount of YBCO powder and epoxy mixture, and I found that the cast HTS composites could be easily controlled to the required thickness. In the early stages of this project, plastic moulds were used to produce HTS composite samples for studying effect of HTS filler distribution in HTS composites. However, the hard plastic mould made the de-casting process difficult, making the plastic mould unsuitable for this laboratory scale study.

Based on these observations, I designed a custom made polytetrafuloroethelene (PTFE) jig to cast 9 units of HTS composites at a time, as shown in Figure 8.1 (c). The jig consists of a 1 mm thick mould, a substrate block and an aluminium frame which was fabricated by the Photofabrication Unit in the Physics Department to my design. All parts are aligned and assembled by nuts and screws, preventing leakage of the polymer solution around the jig.

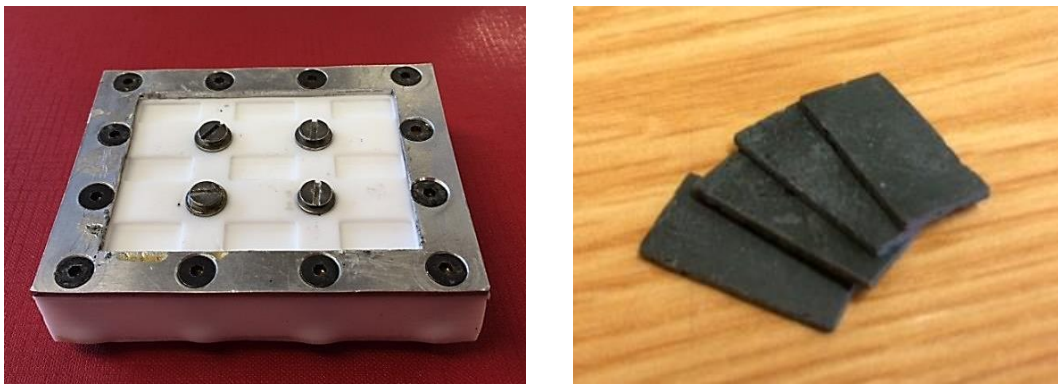
During the curing process, a small amount of the epoxy resin solution may leak underneath the PTFE mould, reducing the amount of epoxy resin mixture for curing. To ensure the thickness for all samples is consistently 1 mm, all cured samples were deliberately fabricated with thickness above 1 mm and were ground and polished before the VNA measurements. However, in the case of HTS composites, the leakage of epoxy resin solution might affect the homogeneity of the particle distribution in the epoxy. In addition, the leakage might affect the volume fractions of epoxy solution, leading to inaccuracy in HTS particle volume fractions in the HTS composites. In order to investigate the efficiency of the PTFE mould on the distribution and volume fraction of the HTS particles, the actual volume fractions of HTS powder incorporated into the HTS composites have been analysed. Study has shown that X-ray computer tomography technique can do volume fraction measurement, which is not available to me. Therefore, the best way to quantify YBCO loadings in the HTS samples is the measured area fraction by calculating the area fraction of HTS particles using SEM and ImageJ software. The method will be discussed in detail in section 8.4.1.



(a) Rubber mould 70 x 40 mm (Kemet International Ltd)



(b) Plastic mould 25 mm x 25 mm



(c) PTFE jig

Figure 8.1 A variety of moulds were used for casting of superconducting composites. (a) Rubber moulds produce HTS composites with size 69.0 x 39.7 mm. (b) Plastic moulds produces HTS composites with size 26.6 x 26.6 mm. (c) A custom -made 9 hole PTFE mould produces HTS composites with size 15.8 x 7.9 mm designed to fit directly into the waveguide assembly.

8.2 Distribution of Particles in HTS Composites

The effect of casting on the HTS composites has been studied in order to gain an understanding of the parameters controlling the fabrication process. This dispersion

study is likely to give us an idea of the uniformity of the casting process, which is important for interpreting the microwave analysis data. In order to achieve homogeneous properties, it is important to ensure that particles are well-dispersed and uniformly distributed in the epoxy matrix.

8.2.1 Dispersion Patterns

The particle distribution study was carried out using HTS composites of BSCCO loaded epoxy. This study was conducted to observe scattering and morphology of particles in epoxy using the casting technique. The study was conducted using BSCCO powder before the decision to concentrate on YBCO powder as a filler. BSCCO powder with a median distribution, $d_{50} = 35.9\,\mu m$, was mixed with epoxy and cured in plastic moulds, resulting in square blocks of thickness 3 mm so that particle distribution pattern can be observed is a wide range of cross sections of the HTS composites (Figure 8.2). HTS composites were thinly sliced into films with thicknesses 1 - 2 μm using a microtome, allowing for morphology observations under transmitted light optical microscopy.

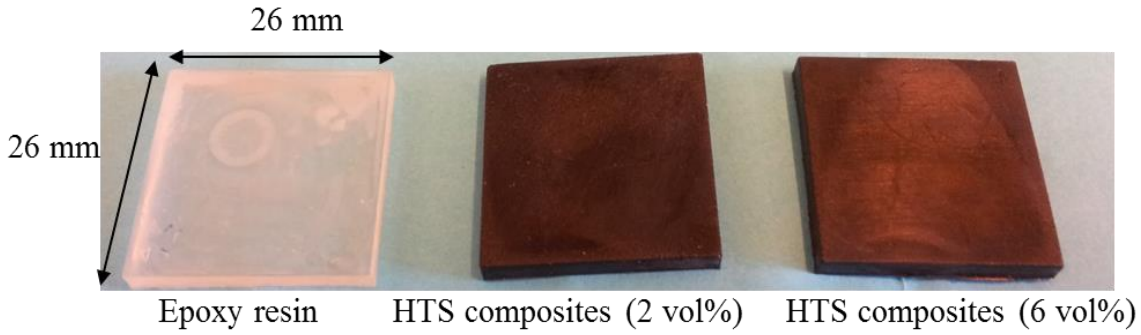


Figure 8.2 Epoxy and HTS composites with nominal volume fractions of 2 vol% and 6 vol% cured in plastic moulds.

Figure 8.3 shows cross sections of HTS composites with nominal volume fractions of 2 vol% and 6 vol%. Both HTS composites have a random dispersion of particle distribution across the cross sections. A high density of small particles can be seen to

cover the entire matrix, indicating that the mixing technique gave a reasonably homogeneous distribution of the BSCCO powder in the epoxy. However, a lower density of relatively larger particles is also present. These large particles are identified as irregular-shaped features from the cross section images. A larger number of these large particles can be seen in the HTS composite containing a higher HTS volume fraction (6 vol%). This also may be indicative that the concentration of these large particles increases with increasing depth of the HTS composite. A large number of them can be seen distributed in specific areas due to sedimentation of large particles to the bottom of the mould.

These irregular-shaped features are identified as agglomeration of particles, which can be clearly seen in higher magnification optical images in Figure 8.4. Powder agglomerations are likely to be developed initially during the powder preparation process, held together by weak forces such as van-der-Waals or static charges during the grinding and sieving process[2], as previously described in the powder preparation process (Chapter 7).

In addition, a few holes (indicated by arrows) can also be identified from the cross section of images in Figure 8.3. These holes may be air gaps developed during the curing process due to entrapped air, but might also be induced from the pull-out of particles during the microtome process. Holes induced by air gaps are likely to be round in shape and those induced from the pull out particles are to be more irregular in shape based on the shape of the particles in Figure 8.3 and Figure 8.4. For this reason, studies were conducted to understand ways to avoid the development of agglomerates and air gaps in the HTS composite, especially at higher concentrations of HTS powder in the epoxy.

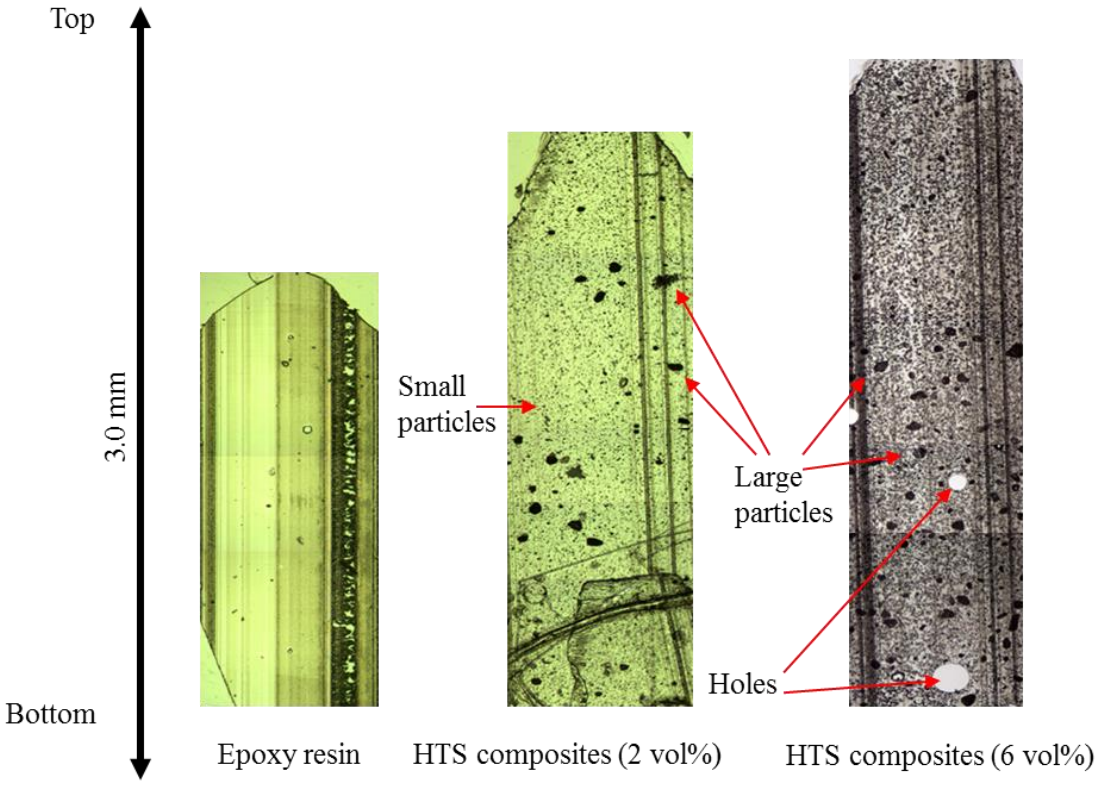


Figure 8.3 Microtomed images of HTS composites. The cross section images show a cross section of randomly dispersed BSCCO powder in an epoxy matrix. Images were taken at 10X magnification. The images were vertically arranged to show patterns of particles from the top to the bottom surface of the plastic mould.

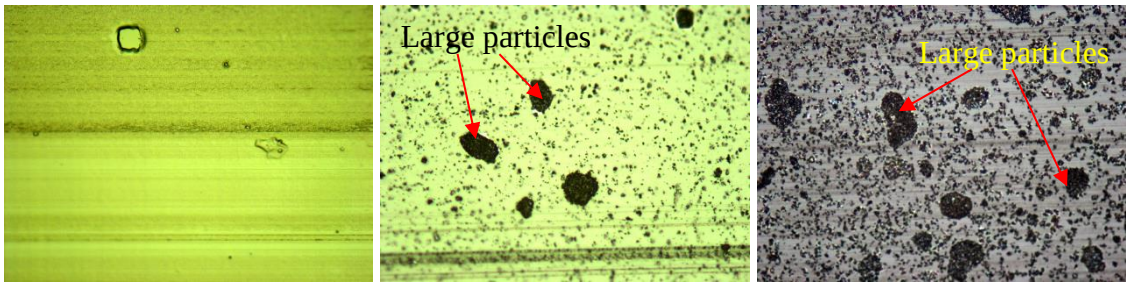


Figure 8.4 The cross section of BSCCO loaded epoxy taken from the middle area of the cross section at 20X magnification.

Due to improved magnetisation properties, the next study was conducted using commercial YBCO powder as a filler in the HTS composite. It should be noted that the powder morphology is very different in BSCCO and YBCO, thus, the powders are expected to behave differently in both mixing and agglomeration. The difference of these HTS powders will be discussed in section 8.5.

8.2.2 Effect of Powder Concentration

In order to understand the effect of powder concentrations on the fabrication of HTS composites, samples were prepared with nominal powder volume fractions of 10%, 28% and 40%. This study was carried out using the commercial YBCO powder with median diameter, d_{50}, of 4.5 μm. The commercial YBCO powder was mixed with epoxy and cured in plastic moulds to produce block samples of size 26 mm x 26 mm x 3 mm. These HTS composites were thinly sliced into films with thicknesses 1 - 2 μm using a microtome.

Figure 8.5 shows the microtomed surfaces of HTS composites with nominal HTS volume fractions of 10%, 28% and 40%. Typically two features can be observed in these HTS composites. A mixture of irregular-shaped features can be seen randomly distributed in the epoxy matrix at all concentrations and a high density of small features can be seen to cover the entire epoxy matrix in the 28 vol% and 40 vol% HTS composites. A high density of holes can also be seen in these higher concentration HTS samples. In contrast to the 28 vol% and 40 vol% samples, the 10 vol% sample is not covered in small particles. Furthermore, only a small number of holes can be seen in this sample.

As described earlier, the irregular-shaped features are identified as agglomerates of particles. These agglomerates can be seen clearly from the optical images of the HTS composites, especially in the 10 vol% HTS composite in Figure 8.5 (b). The number of agglomerates is higher in these high concentration samples than those observed at lower concentrations (Figure 8.4), indicating the dependence of agglomerates on volume loading of particles. However, there are no significant differences in density or size of the agglomerates observed within these higher concentration HTS composites.

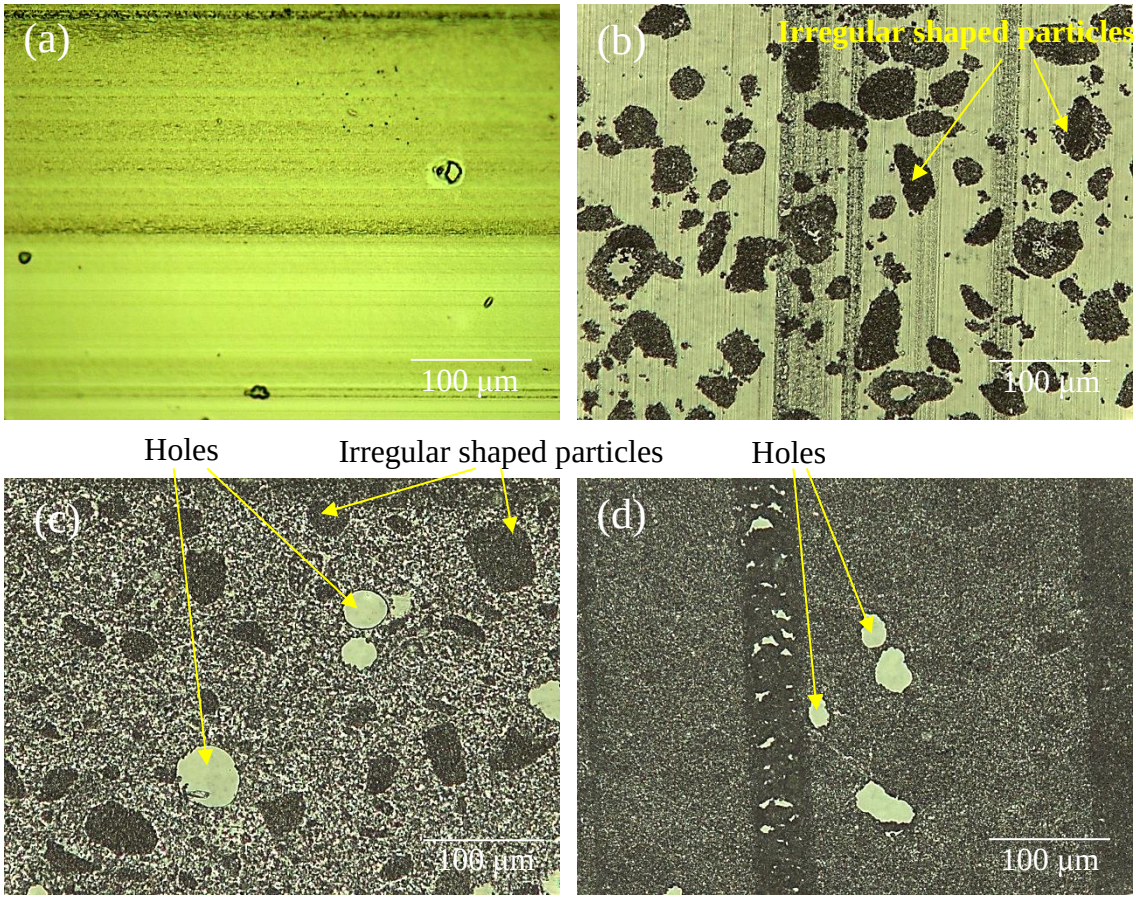


Figure 8.5 Microtomed surfaces of the HTS composites with nominal volume fractions; (a) Reference, (b) 10%, (c) 28% and (d) 40% taken at 20X magnification. The images are arranged to indicate HTS particle dispersion in the epoxy matrix.

The number of holes is also higher in these high concentration HTS composites, indicating the dependence of hole development on the concentrations of particles. Landel *et al.* suggest mixing or mill rolling to break up agglomerates to get a good dispersion of powder to reduce the amount of entrapped air in a composite[3]. This is in contrast with Pietsch who postulates that the mixing process itself has a tendency to develop agglomerates, especially for a small particle size powder which leads to entrapped air in composites[4]. I find that the simple mixing method is practical for low concentrations of HTS composites but problems arise when mixing high concentration HTS composites, where the HTS mixture with higher loading of YBCO powder became too stiff for mixing into a homogeneous composite. The difficulty in mixing resulted in

the distribution and development of agglomerates and holes in the HTS composites above 10 vol% volume fraction.

The casting technique has been shown to produce HTS composites with reasonably good YBCO particle dispersions at all volume fractions. The mixing process is, however, partially responsible for the development of agglomerates and holes. Composites with both agglomerates and holes have a tendency to break fairly easy compared to those with dispersed particles[3]. The effects of the casting process on the fabrication of the HTS composites are discussed in more detail in Section 8.5.

8.3 Effect of Filler

The effect of casting on the electromagnetic and static magnetisation properties of the HTS composites has been investigated using VNA and SQUID measurements respectively. HTS samples were prepared with nominal HTS volume fractions of 35% in the same way as described in section 8.2.2. The nominal volume fraction was made to aid comparison with the fabrication of HTS powder-polymer of other research groups[1,5,6]. Two types of superconducting filler were used in the study; commercial powder (d_{50}= 4.5 μm) and melt-grown YBCO powder. Melt-grown YBCO powder was prepared from a fragment of a melt-grown YBCO bulk, where this bulk was ground and passed through a sieve of size 125 μm-mesh to produce melt-grown YBCO powder of particle size distributions from 0.7 μm to 182.0 μm with the highest particle distribution at 52.5 μm and d_{50}=40.7 μm. The curing process was carried out using the plastic mould to produce blocks of HTS composites with size 26 cm x 26 cm x 3 mm. The blocks were cut and trimmed into thickness of 1 mm and dimensions of 15.8 x 7.9 mm so that the sample can fit into the waveguide for microwave measurements using the VNA (see Figure 8.6). HTS composites also were thinly sliced into films with thicknesses 1 - 2 μm

using a microtome to allow for morphology observations under transmitted light optical microscopy.

Based on the results in Chapter 7, the HTS composites with commercial YBCO powder as filler would not show significant changes of the electromagnetic properties as the magnetic signals are too weak. However, in this study commercial HTS composites were fabricated for microstructural comparison.

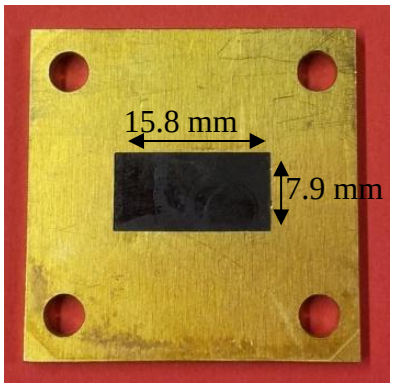


Figure 8.6 A typical 1 mm thick HTS composite fitting completely into the 1 mm sample holder for waveguide measurements using VNA.

8.3.1 Microstructure Studies

The microstructure study was carried out using commercial YBCO powder loaded epoxy composites (CM HTS) and melt-grown YBCO powder loaded epoxy composites (MG HTS) with nominal volume fractions of 35%. Both CM HTS and MG HTS samples were sliced into film of 1 mm thickness using a microtome. Both optical and scanning electron microscopy was carried out on the HTS films for microstructure analysis.

Figure 8.7 shows microtomed images of both CM HTS and MG HTS of 35 vol% loading. The CM HTS sample can be observed to contain a high density of small particles covering the entire epoxy matrix, and a low density of large irregular-shaped particles, Figure 8.7 (a). These features are similar to those described in the CM HTS

composites of 28 vol% and 40 vol% loading in section 8.2.2. The distribution pattern of particles in the MG HTS sample are similar to those described for the CM HTS in some respects, but there are some striking differences. In contrast to the CM HTS sample, the MG HTS sample does not contain small particles, but larger features can be observed with random dispersion, as can be seen in the optical image of Figure 8.7 (b). These large features are more angular in shape with sharper edges than those observed in the CM HTS sample. The optical images, however, do not give much detail about the morphology of the YBCO fillers in the epoxy matrix. Therefore, SEM images were taken to observe shapes and structures of these features in detail. This technique has also been used by Golosovsky *et al.* to observe the morphology of YBCO loaded polymer composites for microwave applications[5].

Figure 8.8 shows SEM images of the CM HTS film taken at various magnifications. The sample has agglomerates of smaller particles covering the entire epoxy matrix. The irregular-shaped features, seen previously in the optical image, can be seen to consist of a high density of small particles in the higher magnification SEM images. Holes can be seen with diameter estimated to be less than 50 μm in Figure 8.8 (a). As previously described, the MG HTS sample was observed to contain no small particles. A substrate layer of epoxy matrix can be seen clearly in Figure 8.9 (a). SEM images show that the melt-grown YBCO filler has irregular shaped particles with relatively larger size and sharper edges than those observed in the commercial YBCO filler. These particles clustered and formed angularly shaped agglomerates, as can be seen in the high magnification SEM images in Figure 8.9. The diameter of these MG HTS particles can be observed to be smaller than 10 μm, which is likely to be the reason of particles agglomerations in epoxy. This is consistent with Golosovsky *et al.* who also described large loose aggregates of irregularly shaped YBCO particles of diameter 20 μm in their

YBCO/PMMA composite samples[5]. Unlike the CM HTS sample, the MG HTS sample is observed to have holes and fractures due to imperfections created during the microtoming process. The larger particle size and hardness of the melt-grown YBCO powder might have caused difficulty in slicing the MG HTS composite into a film using the microtome, hence the deterioration of sample surface for imaging.

Overall, both HTS samples are observed to contain agglomerates of YBCO particles. It has been shown that the CM HTS film has a higher density of agglomerates embedded in the epoxy matrix than the MG HTS film (Figure 8.7). This is likely due to the size of small CM YBCO particles which are in the μm range after the ball milling process. It has been indicated in Chapter 7 that the CM YBCO particles were ball milled for 20 hours to breakdown clusters of agglomerates. Agglomerates in the MG HTS composite are larger and more angular in shape than in the CM HTS. The angular shape of MG YBCO filler is as expected from the source MG YBCO powder but the size is slightly smaller than observed in Figure 7.16 in Chapter 7. This is due to the sieving process, which was only done through the 125 μm-mesh size, giving the highest particle distribution at 52.5 μm, instead of 104.7 μm when using both 63 μm and 125 μm-mesh size sieves as reported in Chapter 7.

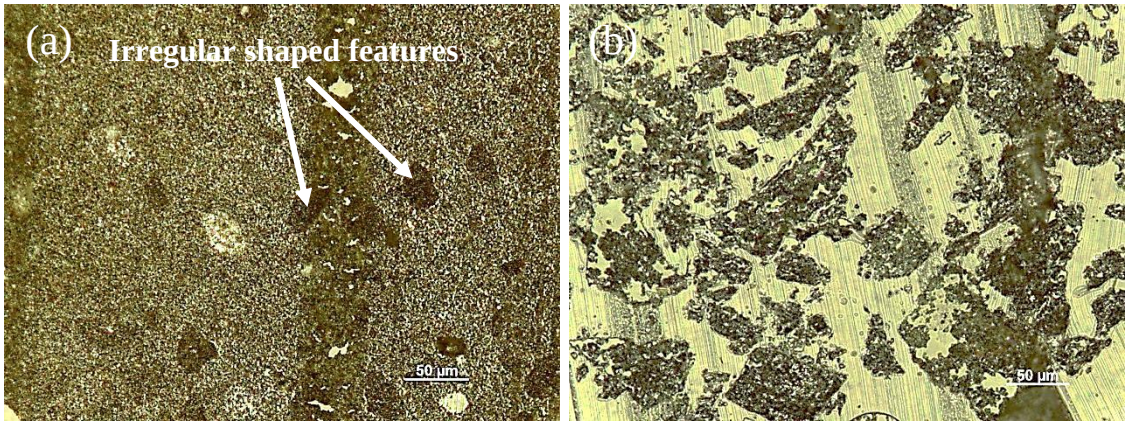


Figure 8.7 Optical images of microtomed surfaces of HTS composites with nominal volume fractions of 35% (a) commercial YBCO powder with d_{50}=4.5 μm, (b) melt-grown YBCO powder with d_{50}=40.7 μm taken at 20X magnification.

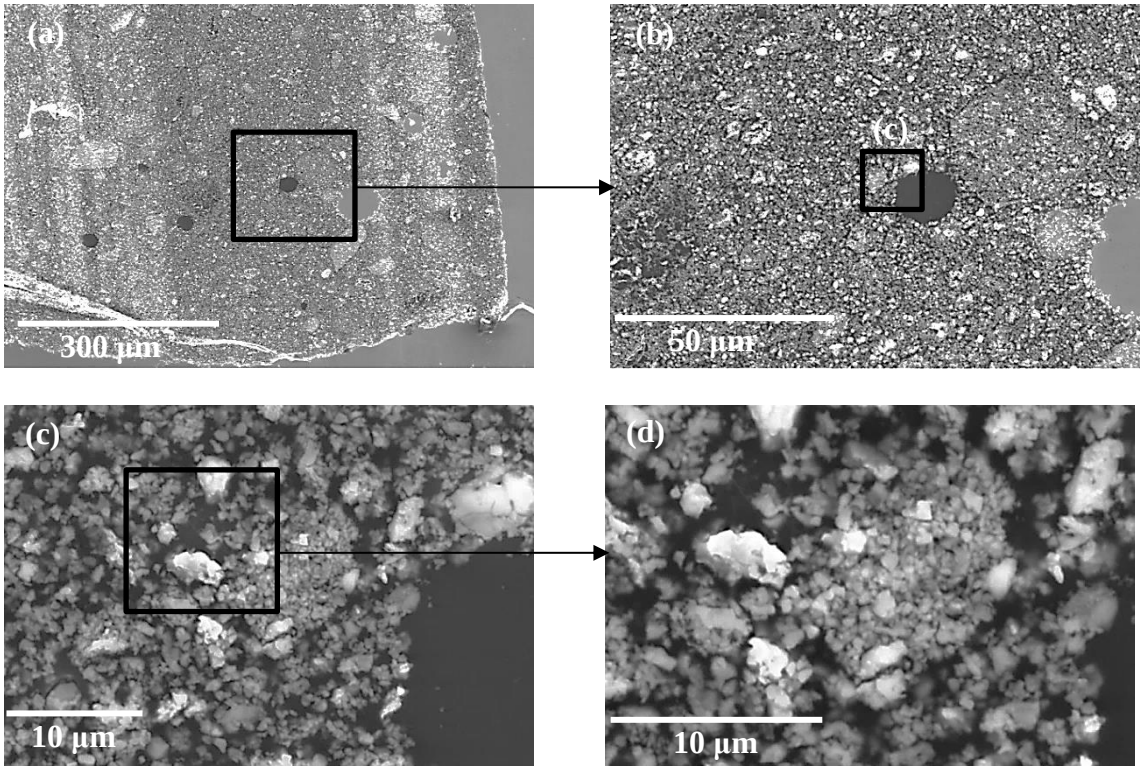


Figure 8.8 SEM images of HTS composites with commercial YBCO powder as a superconducting filler.

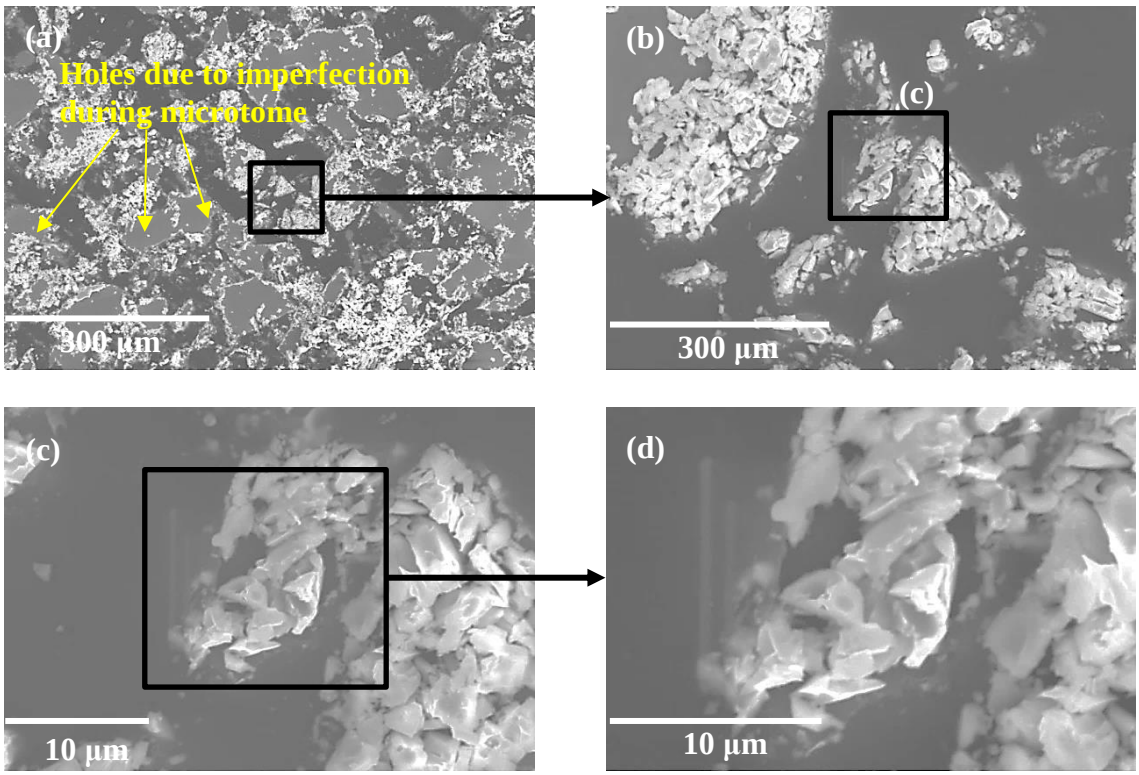


Figure 8.9 SEM images of HTS composites with melt growth YBCO powder as the superconducting filler.

Both samples show poor connectivity of YBCO particles which might affect the microwave properties because there is no continuous superconducting phase. This can be seen from the epoxy layer between clustered particles in the SEM images (Figure 8.8 and Figure 8.9). The connectivity of YBCO particles in HTS composites was tested by measuring the resistivity of these HTS composites using the 4-point probe technique. The measurement was conducted by passing known current through the material, then measuring the potential difference between points a known distance apart[7]. The calculation of resistivity was made by considering the specimen size and shape of the sample using equation (8.1),

$$\rho = R_S \frac{A}{L} \tag{8.1}$$

where $R_S = V/I$ is the resistivity of the materials (V is the potential difference at a known distance and I is the current, A is the cross-sectional area of the sample and L is the known distance of the measured sample length). The resistivity measurement was carried out using a resistivity test rig, A. & M. Fell Ltd. SER 022/09 4-point probe, with maximum voltage indication of 100 mV, where the current was supplied by a power supply and potential difference was detected using a multimeter. A Thurlby PL 154 bench power supply was used to provide current as low as 1 mA with the voltage response detected using Keithley 2000 Multimeter. The resistivity of both CM HTS and MG HTS samples ($A = 0.0079\,m$ and $L = 0.001\,m$) were tested at room temperature, but no current could be passed through either sample in a 4-point probe test. This shows the resistivity of these materials is more than 8 x $10^5\ \Omega\ cm$.

Another factor that might effect on the properties of the HTS composites is the development of holes as described by Landel *et al.*[3]. The development of holes in the HTS composites is expected in the mixing and casting processes especially for high concentration HTS composites. Further investigations of the effect of the morphology

of HTS composites on the microwave and magnetic properties will be discussed in Section 8.5.

8.3.2 Magnetic Levitation Tests

In order to investigate the effect of particle distribution on the superconducting properties of the HTS composites, a simple levitation test was used on the CM and MG HTS samples. The test was conducted by observing the levitation effect of HTS composites with a small magnet. Samples were firstly immersed in liquid nitrogen, and a magnet was placed on the top of HTS samples.

The magnet floatation effect can be observed for an MG HTS composite in Figure 8.10. This indicates a diamagnetic effect of these composites at low temperature, which leads to a sufficiently strong magnetic levitation effect to support the magnet until the liquid nitrogen evaporates. This phenomenon occurs due to the levitation effect from the Meissner expulsion of flux at 77 K, and the fact that it levitates in a stable manner is a result of flux pinning[8]. This levitation test on the HTS composites proves that 'bulk' superconducting properties are preserved in the HTS composites. It is also should be noted from Figure 8.7 (b) and Figure 8.9 that, even though the YBCO particles create no clear d.c. current path through the insulating matrix at room temperature, a reasonable levitation force can be observed. This is proven when no current could be passed through the sample in a 4 point probe test on the HTS composites at room temperature. According to Bhadrakumari *et al.,* the shielding current loops which contribute to the levitation forces are localised in individual grains and not between grains[9], which explains why the isolation of superconducting particles has no effect on the diamagnetic properties of the HTS composites[10]. The CM HTS composites do not, however, show the same levitation effect on the magnet. This is due to the weak magnetisation properties of the commercial YBCO powder as described in Chapter 7.



Figure 8.10 Levitation of a magnet on the melt-grown YBCO loaded HTS composite with a nominal volume fraction of 35 vol%.

8.3.3 Static Magnetisation Measurements

Magnetisation studies have been conducted on both CM and MG HTS composites using a SQUID magnetometer in a magnetic property measurement system (MPMS). The HTS samples were prepared using the method discussed in section 6.4. For comparison purposes the source powder of those YBCO fillers was also measured. All magnetisation measurements were normalised by sample mass.

The critical temperature and magnetisation properties per unit mass of the CM and MG HTS composites are compared with their source powders in Figure 8.11. Both CM and MG HTS composites can be observed to have a negative magnetisation at 93 K. This indicates that the transition temperatures of both HTS composites are similar to those of their source powders. However, the magnetisations of both CM HTS composites and powder have broader transitions, suggesting less uniform distribution of T_c in YBCO particles. Both HTS composites can also be observed to have weaker magnetisation signals than their source powders, as expected for 35 vol% loading of YBCO powder in the HTS composites. The negative magnetisation values in the MG HTS composite are

larger than the CM HTS composite, as can be seen in Figure 8.11. This can also be seen in the magnetic hysteresis loops in Figure 8.12 and Figure 8.13.

Both figures show the diamagnetic properties of the HTS composite at 2 K and 77 K. Typically, HTS composites at 77 K can be observed with hysteresis loops smaller than that observed at 2 K, showing the expected temperature dependence of the magnetisation properties of the HTS composites. This has also been demonstrated by Senoussi *et al.*[11] who shows the magnitude of the hysteresis loop of $YBa_2Cu_3O_7$ samples dropped with increasing temperatures. Results also show that the magnetisation signals from the MG HTS composite are one order of magnitude larger than the CM HTS composite, owing to the strong magnetisation properties of the MG HTS powder. The MG HTS composite can be observed to have typical irreversible hysteresis loops at both 2 K and 77 K. However, the CM HTS composite shows the reversible loop at 77 K, whereas at 2 K there is an irreversible loop caused by flux pinning.

Overall, the MG HTS composite produce a larger diamagnetic magnetisation than the CM HTS at the same nominal volume fraction. This is consistent with the magnet levitation effect which cannot be observed for the CM HTS composite (Section 8.3.2). The differences in magnetisation properties of the CM and MG HTS composites are likely to be due to several reasons. One of the most obvious reasons is the size of YBCO filler, which differs by an order of magnitude, so an increased area of current loops is induced in the larger powder particles. The effects of particle size on the magnetisation properties of YBCO powder were discussed in Chapter 7.

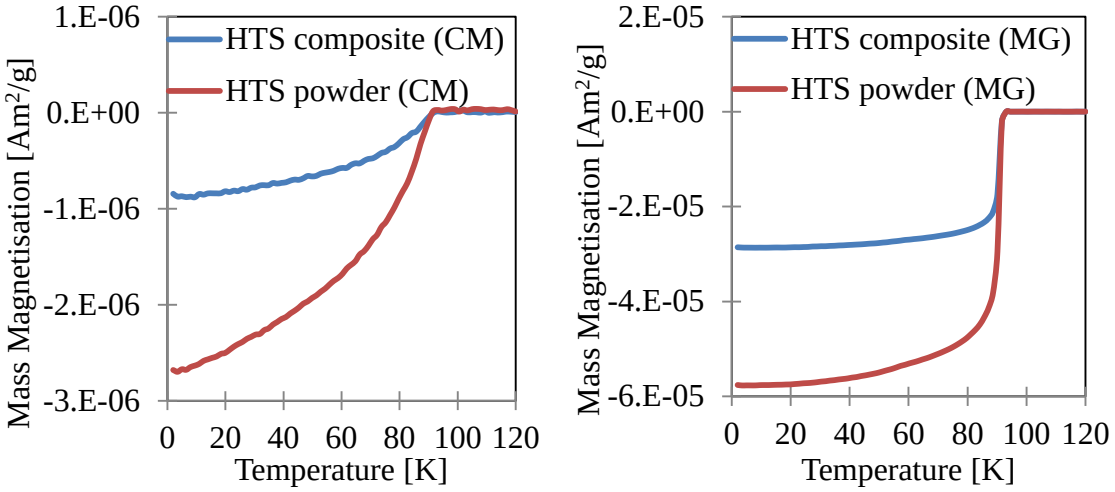


Figure 8.11 The magnetisation of HTS composites from which the T_c value can be seen to be 93 K; CM YBCO filler (CM) (left) and MG YBCO filler (MG).

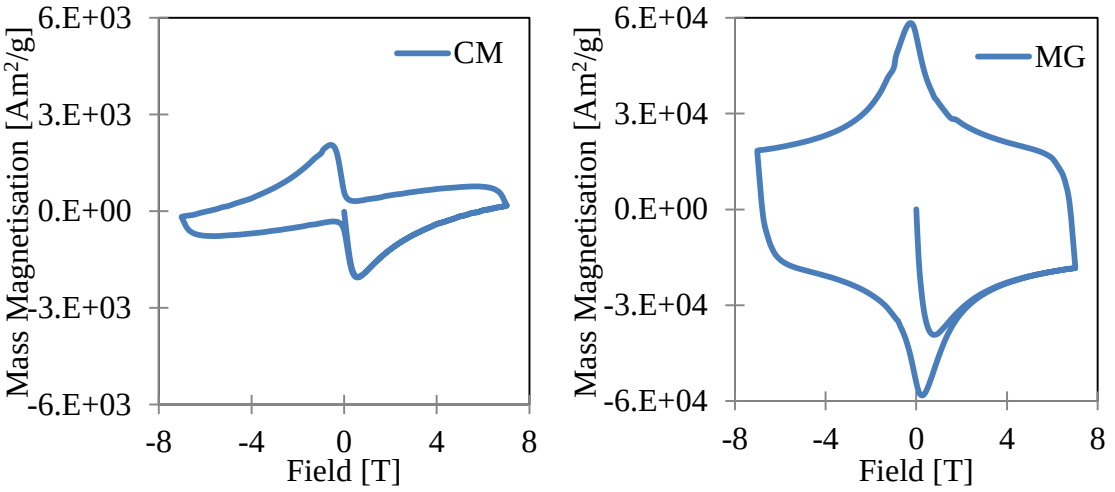


Figure 8.12 The hysteresis loops of the HTS composites measured at 2 K. Note the change of scale.

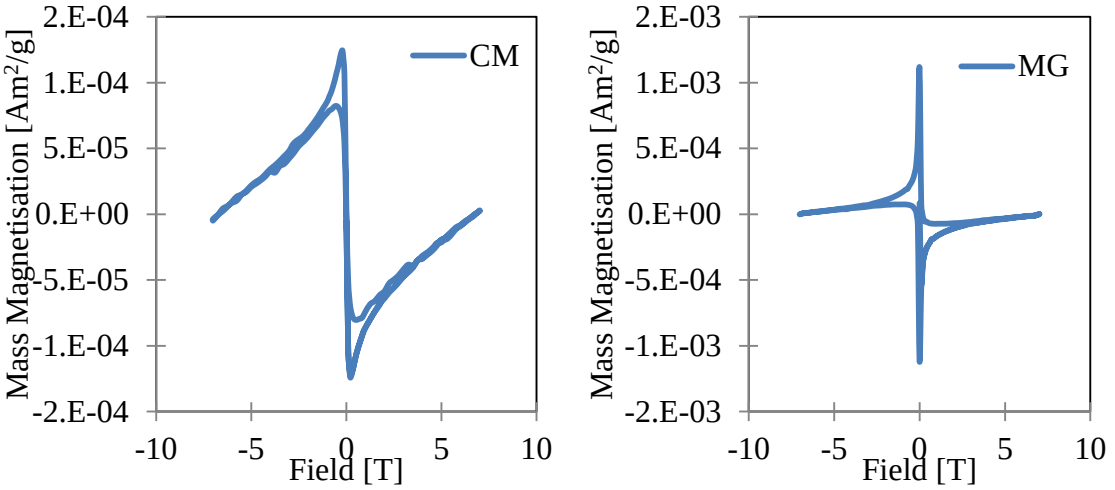


Figure 8.13 The hysteresis loops of the HTS composites measured at 77 K. Note the change of scale.

8.3.4 Microwave Properties

Studies on the effective dielectric constant (ε_{eff}) and magnetic permeability (μ_{eff}) values were carried out by measuring S_{11} and S_{21} of my HTS composites at both room temperature and 77 K using the Vector Network Analyzer (VNA). The ε_{eff} and μ_{eff} values are derived from the S_{11} and S_{21} values using the NRW equation[12] as described in Chapter 6. The S_{11} and S_{21} values at 77 K were measured by immersing the waveguide in liquid nitrogen. In order to provide an understanding of material responses at various frequencies, the ε_{eff} and μ_{eff} values were measured over the frequency range 12 GHz to 18 GHz.

8.3.4.1 Effective Dielectric Constant (ε_{eff})

Figure 8.14 shows the ε_{eff} values of the epoxy matrix and 35 vol% HTS composites of both CM and MG from 12 to 18 GHz at room temperature (red lines) and 77 K (blue lines). All results show the real part of the dielectric constant. The ε_{eff} values for the CM HTS composite are 18.6 at both room temperature and 77 K and the MG HTS composites are 20.4 and 20.0 at room temperature and 77 K respectively, showing the temperature independence of the ε_{eff} values. These increases in the ε_{eff} values (compared to the ε_{eff} values measured for the epoxy matrix) are due to the superconducting filler.

The ε_{eff} values are reasonably consistent from 12 GHz to 18 GHz for all samples. However, unlike the smooth lines measured for the epoxy matrix, the ε_{eff} values of the HTS composites are rather noisy especially at low temperature. The same inconsistent behaviour of the ε_{eff} values of the CM HTS composite can also be observed in the μ_{eff} measurements in section 8.3.4.2.

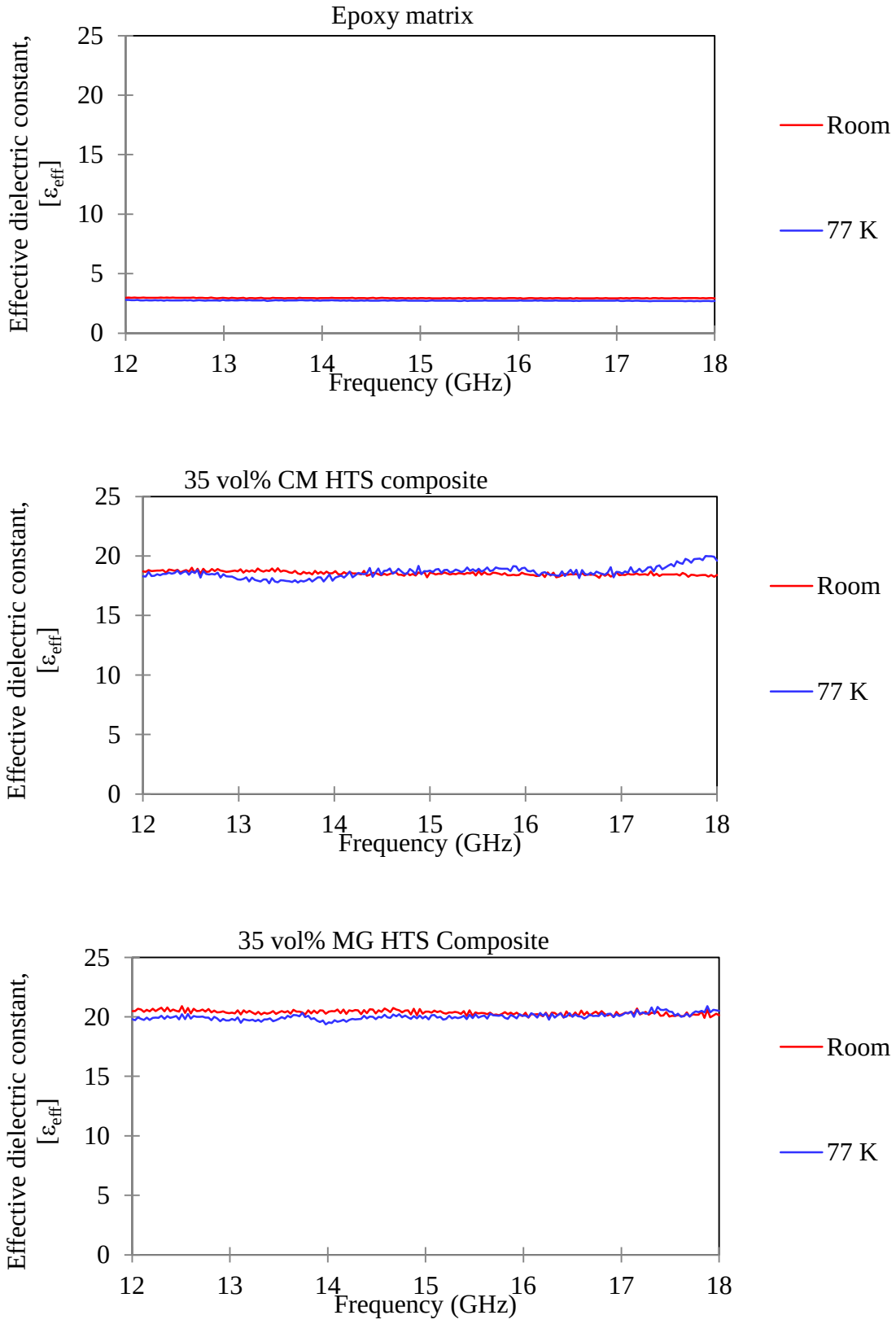


Figure 8.14 The dielectric properties (ε_{eff}) of the HTS composites from 12 GHz to 18 GHz. (Top) Epoxy; (Centre) 35 vol% CM HTS composite and (Bottom) 35 vol% MG HTS composite. Note that the dielectric constant of the epoxy is 2.95 and 2.74 at room temperature and 77 K respectively.

8.3.4.2 Effective Magnetic Permeability (μ_{eff})

Figure 8.15 shows the μ_{eff} values of the epoxy matrix and 35 vol% HTS composites of CM and MG YBCO from 12 to 18 GHz at room temperature (red lines) and 77 K (blue lines). As expected, all the μ_{eff} values are close to 1 in all samples at room temperature due to the non-magnetic properties of both materials at this temperature. For the pure epoxy sample μ_{eff} remained the same at 77 K. However, the μ_{eff} value decreased by ~ 41% for the MG HTS composite at 77 K (Figure 8.15 (bottom panel)). This is in good agreement with the SQUID data presented in 8.3.3 where the YBCO particles become superconducting below a transition temperature of 93 K. As described by Hale *et al.*, large superconducting particles can affect the μ_{eff} values of composites at 77 K[13]. The larger YBCO particles have stronger diamagnetic properties because the effect of the penetration depth on large particles are smaller compared to those on smaller YBCO particles[14] as discussed in Chapter 4. This explains why the change in μ_{eff} of 77 K is very small in the 35 vol% CM composite which contains small YBCO particles, Figure 8.15 (middle).

8.3.4.3 The Refractive Index (n)

In this work, the *n* value of the 35 vol% HTS composites is calculated from ε_{eff} and μ_{eff} values (derived from S_{11} and S_{21} values using NRW equation) using equation 2.2 ($n = \pm\sqrt{\varepsilon_{eff}\mu_{eff}}$) as described in Chapter 2. Figure 8.16 shows the *n* values of the epoxy matrix and HTS composites. There are no significant differences of the n values of either CM or MG HTS composites at room temperature, 4.6 and 4.5 respectively. However, the n value of the MG HTS composite decreases by 23% at 77 K. This decrease in n is due to the decrease in μ_{eff} at 77 K, shown in Figure 8.15. This is in good agreement with the n values reported for a 38 vol% YBCO/PMMA composite by

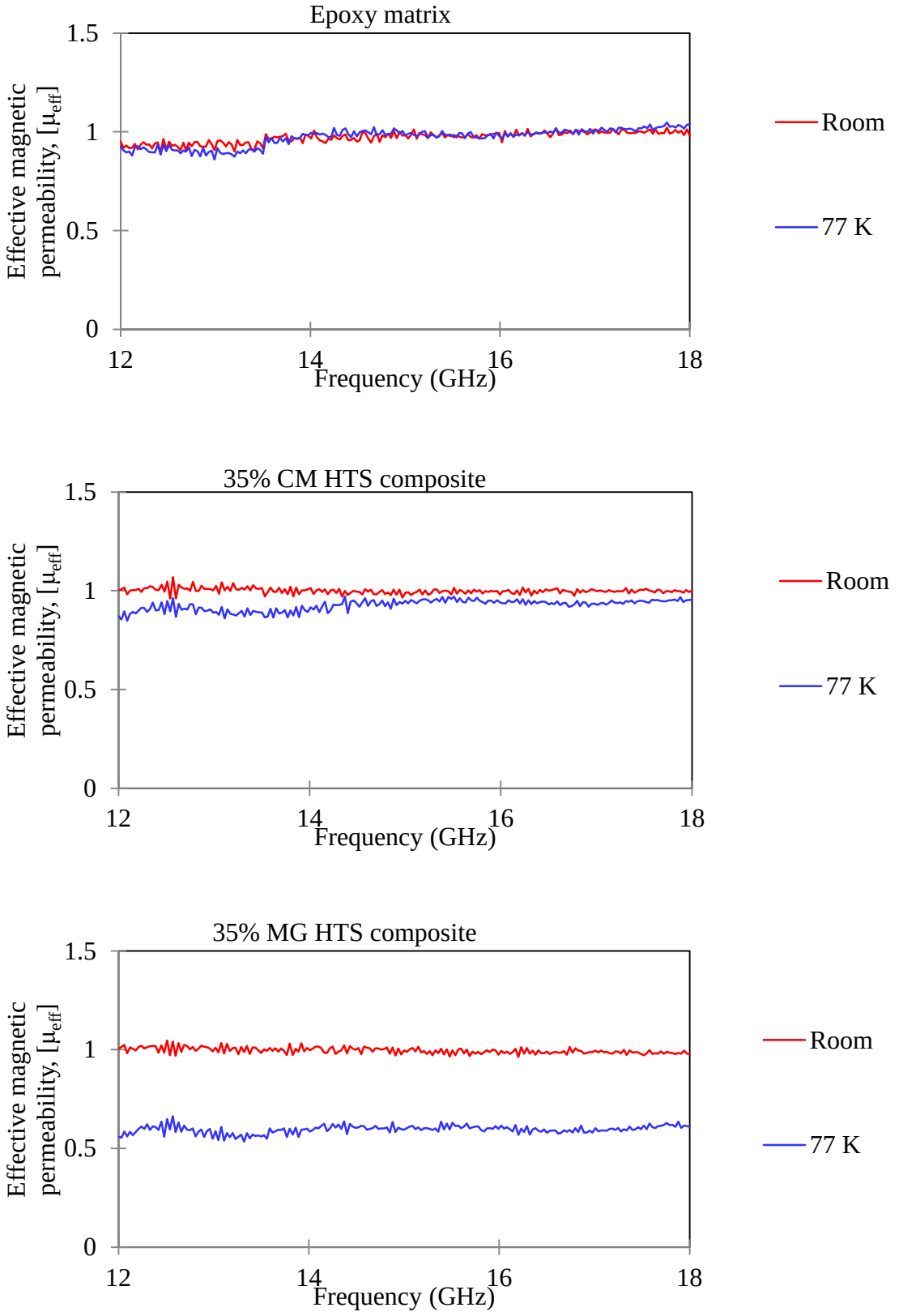


Figure 8.15 The effective magnetic permeability (μ_{eff}) values of HTS composites with nominal volume fractions of 35 vol%. (Top) Epoxy; (Centre) 35 vol% CM HTS composites and (Bottom) 35 vol% MG HTS composite. Note that the μ_{eff} value of the epoxy is 1 at both room temperature and 77 K.

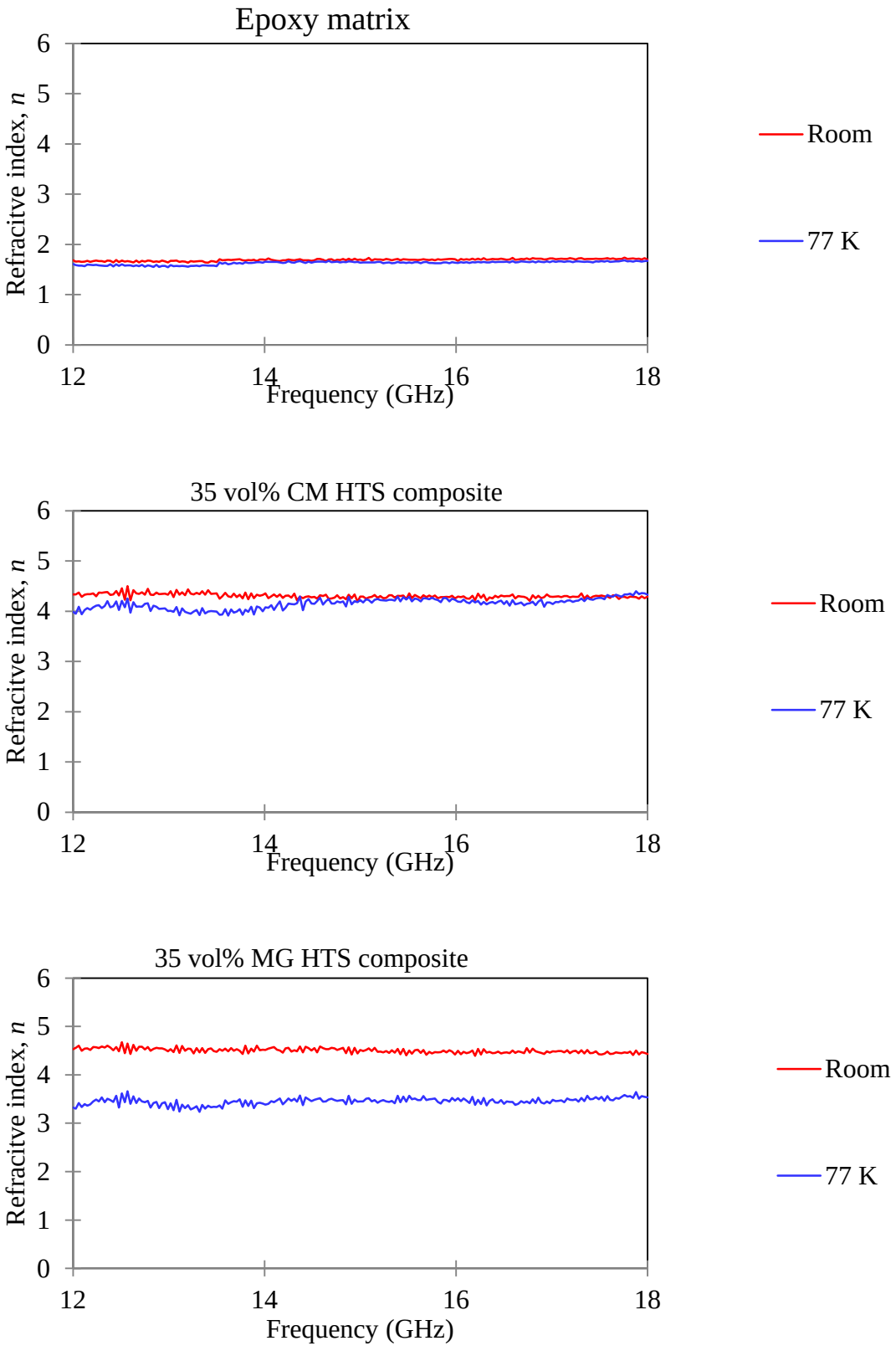


Figure 8.16 The refractive index (*n*) of HTS composites with nominal volume fractions of 35 vol%. Note that the *n* values for epoxy are 1.7 and 1.6 at room temperature and 77 K respectively.

Golosovsky *et al.*who described a decrease in n by ~ 19% at 77 K[5]. This shows that the n values can be controlled by adjusting the temperature of HTS composites.

As can be seen in Figure 8.14, Figure 8.15 and Figure 8.16, the ε_{eff}, μ_{eff} and n values of the 35% CM HTS composite can be observed to be inconsistent in the frequency range 12 to 14 GHz. These are likely to be measurement errors introduced during the VNA measurement, and were compared at different temperatures using the relative standard deviation (RSD) method. The precision of data increases with decreasing values of RSD. The RSD values of both HTS composites are 1% at room temperature, and increased to 3% at 77 K. The reason for this inconsistency is largely due to the contraction of cables, connectors and the coplanar lines during the VNA measurement at 77 K, as described by Lai *et al.*[15].

In summary, MG HTS composites have been observed to show a significant effect on microwave properties at both room and 77 K. This is due to the strong effect of the superconducting properties of the MG YBCO filler, at low temperature on μ_{eff} values and on ε_{eff} values at both measured temperatures. These results on the microwave properties and their relation to the microstructure of the HTS composites are discussed in more detail in Section 8.5.

8.4 Effect of Volume Loading

The effect of electromagnetic properties on the volume loading of YBCO filler has been investigated by measuring the ε_{eff} and μ_{eff} values of the HTS composites at both room temperature and 77 K. A set of HTS composites (Sample 1) with various nominal volume fractions was fabricated using the MG YBCO powder as a filler. This time, these MG YBCO bulks were ground and sieved through 63 μm and 125 μm-mesh

sieves to produce YBCO powder of particle size distribution from 1.0 μm to 363.0 μm, with the highest peak at 104.7 μm and d_{50}=59.2 μm, as measured by Mastersizer in Figure 7.17. The curing process was carried out using the PTFE mould to produce HTS composites with thickness of 1 mm and dimensions of 15.8 mm x 7.9 mm, so that the sample can fit tightly into the waveguide. Another set of CM HTS composites with various nominal volume fractions was also prepared as described above for comparison purposes. A summary of these HTS samples is shown in Table 8.2.

Table 8.2 Samples prepared for the characterisation of HTS composites

Source materials	Grain size, d_{50} [μm]	Nominal volume fractions [vol%]
MG HTS YBCO (Sample 1)	59.2±0.3	6, 10, 20, 30, 39, 42, 45, 51
CM HTS YBCO	4.5±0.1	10, 28, 35, 40, 42

SEM measurements were carried out on the HTS films to observe the particle distribution in the HTS composites. Due to the thickness of the HTS composites, the morphology studies were conducted by scanning cross sections of the HTS composites (Figure 8.17). In order to further understand the effect of YBCO filler on the HTS composite, EDX was used to identify the composition of the YBCO filler in the HTS composite.

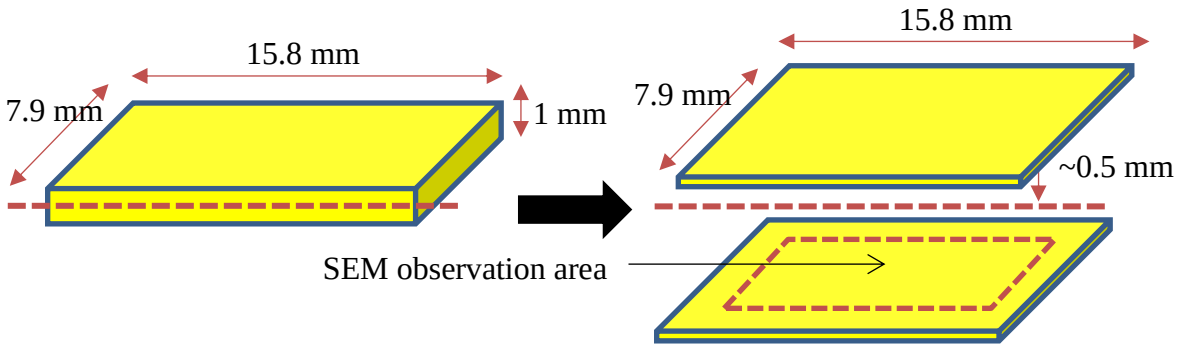


Figure 8.17 Cross sectional area of HTS composites for SEM observation. HTS composite samples were sliced into ~ 0.5 mm using a slow saw. YBCO filler distributions in the epoxy matrix were observed at random in the highlighted area.

8.4.1 Microstructure Studies on HTS Composites

A microstructure study was carried out using the sliced HTS composites (thickness ~0.5 mm) of MG HTS with nominal volume fractions 6, 10, 20, 30, 39, 45, and 51 vol%. The HTS film of 42 vol% was accidently broken during the sample preparation. This is not unexpected due to the brittle nature of these high concentration HTS composites, especially when preparing thin samples. The microstructure study was thus conducted using the 8 remaining HTS films. Scanning electron microscopy was carried out on several random points on the cross section of each HTS film. SQUID magnetometry was used to confirm the magnetisation properties of these HTS films.

Figure 8.18 and Figure 8.19 show the morphology of the HTS films with nominal volume fractions of 20 vol% and 45 vol%, taken at various magnifications using SE and BSE images. The size of filler particles in the samples is larger than those presented in Section 8.3.1. This can be due to inconsistency of the manual grinding process. In these samples flat, irregular plate-shaped features can be observed with size close to 100 μm, which is consistent with the highest particle size distribution as measured by the Mastersizer. These features can be seen distributed randomly and homogenously in the matrix, and tend to remain isolated from one another with epoxy, with no apparent agglomeration of particles. At higher magnifications, lines can be seen on the flat surface of these features, which originate from the slow speed saw blades. In addition, holes can be seen in both 20 vol% and 45 vol% HTS films. These holes were developed due to trapping air during the mixing and curing process. In the higher concentration sample, small features are observed filling in these holes. In order to identify these features, back-scattered images (BSE) have been used to distinguish between areas of different composition based on their average atomic or molecular mass (Figure 8.20 and Figure 8.21). These holes cannot be seen in the BSE, but show up clearly in the SE

images due to the greater sensitivity of SE images to surface topography. BSE images also show that these holes have similar average atomic mass to the bare substrate. All these features in the HTS films can also be identified using EDX mapping.

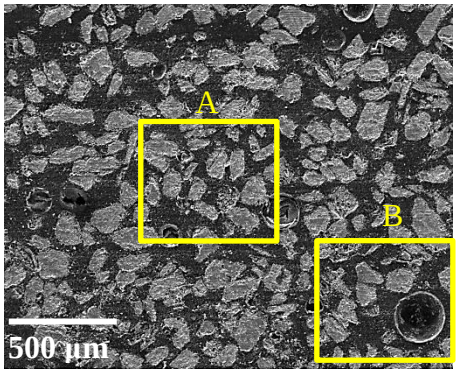
The EDX mapping indicates that the flat and irregular features present in the composite contain Y, Ba, C and O are YBCO powder (Figure 8.18 and Figure 8.19). Other than these flat and irregular features, the rest of the sample contains only C and O in the epoxy matrix. These are in good agreement with EDX spectra of YBCO particles (Figure 8.22 (a)) in the 20 vol% HTS composite and of the epoxy matrix in Figure 8.22 (b) and Figure 8.22 (c) respectively. As described previously in Chapters 6 and 7, the volume fractions of YBCO-211 in the melt-grown YBCO particles were estimated by conducting semi-quantitative analysis on YBCO particles in the composite. Several areas were randomly chosen at low magnification (100X) with field of view of approximately 1263 x 974 μm^2 (see Figure 8.22 (a)). YBCO particles were chosen at random and scanned at higher magnification (500X) with field of view of approximately 252 x 194 μm^2 (typically covering one or two particles) to avoid topographic variations, which can lead to misleading results in these measurements. The atomic percentages of cation elements Y and Ba were taken and the ratio of Y/Ba values was used to estimate the volume percentages of the YBCO-211 phase in YBCO particles using equation (8.2).

$$Estimated\ volume\ fraction\ of\ YBCO-211 = 1/\left(\frac{2-\left(\frac{Y}{Ba}\right)}{2\left(\frac{Y}{Ba}\right)-1}\right) \qquad (8.2)$$

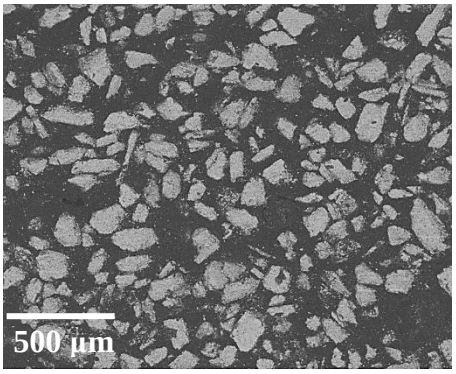
Table 8.3 shows the estimated fractions of the YBCO-211 phase in the YBCO particles of these HTS composites. An average of 23% of YBCO-211 phase can be estimated for this sample. These values are in a good agreement with the EDX results of both YBCO-123 and YBCO-211 phase content measured in the melt-grown YBCO powder (Chapter

7). This suggests that the morphology and structures of the YBCO filler are not affected by the mixing and casting processes. The EDX mapping also shows that the small features in the holes contain only Ba, Cu and O in the EDX mapping, and can possibly be identified as remnants of the BaCuO phases formed during the original melt processing[16,17]. Some of these small particles contain a small amount of Y, and so might be fine YBCO particles.

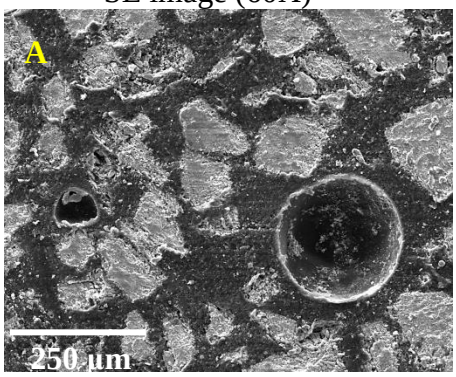
It is not surprising that the density of YBCO particles increases with volume fraction in the HTS composites. This can be observed clearly from Figure 8.23 which shows YBCO particle distributions in the HTS composites with range of nominal volume fractions from 6 vol% to 51 vol%. As can be seen from all these SE images, there is no agglomeration of the YBCO particles. Even though the spacing decreased with increasing concentration of YBCO filler, the microstructure consists of isolated particles separated by layers of epoxy matrix even at high YBCO concentrations. This indicates that no formation of a continuous network or chains of particles has occurred in these HTS composites.



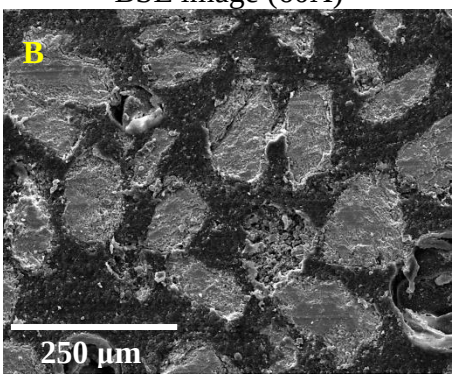
SE image (60X)



BSE image (60X)

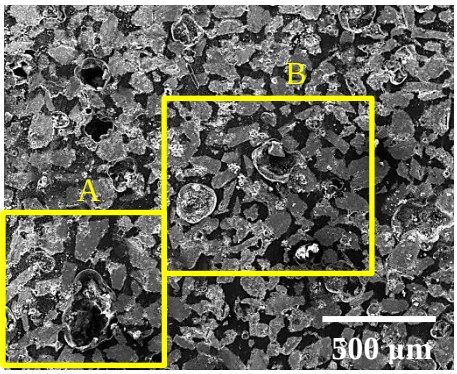


SE image (150X)

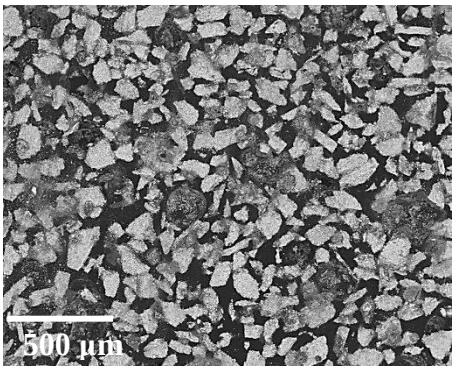


SE image (200X)

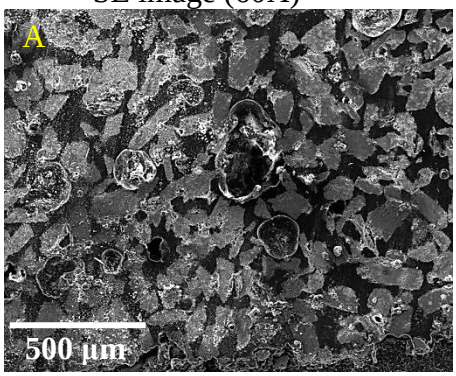
Figure 8.18 SE and BSE images of a 20 vol% HTS composite taken at various magnifications.



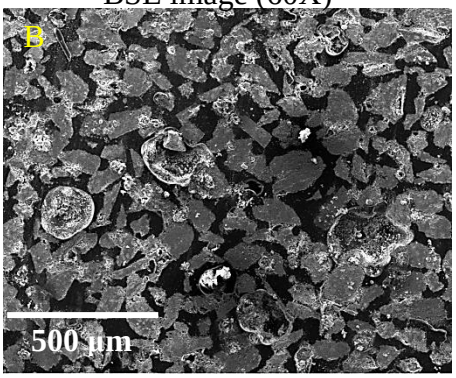
SE image (60X)



BSE image (60X)



SE image (75X)



SE image (80X)

Figure 8.19 SE and BSE images of a 45 vol% HTS composite taken at various magnifications.

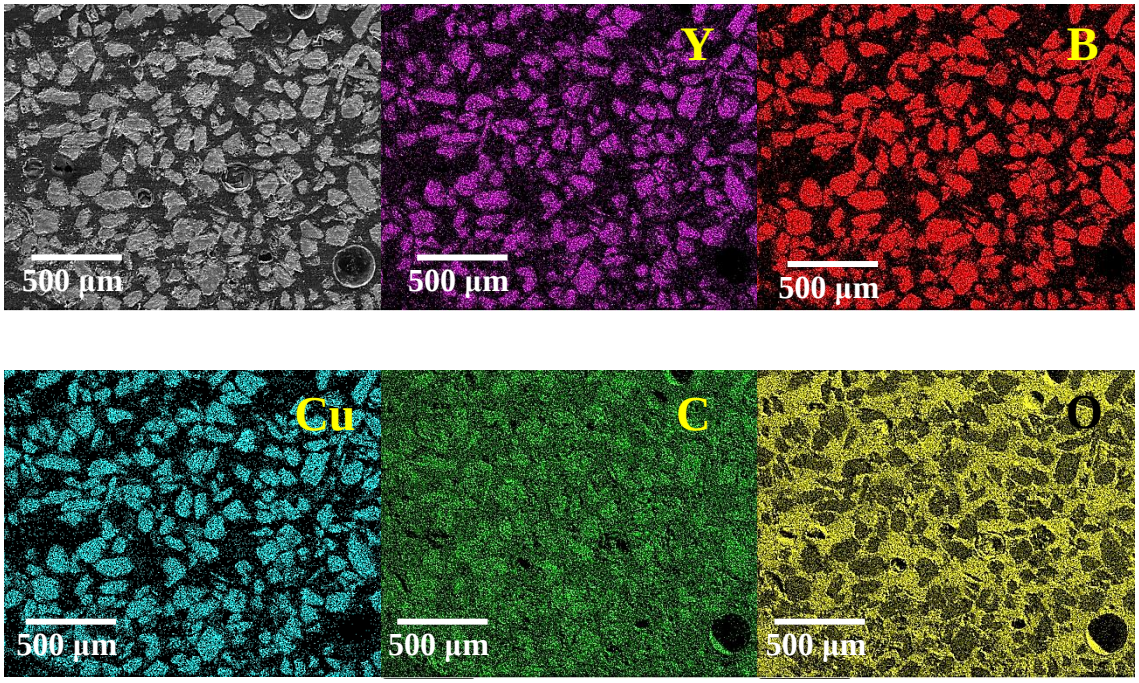


Figure 8.20 EDX mapping of a 20 vol% HTS composite.

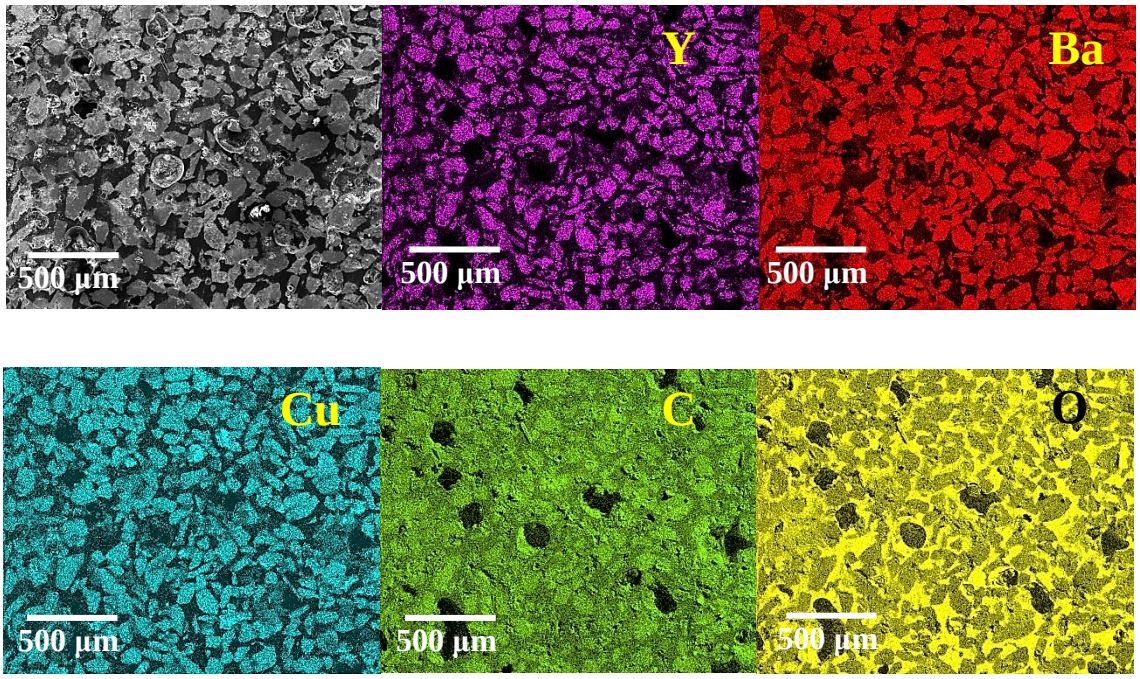


Figure 8.21 EDX mapping of a 45 vol% HTS composite.

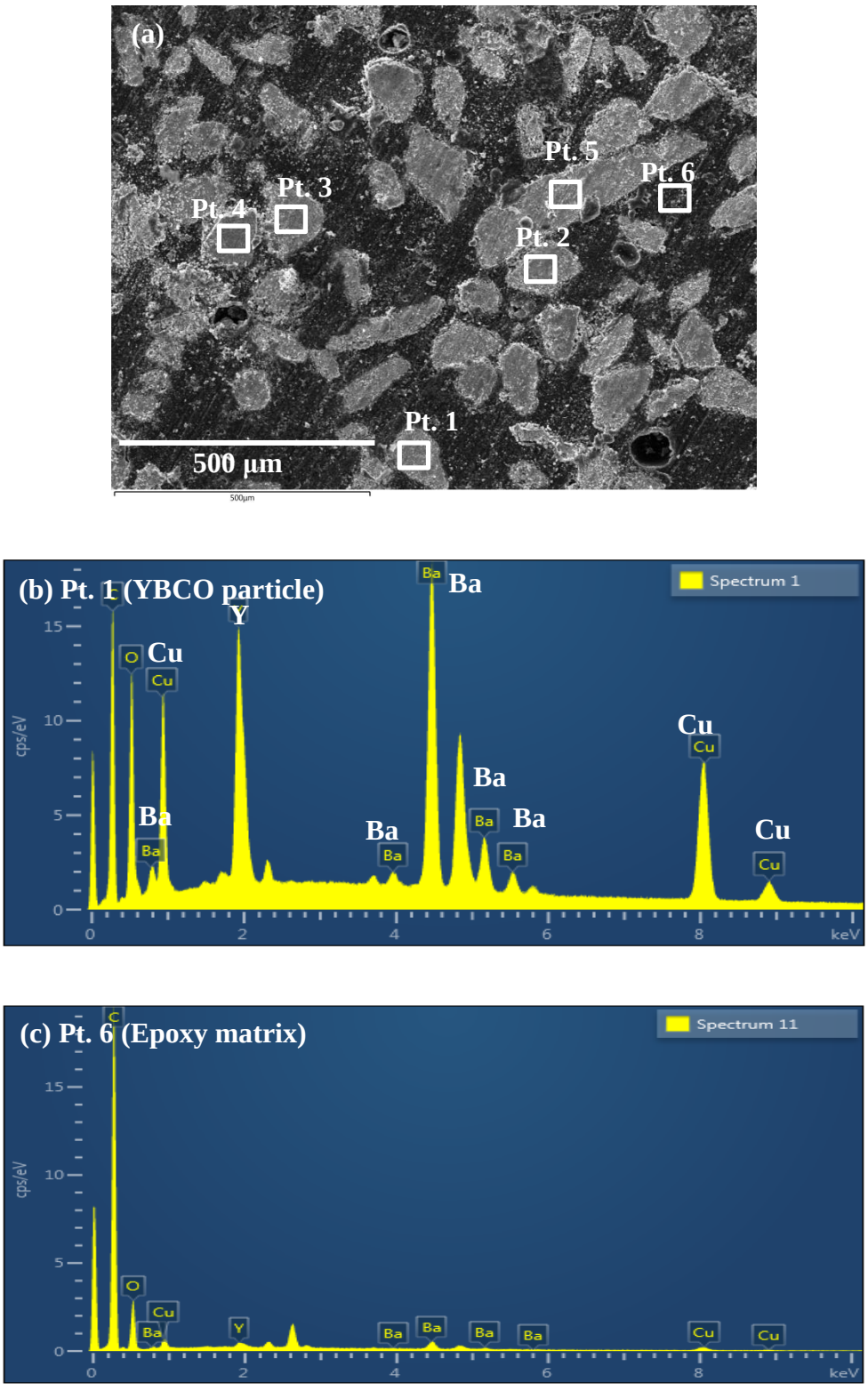
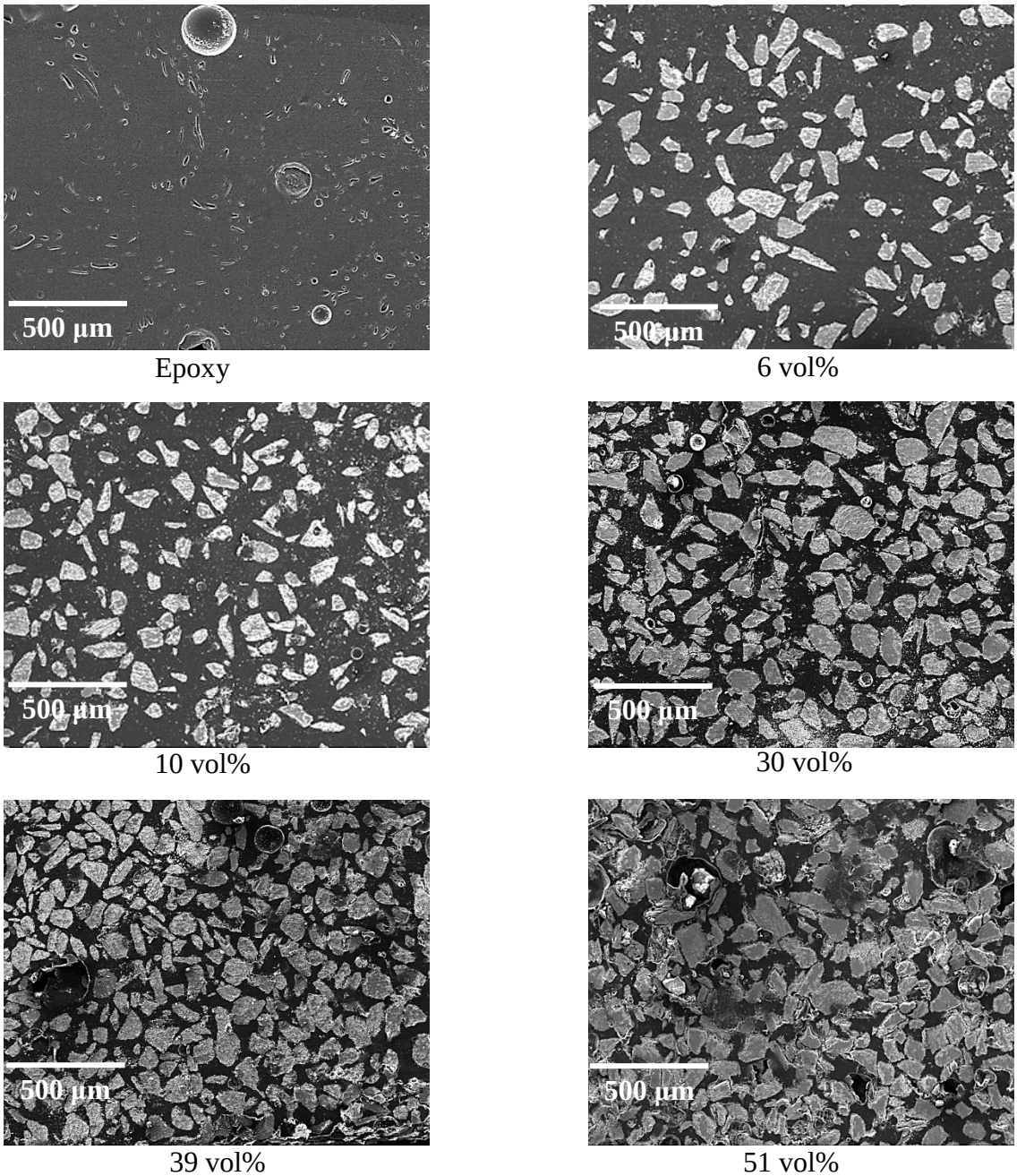


Figure 8.22 EDX analysis of the 20 vol% HTS composite. (a) SEM image indicates scanned area of particles and background for elemental analysis. Pt. 1 and Pt. 6 are EDX spectra for an YBCO particle in the 20 vol% HTS composite and the epoxy matrix respectively.

Table 8.3 EDX analysis of 20 vol% HTS composite

Elements	Y	Ba	Estimated volume fraction of YBCO-211 in YBCO particles [%]
Pt. 1	3.1	5.0	14
Pt. 2	3.9	4.9	33
Pt. 3	2.6	4.0	18
Pt. 4	2.9	4.6	16
Pt. 5	3.9	4.9	33
Pt. 6	0.1	0.3	Nil



Epoxy 6 vol%

10 vol% 30 vol%

39 vol% 51 vol%

Figure 8.23 SEM images of HTS composites with nominal volume fractions of 6, 10, 30, 39 and 51 vol% taken at 60X magnification.

8.4.2 Quantitative Analysis of Particle Distribution in the HTS Composites

In order to further understand the efficiency of the casting process using a PTFE mould on the distribution of the YBCO particles and its effect to the electromagnetic properties, the volume fractions of YBCO particles actually incorporated into the HTS samples have been measured by analysing and calculating the area fraction of YBCO particles using SEM and Image-J software. The same analysis technique has been used by Seuntjens *et al.* who calculated the area fractions of multi-phase superconducting composite filaments from BSE images using an image analysis equipped FESEM and TEM[18]. I found that the same technique can be applied to quantify the area fractions of YBCO particles in my HTS samples using SEM images. The BSE images are used to eliminate hole features, especially in the higher concentration HTS composites, as can be seen in previous SE images (Figure 8.23). The bright contrast from YBCO particles was highlighted as an area of interest and the darker epoxy matrix was set as a background. In order to establish these regions of interest, a brightness threshold between the features and matrix was selected. However, the selection of this threshold needed to be carefully done, so that only white areas of YBCO particles were selected for the area fraction calculation (Figure 8.24).

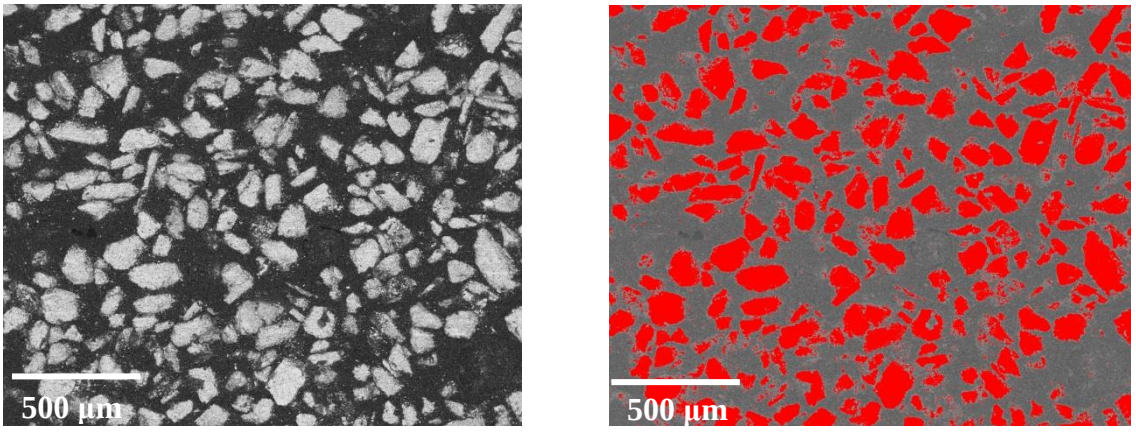


Figure 8.24 20 vol% HTS composite BSE image (left image) thresholded for area fraction analysis. YBCO particles in the HTS composites were highlighted into red pixels to calculate the area fraction (right image).

In this work, three areas across HTS films were randomly chosen at the edges and centre of HTS samples (Figure 8.25) and scanned at 60X magnification to analyse the homogeneity of particle distributions in the HTS composites. The areas were chosen such that the scanned region was roughly representative of the distribution of YBCO fillers in the HTS composites as a whole.

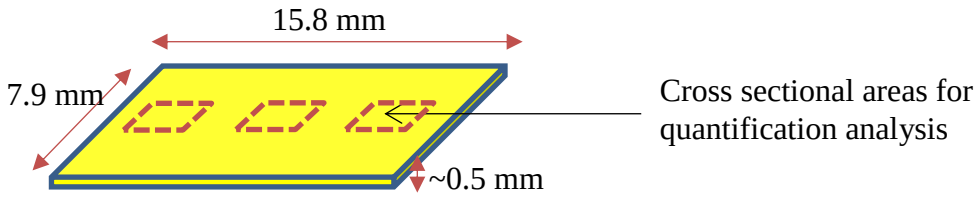
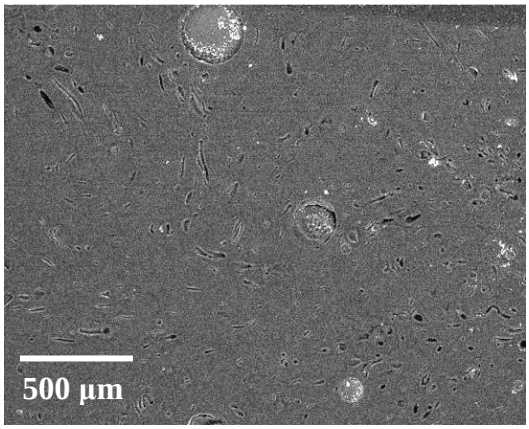


Figure 8.25 Cross sectional areas taken randomly at centre and edges of HTS composite sample for quantification analysis of YBCO fillers.

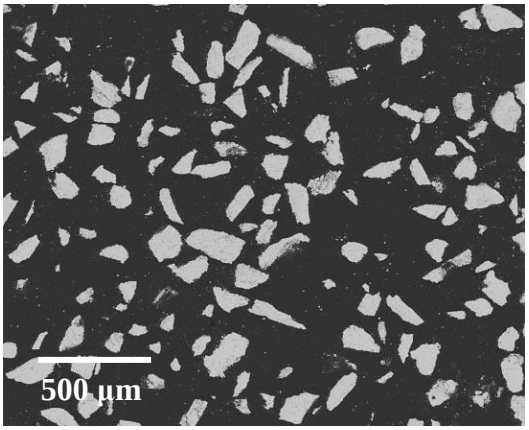
Figure 8.26 shows BSE images of HTS composites with nominal volume fractions of 6, 10, 30, 39, 51 vol% (BSE images of the 20 vol% and 45 vol% materials have been shown earlier in Figure 8.18 and Figure 8.19 respectively). These images have been taken over areas of 2087 x 1700 μm^2, and the high average atomic number of the YBCO particles and low atomic number of the epoxy matrix provide a clear contrast. The coverage of the white area of YBCO particles in the BSE images was plotted against the nominal volume fractions in these HTS composites, and is shown in Figure 8.27.

As expected, the area fractions of YBCO particles monotonically increase with the nominal volume fractions (Figure 8.27). However, the area fraction does not show a simple linear dependence on the nominal volume fractions, and the maximum variation between data points is 5%. This is partly due to the uneven distribution of YBCO particles in the HTS composite. This can be seen from the lowest volume fraction samples, 6 vol%, which has an area fraction of YBCO particles of 23±2%. During the fabrication process it is difficult to mix and cure a low density of YBCO particles uniformly in the high viscosity epoxy mixture using the PTFE mould. Some of the

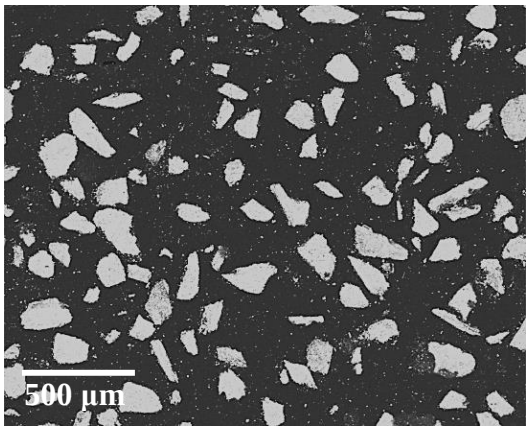
epoxy mixture may have leaked during the curing process, resulting in locally high concentrations of YBCO particles in the HTS composites.



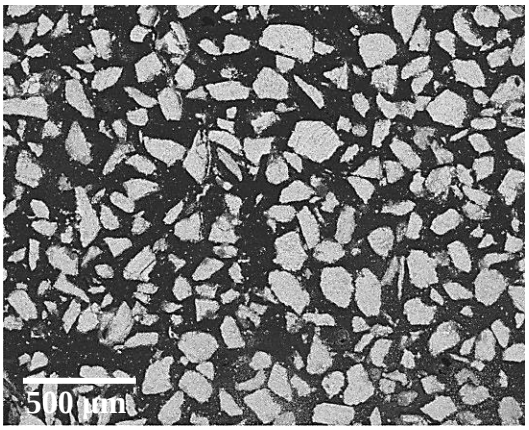
Epoxy



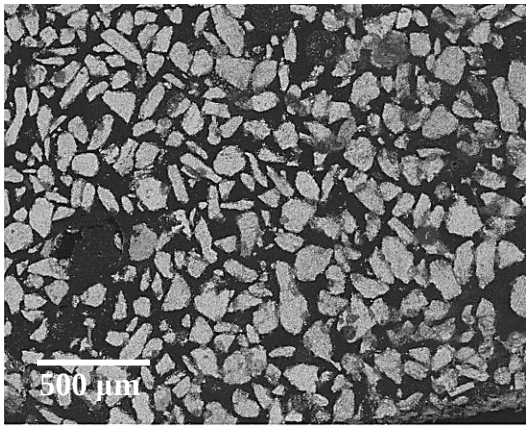
Vf=6 vol% (Af=23±2%)



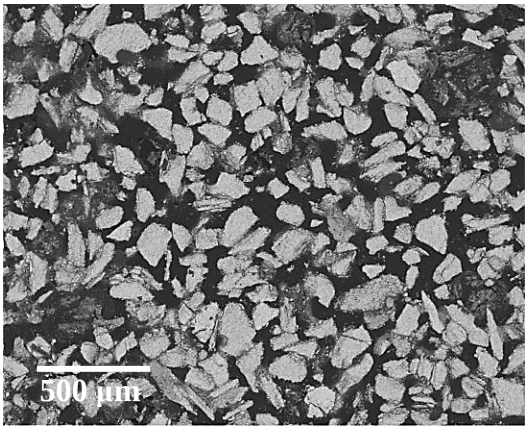
Vf=10 vol% (Af=25±3%)



Vf=30 vol% (Af=52±5%)



Vf=39 vol% (Af=53±1%)



Vf=51 vol% (Af=63±3%)

Figure 8.26 BSE images of the HTS composites with nominal volume fractions (Vf) of 6, 10, 30, 39, and 51 vol% taken at 60X magnifications. These images were used for the calculation of area fraction of YBCO particles in the HTS film using Image-J software. The measured area fractions (Af) of the HTS composites are 23±2%, 25±3%, 52±5%, 53±1%, 63±3%. (Not in the images are 20 vol% and 45 vol% HTS composites with measured area fractions of 34±1% and 55±2% respectively).

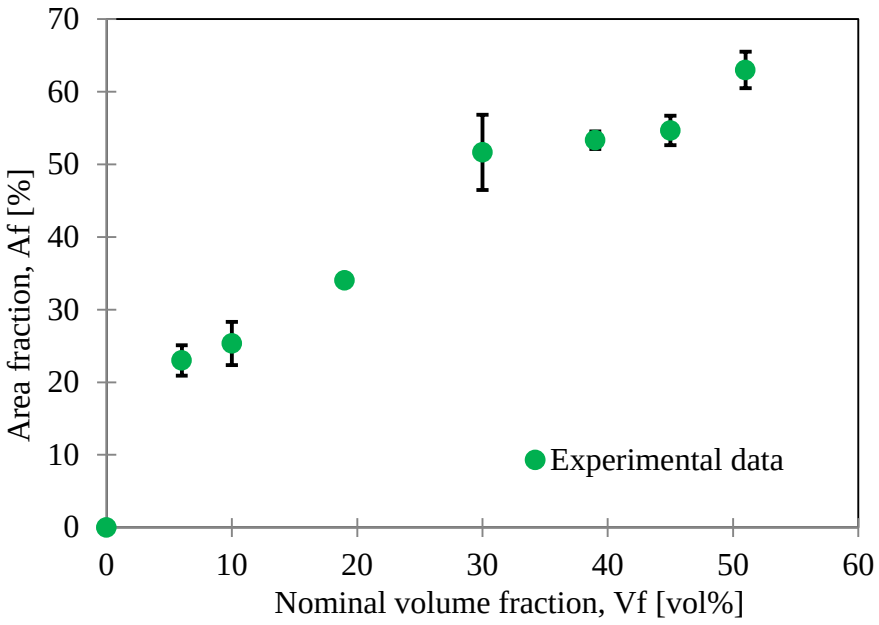


Figure 8.27. Area fractions of YBCO particles as a function of nominal volume fractions in MG HTS composites. The error bars refer to 3 areas measured on each HTS film. (Error bars for 20 vol% and 40 vol% HTS composite samples are smaller than the green spot).

This fault in fabrication is likely to be responsible for the high concentrations of powder in these HTS composites, which would lead to higher ε_{eff} and μ_{eff} values than expected. This can be seen from Figure 8.27 where the measured area fractions are higher than the nominal volume fractions, leading to misinterpretation of YBCO loadings in the HTS composites. There are ways to do volume fraction measurement such as X-ray computer tomography, which are not available to me. In this case, the best way to quantify YBCO loadings in the HTS samples is the measured area fraction, and I used the measured area fraction for discussion of microwave and superconducting properties in sections below.

8.4.3 Microwave Properties of HTS Composites

All the electromagnetic properties of ε_{eff}, μ_{eff} and n were measured using the waveguide technique at both room temperature and 77 K. Based on the previous microwave measurements on the HTS composites, the ε_{eff}, μ_{eff} and n values were

consistent from 12 GHz to 18 GHz. Therefore, this time the ε_{eff}, μ_{eff} and n values were measured only at 15 GHz, and the results plotted against the measured area fraction in the HTS composites. For comparison purposes, the electromagnetic properties of the CM HTS composites are also presented.

8.4.3.1 Effective Dielectric Constant (ε_{eff})

Figure 8.28 shows the ε_{eff} values of both MG HTS and CM HTS composites at 15 GHz. The ε_{eff} values of HTS composite samples increased with increasing area fraction of YBCO powder at both room temperature and 77 K. The increasing ε_{eff} values have a reasonable consistency with the increasing HTS area fractions. However, the ε_{eff} values of CM HTS composites are relatively lower than for MG HTS composites, as can be seen from the sample with area fraction 36%. Figure 8.28 also shows that the ε_{eff} values of the CM HTS composites are likely to be saturated at ~ 18 above ~ 50% area fraction, while the ε_{eff} values of the MG HTS composites were as high as ~ 25 at room temperature for high loading fractions. These values differ by 28%, and can be due to differences of YBCO filler density or porosity. Trybula *et al.* described how the ε_r properties of YBCO ceramic below T_c are related to the concentration of the normal component of superconducting material[19]. Since the normal component of a superconductor is basically a poorly conducting material, the internal inductance and skin depth effect of conducting grains can strongly influence the real part of the ε_{eff} at microwave frequencies[20]. Hence, the relatively smaller size of CM HTS filler and its weak superconducting properties as described in Chapter 7 are likely to be the reasons for the lower ε_{eff} values.

By assuming that these particles are homogenously distributed and individually isolated within the epoxy matrix (based on observation of BSE images of YBCO particles

distribution in Figure 8.18, Figure 8.19 and Figure 8.26), the ε_{eff} values can be compared with those predicted by effective-medium models such as the Maxwell-Garnett[21], Bruggeman[22] and Lichtenecker[23] (refer to equations in Chapter 5 section 5.3.2) with focus on the ε_{eff} values of MG HTS YBCO. The measured dielectric constant of pure epoxy, ε_m=2.98, was used in these models as a constant, while the dielectric constant of YBCO filler was varied to achieve the approximately best-fit, referring to the reported dielectric constant of polycrystalline YBCO, $\varepsilon_i = 100 - 700$[24,25] at room temperature. The effective medium equations used in the fitting are,

Maxwell-Garnett equation:

$$\varepsilon_{eff} = \varepsilon_m + 3f\varepsilon_m \frac{\varepsilon_i - \varepsilon_m}{\varepsilon_i + 2\varepsilon_m - f(\varepsilon_i - \varepsilon_m)} \quad (8.3)$$

Bruggeman equation:

$$(1-f)\frac{\varepsilon_m - \varepsilon_{eff}}{\varepsilon_e + 2\varepsilon_{eff}} + f\frac{\varepsilon_i - \varepsilon_{eff}}{\varepsilon_i + 2\varepsilon_{eff}} = 0 \quad (8.4)$$

Lichtenecker equation:

$$\varepsilon_{eff}^{\alpha} = f_i\varepsilon_i^{\alpha} + (1-f)\varepsilon_m^{\alpha} \quad (8.5)$$

where ε_m is the dielectric constant of the epoxy matrix, ε_i is the dielectric constant of the YBCO fillers, f is the volume fractions of YBCO fillers in the composites.

The equations (models) use volume fractions (Vf). However, it is only possible to measure area fractions (Af) using SEM analysis. Whilst area fraction is not the same as volume fraction (except for the case of uniformly distributed spherical particles), it is not obvious how to obtain a more accurate measure of volume fraction in these samples. Therefore, the experimental data is presented as a function of the measured area fraction. Comparison with the models assumes that Af ≈ Vf.

Figure 8.28 shows the ε_{eff} values of both MG HTS and CM HTS composites at 15 GHz. The horizontal errors were averaged over measured area fractions from three locations on a cross-sectional area of HTS samples. However, there are no dielectric constant measurement errors available for the HTS composites. Therefore, the vertical errors in these ε_{eff} values were estimated for the pure epoxy samples based on the measurements reported in Chapter 6, section 6.3.3.2. The estimated microwave measurement errors for the pure epoxy samples are used for all the microwave measurements in this work.

From Figure 8.28, I found that the ε_{eff} values of the MG HTS composites only fit Maxwell-Garnett formula at low loadings (area fractions less than 30%) with predicted $\varepsilon_i = 700$, while the ε_{eff} values of the MG HTS composites were approximately fitted especially at higher loading of YBCO filler by the Bruggeman equation with predicted $\varepsilon_i = 55$, and Lichtenecker equation with predicted $\varepsilon_{filler} = 100$. The predicted ε_{filler} values are in agreement with those reported for polycrystalline YBCO by Behrooz *et al.*[24] and Testardi *et al.*[25], except the predicted dielectric constant of the YBCO filler in Bruggeman equation ($\varepsilon_i = 55$) is lower than that reported for polycrystalline YBCO, but higher than those reported by Abraham's and Trybula's work at 24.0[6] and 26.5[19] respectively. These differences in ε_{filler} values could be due to the difference in oxygen concentration in the YBCO filler and density or porosity variations as reported by Behrooz *et al.*[24].

Among these equations, both Bruggeman and Lichtenecker equations have been shown to have better agreement with data from the MG HTS composites than the Maxwell-Garnett mixing formula due to the consideration of fractions of both YBCO filler (ε_i) and epoxy matrix (ε_m) in the prediction of ε_{eff} values. As can be seen in Figure 8.28,

the ε_{eff} values of MG HTS composites do not fit well with Maxwell-Garnett equations especially at higher loadings (above area fractions of 30%). This is in agreement with Dang *et al.*[26] who reported that Maxwell-Garnett equations can cause underestimation of ε_{eff} values for high loading $BaTiO_3$/PVDF composites ($f > 0.15$). This is due to the applicability of Maxwell-Garnett equations, which can only be applied to low loadings mixture or mixtures with low dielectric constant values[27]. This is because the Maxwell-Garnett equations assume a continuous media filled with embedded spherical fillers, homogeneously distributed and well-separated. In my work, the separation of YBCO fillers in epoxy matrix can be seen clearly at lower YBCO loadings (below 30% of area fractions) from the BSE images at Figure 8.26. However, this separation distance between YBCO fillers decreases with increasing concentration of YBCO fillers in the MG HTS composites, so interactions between fillers can not be ignored. This is where the Bruggeman equation is useful in the data fitting, where both matrix and filler materials are considered as the similar shaped particles embedded in an effective composite media, which is more relevant at higher loadings. In the Bruggeman equation the dielectric constant of both inclusions and matrix are treated equally, and contribute to the effective dielectric constant of HTS composites[28]. The Lichtenecker equation is also useful in the data fitting by considering the shape and orientation of fillers and matrix, which can be defined by $\propto$ as indicated in equation (8.5). In the case of randomly distributed nearly spherical fillers in media, $\propto \rightarrow 0$, which has given a reasonable fit to the ε_{eff} values of my MG HTS composites as shown in Figure 8.28. Goncharenko *et al.* stated that $\propto \rightarrow 0$ can also be used in describing a composite system of randomly oriented spheroids, provided these randomly oriented spheroids must be uniformly distributed in shape and volume in the composite system[29].

From the study above, the Bruggeman and Lichtenecker equations can be used to give an approximate fit to the ε_{eff} values of HTS composites. However, factor such as shape of YBCO filler should be considered in order to improve the accuracy of fitting. It should be noted that most of these mixing rule equations were made based on the spherical shape or nearly spherical shape of fillers. However, the shape of YBCO fillers used in this work is mostly non-spherical (Figure 8.26), which could contribute to deviations from these fitting curves.

In addition, the lack of accurate control over YBCO loading can contribute to the deviations from the effective medium equations. In my case, the leakage of epoxy solution from the PTFE mould can cause the lack of control over YBCO loadings in the HTS composites. The lack of control over YBCO loadings in the HTS composites can cause a large deviation to the fitting curves, leading to overestimation of ε_{eff} values. For example, the HTS composite sample with 10 vol% nominal volume fractions was measured to have $\varepsilon_{eff} = 6.9$ and could not fit to any of the effective medium curves discussed above. Based on the measured area fraction of YBCO fillers in the HTS composites in Figure 8.27, the same sample was measured with 25% YBCO area fraction, giving a better fitting to Maxwell-Garnett, Bruggeman and Lichtenecker curves as can be seen in Figure 8.28. This time, deviations from the fitting curves may arise due to shape or size of particles and porosity (holes) induced by mixing or curing process. This is in agreement with Golosovsky *et al.* who suggested that the dielectric properties of the HTS composites are not well-described by these effective-medium models for two reasons; (1) microgeometry effects of the YBCO filler and (2) the presence of a d.c. percolation threshold at 20 vol%[1]. It has been shown in Figure 8.28 that no abrupt changes in the ε_{eff} properties were observed at all area fractions, suggesting no percolation threshold can be observed in the MG HTS composites.

Hence, the morphology of the YBCO filler may have influence to the ε_{eff} values of the MG HTS composites.

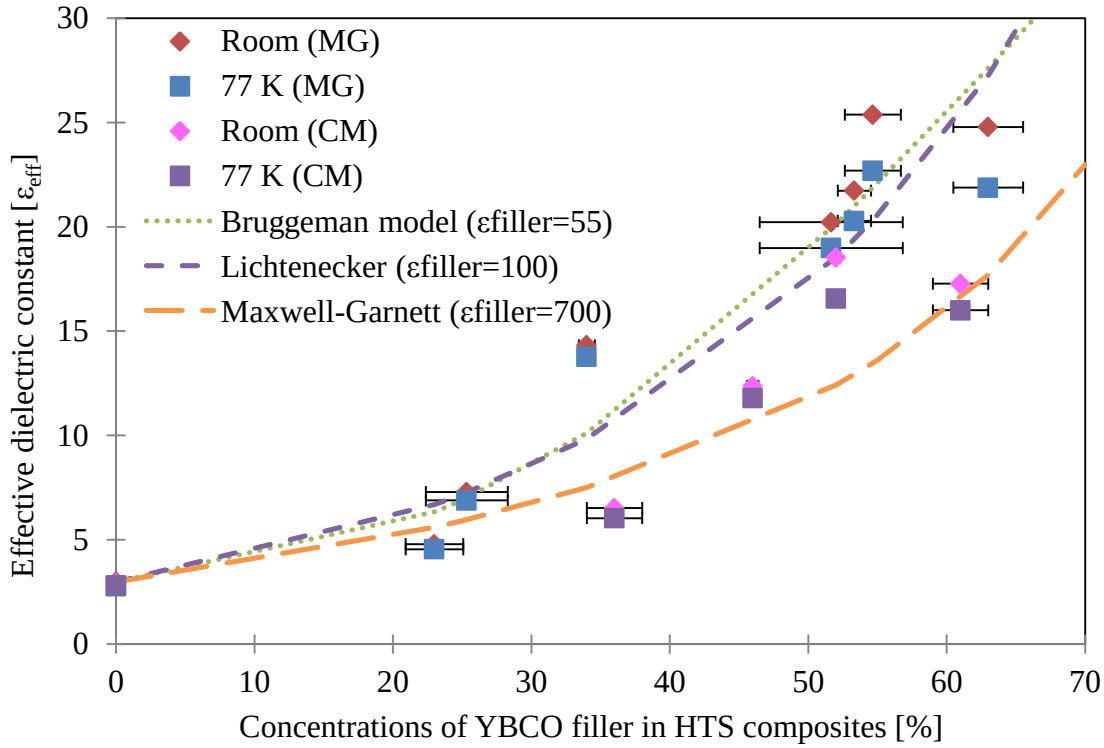


Figure 8.28 ε_{eff} values as a function of concentrations of YBCO filler in HTS composites. The horizontal error bars for 20% and 40% MG, and 46% and 52% CM HTS samples are smaller than the markers. The estimated vertical errors in these ε_{eff} values are shown for the pure epoxy samples based on the measurements reported in section 6.3.3.2 are smaller than the markers. The ε_{eff} values for all models are as a function of volume fractions of YBCO fillers in the HTS composites.

8.4.3.2 Effective Magnetic Permeability (μ_{eff})

Figure 8.29 shows the μ_{eff} values of MG and CM HTS composites at both room temperature and 77 K. All the μ_{eff} values are close to 1 at room temperature as expected. In contrast, a large drop of μ_{eff} values with area fraction is observed at 77 K for the MG composites. The μ_{eff} value of the lowest of MG HTS area fraction of 23% decreases by 13% at 77 K. The decrease in μ_{eff} values from 1.0 to 0.5 against area fractions from 0 to 63% can be described by a roughly linear dependence. This is due to the diamagnetic response of the superconducting particles upon cooling of the HTS

composites below T_c, saturating at higher HTS loadings. The result is roughly in agreement with Golosovsky *et al.* who predicted a linear dependence of μ_{eff} values from 1.0 to 0.6 of YBCO/PMMA composites with YBCO volume fraction from 12% to 48%[1].

The μ_{eff} values of the CM HTS composites, however, are close to 1 at all volume fractions, as seen in Figure 8.29. The change in μ_{eff} values of CM HTS composite shows no significant difference at either room temperature or 77 K as seen in Figure 8.30, due to the weak magnetic properties of the source powder (see Chapter 7).

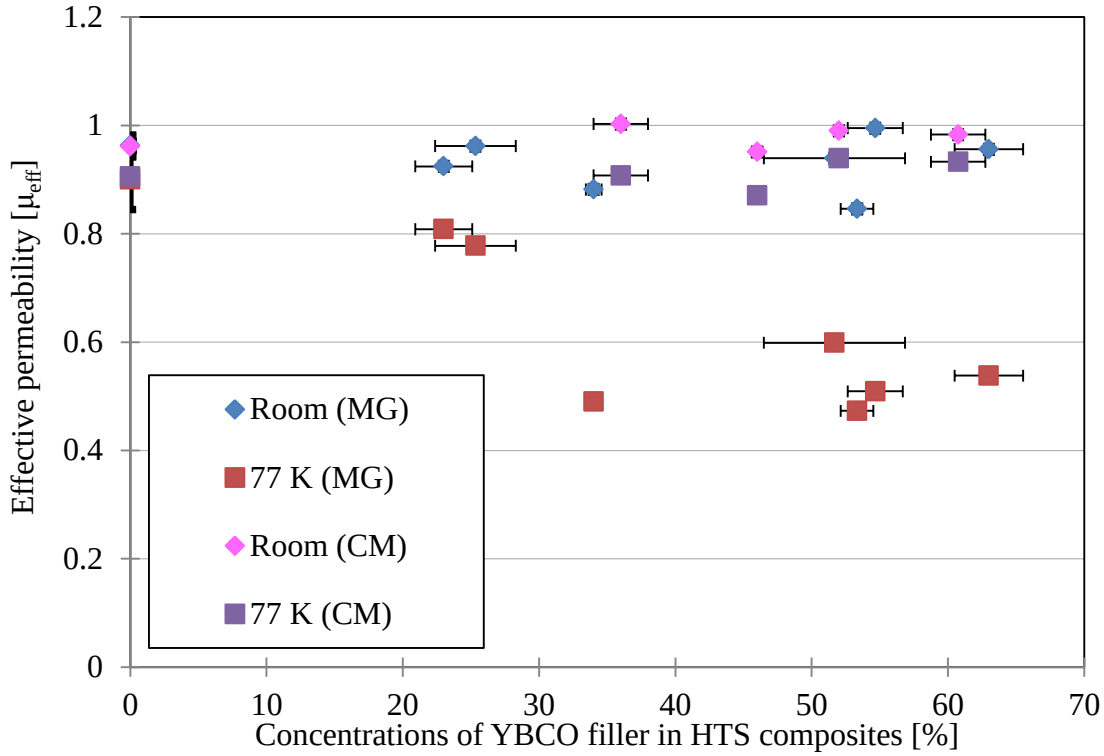


Figure 8.29 μ_{eff} values as a function of concentrations of YBCO filler in HTS composites. The horizontal error bars for 20% and 40% MG, and 46% and 52% CM HTS samples are smaller than markers. The estimated vertical errors in these μ_{eff} values are shown for the pure epoxy sample based on the measurements reported in Chapter 6, section 6.3.3.2.

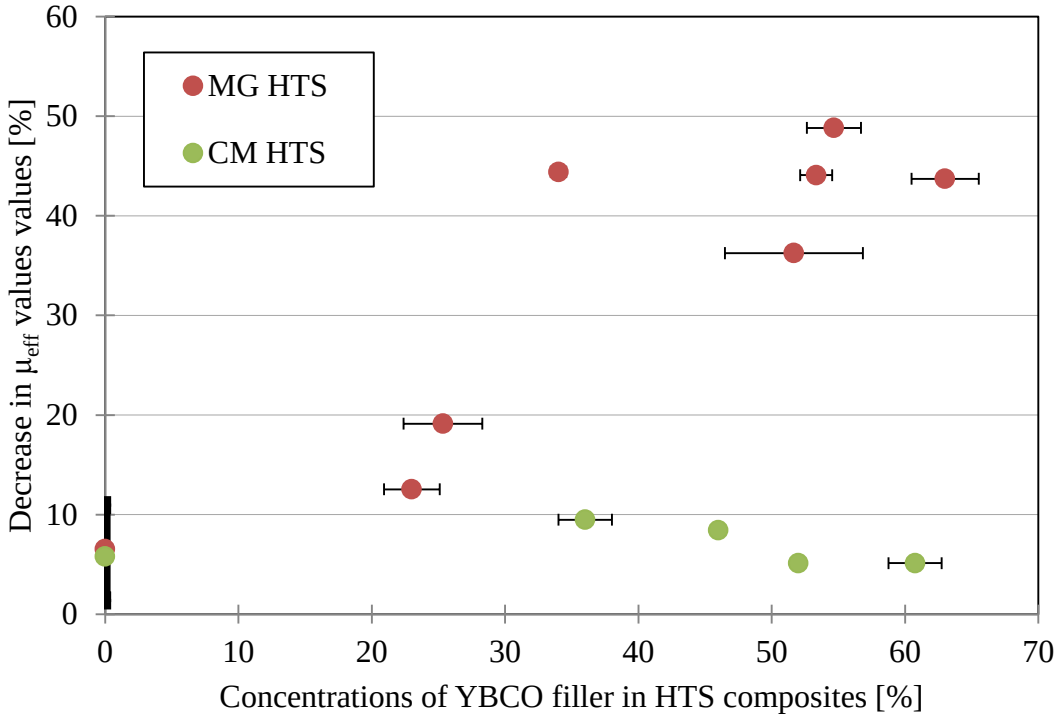


Figure 8.30 Percentages decrease of the μ_{eff} values of HTS composites from room temperature to 77 K. The horizontal error bars for 20% and 40% MG, and 46% and 52% CM HTS samples are smaller than the red and green spots. The estimated vertical errors in these μ_{eff} values are shown for the pure epoxy samples based on the measurements reported in Chapter 6, section 6.3.3.2.

8.4.3.3 The Refractive Index (n)

Figure 8.31 shows the calculated n of HTS composites with area fractions from 23% to 63%. The n values increase with area fractions of the HTS component at all temperatures due to the increase in ε_{eff} values, but are decreased at 77 K due to the decrease in μ_{eff} values. This is in good agreement with Golosovsky *et a.l* who demonstrated the same effect of μ_{eff} values on the refractive index of YBCO/PMMA composites on cooling to 77 K[1]. A steep increase of n values can be seen up to 30% area fraction for the MG HTS samples at both room temperature and 77 K. Above this HTS volume fraction, n values increase gradually with area fractions at room temperature, but the effect is almost saturated at 77 K. The same trend can be observed for the μ_{eff} values of the MG HTS composites at 77 K, as seen in Figure 8.29, which explains the saturation of n values at 77 K.

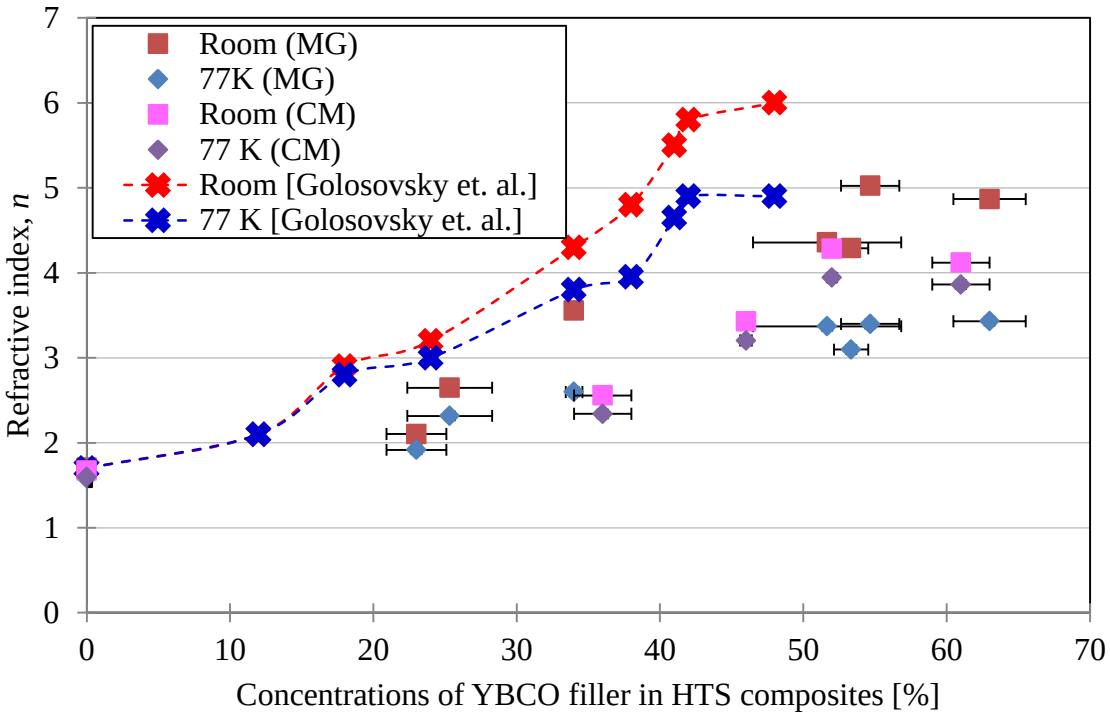


Figure 8.31 n values as a function of concentrations of YBCO filler in HTS composites. The horizontal error bars for 20% and 40% MG, and 46% and 52% CM HTS samples are smaller than the squares and diamonds. The estimated vertical errors in these n values are shown for the pure epoxy samples based on the measurements reported in Chapter 6, section 6.3.3.2 are smaller than the squares and diamonds. Red and blue dashed lines are n values at room temperature and 77 K from Golosovsky *et al.*[5].

The n values of the CM HTS composites also increase with HTS area fraction, but show no significant change at 77 K. This increasing trend in n is observed to be similar to the ε_{eff} values of CM HTS composites as seen in Figure 8.28. This is because the CM HTS composites have μ_{eff}~1 at both room temperature and 77 K (as seen in Figure 8.29), resulting in $n \sim \sqrt{\varepsilon_{eff}}$, which explains the similar increasing pattern of the n values to the ε_{eff} of CM HTS composites at both room temperature and 77 K.

My results show that the n value of the HTS composites can be tuned by changing both the ε_{eff} and μ_{eff} values. These values can be controlled over a significant range both by the volume fraction of YBCO filler and by temperature. The n values of my HTS composites are slightly lower than those reported for the YBCO/PMMA composites by

Golosovsky *et al.*[5] in Figure 8.31. The lower ε_{eff} value of my HTS composites is one of the main reasons for the low n values. This difference could be due to the type of YBCO filler used in HTS composites, where Golosovsky *et al.* used 20 μm YBCO powder[5]. Other reasons such as the microstructure of the HTS composites, dielectric and magnetic properties of the source powder and polymer, and volume fraction of superconducting phase of YBCO filler will also effect the ε_{eff} and μ_{eff} properties. The effect of types and sizes of source powder on the magnetic and superconducting properties have already been discussed in detail in Chapter 7. The effect of other parameters on the ε_{eff} and μ_{eff} values of HTS composites will be discussed further in section 8.5.

The change of the electromagnetic properties (Δn, $\Delta\varepsilon_{eff}$ and $\Delta\mu_{eff}$) from room temperature to 77 K increases with area fractions of the HTS composites (Figure 8.32). This indicates that the electromagnetic properties of the HTS composites are strongly related with the loadings of HTS filler. As suggested earlier in the literature review, the percolation threshold is expected at ~20% volume fraction in these HTS composites (based on Golosovsky *et al.*[5]). However, there is no abrupt change at this loading in the ε_{eff}, μ_{eff} and n properties of my HTS composites in Figure 8.28, Figure 8.29 and Figure 8.31. This suggests no high frequency conductivity between the superconducting particles in the HTS composites even at the high YBCO filler concentrations. The resistivity measurement of the MG HTS sample with the highest area fraction (Af=63%) was carried out using the 4-point probe technique at room temperature (the technique is discussed in section 8.3.1). The conductivity of the sample is ~10^{-6} $\Omega^{-1}m^{-1}$, suggesting no significant current could be passed through the sample even at the highest concentration of YBCO fillers. This explained the lack of percolation threshold in the MG HTS composites at all volume fractions. This is consistent with

Golosovsky *et al.*[5] who observed no dramatic change of microwave properties (*n* and *k*) in YBCO/PMMA composites at 10 GHz, suggesting that capacitive coupling of the grains dominates over resistivity coupling at high frequencies as discussed in section 4.2.1.

Among these values, it can be seen that only the ε_{eff} values of the HTS composite with 34% area fraction did not fit with the effective-medium models in Figure 8.28. A large change in μ_{eff} can also be seen from this sample in Figure 8.32 (c). This indicates a particularly strong superconducting diamagnetic property of the YBCO filler in this sample at 77 K, which can be due to reasons such as variations of the properties of YBCO filler taken from the melt-growth YBCO bulk, which in this sample gives high ε_{eff} and μ_{eff} values. The effect of the YBCO filler characteristics on the microwave properties of the HTS composites are analysed in more detail in section 8.4.5.

As can be seen from Figure 8.32 (b), the $\Delta\varepsilon_{eff}$ values of the higher loading MG HTS composites (> 52 vol%) at room temperature and 77 K differ by ~ 12%, while the ε_{eff} values of lower loading MG HTS composites (< 52 vol%) only differ by ~ 5%. The difference of ε_{eff} values for the lower loading MG HTS composites is insignificant due to the ±5.0% uncertainty in the VNA measurement, as discussed in section 6.3.3.2 in Chapter 6. However, the difference in ε_{eff} values for higher loading MG HTS composites could be due to holes. The effects of holes will be discussed in section

8.4.3.4.

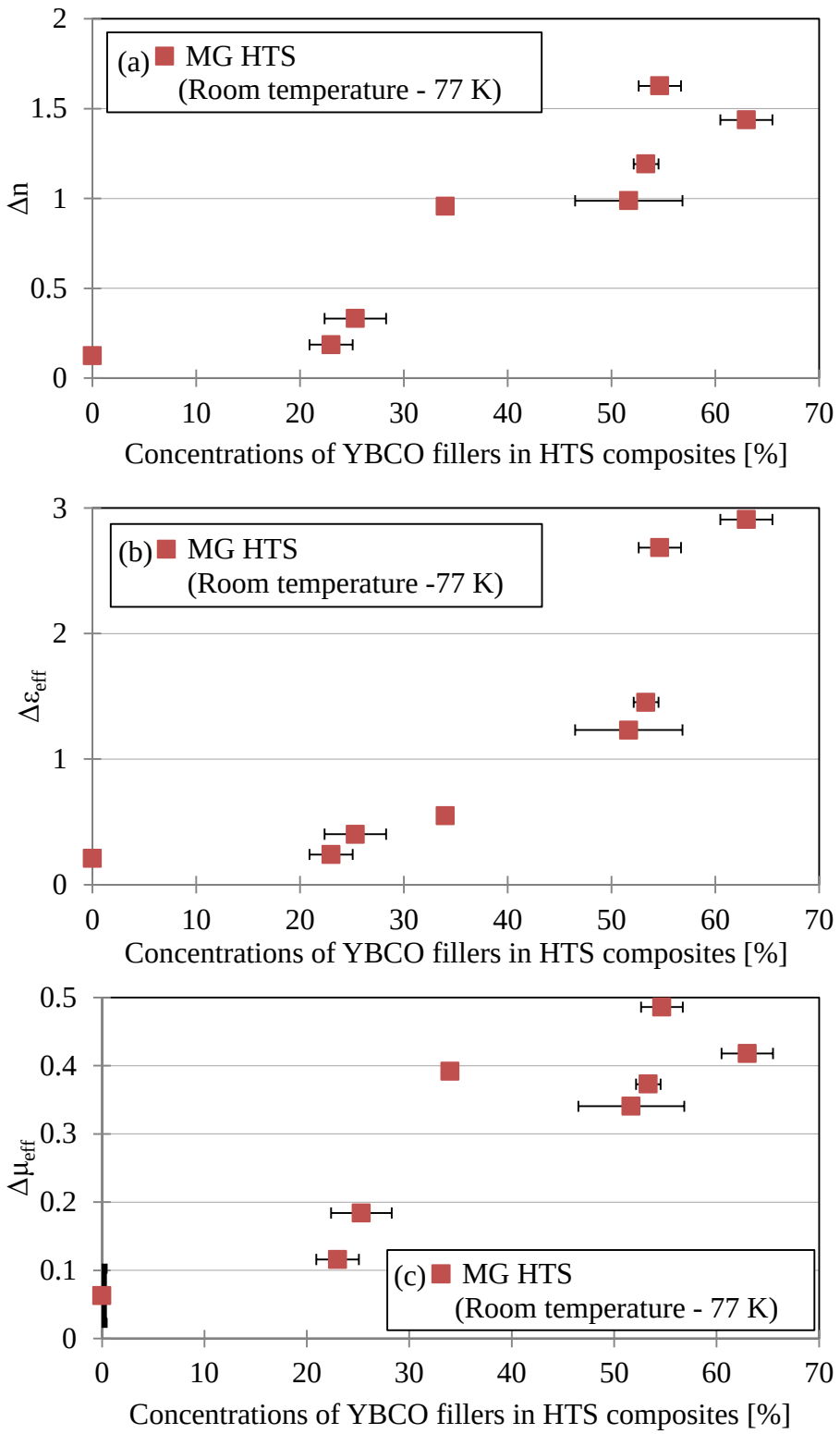


Figure 8.32 The change of electromagnetic properties from room temperature to 77 K; (a) Δn, (b) $\Delta\varepsilon_{eff}$ and (c) $\Delta\mu_{eff}$ properties. The horizontal error bars for 20% and 40% are smaller than the red squares. The estimated vertical errors in these (a) Δn, (b) $\Delta\varepsilon_{eff}$ and (c) $\Delta\mu_{eff}$ values are shown for the pure epoxy samples based on the measurements reported in section 6.3.3.2 (error bars for (a) Δn, and (b) $\Delta\varepsilon_{eff}$ are smaller than the red squares).

8.4.3.4 Study of holes

The YBCO particle quantification technique has been applied to estimate the area fraction of holes in the MG HTS samples. Air gap features were determined using both SE and BSE images (Figure 8.33), where round holes can be seen on the SE images due to sensitivity of electron beam to surface topology (section 6.5.3.1). The coverage of the holes area was calculated for all the samples.

The estimated area fractions of holes for the MG HTS samples are shown in Figure 8.34. Area fractions of holes increase with higher loading in the MG HTS composite samples. Holes coverage in the epoxy sample (MG HTS sample = 0%) is ~3%. The formation of holes in this sample is due to the stirring process. However, coverage in the MG HTS samples (> 52% loading of YBCO filler) are ~7%. This is likely due to both the stirring effect and out-gassing of YBCO particles during mixing. As explained earlier, the stirring process was difficult for higher loading of YBCO filler in epoxy, and the forceful mixing might have formed air bubbles in the HTS/Epoxy mixture. Holes could affect porosity and density of the HTS composites, which can affect the ε_{eff} values especially at 77 K. This effect of holes explains the difference of the ε_{eff} values at room temperature 77 K as presented in Figure 8.28 and Figure 8.32 (b).

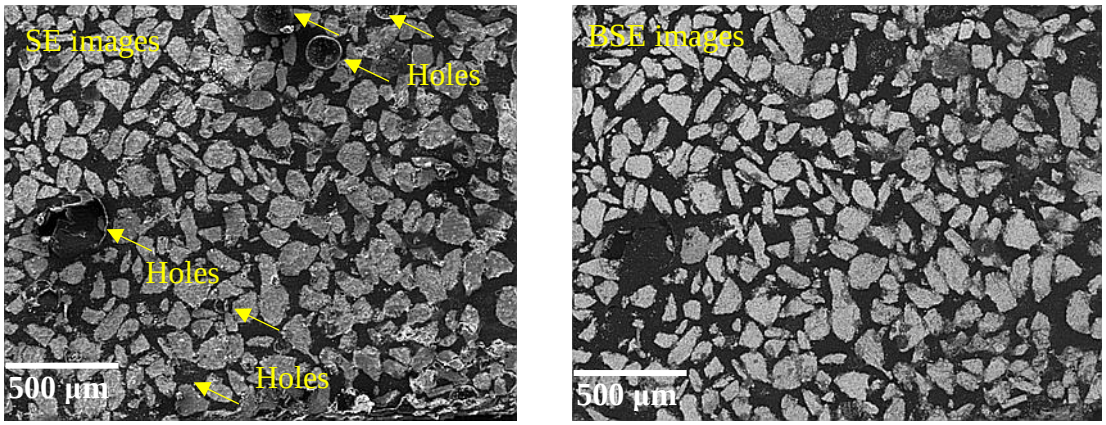


Figure 8.33 Identification of air gaps from SE and BSE images.

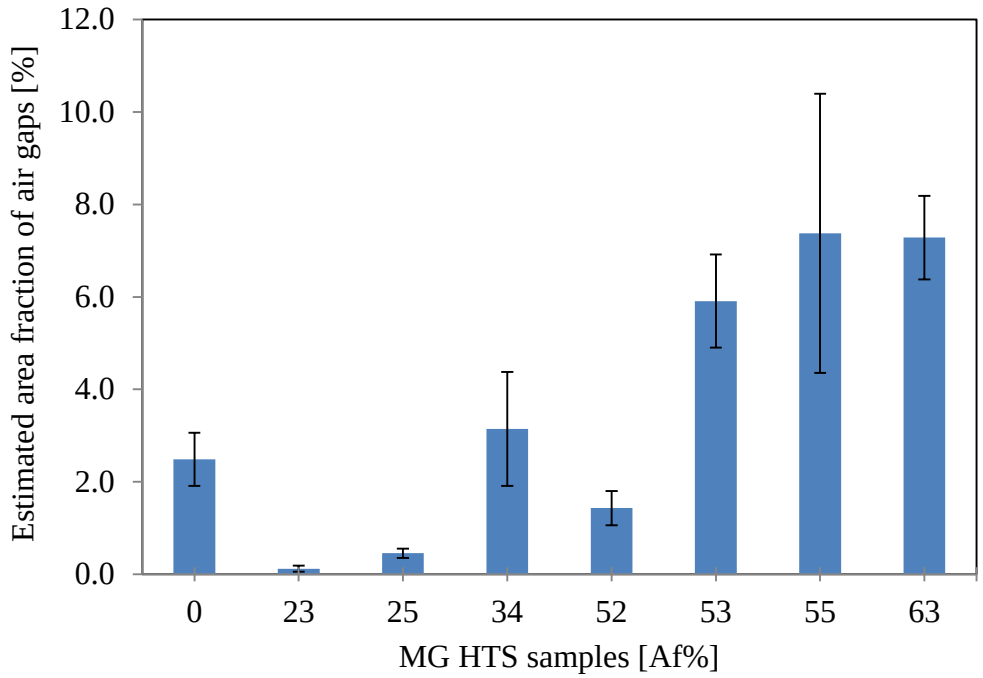


Figure 8.34 Estimated area fractions of holes for the MG HTS samples.

8.4.4 Magnetisation Properties

Magnetic measurements have been conducted on selected samples using the SQUID magnetometer. The MG HTS samples were cut into ellipsoids of approximate size 2.5 x 2.5 x 1 mm. Since all the HTS samples in this work are using the same source powder, the magnetic measurement of the melt-grown (MG) YBCO powder is a useful qualitative comparison for the amplitude of the hysteresis curves.

The critical temperature and magnetisation properties of MG HTS composites are compared with the MG YBCO powder in Figure 8.35 and Figure 8.37 respectively. The magnetisation values were normalised to mass of YBCO powder for comparison purposes. All the HTS composites are diamagnetic with a transition temperature of 93 K, indicating that the HTS composites have similar superconducting properties to the starting YBCO powder. The decrease in the magnitude of the magnetisation signal below 93 K scales roughly with the area fraction of YBCO filler, which can be seen in Figure 8.36. This is consistent with change in area of the hysteresis loops in Figure 8.37.

The magnetisation properties of my HTS composites are in a good agreement with the measured ε_{eff} and μ_{eff} values in Figure 8.28 and Figure 8.29. This can be seen from the increase of magnetic properties with HTS area fraction at 20 K (Figure 8.36) and the increase of $\Delta\mu_{eff}$ with the same HTS area fraction in Figure 8.32 (c), indicating the dependence of μ_{eff} on the magnetic properties of the HTS composites. In Figure 8.37, the HTS sample with 55% area fraction has shown hysteresis amplitude almost comparable to MG YBCO powder. The reasons for these are likely due to combination of several factors such as inconsistent sizes of YBCO particles and superconducting phase concentrations in HTS composites, and thickness of the impurity layer on YBCO particles that are likely to contribute to these variations in the MG HTS magnetic properties. These factors affecting the magnetisation properties of the HTS composites are discussed in detail in section 8.4.5.

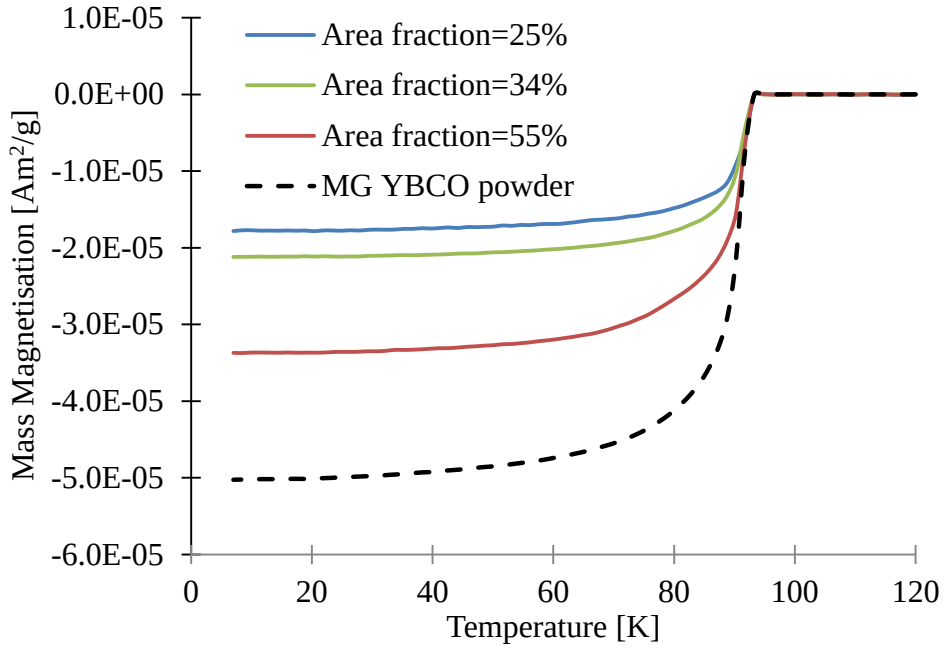


Figure 8.35 The mass magnetisation of HTS composites from which the T_c value can be seen to be 93 K.

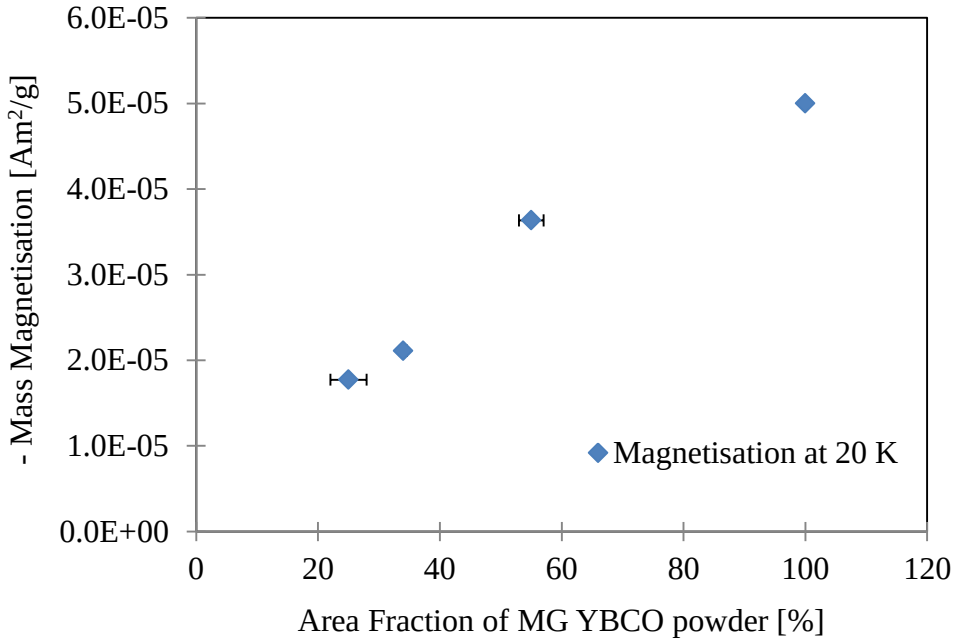


Figure 8.36 The decrease of the magnetisation values of the MG HTS composites with HTS area fractions at 20 K. MG YBCO powder represents as 100% area fraction. (Vertical errors bar are too small for the scale with each point having less than ±1% error).

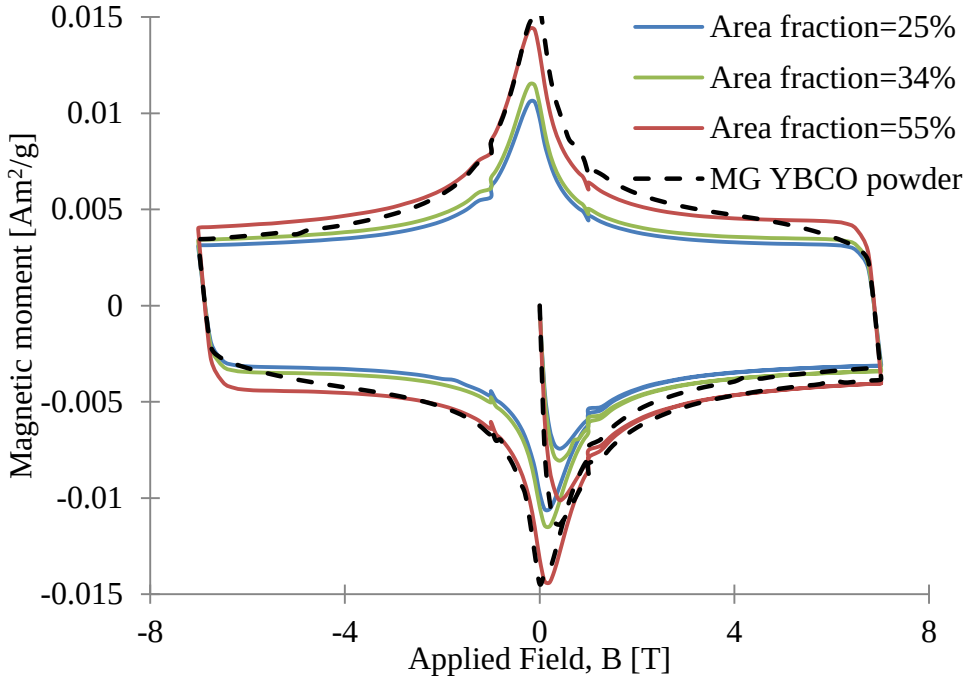


Figure 8.37 The hysteresis loops of the MG HTS composites of different area fraction samples measured at 7 K. The dashed line presents the hysteresis curve of the source MG YBCO powder.

8.4.5 Susceptibility of the HTS Composites

The susceptibility of the HTS composites ($\chi_{composite}$) at 77 K has been analysed in this work to study their magnetic and superconducting properties with the help of Prof. S.C. Speller following methods described by Campbell *et al.*[14]. This theory is described for static magnetic properties of a granular superconductor. As has been explained earlier, the $\chi_{composite}$ of the HTS composites depends strongly on the superconducting properties of the YBCO filler. The susceptibility of the YBCO filler (χ_p) depends on the size and shape of the YBCO particles. For a spherical shaped superconducting particle, χ_p can be written as[30],

$$\chi_p = -\frac{3}{2} f P(x) \tag{8.6}$$

where $-\frac{3}{2}$ is a demagnetisation factor for a spherical sample, f is the volume fraction of a sample occupied by the superconducting grains (YBCO-123) and $P(x)$ is the magnetisation suppression factor of a YBCO particle[31]. The magnetic suppression factor arises from the penetration depth effect that can affect the magnetisation property of a superconducting particle if the size of the particle is of the same order of magnitude as the penetration depth[31]. Clem *et al.*[31] indicate that the superconducting particles are magnetically invisible when $r < \lambda$, and their magnetic signal increases with $r > \lambda$. Thus, the effect of penetration depth, λ on the size of a superconducting particle, r is taken as a ratio of $x = \frac{r}{\lambda}$, which can be written as[31],

$$P\left(\frac{r}{\lambda}\right) = \left[1 - \frac{3\lambda}{r} coth\left(\frac{r}{\lambda}\right) + 3\left(\frac{\lambda}{r}\right)^2\right] \tag{8.7}$$

Since the MG YBCO particles consist of both superconducting YBCO-123 and non-superconducting YBCO-211 phase, the χ_p value depends strongly on the volume fraction of superconducting phase. The volume fraction of YBCO-123 (V_{123}) in YBCO

particles is essential to determine the effective χ_p value, which is expected to be lower than the susceptibility of an ideal 100% superconducting YBCO-123 ($\chi_p < \chi_{ideal}$) because the YBCO particle contains YBCO-211 non-superconducting phase in addition to YBCO-123. For example, YBCO particles used in this work contained approximately 23% non-superconducting YBCO-211 in addition to 77% YBCO-123 phase as shown in the EDX results in section 8.4.1. By considering the volume fraction of YBCO-123 and the size of the YBCO filler in the YBCO composites, the $\chi_{composite}$ equation can be written as,

$$\chi_{composite} = -V_{123}P\left(\frac{r}{\lambda}\right)\left[\frac{1}{1-\frac{V_{123}}{3}P\left(\frac{r}{\lambda}\right)(1+3fn-f)}\right] \quad (8.8)$$

where f is a volume fraction of a YBCO filler in the composite and n is a demagnetising factor of the composite sample.

Equation 8.4 was used to predict the $\chi_{composite}$ of my MG HTS composites. MG HTS YBCO parameters such as $V_{123} = 0.77$ (data from semi-quantitative EDX analysis of estimated volume fractions of YBCO-123 in MG HTS YBCO powder in section 8.4.1), $\lambda = 0.45\,\mu m$[32] (the penetration depth of YBCO measured along the c-axis at low temperature, which was based on the penetration depth of unaligned YBCO powders being quoted between 0.23 μm and 1.7 μm at room temperature[33]), $r = 29.6\,\mu m$ (Mastersizer measurement of MG HTS YBCO powder in section 7.3.3) and $n = 0$ by considering the shape of YBCO composites as a long thin rod parallel to the magnetisation field were used in the equation[34]. Unless otherwise stated these parameters were used for all the calculations to predict $\chi_{composite}$ of my MG HTS composites.

The size of YBCO filler used in the CM YBCO composites was also substituted into the equation to compare with the $\chi_{composite}$ of the MG HTS YBCO composites. The size was $2.2\ \mu m$ from the CM YBCO filler measured by the Mastersizer in Section 7.3.1. The predicted data were compared with the experimental data, which can be derived from the μ_{eff} using $\chi_{eff} = \mu_{eff} - 1$, where μ_{eff} values were derived from the NRW method using the VNA with area fractions of YBCO filler ranged from 23% to 63% at 77 K (section 8.4.3.2).

Figure 8.38 shows a comparison of the predicted and experimental $\chi_{composite}$ values of the HTS composites. Both experimental and predicted $\chi_{composite}$ values of the MG HTS composites show a reasonable agreement over the relatively few experimental points. The predicted $\chi_{composite}$ values of the YBCO composites with $29.6\ \mu m$ YBCO filler are consistent with most of my experimental data. The experimental data are also consistent with the volume fraction of superconducting grains in the YBCO filler ($V_{123} = 0.77$), Figure 8.39. Several points of the experimental values are found to deviate from the predicted values. This may be due to morphology effects such as particles agglomerations or air gaps in the composites, which lead to a lack of precise control on the volume fractions of filler during mixing process, as suggested by Wang *et al.*[35].

Figure 8.38 also shows that the predicted $\chi_{composite}$ values decrease with the size of YBCO filler in the HTS composites. This clearly indicates that the predicted values can be affected by the size of YBCO filler, explaining the lower susceptibility values of CM HTS composites than of MG HTS composites. This is in agreement with experimental work by Campbell *et al.* that reported the decrease in susceptibility values of YBCO powder with the size of particles[14]. The experimental $\chi_{composite}$ values of the CM HTS

composites are found to be lower than the predicted values. This can be due to the volume fractions of the superconducting phase in the CM particle being lower than 77% as seen in Figure 8.38. However, the experimental values of the CM HTS are consistent with the predicted values of 30% superconducting phase in the CM YBCO particle (Figure 8.40), much lower than the measured superconducting phase fraction in the CM YBCO particles, which contain no YBCO-211 phase.

The $\chi_{composite}$ of YBCO composites can also be affected by a layer of impurity at the surface of the superconducting grains[36]. This impurity can be a layer of a non-superconducting material from environmental exposure or extended storage of YBCO filler. The non-superconducting layer of thickness, d (Figure 8.41), is added in equation 8.4 by modifying the size of a particle, $r = R - d$, which can now be written as,

$$\chi_{composite} = -fV_{123}P\left(\frac{R-d}{\lambda}\right)\left[\frac{R-3d}{R}\right]\left[\frac{1}{1-\frac{V_{123}}{3}P\left(\frac{R-d}{\lambda}\right)\left[\frac{R-3d}{R}\right](1+3fn-f)}\right] \quad (8.9)$$

where $\frac{R-3d}{R}$ is the volume fraction of an inner sphere that is superconducting in a YBCO particle. Hibbs *et al.*[36] reported that a non-superconducting layer of 1 μm thickness can be formed on the surface of superconducting particles by the diffusion of CO_2 or O_2 during long storage or powdering process, which can affect the magnetisation properties. The same thickness value was used in this work to analyse the effect of a non-superconducting layer on the YBCO particles on the $\chi_{composite}$ values. Figure 8.42 shows the effect of a non-superconducting layer on the $\chi_{composite}$ properties. The predicted values were found to be ~10% lower than those of YBCO particles without any non-superconducting layer ($d = 0$). Figure 8.42 shows that the predicted $\chi_{composite}$ values of the CM HTS composites are close to 0 with the non-superconducting layer coating the YBCO particles. This indicates, as we expect, that a non-superconducting layer on the surface of YBCO powder is detrimental to fine

YBCO powders, which can affect the superconducting properties of the YBCO composites (Figure 8.42). The result may also suggest that the effect of a non-superconducting layer on the YBCO composites can be negligible if large YBCO particles are used as a filler. It may also be indicative that the long storage or exposure to environment will affect the magnetisation and superconducting properties of YBCO powder as suggested by Hibbs *et al.*[36]. In this case, long exposure to environment during handling and fabrication process might have effect to the magnetisation and superconducting properties of CM YBCO powder.

It is clear from this $\chi_{composite}$ analysis that large YBCO particles with a high amount of superconducting phase (V_{123}) and a minimum thickness of non-superconducting layer on the YBCO filler results in the best superconducting properties of the HTS composites at all area fractions. It has been shown in Figure 8.39 that the susceptibility values of the HTS composites can be improved using a YBCO filler with higher volume fraction of YBCO-123 phase. Even though it is difficult to source a YBCO filler with 100% superconducting phase from my current bulk sources, good quality YBCO filler with reasonable volume fractions of superconducting phase can be collected close to the seed region of the melt-grown YBCO bulk samples, which also can be grown specifically with low YBCO-211 content if desired. It is almost impossible to avoid the formation of non-superconducting layers on YBCO particles due to storage and powder processing, but the effect can be minimised using large YBCO particles. The sizes of YBCO particles are also limited by the processability to produce microwave devices. However, optimisation study can be carried out on a large YBCO fillers to fabricate YBCO composites with excellent superconducting and microwave performance.

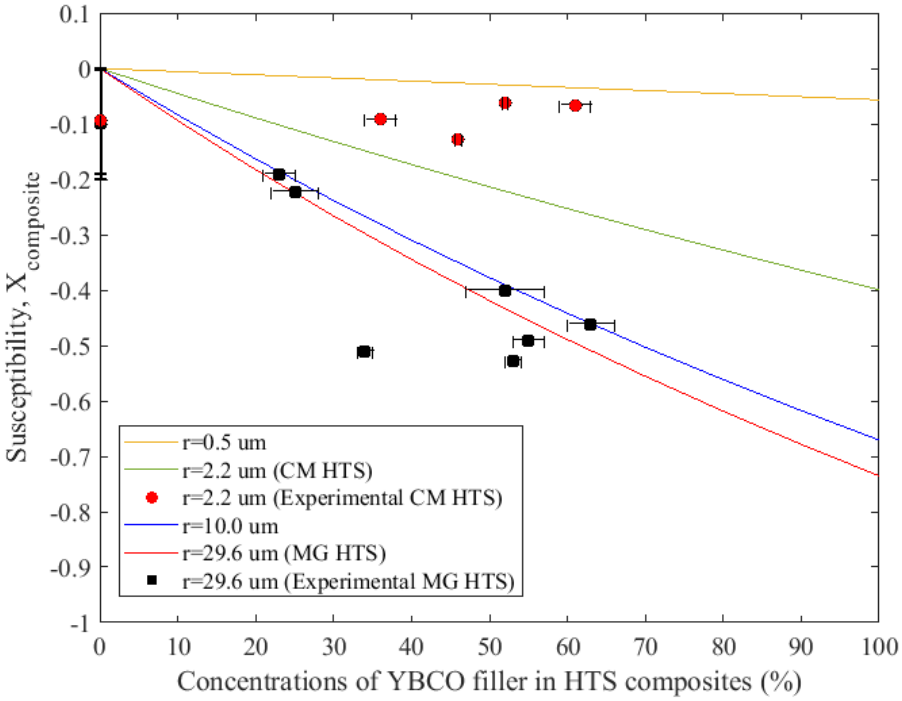


Figure 8.38 The susceptibility of the HTS composites as a function of concentrations of YBCO filler in epoxy matrix with differing YBCO particle sizes. The estimated vertical errors in these $\chi_{composite}$ values are shown for the pure epoxy samples based on the measurements reported in section 6.3.3.2. The $\chi_{composite}$ values for the models are as a function of volume fraction of YBCO filler in epoxy matrix.

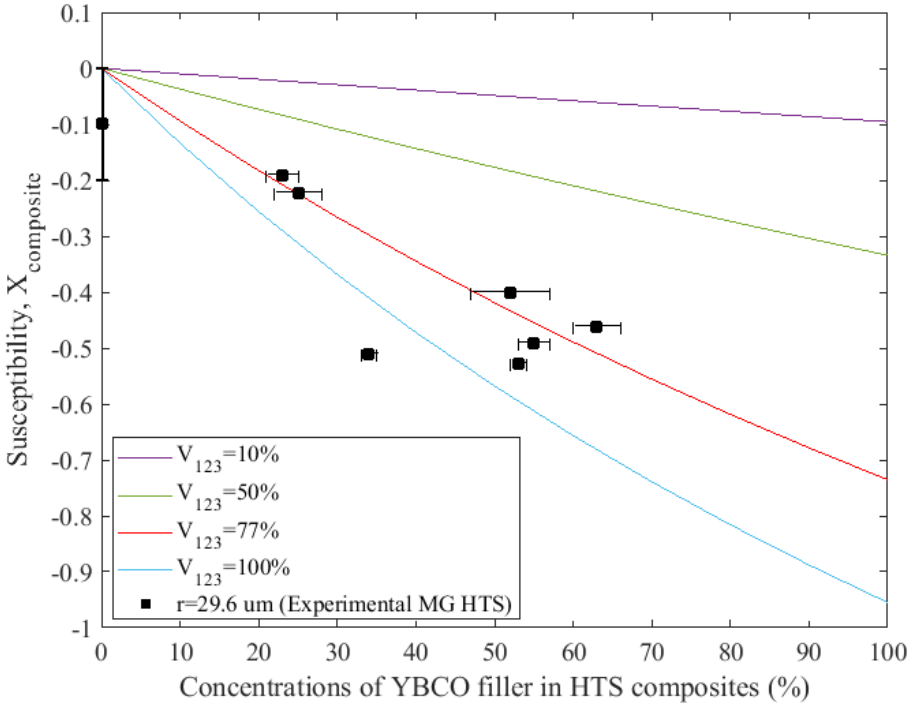


Figure 8.39 The susceptibility of the MG YBCO composites as a function of concentrations of YBCO filler in epoxy matrix with volume fractions of the spherical particles that are superconducting (V_{123}). The size of the YBCO filler is 29.6 μm. The estimated vertical error in this $\chi_{composite}$ value is shown for the pure epoxy samples based on the measurements reported in section 6.3.3.2. The $\chi_{composite}$ values for the models are as a function of volume fraction of YBCO filler in epoxy matrix.

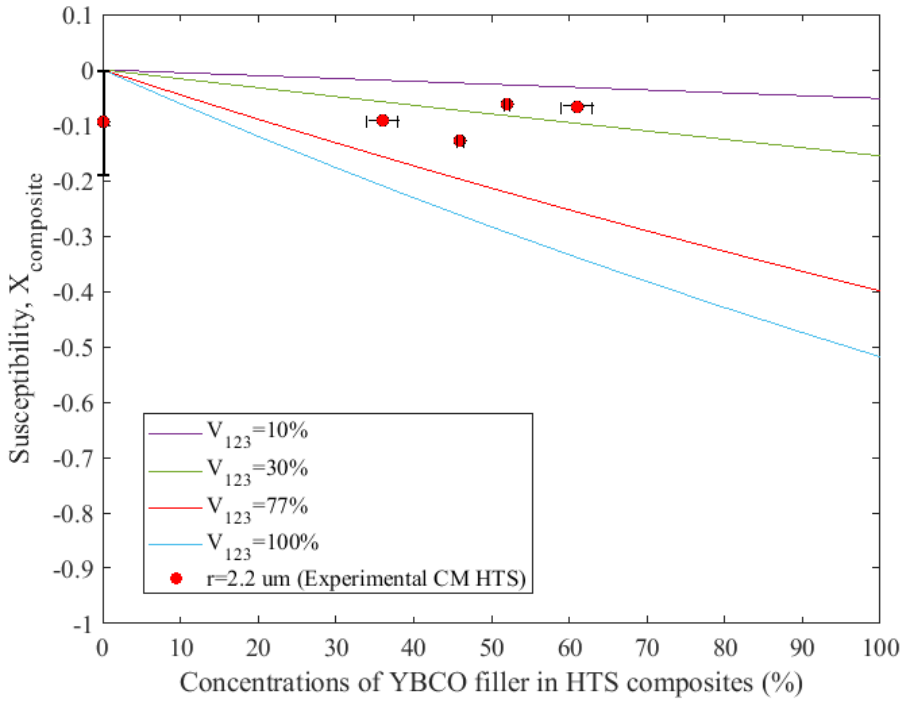


Figure 8.40 The susceptibility of the CM YBCO composites as a function of concentrations of YBCO filler in epoxy matrix with volume fractions of the spherical particles that are superconducting (V_{123}). The size of the YBCO filler is 2.2 μm. The estimated vertical error in this $\chi_{composite}$ value is shown for the pure epoxy samples based on the measurements reported in section 6.3.3.2. The $\chi_{composite}$ values for the models are as a function of volume fraction of YBCO filler in epoxy matrix.

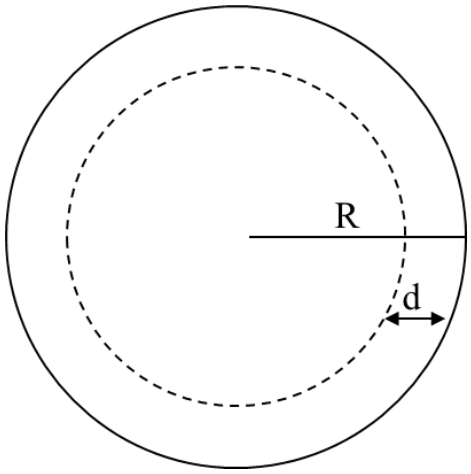


Figure 8.41 A schematic image shows a non-superconducting layer with thickness d on the surface of the superconducting grain with radius size, R.

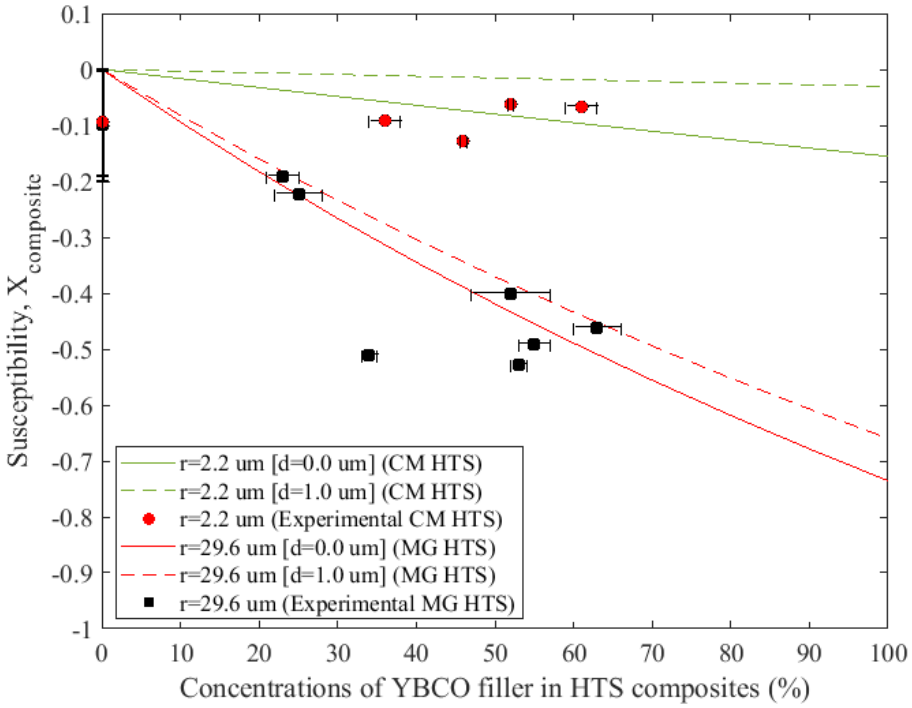


Figure 8.42 The susceptibility of the HTS composites as a function of concentrations of YBCO filler in epoxy matrix with a non-superconducting material layer on the YBCO filler. Dashed and straight lines are YBCO fillers with and without 1 μm non-superconducting material layer respectively. The estimated vertical errors in these $\chi_{composite}$ values are shown for the pure epoxy samples based on the measurements reported in section 6.3.3.2. The $\chi_{composite}$ values for the models are as a function of volume fractions of YBCO fillers in epoxy matrix.

8.5 Discussion and Conclusions

In this work, the HTS composites with the best microwave properties are fabricated using the melt-grown (MG) YBCO powder as a filler loaded in epoxy by the casting technique. This can be observed from the ε_{eff}, μ_{eff} and n values of MG HTS composites in Figure 8.28, Figure 8.29 and Figure 8.31. It has been found that the volume fraction and size of the YBCO filler makes a very significant impact on the electromagnetic properties of the HTS composites.

8.5.1 Influence of Sizes and Volume Fraction of YBCO fillers on Microwave Properties of the HTS composites

The n values increase with increasing volume fractions of YBCO filler in the HTS composites. This increase in n is due to the increase of the ε_{eff} of the HTS composites. This also means that the increase in ε_{eff} of HTS composites with increasing volume fraction of YBCO fillers are mainly attributed to the polarisation in the YBCO filler. The increase in ε_{eff} properties of the HTS composites is caused by ionic polarisation of the polymer and both atomic and ionic polarisation of the YBCO powder, which was largely independent of temperature and frequency in the range of 12 to 18 GHz used in this work. Another large contribution to ε_{eff} values of the HTS composites is interfacial polarisation, which occurs at the interface of the epoxy and YBCO particles within the HTS composites. Charges occur when an external field is applied to the HTS composite, and build up at the phase boundaries of YBCO particles and epoxy[6]. In this case, the higher the concentration of YBCO filler, the higher occurrence of interfacial polarisation in the HTS composites.

It has been found experimentally that the decrease of n at 77 K is caused by the decrease of μ_{eff} in the YBCO filler. This is in agreement with Golosovky *et al*. who has predicted the effect of μ_{eff} on the n values of YBCO/PMMA composites at 77 K[5]. It has been shown in this work that the use of the large YBCO filler (MG HTS YBCO) results in a significant drop in μ_{eff} from 1 to 0.6 at 77 K, with increasing area fractions from 0% to 63%. The decrease in μ_{eff} is due to the diamagnetic properties of the MG HTS composites at 77 K, which depend on particle size and concentrations. This diamagnetic effect can be observed from the negative magnetisation and irreversibility component of the hysteresis loops in Figure 8.37. The increase in magnitude of the

irreversibility loops with increasing volume fractions of YBCO filler in the MG HTS composites indicates the dependence of magnetisation properties on the area fraction of YBCO fillers in the HTS composites.

Figure 8.38, Figure 8.39 and Figure 8.42 have shown that these diamagnetic properties of the HTS composites depend strongly on the quality of YBCO powder, and were further analysed by their susceptibility values. The susceptibility values of the YBCO powder have been found to be affected by the volume fractions of superconducting phase YBCO-123 and the thickness of a non-superconducting layer on these YBCO particles. Ideally, the use of 100% superconducting phase MG YBCO particles without non-superconducting layer as a filler would be expected to show a larger decrease in susceptibility values of the HTS composites at 77 K. The non-uniform distribution of superconducting phase and existence of non-superconducting layer in my MG YBCO filler might have caused variations in the susceptibility values of the MG HTS composites. It has also been found in the same susceptibility analysis, that the use of small diameter commercial YBCO filler in the HTS composites caused no significant change in μ_{eff} at 77 K, indicating the crucial effect of particle size and quality of YBCO filler on the electromagnetic properties of HTS composites.

8.5.2 Effect of Casting Technique on Microstructure of HTS Composites

A higher density of agglomeration was observed in the CM HTS composites than the MG HTS composites. This is due to the particle size of CM YBCO filler which is smaller by one order of magnitude than the MG YBCO filler. This is expected as Pietsch described that particles with sizes less a few μm have a natural tendency to adhere to another particles and form agglomerates[4]. Since the particle sizes of the CM HTS powders used in this work fall into this range, it is not surprising that we observe

this high density of agglomerates in the HTS composites. Agglomeration of particles was initially developed in the powder preparation process as observed in Chapter 7. This is in agreement with Dancer *et al.* who has reported that agglomerations of dried powder occurs due to capillary and inter-particle forces[37]. It has been found in this work that the slow stirring process can reduce this agglomeration of particles and disperse powder uniformly in epoxy matrix. However, the stirring process does not seem able to eliminate the development of holes in the epoxy matrix.

Unlike particle agglomerations, holes are observed in both CM and MG HTS samples. Round holes are likely to be air trapped between the particles due to the difficulty in achieving good particle dispersion when mixing fine powders with the high viscosity polymer solution[3]. This air entrapment can be reduced by slowly stirring until the HTS/Epoxy mixture achieved gel condition, before pouring the mixtures into the mould. The slow stirring avoids agitation that can induce the trapping of air in the HTS mixture. However, this delicate process is not efficient at higher concentrations of HTS powder in the epoxy, due to the very low viscosity of the mixture, and hence holes are observed in HTS composites at high volume fractions of YBCO filler. This holes development might have induced porosity in the HTS composites and results in difficulty in precise control over the volume fractions of YBCO filler, and can cause some deviations from predicted values in electromagnetic properties, as can be seen in the HTS susceptibility values.

8.5.3 Conclusions

Casting is a conventional fabrication technique to produce simple shapes of HTS composites. However, there are several factors need to be carefully considered to control the production of high quality materials. A slow and delicate stirring process is required to reduce agglomerations of particles and holes in the HTS composites.

However, it has been observed that the use of larger MG YBCO particles can reduce agglomeration in the HTS composites. However, the formation of holes is unavoidable. Holes are likely to occur due to the stirring process during the mixing process.

Both MG HTS and CM HTS composites have been produced with a transition temperature 93 K and diamagnetic effect at 77 K. The electromagnetic and superconducting properties of the MG HTS composites are superior to the CM HTS composites. The size and quality of MG YBCO powder tends to produce MG HTS composites with larger magnetisation and superconducting properties than the CM HTS composites. The susceptibility studies have shown that the size of particles, volume fractions of these particles that are superconducting, and the thickness of any non-superconducting layer on the YBCO particles all have an effect on superconducting properties of the HTS composites.

The fault in the fabrication using the custom made PTFE jig has caused leakage of the epoxy mixture during the curing process, resulting in errors in the volume fraction (Vf) measurement of HTS composites. Due to the limited availability of the volume measurement technique, it is not obvious how to obtain more accurate measurements of volume fraction in these samples. Therefore, the measured area fraction (Af) using SEM analysis is the best method available to describe the composition of the HTS sample, and Af $\approx$ Vf was assumed for comparison with the mixing models to evaluate the microwave properties. Using this method, the mixing models such as Bruggeman and Lichtenecker equations can be used to approximate the concentrations of YBCO fillers in the HTS composites. However, the shape of the YBCO fillers used in this work is mostly non-spherical, causing deviations from the fitting curves. The leakage of epoxy resin solution during the curing process might affect the volume fractions of epoxy solution, leading to inaccuracy in YBCO filler volume fractions in the HTS composites.

This has caused limitations in providing VNA measurement errors based on sample-to-sample variability. The estimated errors in the microwave properties for the pure epoxy samples based on the measurements reported in section 6.3.3.2 are provided as errors for the microwave measurements in this work. The ε_{eff} values of MG HTS composites are enhanced with increasing area fractions of MG YBCO filler at both room and low temperature. A large drop of the μ_{eff} values are observed at 77 K, leading to a decrease in n at 77 K. This has enabled the electromagnetic properties of the MG HTS composites to be controlled by choice of loading fractions of YBCO fillers and temperature.

References

1 Golosovsky, M., Tsindlekht, M., Davidov, D. & Sarychev, A. Effective-medium approach to the microwave properties of the high-T_c superconductor-insulator composites. *Physica C: Superconductivity* **209**, 337-340 (1993).

2 Dancer, C. *Ceramic processing of magnesium diboride*, Thesis (D.Phil.)-University of Oxford, (2008).

3 Landel, R. F. & Nielsen, L. E. *Mechanical Properties of Polymers and Composites, Second Edition*. (Taylor & Francis, 1993).

4 Pietsch, W. *Agglomeration Processes: Phenomena, Technologies, Equipment*. (Wiley, 2008).

5 Golosovsky, M., Tsindlekht, M. & Davidov, D. Microwave propagation through superconductor-polymer composites. *Physical Review B* **46**, 11439-11444 (1992).

6 Abraham, R., Kuryan, S., Isac, J., Zacharia, A. K. & Thomas, S. Yttrium barium copper oxide-filled polystyrene as a dielectric material. *Journal of applied polymer science* **120**, 2233-2241 (2011).

7 A&M Fell (Manufacturing) Limited. *Liner 4-point probe*, <http://four-point-probes.com/fell.pdf> (1967).

8 Kes, P. H., Cardwell, D. A. & Ginley, D. S. *Handbook of Superconducting Materials: Flux pinning*. pp. 195 (Institute of Physics, 2003).

9 Bhadrakumari, S., Predeep, P. & Sheela, A. Magnetic levitation force measurement on HTSC ceramic/thermoplastic polymer composites. *Composites Science and Technology* **68**, 3230-3233 (2008).

10 Bhadrakumari, S. & Predeep, P. High-Tc superconductor/linear low density polyethylene (LLDPE) composite materials for diamagnetic applications. *Superconductor Science and Technology* **19**, 808 (2006).

11 Senoussi, S., Oussena, M. & Hadjoudj, S. On the critical fields and current densities of $YBa_2Cu_3O_7$ and $La_{1.85}Sr_{0.15}CuO_4$ superconductors. *Journal of Applied Physics* **63**, 4176-4178 (1988).

12 Nicolson, A. M. & Ross, G. F. Measurement of the Intrinsic Properties of Materials by Time-Domain Techniques. *IEEE Transactions on Instrumentation and Measurement* **19**, 377-382 (1970).

13 Hale, D. K. The physical properties of composite materials. *Journal of Materials Science* **11**, 2105-2141 (1976).

14 Campbell, A., Blunt, F., Johnson, J. & Freeman, P. Quantitative determination of percentage superconductor in a new compound. *Cryogenics* **31**, 732-737 (1991).

15 Lai, R., Bhattacharya, P. K., Alterovitz, S., Downey, A. & Chorey, C. Low-temperature microwave characteristics of pseudomorphic $In_xGa_{1-x}As/In_{0.52}Al_{0.48}As$ modulation-doped field-effect transistors. *IEEE Electron Device Letters* **11**, 564-566 (1990).

16 Shi, Y., Babu, N. H. & Cardwell, D. Development of a generic seed crystal for the fabrication of large grain (RE)–Ba–Cu–O bulk superconductors. *Superconductor Science and Technology* **18**, L13-L16 (2005).

17 Shi, Y., Babu, N. H., Iida, K. & Cardwell, D. A. The effect of very high barium content in the precursor on the properties of GdBCO single grain bulk superconductors. *Journal of Materials Research* **24**, 10-18 (2009).

18 Seuntjens, J. M., Clark, F. Y., Headley, T. J., Geulich, F. E. & Yang, N. Y. C. Image analysis of superconducting composites. *IEEE Transactions on Applied Superconductivity* **3**, 729-733 (1993).

19 Trybuła, Z., Stankowski, J. & Baszyński, J. Dielectric study of $YBa_2Cu_3O_{7-\delta}$ ceramic in a microwave electric field. *Physica C: Superconductivity* **156**, 485-488 (1988).

20 Lagarkov, A., Sarychev, A., Smychkovich, Y. R. & Vinogradov, A. Effective medium theory for microwave dielectric constant and magnetic permeability of conducting stick composites. *Journal of Electromagnetic Waves and Applications* **6**, 1159-1176 (1992).

21 Maxwell, G. JC,"Colours in metal glasses and metal films,". *Philos. Trans. R. Soc. London, Sect. A* **3**, 385-420 (1904).

22 Bruggeman, D. Dielectric constant and conductivity of mixtures of isotropic materials. *Ann Phys (Leipzig)* **24**, 636-679 (1935).

23 Lichtenecker, K. v. Der elektrische Leitungswiderstand künstlicher und natürlicher Aggregate. *Phys. Z* **25**, 225-233 (1924).

24 Behrooz, A. & Zettl, A. Normal state a.c. conductivity of $YBa_2Cu_3O_{7-\delta}$. *Solid State Communications* **70**, 1059-1063 (1989).

25 Testardi, L. R., Moulton, W. G., Mathias, H., Ng, H. K. & Rey, C. M. Large static dielectric constant in the high-temperature phase of polycrystalline $YBa_2Cu_3O_x$. *Physical Review B* **37**, 2324-2325 (1988).

26 Dang, Z. M., Shen, Y. & Nan, C. W. Dielectric behavior of three-phase percolative Ni–$BaTiO_3$/polyvinylidene fluoride composites. *Applied Physics Letters* **81**, 4814-4816 (2002).

27 Lei, Q. *All-dielectric composites for metamaterial applications*, Thesis (D.Phil.)--University of Oxford, (2016).

28 Dang, Z. M. *et al.* Fundamentals, processes and applications of high-permittivity polymer–matrix composites. *Progress in Materials Science* **57**, 660-723 (2012).

29 Goncharenko, A. V., Lozovski, V. Z. & Venger, E. F. Lichtenecker's equation: applicability and limitations. *Optics Communications* **174**, 19-32 (2000).

30 Poole, C. P., Farach, H. A. & Creswick, R. J. *Superconductivity 2nd Edition*. Vol. 2nd Edition pp. 141-415, (Academic Press, 2007).

31 Clem, J. R. & Kogan, V. G. Theory of the Magnetization of Granular Superconductors: Application to High-Tc Superconductors. *Japanese Journal of Applied Physics* **26**, 1161 (1987).

32 Krusin-Elbaum, L., Malozemoff, A. P., Yeshurun, Y., Cronemeyer, D. C. & Holtzberg, F. Temperature dependence of lower critical fields in Y-Ba-Cu-O crystals. *Physical Review B* **39**, 2936-2939 (1989).

33 Cheah, H., Porch, A. & Waldram, J. Microwave conductivity of powdered unaligned $YBa_2Cu_3O_{7-\delta}$. *Physica B: Condensed Matter* **165**, 1195-1196 (1990).

34 Goldfarb, R. B. & Minervini, J. V. Calibration of ac susceptometer for cylindrical specimens. *Review of Scientific Instruments* **55**, 761-764 (1984).

35 Wang, Y., Edwards, E., Hooper, I., Clow, N. & Grant, P. Scalable polymer-based ferrite composites with matching permeability and permittivity for high-frequency applications. *Applied Physics A* **120**, 609-614 (2015).

36 Hibbs, A., Eberhardt, F., Campbell, A. & Male, S. Effect of particle size on the magnetization of high T_c powders. *Cryogenics* **28**, 678-680 (1988).

37 Dancer, C., Prabhakaran, D., Crossley, A., Todd, R. & Grovenor, C. The effects of attrition and ball milling on the properties of magnesium diboride. *Superconductor Science and Technology* **23**, 065015 (2010).

9 Fabrication of HTS Composites by 3-D Printing

9.1 Making YBCO/ABS Composites 214
9.2 Extrusion of YBCO/ABS Filaments 215
9.2.1 Optimising Extrusion for YBCO Loaded ABS Filaments 216
9.2.2 Distribution of YBCO Particles in The ABS filament 219
9.2.3 Effect of Particle Size on The Extrusion Process 223
9.2.4 Magnetisation Properties of YBCO Loaded ABS Filaments 226
9.2.5 Magnetic Susceptibilities and Permeability of YBCO Loaded ABS Filaments 229
9.3 3-D Printing Process 230
9.3.1 Optimising 3-D Printing Parameters 230
9.4 Characterisation of 3-D Printed YBCO/ABS Composites 234
9.4.1 Single Printed Material 235
9.4.2 Graded Materials 246
9.4.3 3-D Printed Split-Ring Resonator Structures (SRRs) 254
9.5 Discussion and Conclusions 260
References 262

It has been shown previously in Chapter 8 that HTS composites with controllable electromagnetic properties can be produced by a simple casting technique. In order to realise spatial variations of properties in electromagnetic applications, a rapid prototyping technique has been used for the fabrication of HTS composites. The chosen technique is an additive manufacturing (AM) process which has been increasingly used to fabricate metamaterials for microwave applications[1,2].

One of the most established and affordable AM processes is fused deposition modelling (FDM) using a 3-dimensional (3-D) printer, which has been reported to be one of the most mature technologies for printing 3-D dielectrics[3] as well as artificial magnetic materials[4]. The work in this chapter aims to investigate 3-D printing of HTS composites

with controlled ε_{eff} and μ_{eff} values. This work includes fabricating the feedstock filament using extrusion as well as optimising the printing processes for HTS composites. Characterisation of the HTS composites produced by this technique will be reported later in the chapter. The microstructure and electromagnetic properties of these printed HTS composites are compared with samples produced using the casting technique, and these results will be discussed at the end of this chapter.

Three stages were involved in the 3-D printing process; preparing a mixture of YBCO powder and ABS to form a composite, extruding a YBCO/ABS composite filament suitable for use in our 3-D printers and printing HTS composite structures. The optimisation of the filament extrusion and 3-D printing process to produce reproducible YBCO/ABS composites needed careful study because 3-D printers are only able to operate with filaments with a limited range of properties. For example, higher loading fillers in HTS composites produce brittle feedstock filaments which are not suitable for the 3-D printing process. The 3-D printer parameters were set initially to suit the pure ABS filament, but needed to be altered for YBCO/ABS composite filaments as discussed in the following sections.

9.1 Making YBCO/ABS Composites

The general method for mixing HTS powders and ABS was discussed in Chapter 6, and I applied this by adding my YBCO powder to the ABS polymer to produce YBCO/ABS composites. MG HTS YBCO powder with size d_{50} =59.2 μm (Mastersizer measurement of median value in section 7.3.3) was used as a superconducting filler in the composite. Based on the results of cast HTS composites (Chapter 8), I prepared YBCO/ABS composites by mixing 40 g of YBCO powder (mix of melt-grown YBCO fragments) and 26 g of ABS pellets (MFI-22, Styrolution, Frankfurt am Main) in 200 ml

acetone to produce YBCO/ABS powder with nominal YBCO volume fractions of 20 vol%.

9.2 Extrusion of YBCO/ABS Filaments

YBCO loaded ABS filaments were extruded from the YBCO/ABS powder using a Noztek extruder (see Figure 6.1 in Chapter 6). The working principles of the extruder can be found in section 6.2.3 of Chapter 6. These YBCO loaded ABS filaments were later to be used as the feedstock material in the 3-D printer. In order to fit into the 3-D printer, the diameter of the feedstock filaments must be close to 1.75 mm[5].

In the standard extruding process for pure ABS filaments, a 1.75 mm die with extrusion temperature between 180 to 200 ºC typically produces 1.75±0.04 mm diameter filament[6], which is the optimum size to be used as a feedstock filament for our 3-D printer. However, in my preliminary work the extrusion of 20 vol% YBCO loaded ABS composites using MG YBCO filler ($d_{50} = 59.2\ \mu m$) produced 2.20±0.01 mm diameter filament using a 1.75 mm nozzle at a similar extruding temperature. This 47% oversized filament is due to YBCO particles, which added to the extra size on the die swell. This die swelling can cause an expansion of extruded filament that will limit its application in the 3-D printer. To overcome this problem, a smaller die was used to produce a filament with size less than 1.8 mm in diameter for 3-D printing in the instruments available to this project. However, the filament fabrication process is limited by the high loading YBCO filler that can caused the filament becomes "too brittle and fragile" to handle[4].

In this study, all of the extruding parameters had to be fine-tuned to achieve the optimum diameter of 20 vol% YBCO loaded ABS filament without losing the superconducting properties. In order to extrude YBCO loaded ABS composite with

precise control on the diameter of the filament, the optimum extruding conditions for YBCO loaded ABS filament were studied by changing both the extrusion temperature and the die diameter.

9.2.1 Optimising Extrusion for YBCO Loaded ABS Filaments

Since the availability of YBCO powder was limited in this work, the process parameters were first studied using pure ABS pellets. The reason for this study was to understand the effect of tuning the extrusion temperature and die diameter on the final size of the extruded filament. As documented in the *Noztek User Manual*[6], the recommended set temperature for ABS extrusion is between 180 to 200 ºC[6], thus the melt temperature of 180 ºC was used as a baseline for this study. In order to study the effect of smaller dies on the extrusion process, custom made dies of size 1.3, 1.4 and 1.5 mm designed by Dr. F. Castles were used.

Figure 9.1 shows the diameter of the extruded ABS filaments as a function of both extrusion temperatures and die size. The diameter of the extruded filaments increases with the diameter of the die as expected. Moreover, the diameter of the filament decreases with increasing temperature for all sizes of dies, as predicted by the Noztek manual[6]. The reason for the increase in the diameter of the filament is swelling of the molten ABS as it leaves the die, which caused expansion of the filament. By increasing the melt temperature, the melt viscosity is decreased which leads to slower polymer flow exiting the die, which gives time for the filament to recover its die shape, resulting in less apparent die-swelling[7], hence smaller die expansion.

Since the required filament size for the 3-D printer is 1.75±0.04 mm, the extrusion temperature and die diameter that can produce ABS filaments within 1.7 mm and 1.8 mm (indicated by dashed lines on Figure 9.1) were studied. Ten measurements were

taken along 1 m of each extruded ABS filament using a digital vernier. The targeted filament sizes can be achieved using 1.5 mm die and extruding temperatures of 170 °C and 180 °C. This tolerance value was set based on the direct observation of the size of the feedstock filament that can be manually fed through the feed pinch roller of the 3-D printer.

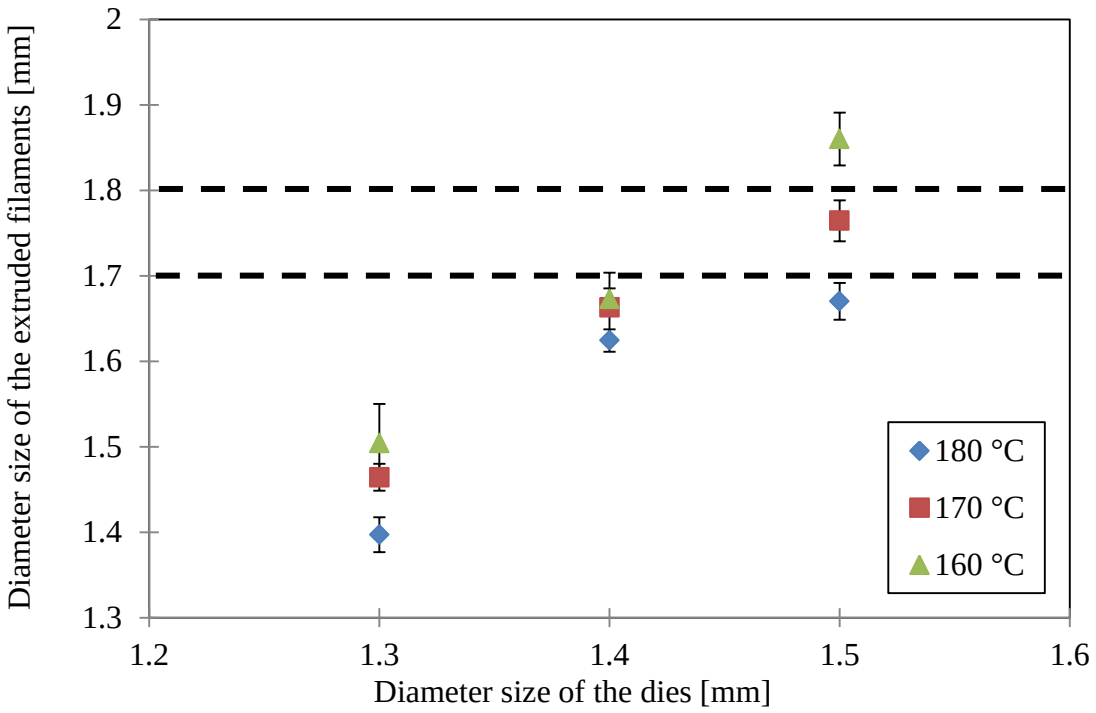


Figure 9.1 The diameter of the extruded ABS filaments as a function of the dimension of the dies and extrusion temperature. The filament sizes were the average of 6 points measured along 1 m of extruded filament. The dashed lines at 1.7 and 1.8 mm indicate the range of diameter required for feedstock for the 3-D printer.

The optimum parameters for extruding YBCO loaded ABS filaments were also investigated by considering the effect of die sizes, the die swelling phenomenon and the particle size effect on the YBCO powder in the ABS filament. Temperature adjustments were made by changing the extrusion temperature in 5 ºC steps as recommended by Noztek[6]. In order to optimise the die, two sizes were used, the standard 1.75 mm die provided by Noztek to produce pure ABS filament with dimension of size 1.75±0.04 mm, and a custom made 1.5 mm die designed by Dr. F. Castles used to produce loaded ABS filaments.

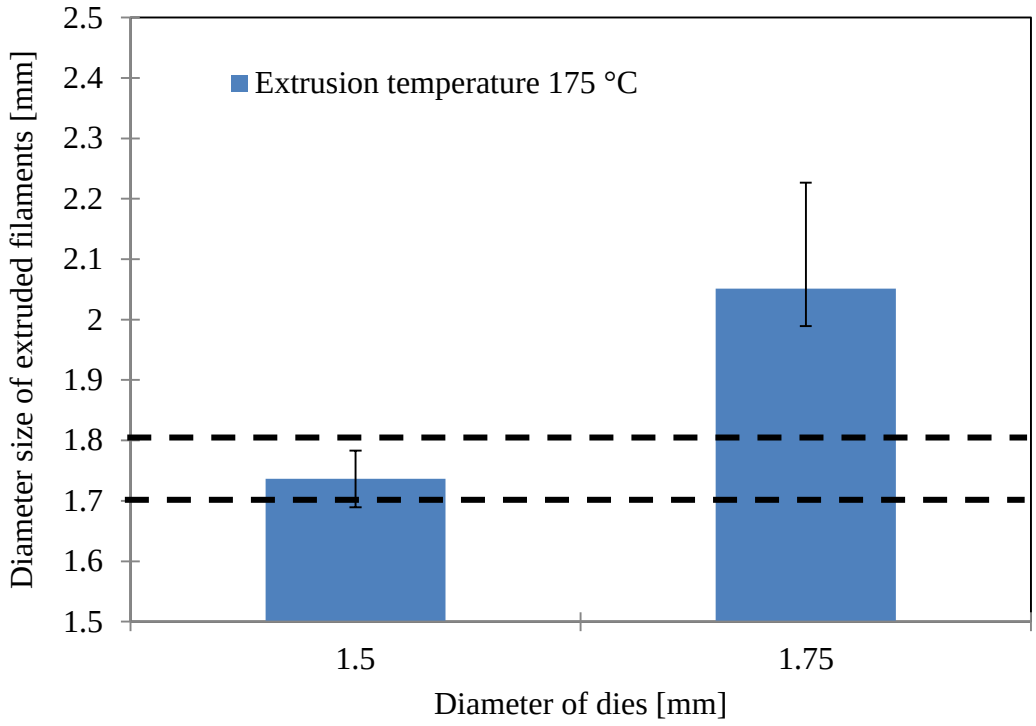


Figure 9.2 The diameter of extruded YBCO loaded ABS filaments. The dashed lines at 1.7 and 1.8 mm indicate the range of diameter required for the feedstock of the 3-D printer.

Figure 9.2 shows the diameters of YBCO loaded ABS filaments extruded at 175 °C. The average diameter of the YBCO loaded ABS filaments with the smaller die was 1.74±0.05 mm, and 2.05±0.06 mm with the larger die indicating as before an expansion of the composite filaments of 16 and 17% respectively due to die swelling. The choice of 175 ºC as the extrusion temperature has shown good control over the diameter of the YBCO loaded ABS filaments, especially with the 1.5 mm die. Even though the tolerance values are slightly higher than those documented by Noztek (±0.04 mm), the diameter of these composite filaments is still within the required filament size for the 3-D printing process. Hence, the extrusion of YBCO loaded ABS filament was optimised to produce the filament of dimension sizes between 1.7 mm and 1.8 mm by using a 1.5 mm die and 175 °C extrusion temperature.

9.2.2 Distribution of YBCO Particles in The ABS filament

The particle distribution study was aimed to provide an understanding on the effect of the extrusion process on the uniformity of particle distribution in the filament. Cross sections of YBCO loaded ABS filaments were cut and ground into rods with thicknesses around 2-4 mm. The YBCO loaded ABS rods were fixed between stacked aluminium bars with thickness around 2-4 mm and mounted on an aluminium stub (diameter size 25 mm and height 10 mm) before grinding on a wet silicon carbide paper (SiC Grinding Disc, Grade 4000, dimension 250 mm in diameter) as in Figure 9.3. The polishing ensemble was made to produce YBCO loaded ABS rod with a flat cross sectional surface and thickness suitable for morphology observation using optical microscopy and SEM.

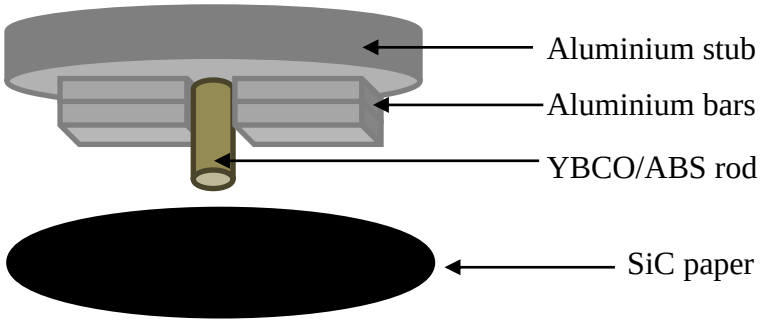


Figure 9.3 Grinding set up for YBCO loaded ABS rod.

Figure 9.4 shows typical cross sectional images of the extruded pure ABS and YBCO. loaded ABS filaments. The YBCO loaded ABS filament can be observed to contain embedded bright particles of sizes 10 – 50 μm uniformly distributed across the matrix. No holes can be seen in these optical images, although both samples show scratches from the grinding process. The BSE and SE images show more detailed morphology images of the YBCO particles in the ABS matrix, Figure 9.5 and Figure 9.6.

The disc samples were carbon coated and painted with carbon dag to reduce charging. Particles with sizes less than 100 μm were observed dispersed uniformly in the YBCO loaded filament. This can be seen clearly from the BSE images of the composite filament, Figure 9.5, where the bright contrast of the YBCO particles are shown to be individually scattered in the low contrast matrix. The image shows good uniform YBCO particles distribution, indicating a well-controlled extrusion process. The YBCO loaded ABS filament can be seen to contain individual ceramic particles separated by the matrix, indicating no formation of an interconnected network between YBCO particles. Other than YBCO particles, a small number of holes can be seen in the YBCO loaded ABS filament in Figure 9.6 (f)), which I suspect pull out of the YBCO particles during the sample preparation procedures for SEM measurement such as cutting and grinding.

EDX analysis, Figure 9.7, confirms that the bright particles are YBCO powder, with an estimated volume fraction of YBCO-211 ranging from 24% to 47% as shown in Table 9.1. This is in good agreement with the estimated volume fraction of YBCO-211 in YBCO powder analysed in Chapter 7, indicating that the extrusion process has no effect on the YBCO phase distribution. A small amount of YBCO powder can be also observed in the ABS filament. This is due to cross contamination in the Noztek extruder.

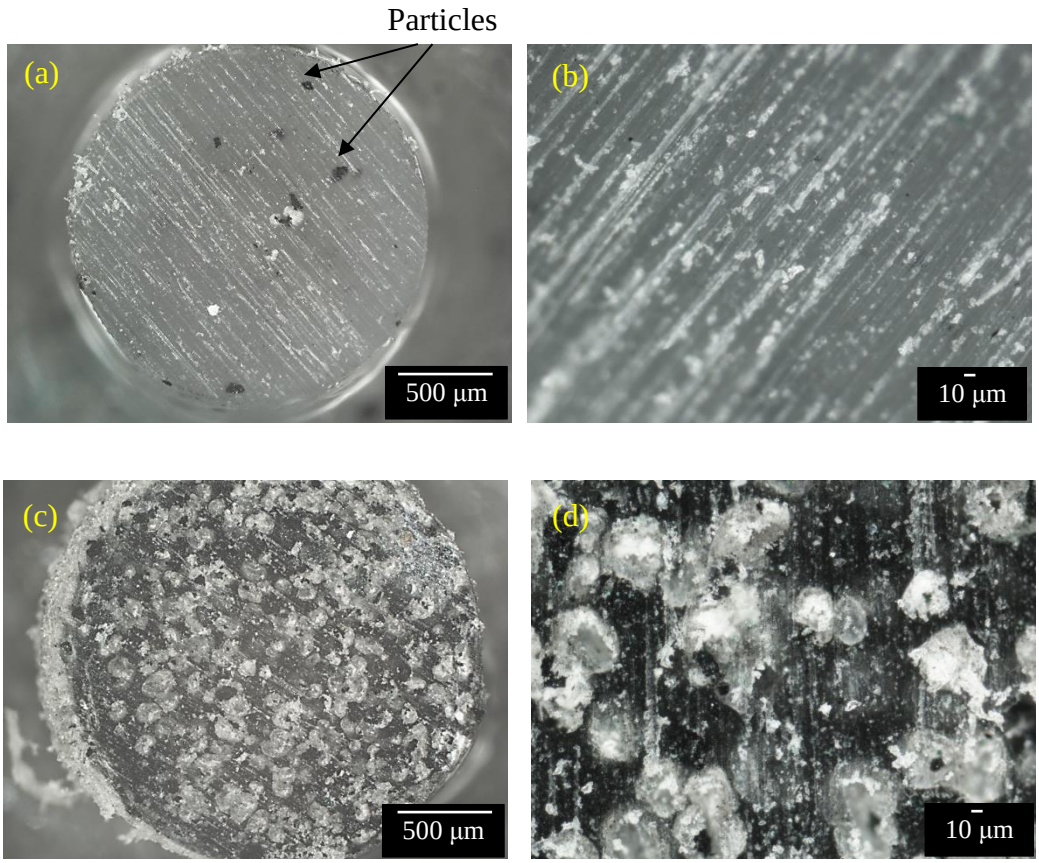


Figure 9.4 Optical images of the cross section of extruded ABS and YBCO loaded ABS filaments. (a) and (b) are an ABS filament taken at 2.5X and 10X magnifications respectively, (c) and (d) are a YBCO loaded ABS filament.

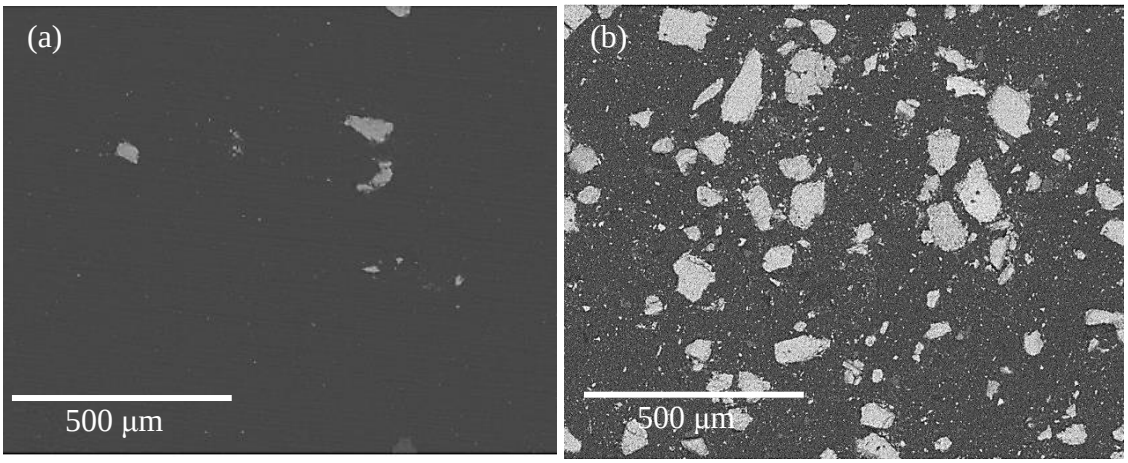


Figure 9.5 BSE images of the cross section of the (a) ABS and (b) YBCO loaded ABS filament.

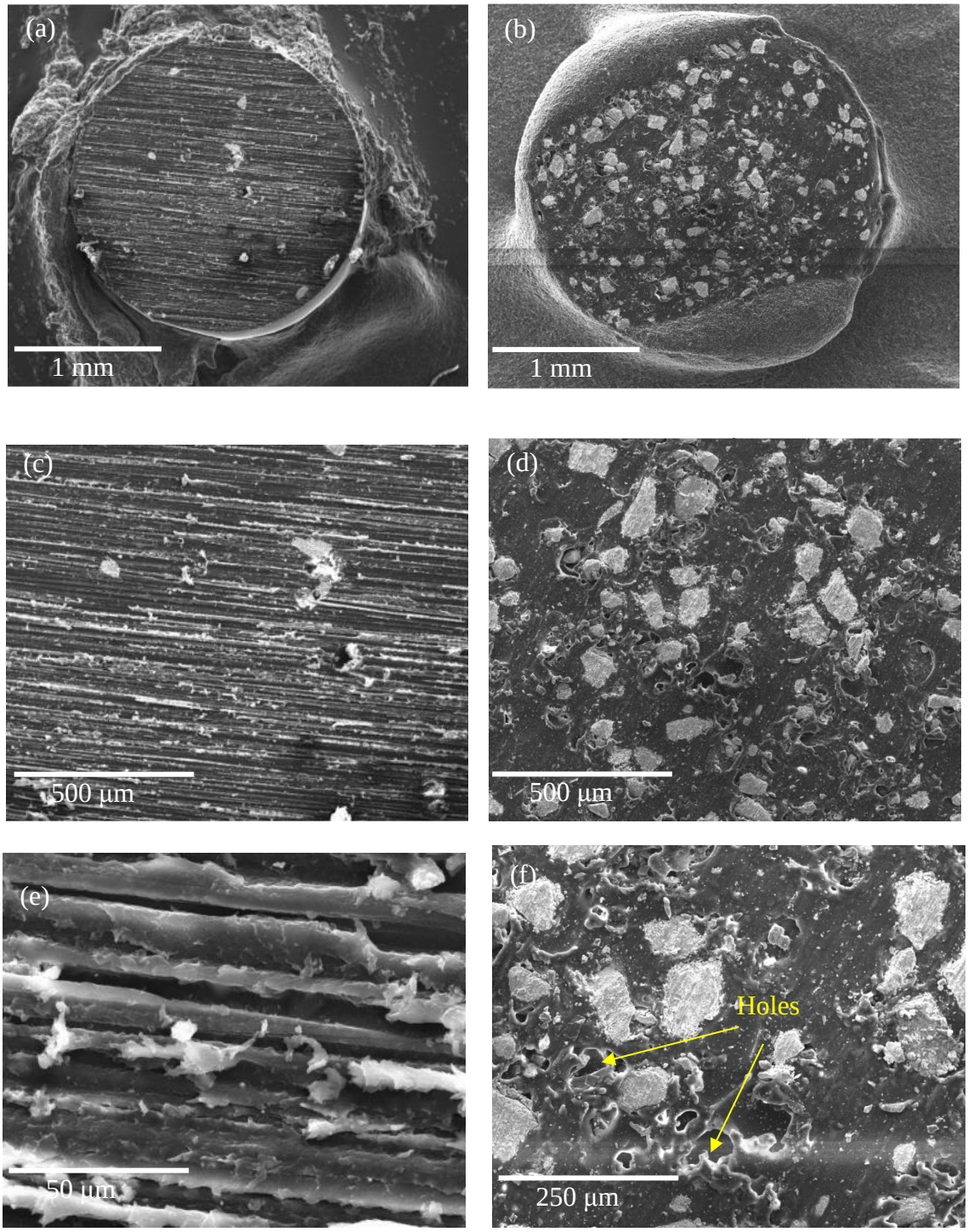


Figure 9.6 SEM images of the cross sections of both ABS and YBCO loaded ABS filaments. (a), (c) and (e) are images of the cross section of the ABS filament and (b), (d) and (f) are images of the YBCO loaded ABS filament.

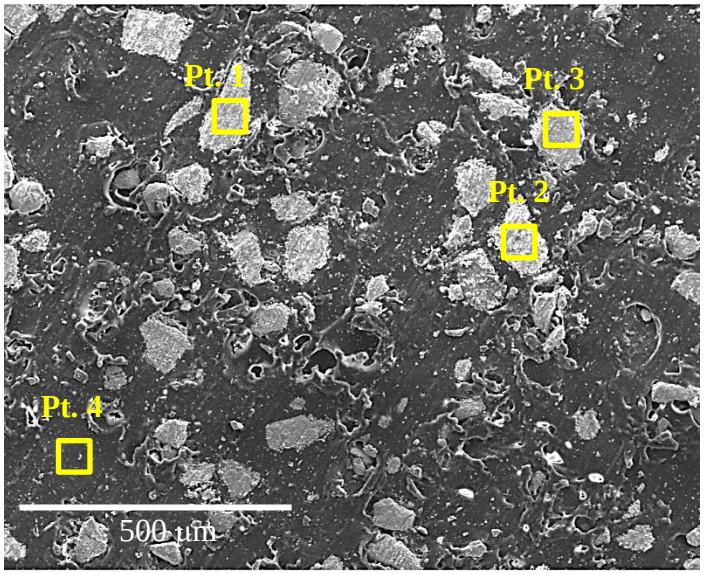


Figure 9.7 EDX analysis of the YBCO loaded ABS filament. Boxes indicate area scanning of particles and background for elemental analysis.

Table 9.1 EDX analysis of the YBCO loaded ABS filament

Elements	Y	Ba	Estimated volume fraction of YBCO-211 in YBCO particles [%]
Pt. 1	8.0	8.3	47
Pt. 2	1.9	2.7	24
Pt. 3	10.3	6.0	32
Pt. 4	0.1	0.2	Nil

9.2.3 Effect of Particle Size on The Extrusion Process

The effect of YBCO powder size on the extrusion process has been investigated. 20 vol% YBCO loaded ABS filament was prepared using YBCO powder of average size, $d_{50} = 20.3\,\mu m$. A similar 1.5 mm die was used to extrude an YBCO loaded ABS filament with these smaller particles. Figure 9.8 shows the diameter of the YBCO loaded ABS filament with smaller YBCO powder is 1.73±0.04 mm, which is comparable with the documented tolerance value of the ABS filament, 1.75±0.04 mm[6]. This is an ideal extrusion condition to produce consistent and small tolerance values in the size of YBCO loaded ABS filament.

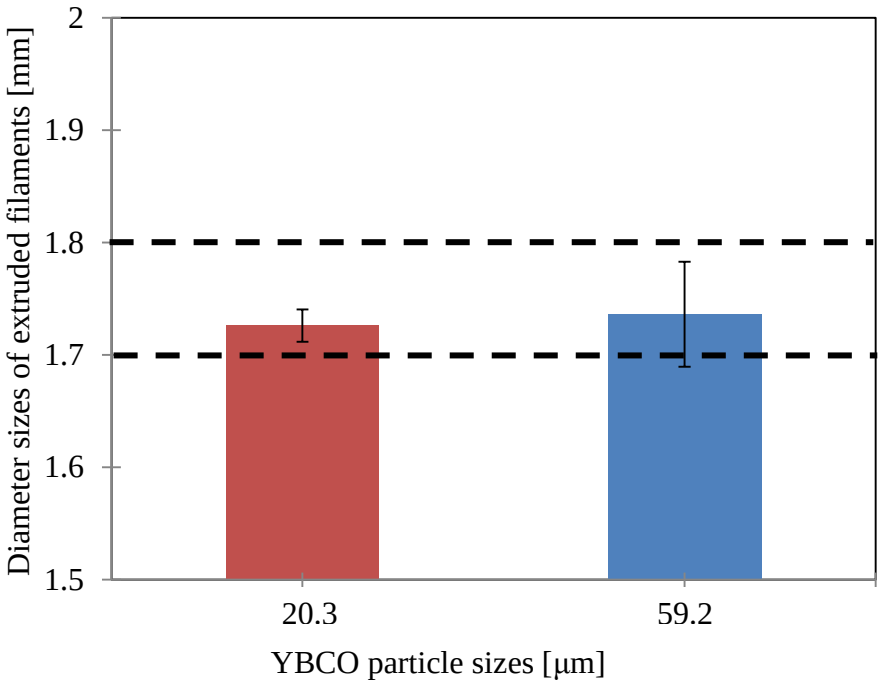


Figure 9.8 The diameter of the extruded YBCO loaded ABS filaments using the 1.5 mm die. The bar colour indicates particle sizes of the YBCO powder. The dashed lines at 1.7 and 1.8 mm indicate the range of diameter required for the feedstock of the 3-D printer.

The effect of the extrusion process on the distribution of the finer YBCO powder in the ABS matrix has been investigated. Figure 9.9 and Figure 9.10 show SE and BSE images of the cross section of these YBCO loaded ABS filaments, with particles of size less than 10 μm uniformly distributed in the ABS matrix, indicating a well-controlled extrusion process for small YBCO particles. Figure 9.9 (d) shows those irregular holes with size approximately similar to the YBCO particles (< 10 μm) could be seen from the cross-sectional surface of YBCO/ABS composite. From the irregular shape of holes, these could be artefacts resulting from pull out of the YBCO particles during the sample preparation procedures for SEM measurement such as cutting and grinding.

There is also a possibility that holes can be developed from the manufacturing process. This type of hole is likely to be induced due to insufficient drying of the precursor YBCO/ABS composite before extrusion. However, these holes are likely to be spherical or near-spherical in shape (see Figure 5.2 in Chapter 5). Even though the drying process

of YBCO/ABS composites was carried out at room temperature for 24 hours, there is still a possibility of the moisture trapped in the YBCO/ABS composites. As discussed in Chapter 5 section 5.1.2, the precursor YBCO/ABS composite was prepared using the *indirect method*, which required mixing YBCO fillers into dissolved ABS solution and dried at room temperature to form YBCO/ABS powder. According to Giles *et al*., improper drying process could result in moisture trapped in the polymer and this could convert to steam in the high temperature extrusion process, causing defects and surface imperfections such as holes, splay or foamy products depending on the amount of the trapped moisture in the polymer[8]. There are several ways to reduce the moisture trapped in the precursor powder. Implementing the *direct method* (refer to Chapter 5 in section 5.1.2) for preparing precursor powder could ideally reduce the potential for moisture trapping in the polymer without having the need to dissolve the polymer into solution, and fillers can directly mix to the melted polymer in the extruder prior to the extrusion process. Another method to remove moisture from the precursor powder is evaporation in an oven. Huang *et al*. suggested that the subsequent vacuum treatment on the precursor mixture after drying process could remove moisture efficiently[9].

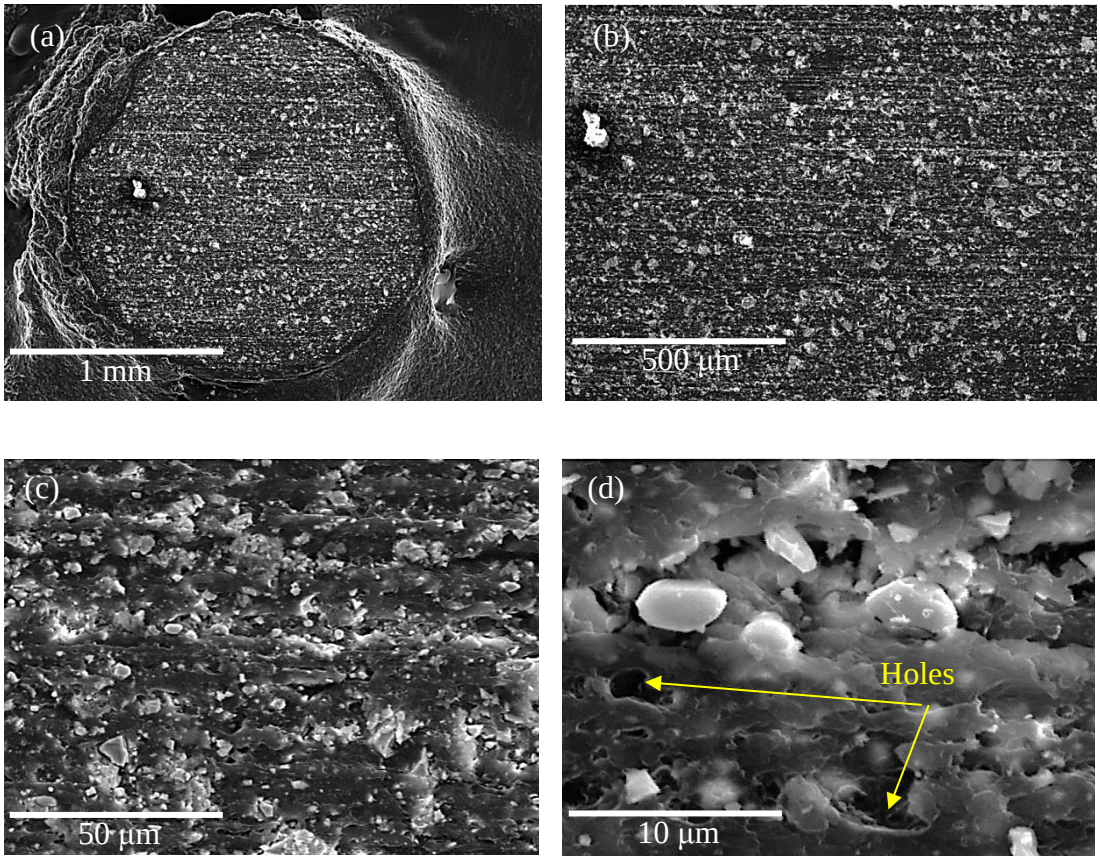


Figure 9.9 SEM images of the extruded YBCO loaded ABS filament with smaller YBCO particles taken at (a) 50X, (b) 100X, (c) 1000X and (d) 5000X.

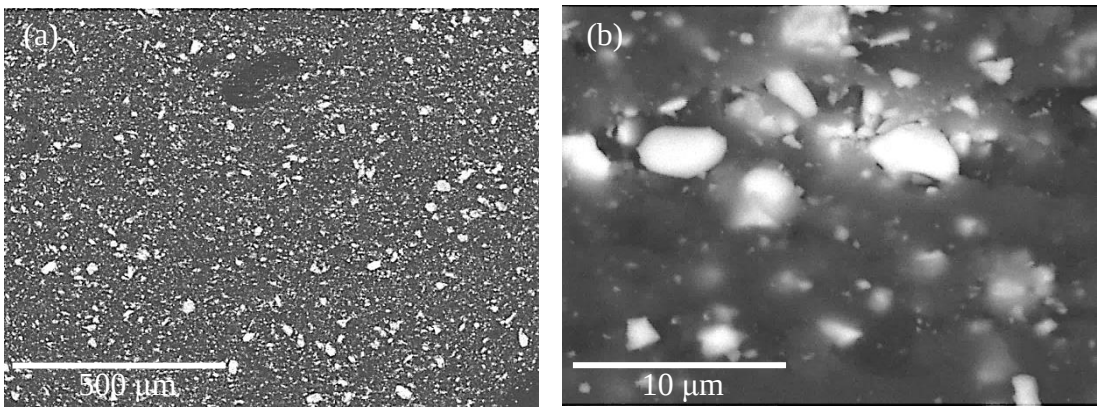


Figure 9.10 BSE images of the extruded YBCO loaded ABS filament with smaller YBCO particles taken at (a) 100X and (b) 5000X.

9.2.4 Magnetisation Properties of YBCO Loaded ABS Filaments

These YBCO loaded ABS filaments (large and small YBCO powders) have been measured for their magnetisation properties. The sizes of YBCO powder for these two types of samples are described in Table 9.2. Each YBCO/ABS filament was cut into

cylindrical samples and loaded into a plastic capsule for SQUID measurements. The critical temperature and magnetisation properties of these YBCO/ABS filaments were measured at 7 K and 77 K.

Table 9.2 YBCO powder size loaded in ABS filaments

Samples	**Powder size, d_{50} [µm]**
Fine YBCO/ABS	20.3
Coarse YBCO/ABS	59.2

Figure 9.11 shows a large drop of magnetic moment at 93 K, corresponding to the superconducting transition temperature, T_c, of both fine and coarse YBCO/ABS filaments. The T_c is consistent with the properties of the source powder. As expected the magnetisation properties of both fine and coarse YBCO/ABS have weaker magnetisation signals than their source powder, due to the 20 vol% loading of YBCO powder in the composite filaments.

A typical hysteresis loop characteristic of the HTS composites can be seen for the YBCO/ABS filaments at both 7 K and 77 K, Figure 9.12 and Figure 9.13 respectively. Unlike the cast HTS composite, the hysteresis loop was measured at 7 K instead of 2 K. The amplitude of the hysteresis loop of the coarse YBCO powder is one order of magnitude larger than that filament with fine YBCO powder at both 7 K and 77 K. This is consistent with the properties of the source powder, and is related to the size of particle and estimated volume fraction of YBCO-211 in the YBCO particles in the filament as discussed in Chapter 4.

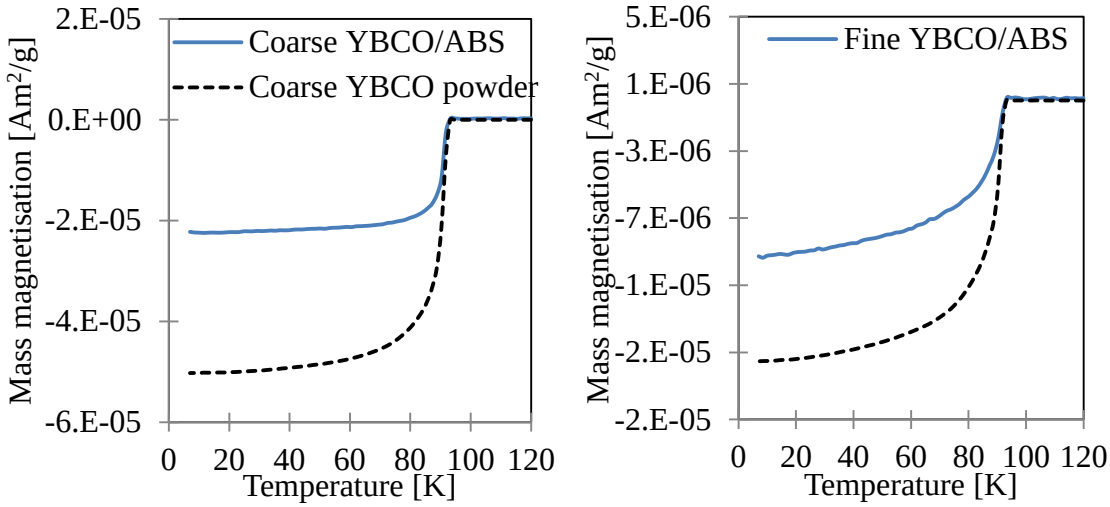


Figure 9.11 Magnetisation measurements showing T_c at 93 K for YBCO loaded ABS filaments.

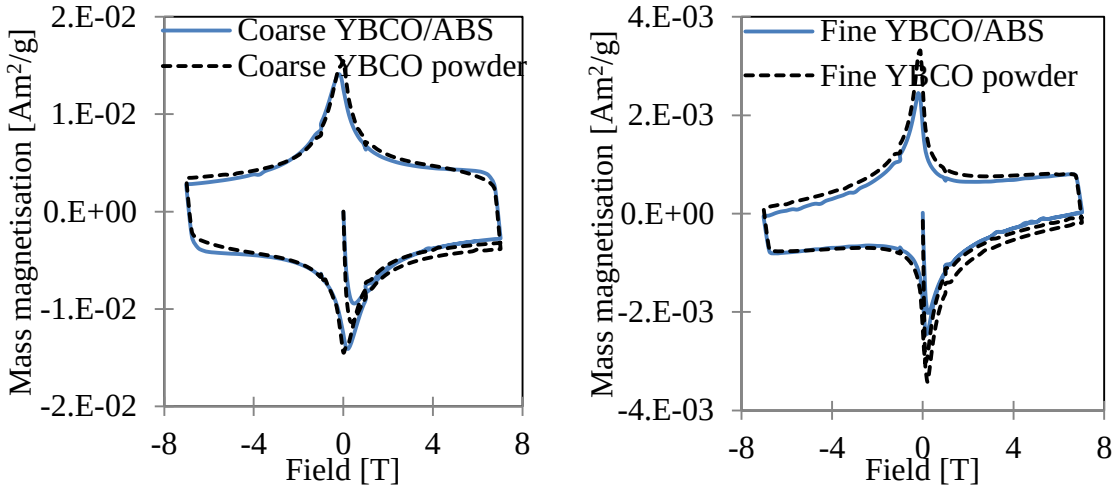


Figure 9.12 The hysteresis curve of YBCO loaded ABS filament at 7 K. Note the change of scales.

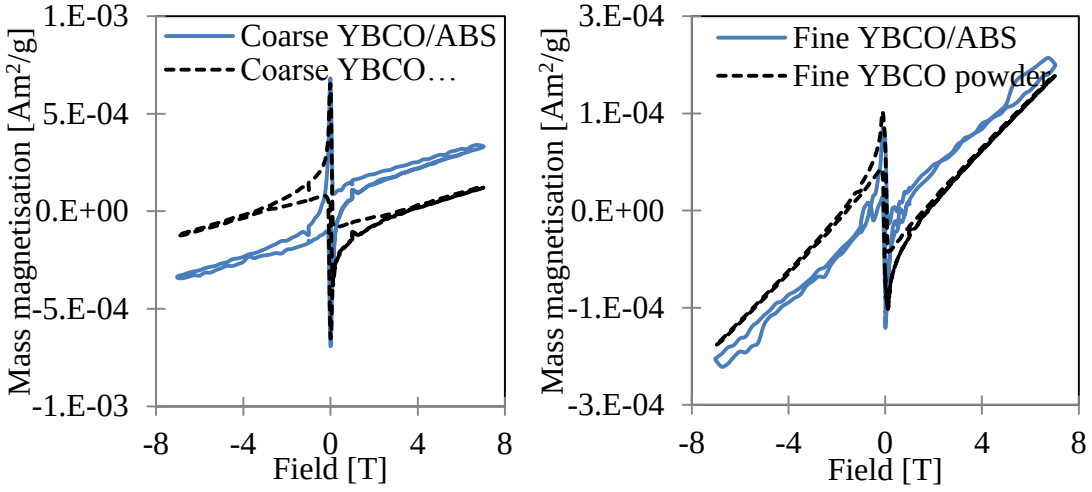


Figure 9.13 The hysteresis curve of YBCO loaded ABS filament at 77 K. Note the change of scales.

9.2.5 Magnetic Susceptibilities and Permeability of YBCO Loaded ABS Filaments

SEM images of both fine and coarse YBCO/ABS filaments have shown isolation of YBCO particles embedded in the ABS matrices. The isolation of the YBCO particles has enabled the calculation of effective magnetisation susceptibility, χ_{eff}, of both YBCO/ABS filaments.

The lower critical field values for single crystal YBCO are 520 mT[10] and 10-20 mT[11] at 7 K and 77 K respectively for field in the c-direction. This enabled measurement of several points of the magnetisations, M, below the lower critical field values using the SQUID results. The χ_{eff} values can be calculated using $M = \chi_{eff}H$, where H is the applied field. μ_{eff} was then calculated using $\mu_{eff} = \chi_{eff} - 1$, and Table 9.3 summarised the μ_{eff} values of YBCO loaded ABS filaments of both fine and large YBCO powder at 7 K and 77 K.

Table 9.3 Magnetic permeability μ_{eff} of 20 vol% YBCO/ABS filament

Temperature [K]	**μ_{eff} of YBCO/ABS filament**	
	Fine YBCO powder	**Coarse YBCO powder**
7	0.96	0.88
77	0.97	0.92

Overall, the μ_{eff} value of the coarse YBCO/ABS filament is lower than for the fine YBCO/ABS filament. The difference in μ_{eff} values is due to the effect of YBCO particle size on the superconducting properties of the composite, as discussed in Chapters 7 and 8. Also, as described in section 8.4.4, the superconducting properties of YBCO composites depends on volume fraction of superconducting phase of YBCO-123 in YBCO particles as opposed to the non-superconducting YBCO-211 phase.

9.3 3-D Printing Process

A "Makerbot" 3-D printer (Replicator) (Figure 9.14) was used for fabrication of the superconducting composites. In general, printing starts with a model design. The 3-D model is designed using computer-aided design (CAD) software. The design file is converted into the standard tessellation language (STL) format, so that it can be read by the built-in printer software. This software positions and slices the 3-D model into layers. The software also calculates a path to extrude the filament to create the desired 3-D patterns.

There are many process parameters involved in controlling the fabrication process by this kind of 3-D printer, such as raster angle, tool path, slice thickness, build orientation and deposition speed[12]. However, most of these parameters are typically based on the compatibility of the selected polymeric materials with the AM process. More details of the overall printing process are described in *Addictive Manufacturing Technologies: Rapid Prototyping to Direct Digital Manufacturing*[13].

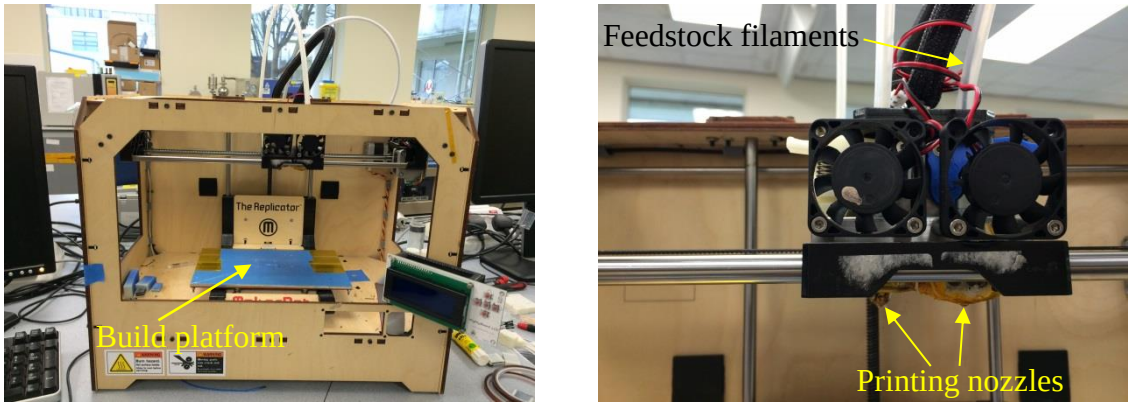


Figure 9.14 A Makerbot 3-D printer used for fabrication of superconductor composites. Right: Head of the 3-D printer.

9.3.1 Optimising 3-D Printing Parameters

In this work, the previously extruded YBCO/ABS filaments were used as the feedstock for the 3-D printing process. The common parameters requiring set up for 3-D printing

such as air gap distance, nozzle temperature, feed rate and traverse speed of the printer head needed to be optimised for the composite materials[4]. As discussed in section 5.1.3, the air gap distance was set to zero in order to reduce air gaps and improve the density of the samples. Other processing parameters were set up with help from Dr. F. Castle and Dr. D. Isakov in the Materials Department of Oxford University. In this work, a nozzle temperature of 230 ºC was used. 230 °C is a MakerBot's default 3-D printing temperature for ABS extrusion. The temperature was set higher than the glass transition temperature (105°C), so that ABS filament melts quickly inside the extruder (inside the head of the 3-D printer in Figure 9.14 (right)) and remains fairly viscous when pressing through the print nozzle without dripping on the build platform during the printing process[14]. Controlling the viscosity is important to reduce the problem of polymer clogging in the print nozzle during printing.

Before printing, YBCO/ABS filaments are fed through the extruder's loading tube on the printer head, which are then pulled through the feed pinch rollers by a rotating motor. The rollers forced the filament into the heated liquefier, which was pre-heated before the printing process. The filament was melted through a heated nozzle and deposited as ultra-fine beads. The printing process was conducted by moving the nozzle in both horizontal and vertical directions. The movement of the printer head is operated by a motorised stepper controlled by the 3-D printer software.

The fabrication process starts by forming a base layer of the structure on the build platform. The exterior wall of the pattern is then printed on this base, and followed by continuous YBCO/ABS deposition filling in the interior area. The printing process is continuously repeated until the 3-D geometry is completely built. The route followed by the nozzle to print the 3-D pattern is referred to as a toolpath. The toolpath setting used in my work was set up by the software, where beads were deposited at fixed raster

angle, $\alpha = 45°$ starting from a corner towards the other corner (Figure 9.15). A similar toolpath pattern was reported by Turner *et al.*[15] and Lee *et al.*[16].

The resolution of the 3-D structures can be adjusted by selecting the thickness of each deposited layer in the geometrical pattern. In the built-in 3-D printer software setting, a "high" resolution indicates smaller layer heights, resulting in more detailed model structures but longer printing times. Since dimensional accuracy and good resolution are important for the fabrication of the HTS composites, a high quality structure produced at "high" resolution is the best selection to produce a high quality structure.

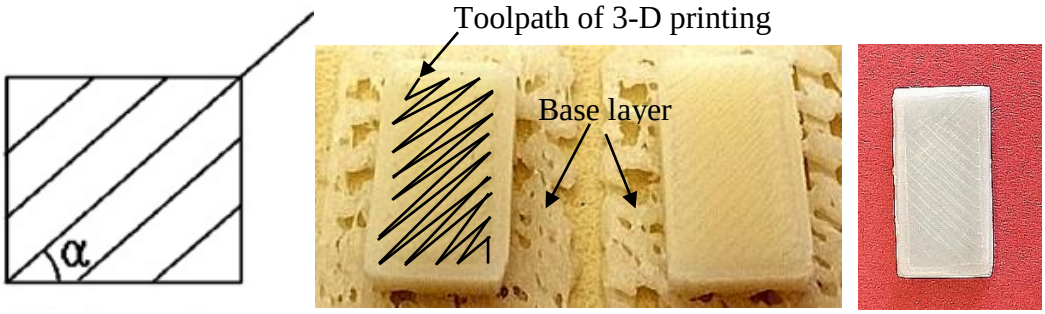


Figure 9.15 A schematic drawing of 3-D geometry build direction with 45° raster angle[16]. Figure reproduced after Lee et al.[16], with permission from Elsevier. 3-D printed samples of pure ABS using the same build direction by Makerbot in this work (dimension, 15.8 mm x 8.1 mm x 1.5 mm). The right image is the post-polished sample for the waveguide measurement (dimension, 15.8 mm x 7.9 mm x 1.0 mm).

The density of the YBCO/ABS filament loading can be controlled by the size of the print nozzle. Initially, a standard nozzle (provided by Makerbot) with size 0.4 mm was used to print both ABS and YBCO/ABS samples. However, I found that the printing process was successful with the pure ABS filament (Figure 9.15 (right image)), but not with the YBCO/ABS filament using this standard size nozzle. The reason for this is because the size and loading of YBCO filler tends to clog the nozzle opening. Several commercially available nozzles with size 0.5 mm were purchased and enlarged into sizes 0.7, 0.8 and 0.9 mm in the Materials workshop. The YBCO/ABS samples were printed using these nozzles, and the results are shown in Figure 9.16.

Nozzles with sizes of 0.5 mm and 0.7 mm produced samples with a lot of holes in the interior. However, nozzles with sizes 0.8 and 0.9 mm can be used to print dense and complete structures of YBCO/ABS composites. Even then, the exterior of this printed YBCO/ABS has a rough surface structure caused by the limited resolution and dimensional control of the nozzles. This surface roughness can be reduced by choosing a nozzle with a smaller size, but as shown above this is not possible considering the size and loading of the YBCO powder in the ABS filament. Therefore, the 0.8 mm nozzle was selected for 3-D printing of YBCO/ABS composites.

A post print polishing process is conducted to give a smooth surface finish to the YBCO/ABS composites to fit into the waveguide holder for electromagnetic measurements. The post print polishing set up was similar to the sample preparation of the YBCO loaded ABS filament in section 9.2.2. A YBCO/ABS composite was mounted on an aluminium stub ((diameter size 25 mm and height 10 mm)) before grinding down from coarse to fine grades of wet Silicon Carbide papers (SiC Grinding Disc, dimension 250 mm in diameter- Grade 2500 and 4000) to size 15.8 mm x 7.9 mm x 1 mm.

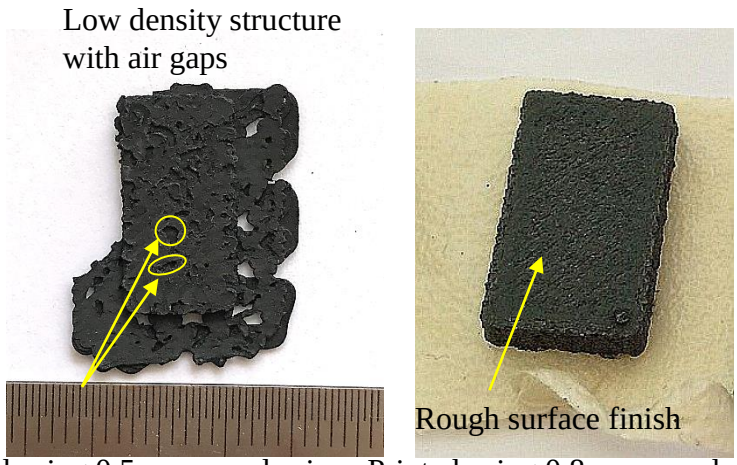


Figure 9.16 YBCO/ABS samples printed using 0.5 and 0.8 mm nozzle sizes. The size of the as-printed YBCO/ABS sample is 16.7 mm x 9.0 mm x 1.5 mm (right image).

The same 3-D printing conditions for the filament with coarse YBCO powder have been used to print samples using filament with fine YCBO powder. This time using the smaller particle size allows a smaller nozzle size of 0.7 mm to be used to achieve a better printing resolution and to avoid the development of air gaps between printed layers. This shows that the use of small nozzles can improve the resolution of the 3-D printing when the filament is suitable.

9.4 Characterisation of 3-D Printed YBCO/ABS Composites

The effect of the printing process on the microstructure and electromagnetic properties of YBCO/ABS composites has been investigated. Two types of samples were produced using the 3-D printing technique. The simplest and most basic is a block sample designed for the microwave measurement used previously on cast samples (Chapter 8). The block sample is printed using a single nozzle fed by a YBCO/ABS filament with nominal volume fraction of 20 vol%. Graded materials were printed using two nozzles, fed by pure ABS and 20 vol% YBCO loaded ABS filament respectively. In order to reduce air gaps in the 3-D structure, these two materials were printed using similar size nozzles and printing conditions. Both single and graded materials were printed using fine and coarse YBCO/ABS.

The efficiency of the printing process in producing these YBCO/ABS samples was investigated by observing the microstructure of YBCO/ABS samples using SEM. The electromagnetic properties of the printed YBCO/ABS samples were measured using the VNA.

9.4.1 Single Printed Material

Block samples of YBCO/ABS composites with dimensions approximately 15.8 x 7.9 x 1.0 mm^2 were printed (Figure 9.17). The samples were slightly polished to remove rough surface and filament debris that loosely bonds to the exterior.

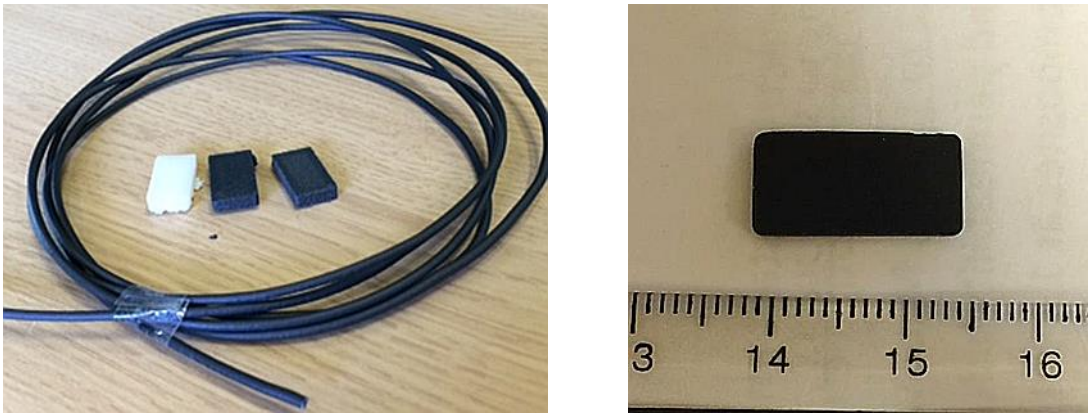


Figure 9.17 Extruded YBCO/ABS composite filaments and samples for the electromagnetic measurements.

Figure 9.18, Figure 9.19 and Figure 9.20 show cross sections of as-polished ABS, YBCO/ABS composite with coarse particles and YBCO/ABS composite with fine particles respectively. The YBCO particle distribution was observed in cross section, Figure 9.19 and Figure 9.20. For the coarse YBCO/ABS sample, SEM images show a homogenous particle distribution in the matrix, Figure 9.19. In the fine YBCO/ABS composite, the particle distributions are similar to that described for the bigger YBCO particles in some respects, but there are some striking differences (Figure 9.20). In contrast to the printed YBCO/ABS with bigger particles, cross sections of samples with smaller YBCO particles are covered with high density of particles with size less than 25 μm. Some of these particles can be found clustered in the matrix (Figure 9.20). From the SEM image in Figure 9.18, no YBCO particles are observed as expected. At higher magnification, striations (lines) can be seen with small debris and loose particles. The

distance between striations is approximately 2-5 μm, which is likely to have originated from the silica carbide abrasive surface during polishing.

The efficiency of the 3-D printing technique in producing the YBCO/ABS samples has been investigated by calculating the area fraction of YBCO particles in the sample using BSE image and ImageJ software from an area of 2087 x 1700 μm^2 for coarse YBCO/ABS samples and 634 μm x 480 μm for fine samples. The area fraction coverage of YBCO particles in the fine and coarse of 20 vol% YBCO/ABS composites are 21±3% and 20±1% indicating a good transfer of YBCO loading by 3-D printing. In these samples, the nominal volume fractions and the measured area fractions of YBCO filler in the YBCO/ABS composites are very alike, and I will use 20 vol% for the discussion below.

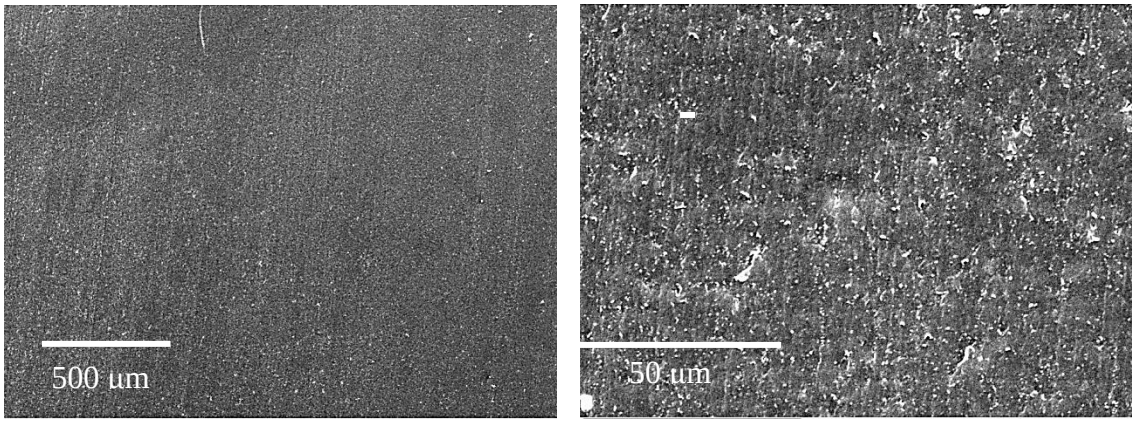


Figure 9.18 SEM images of polished printed ABS samples at 60X and 1000X respectively.

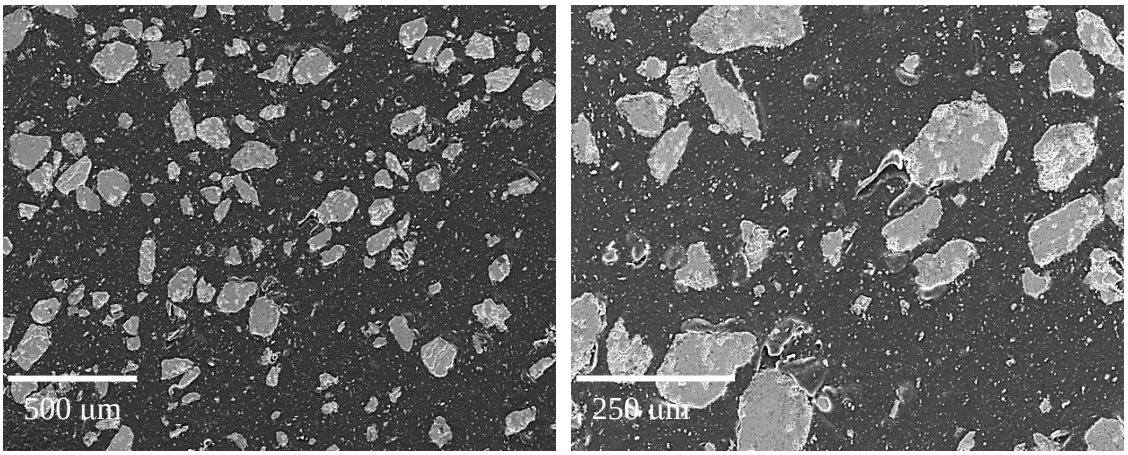


Figure 9.19 SEM images of polished printed YBCO/ABS sample using coarse YBCO particles loaded ABS filament. Images are taken at 60X and 150X respectively.

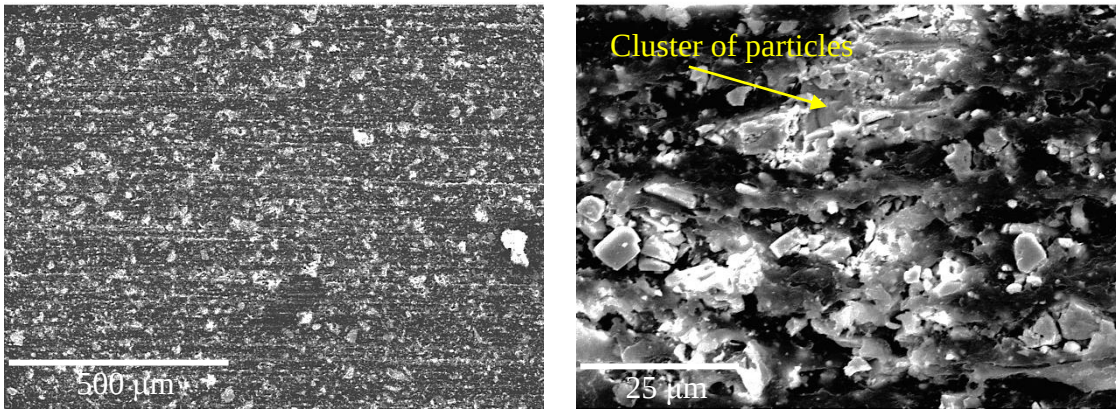


Figure 9.20 SEM images of polished printed YBCO/ABS sample using fine YBCO particles loaded ABS filament. Images are taken at 100X and 1500X.

9.4.1.1 Electromagnetic Properties

Printed fine and coarse YBCO/ABS samples were loaded into the waveguide holder for ε_{eff} and μ_{eff} measurement using the VNA at both room temperature and 77 K. The ε_{eff} and μ_{eff} values of printed YBCO/ABS samples were expected to be similar to the ε_{eff} and μ_{eff} values of cast YBCO/Epoxy samples at the same volume fraction. Figure 9.21 and Figure 9.22 show the real part of ε_{eff} and μ_{eff} values of the printed 20 vol% fine and coarse YBCO/ABS composites and pure ABS samples from 12 to 18 GHz at room temperature and 77 K. The ε_{eff} values of the coarse YBCO/ABS composite are 5.14 and 5.02 at room temperature and 77 K respectively. The ε_{eff} values of the fine YBCO/ABS composite are 4.50 and 4.42 at both room temperature and 77 K. As expected, there is no dramatic difference in the ε_{eff} values of these printed YBCO/ABS samples because they have the same nominal volume loading of YBCO.

The μ_{eff} values of these printed YBCO/ABS samples decrease at 77 K, Figure 9.22. The μ_{eff} values drop from close to 1.00 to approximately 0.82 for the printed coarse YBCO/ABS sample and 0.85 for the fine YBCO/ABS sample. This is consistent with the magnetic properties of these YBCO/ABS filaments, where the hysteresis loop of the fine YBCO/ABS composite is smaller than the coarse YBCO composite (Figure 9.4).

This is due to the effect of particle size and quality of YBCO powder, which is likely to affect the μ_{eff} values at low temperature when the YBCO is in its superconducting state. Both Figure 9.21 and Figure 9.22 show that the values of ε_{eff} and μ_{eff} at 77 K are noisier than at room temperature, and this instability in values at low temperature is likely to be due to the calibration of the waveguide, connectors and cables of the VNA.

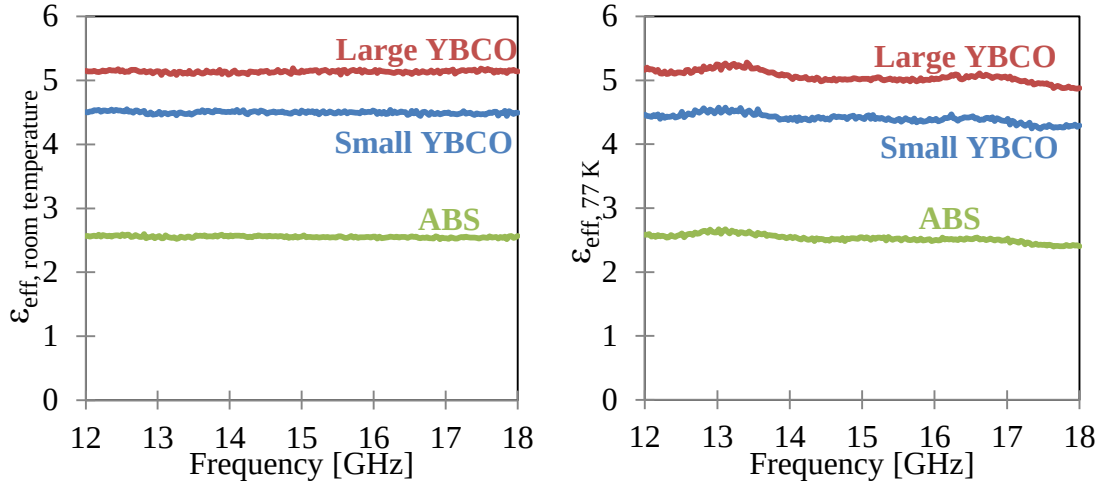


Figure 9.21 The effective dielectric constant (ε_{eff}) of printed 20 vol% fine and coarse YBCO/ABS and pure ABS samples from 12 GHz to 18 GHz at room temperature (left) and 77 K (right). Note that the ε_{eff} values of ABS are 2.55 and 2.53 at room temperature and 77 K respectively.

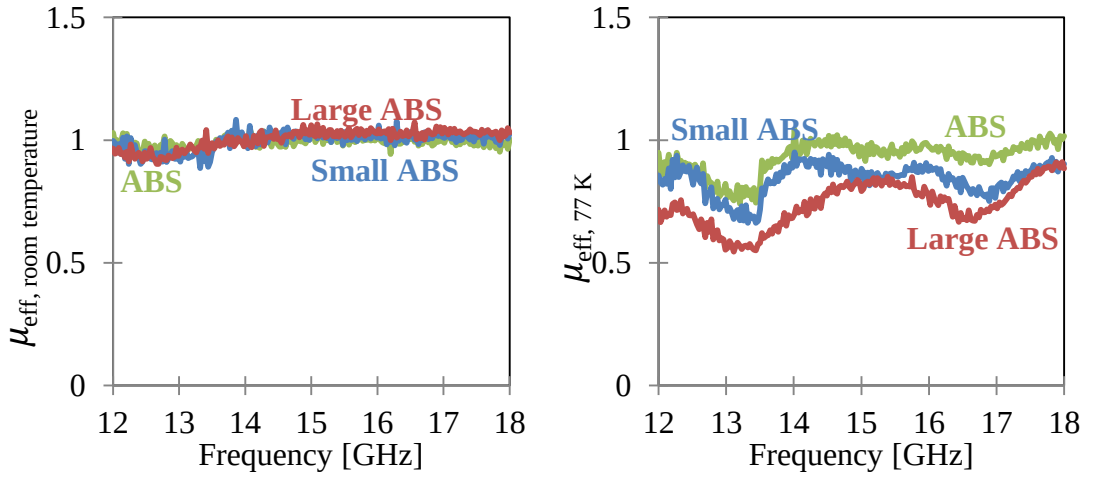


Figure 9.22 The effective magnetic permeability (μ_{eff}) of printed 20 vol% fine and coarse YBCO/ABS and pure ABS samples from 12 GHz to 18 GHz at room temperature (left) and 77 K (right). Note that the μ_{eff} values of printed ABS are 1.01 and 0.96 at both room temperature and 77 K.

In order to aid comparison with the microwave results from the previous YBCO/Epoxy sample, the ε_{eff} and μ_{eff} values of the coarse YBCO/ABS sample were measured at 15

GHz. Since the coarse YBCO/ABS sample was estimated to have a YBCO area fraction of 21%, the microwave results were compared with those of the YBCO/epoxy samples with approximately the same area fraction. Table 9.4 summarises the ε_{eff} and μ_{eff} values of YBCO/ABS composite with 21% area fraction and YBCO/epoxy composite with 23% area fraction, showing a good agreement at both room temperature and 77 K. This is due to the similar of volume fraction and particle size of the YBCO powders used and shows that the choice of polymer matrix has little effect on overall dielectric properties. Both samples show no effect of temperature on the ε_{eff} values, but show a slight decrease of μ_{eff} at 77 K.

Table 9.4 ε_{eff} and μ_{eff} values of YBCO/polymer composites at 15 GHz

Samples	$\boldsymbol{\varepsilon_{eff}}$ **values**		$\boldsymbol{\mu_{eff}}$ **values**	
	$\boldsymbol{\varepsilon_{eff,Room}}$	$\boldsymbol{\varepsilon_{eff,77\,K}}$	$\boldsymbol{\mu_{eff,Room}}$	$\boldsymbol{\mu_{eff,77K}}$
ABS	2.55	2.53	1.01	0.96
Epoxy	2.55	2.43	0.98	1.00
YBCO/ABS	5.14	5.02	1.04	0.82
YBCO/Epoxy	4.79	4.55	0.92	0.81

9.4.1.2 Magnetisation Properties

The magnetisation properties of the printed YBCO/ABS samples were measured using the SQUID technique. Since the area fraction of printed fine and coarse YBCO/ABS samples were ~21%, the magnetisation properties were compared with the cast 25% YBCO/Epoxy sample from section 8.4.3.

The values were normalised by the mass of YBCO powder for comparison purposes. Figure 9.23 and Figure 9.24 show the hysteresis loops of printed fine and coarse YBCO/ABS at 7 K and 77 K respectively. Both hysteresis loops from the printed YBCO/ABS samples are similar to the cast YBCO/Epoxy sample, especially for the

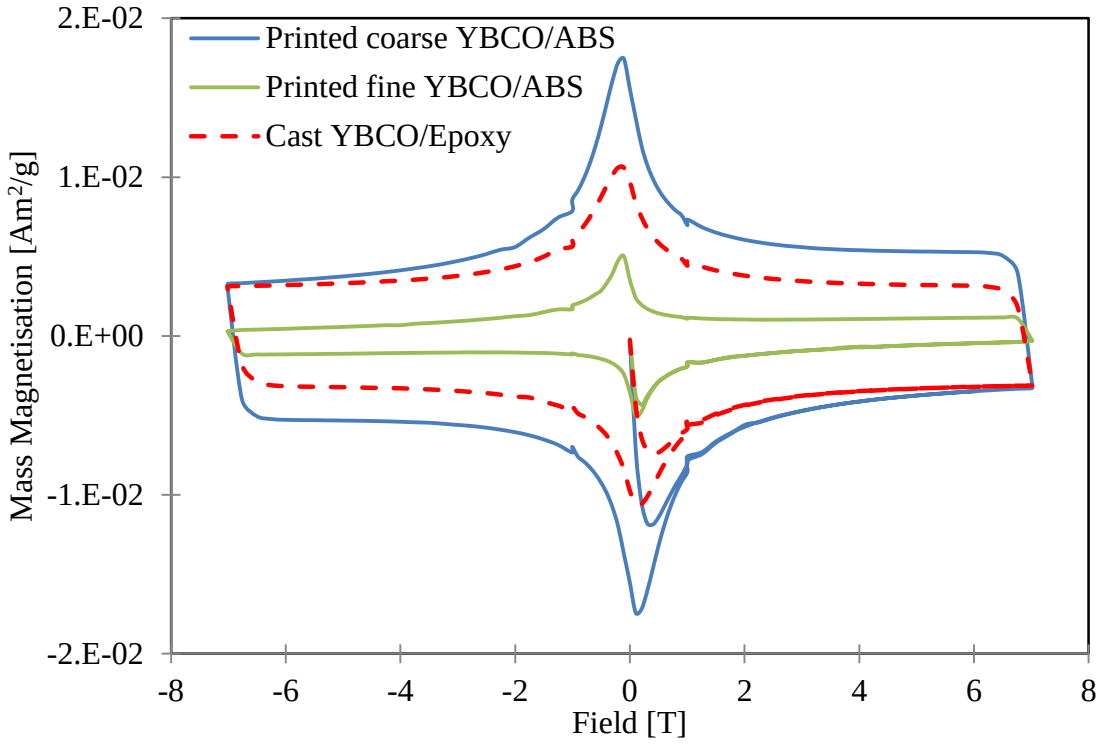


Figure 9.23 The hysteresis loops of 20 vol% printed YBCO/ABS samples (area fractions for fine and coarse YBCO/ABS samples are 21±3% and 20±1%) and 25% area fraction of cast YBCO/Epoxy at 7 K.

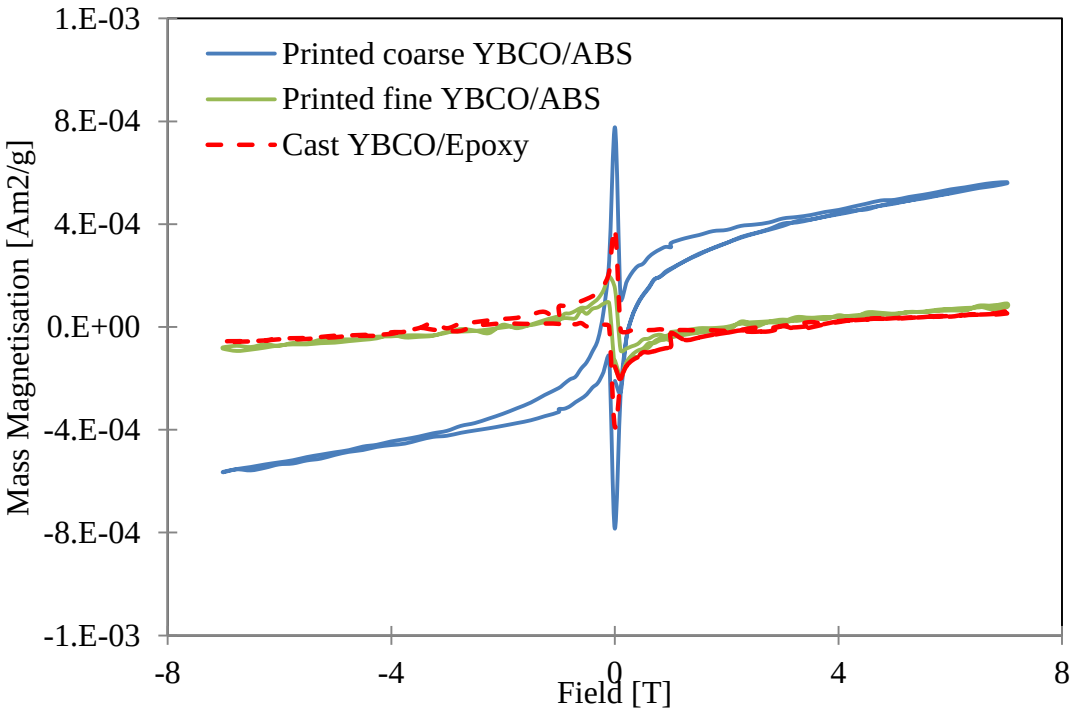


Figure 9.24 The hysteresis loops of 20 vol% printed YBCO/ABS samples (area fractions for fine and coarse YBCO/ABS samples are 21±3% and 20±1%) and 25% area fractions of cast YBCO/Epoxy at 77 K.

coarse YBCO/ABS sample. This is due to the similar range of YBCO powder sizes used as a filler in these HTS composites. The slight difference in amplitude is likely due to particle distribution in the samples. As expected, the hysteresis loop of the fine YBCO/ABS sample is smaller than the coarse YBCO/ABS sample. This is due to the effect of size and volume fractions of the superconducting phase. The difference in magnetisation between these printed YBCO/ABS samples is consistent with their filaments, where fine YBCO/ABS filament has magnetisation properties at one order of magnitude lower than the coarse YBCO/ABS filament.

9.4.1.3 Loss properties

The dielectric loss is one of the main parameters of dielectric based composite materials that must be considered for electromagnetic device applications. The dielectric loss or loss tangent, $\tan\delta$, is defined above (Chapter 2). Both ε_{eff}'' and ε_{eff}' values can be measured and extracted from waveguide measurements using the NRW method as discussed in Chapter 6. However, the measurement of materials with ε_{eff}'' less than ~0.05 renders to be inaccurate due to the mismatch impedance of joints between the waveguide and the network analyzer[17]. This is critical for the measurement of ABS based dielectric materials with maximum tangent loss value of 0.01[4].

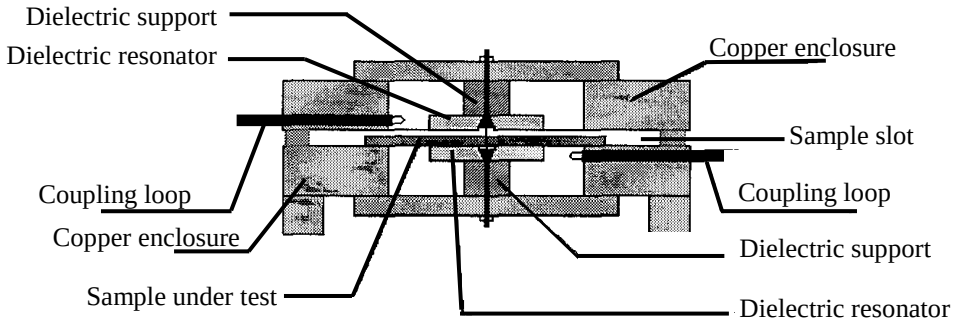


Figure 9.25 Modified schematic diagram of the cross-section split-post resonator reproduced after Mazierska *et al.*[18]. Copyright © 2004, IEEE.

The split-post dielectric resonator technique can provide better sensitivity for loss tangent measurements of polymeric and ferroelectrics materials, provided uniform and properly chosen thickness of materials is available. In this technique, a sample under test is slotted between two low loss dielectric rods and coupling loops confined in a copper enclosure as shown in Figure 9.25. A large test sample with maximum thickness of <0.6 mm is preferable for easy insertion and removal in the split-post method[19]. The assembly is connected to the vector network analyser to measure resonant frequencies and Q-factors. Dedicated QuickWave (QWED) software was used to calculate the dielectric constant and loss tangent of the sample by filling in the thickness of the sample under test, resonant frequencies and Q-factors of split-post dielectric resonators with and without sample.

Dielectric loss tangents can be accurately measured by this method to values as low as 0.00002, but measurements are limited to a single frequency[20]. In this technique, dielectric samples with a uniform thickness need to be prepared to fit into the cylindrical resonator. The flexibility of the 3-D printing in producing such samples has enabled the study of the dielectric loss tangent of YBCO/ABS composites. For the split-post dielectric resonator measurement at 15 GHz, the minimum dimension of the sample is 15 x 15 mm and maximum thickness is 0.6 mm.

In this work, the basic cylindrical disc was designed using CAD software by Dr. D. Isakov in the Materials Department. The diameter and thickness of the cylindrical discs were set at ϕ = 40 mm and $t = 0.5$ mm for 3-D printing. It should be noted that the shape of samples could be in any form provided the test substrates is placed within the coupling loops (Figure 9.25) with uniform thickness of less than 0.6 mm. The cylindrical disc shape was chosen to accommodate the limited availability of the melt-grown YBCO powder.

Three cylindrical discs of 20 vol% fine and coarse YBCO/ABS and pure ABS samples were printed (Figure 9.26) using the same 3-D printing parameters as described in the previous section. A reasonable cylindrical shaped sample was printed with average diameter 40.05 ± 0.04 mm for pure ABS, 40.22 ± 0.03 mm and 40.21 ± 0.04 mm for fine and coarse YBCO/ABS samples respectively (average diameter was measured over 4 points at cross sections of the cylindrical discs). Samples were observed with sharp edges and simple grinding was carried out to give smooth edges. The thicknesses of the as-printed samples were more than 0.5 mm due to the 0.8 mm nozzle used in the 3-D printing process. A post print polishing process was conducted to give a smooth surface finish to the cylindrical discs to fit into the split-post dielectric for loss tangent measurement. The polishing was carried out on the surface of the cylindrical discs using the post polishing method explained in the previous section. After the post-polishing process, samples thicknesses were reduced to 0.46, 0.47 and 0.47 mm for pure ABS, fine and coarse YBCO/ABS samples respectively. The measurement was conducted at room temperature and results were compared with the dielectric loss values from the waveguide measurement.

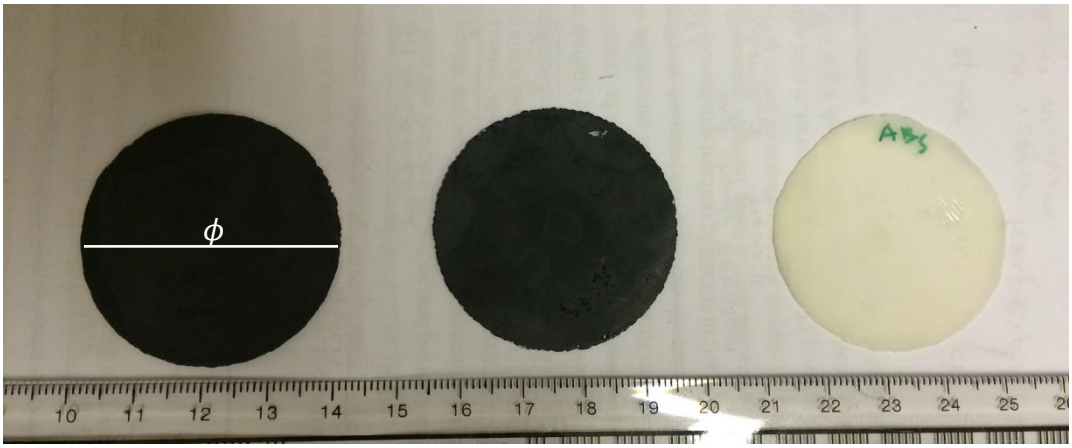


Figure 9.26 Samples for dielectric loss measurement by the split-post dielectric resonator technique. The ϕ of the as-printed samples are 40.05 ± 0.04 mm for pure ABS, 40.22 ± 0.03 mm and 40.21 ± 0.04 for fine and coarse YBCO/ABS samples respectively.

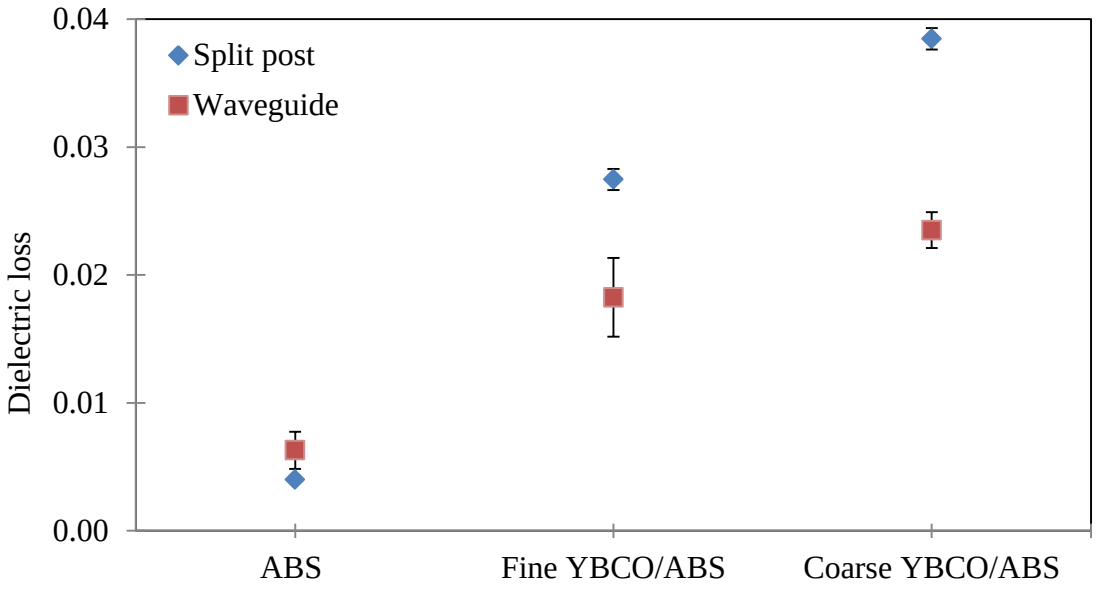


Figure 9.27 Dielectric loss of 20 vol% fine and coarse YBCO/ABS and pure ABS samples at 15 GHz by split-post dielectric resonator and waveguide techniques at room temperature.

Figure 9.27 shows the dielectric loss of printed ABS, fine and coarse YBCO/ABS samples. The dielectric loss tangent of pure ABS sample was $0.004 \pm 0.8\%$ as measured by the split-post dielectric resonator at 15 GHz, and $0.006 \pm 13.0\%$ by the waveguide at the same frequency. These values are in good agreement with the pure ABS value from the literature ($\tan \delta = 0.008$)[21]. As expected, the dielectric loss tangent values of both fine and coarse YBCO/ABS samples are higher by one order of magnitude than the pure ABS sample, $\tan \delta_{fine\ YBCO/ABS} = 0.027 \pm 1.0\%$ and $\tan \delta_{coarse\ YBCO/ABS} = 0.038 \pm 0.7\%$. The increase in dielectric loss tangent is due to the YBCO filler in the ABS matrix, which is lossy at room temperature. However, the dielectric loss tangents measured by the waveguide measurement ($\tan \delta_{fine\ YBCO/ABS} = 0.015 \pm 4.9\%$ and $\tan \delta_{coarse\ YBCO/ABS} = 0.024 \pm 1.4\%$) are found to be lower by ~30%. The value differ greatly, and this indicates the waveguide measurements are inaccurate for loss measurements, as reported by Barry[17].

Since the loss tangent values of the HTS composites differ greatly to those from the split-post dielectric resonator technique, the loss measurements at 77 K were not carried out by the waveguide technique, but it is expected that the loss properties would be lower than at room temperature due to the reduced microwave loss of YBCO at low temperature[22].

The split-post method can be used to measure the loss tangents of HTS composites at 77 K, but must include consideration of uncertainties in dimensions and the dielectric properties of resonators[18], as well as uncertainties of sample thickness[23]. This suggests that if more detailed investigations are carried out on the split-post dielectric at low temperature, the loss tangent measurements could be accurately carried out on these HTS composite. It is difficult to conduct low temperature measurements using the split-post method with the current cooling system for waveguide measurements in Chapter 6, where both the waveguide and sample are immersed in liquid nitrogen. This is because the rectangular waveguide is an enclosed system where both sample and coupling stubs are shielded from direct contact with liquid nitrogen. In contrast, the liquid nitrogen can get into direct contact with the sample, dielectric resonators and coupling loops in the split-post assembly through the air gaps in the sample slot (Figure 9.25), which can cause misleading results at low temperature. It is possible to conduct low temperature measurements using a split-post assembly by applying the Transmission Mode Q-factor technique[24] where data is collected in the transmission mode, as long as consideration is made of the effect of cables and connectors, which are difficult to calibrate at low temperatures[24,25].

9.4.2 Graded Materials

Functionally graded composite materials engineered to have a spatial variation in electromagnetic properties can be prepared by combining two or more materials during printing[26]. Anisotropy is one of the electromagnetic properties that can be achieved by fabricating graded composites of materials with different electromagnetic properties in alternating structures. The arrangement and fractions of these structures determine the electromagnetic properties of the devices, and control the direction of propagation of electromagnetic waves.

These anisotropic devices can be fabricated by making layers out of two-phase materials lying parallel or perpendicular to the electric field (E-field) orientations[27] as shown in Figure 9.28. The maximum and minimum ε_{eff} values of the devices are bound to the dielectric properties of these two-phase materials. These two 'absolute bounds' are known as the Wiener bounds[28,29], where the upper bound is a maximum ε_{eff} value of a given volume fractions of filler and can be achieved when the layers are arranged parallel to the electric flux, and the lower bound is a minimum ε_{eff} value can be achieved when the fillers are arranged perpendicular to the electric flux as demonstrated in Figure 9.28.

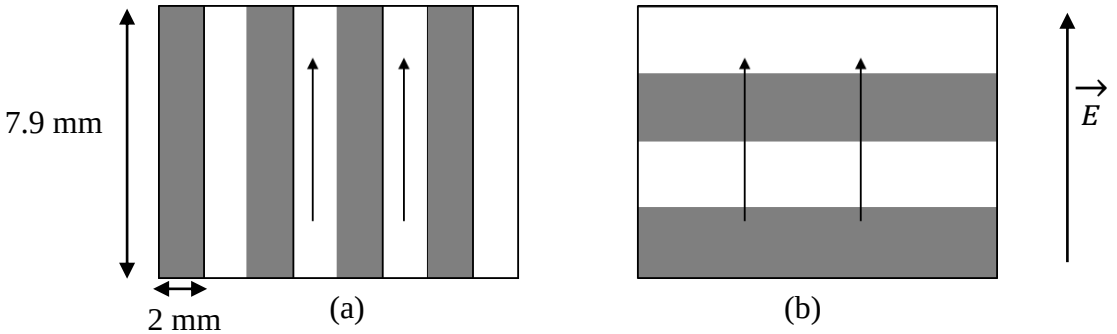


Figure 9.28 The arrangement of layers of two different materials into anisotropic devices arranged according to the electric field (E-field) orientation, (a) parallel structure and (b) perpendicular structure.

The Wiener bounds model can be used to determine the maximum and minimum ε_{eff} values of the anisotropic structures, and are given by,

$$\varepsilon_{eff}, max = f\varepsilon_1 + (1-f)\varepsilon_2 \quad (9.1)$$

$$\varepsilon_{eff}, min = \frac{\varepsilon_1\varepsilon_2}{f\varepsilon_2+(1-f)\varepsilon_1} \quad (9.2)$$

where f is a volume fraction of the YBCO/ABS composite, and ε_1 and ε_2 are the dielectric constants of the YBCO/ABS composite and pure ABS respectively.

In order to assess the possibility of using anisotropic superconducting composites, the YBCO/ABS composites with the structures shown in Figure 9.28 were printed.

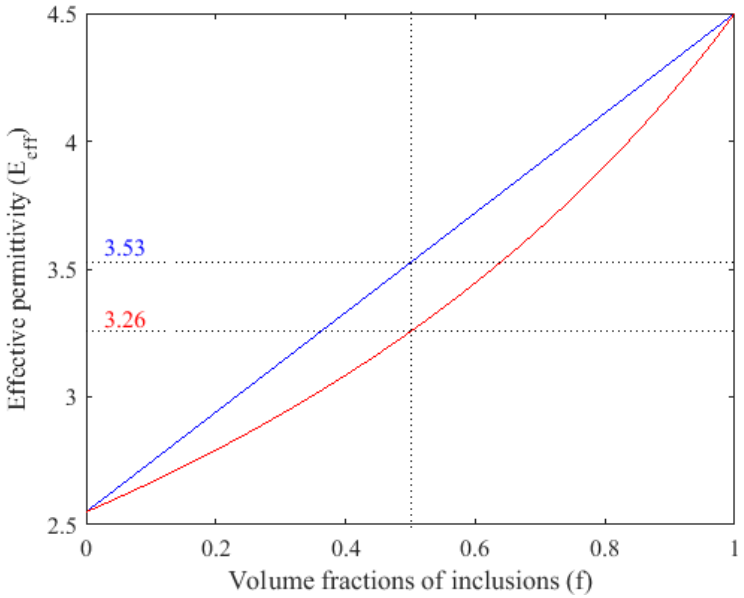


Figure 9.29 Upper (blue line) and lower (red line) Wiener bounds for the two-phase mixture of 20 vol% YBCO/ABS and pure ABS samples with dielectric constants, $\varepsilon_1 = 4.50$ and $\varepsilon_2 = 2.55$ respectively. The predicted maximum and minimum effective dielectric constants, ε_{eff} of 0.5 volume fraction YBCO/ABS samples are estimated to be 3.53 and 3.26 respectively.

Equations 9.1 and 9.2 were used to predict the maximum and minimum ε_{eff} values of both parallel and perpendicular structures. 20 vol% YBCO/ABS and pure ABS filaments were used as the two-phase materials with dielectric constants $\varepsilon_1 = 4.50$ and $\varepsilon_2 = 2.55$ at 15 GHz as previously measured in Section 9.4.1.1. A volume fraction, f,

of 50 vol% was chosen that gives equal contribution of both phases. According to the Wiener bounds model, the maximum and minimum ε_{eff} values of 50 vol% YBCO/ABS are estimated to be $\varepsilon_{eff,\parallel}$ =3.53 and $\varepsilon_{eff,\perp}$ =3.26 respectively, as can be seen in Figure 9.29. Since the ε_{eff} properties are temperature independent (Chapter 8), the same ε_{eff} values of both anisotropic structures (perpendicular and parallel structures) are expected at 77 K.

As predicted, the ε_{eff} values indicate an anisotropic effect of YBCO/ABS composites at the same volume fraction, but different layer arrangements. The anisotropic effect, however, could be significantly enhanced by using a higher loading of the YBCO/ABS composite. For example, if we use the dielectric constant data from the measured YBCO/Epoxy in section 8.4.2, the ε_{eff} values of the measured area fraction of 53% YBCO/Epoxy is 21.73 (as discussed in Chapter 8, page 181 by assuming that the measured area fractions and the nominal volume fractions of YBCO/Epoxy are alike (Af≈Vf), so the ε_{eff} value of the 53% area fraction of YBCO/Epoxy sample is approximately equal to 53 vol% YBCO/Epoxy sample). If we assume that the dielectric constant of YBCO/ABS at the same concentrations is ε_1=21.73, the maximum and minimum ε_{eff} values of YBCO/ABS sample are estimated to be 12.14 and 4.56 respectively. However, the brittle nature of the YBCO powder makes this filament difficult to use in both extrusion and 3-D printing processes.

The Wiener bounds model can also be used to study the anisotropic effect of μ_{eff} values on printed YBCO/ABS samples by assuming uniform distribution of magnetic field within the materials[30]. Equations 9.1 and 9.2 can be used to predict the anisotropic effect of μ_{eff} by substituting the ε_1 and ε_2 values by μ_1 and μ_2 values of the 20 vol% YBCO/ABS and pure ABS samples respectively. Since the μ_{eff} values of YBCO/ABS

samples are temperature dependent ($\mu_{eff} = 1$ at room temperature), the anisotropic effect of μ_{eff} is only expected at 77 K. The μ_1 and μ_2 values were taken from the previously measured single printed pure ABS and YBCO/ABS samples at 15 GHz, which are 0.852 and 0.956 respectively. According to the Wiener bounds, the predicted values for parallel and perpendicular structures to magnetic field (B-field) of YBCO/ABS samples are $\mu_{eff,\parallel} = 0.904$ and $\mu_{eff,\perp} = 0.901$ at 77 K as indicated in Figure 9.30.

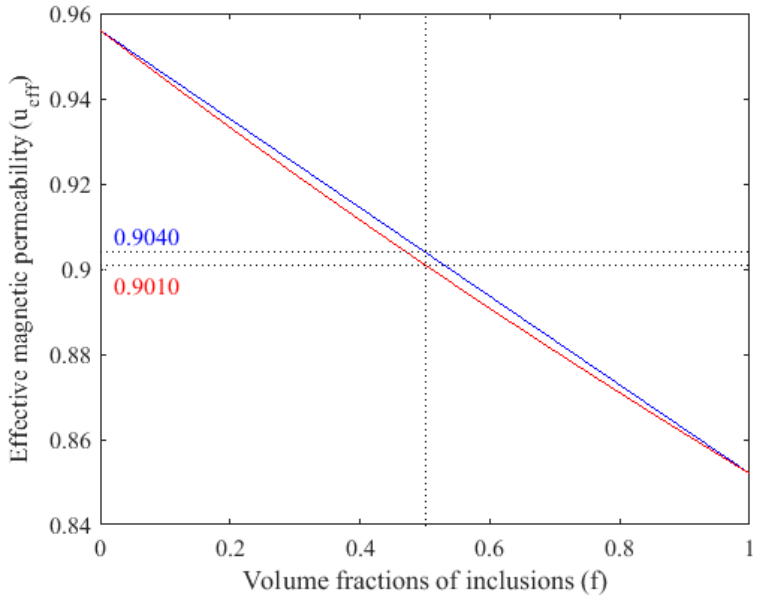


Figure 9.30 Wiener bounds for the two-phase mixture of 20 vol% YBCO/ABS and pure ABS samples with magnetic permeability $\mu_1 = 0.852$ and $\mu_2 = 0.956$ respectively. The predicted maximum and minimum effective dielectric constants, μ_{eff} of 0.5 volume fraction YBCO/ABS samples are estimated to be 0.904 and 0.901 respectively.

As would be expected, the Wiener upper and lower bounds of the μ_{eff} values deviate in opposite directions to the ε_{eff} values. This is because the B-field and E-field are perpendicular to each other. The difference between $\mu_{eff,\parallel}$ and $\mu_{eff,\perp}$ values is only 0.3% making it difficult to measure by the waveguide technique, where the inaccuracy of the measurement technique is about $\pm 5.0\%$ at 77 K (section 6.3.2). The anisotropy of μ_{eff} values could be distinguished if a higher volume fraction of YBCO filler is used in

the filament. For example, $\mu_{eff,\parallel} = 0.728$ and $\mu_{eff,\perp} = 0.657$ are predicted for 53% area fractions of YBCO/ABS composites. Therefore, the investigation of the anisotropic effect is mainly conducted on the dielectric property ε_{eff} of YBCO/ABS samples in this work.

9.4.2.1 Fabrication of Anisotropic Structures by 3-D Printing

In this work, the anisotropic structures were printed with alternate 'black' and 'white' stripes of YBCO/ABS composite and pure ABS filaments. The structures with alternate layers are one of the simplest structures using two materials, yet even these would require proper technique to be produced with homogenous particle distribution by casting. The same alternate 'black' and 'white' stripes of YBCO/ABS composite and pure ABS filaments could be done using the 3-D printer with two nozzles, so that two types of materials with specific nozzle size requirements can be printed at the same time. These structures were originally designed by Dr. D. Isakov using the built-in software of the 3-D printer. However, some adjustments were made to accommodate the nozzle size used to print the YBCO/ABS samples. Both pure ABS and YBCO/ABS filaments were vertically and horizontally printed to produce alternating black and white layers with thicknesses of 1 mm, with the "high" resolution setting for quality.

The alternate structures were printed in block samples with dimensions 15.8 x 7.9 mm x 1 mm for easy microwave measurements using the VNA. Both coarse and fine YBCO/ABS filaments were printed into anisotropic structures. However, only composite filaments with fine YBCO particles were successful. This is because the filament with coarse YBCO powder was brittle and easy to break during the printing process. The size of these printed samples were found to be slightly larger than the intended dimensions, due to the low resolution caused by the large nozzles used in the

3-D printing. Samples were carefully trimmed and polished to fit into the waveguide holder. Microstructural analysis of the printed structures has been carried by SEM, and ε_{eff} and μ_{eff} measurements were conducted using the waveguide technique.

Figure 9.31 shows printed samples with an 8 layer parallel structure (top) with a 4 layers perpendicular structure (bottom) using ABS and YBCO/ABS filaments. Both 3-D printed samples show good interface integrity. This is in good agreement with the SEM image (Figure 9.32), where a clear boundary between the pure ABS and 20 vol% YBCO/ABS layers can be observed. The ABS layer has a plain dark contrast, while the YBCO/ABS composite layer contains a uniform distribution of bright YBCO particles in the ABS matrix. The boundary between the ABS and YBCO/ABS composite looks well-attached with no air gaps but with a small amount of interface roughness due to the size of nozzle used, which was unable to print high resolution structures. Printing lines can be seen from the SEM image, showing the layer height of the printed structure achieved when the 3-D printer is set for high resolution printing.

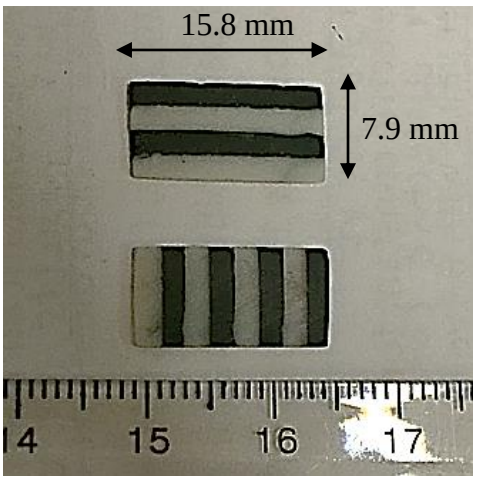


Figure 9.31 Typical anisotropic bound structures created by 3-D printing using ABS and 20 vol% YBCO/ABS filament with fine YBCO particles.

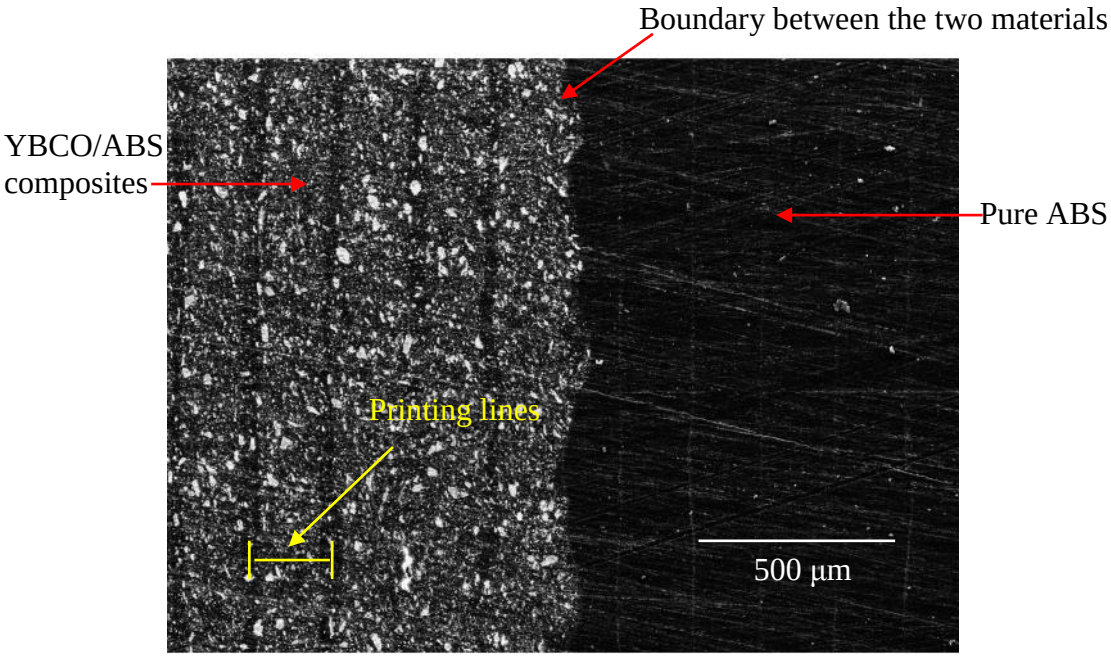


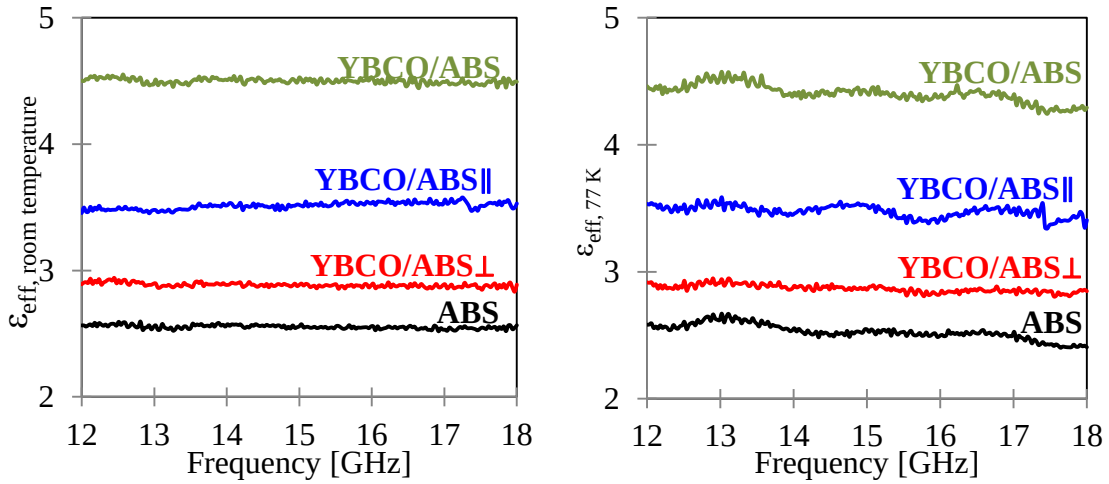
Figure 9.32 SEM image of the boundary between the printed ABS and YBCO/ABS structures taken at 200X.

9.4.2.2 Dielectric Properties of The YBCO/ABS Structures

In order to investigate the efficiency of the 3-D printing on the anisotropic structures, ε_{eff} and μ_{eff} values were measured at both room temperature and 77 K using the VNA. The microwave measurements were conducted on both structures, parallel and perpendicular to the electric field orientation in the waveguide.

Figure 9.33 shows the ε_{eff} values of the printed parallel and perpendicular structures of pure ABS and 20 vol% YBCO/ABS samples from 12 to 18 GHz at room temperature (a) and 77 K (b). The differences in the ε_{eff} values for the parallel and perpendicular structures with the same volume fraction of each material indicate the anisotropic effect. The ε_{eff} values of these structures are $\varepsilon_{eff,\parallel} = 3.51$ and $\varepsilon_{eff,\perp} = 2.89$ at room temperature. As expected, the ε_{eff} values of these printed structures at 77 K, $\varepsilon_{eff,\parallel} = 3.48$ and $\varepsilon_{eff,\perp} = 2.87$ are not much different to the dielectric values at room temperature. The low ε_{eff} values of the anisotropic structures are a result of the lower

overall volume fraction of YBCO powder in the YBCO/ABS sample, as expected. Figure 9.33 shows that the experimental $\varepsilon_{eff,\parallel}$ values of the parallel structure at both room temperature (3.51) and 77 K (3.48) are in good agreement with the Wiener bounds prediction $\varepsilon_{eff,\parallel} = 3.53$ at 15 GHz. However, a large difference can be observed from the perpendicular structure, where $\varepsilon_{eff,\perp}$values at both room temperature (2.89) and 77 K (2.87) are lower than the Wiener bound prediction of $\varepsilon_{eff,\perp} = 3.26$ at 15 GHz.



(a) Room temperature (b) 77 K

Figure 9.33 The effective dielectric constants (ε_{eff}) of pure ABS and 20 vol% YBCO/ABS composites at room temperature and 77 K.

In Figure 9.33, perturbations are observed at 17 GHz in the $\varepsilon_{eff,\parallel}$ values of YBCO/ABS samples at room temperature and 77 K. Isakov *et al*. found perturbations from the ε_{eff} values of the alternately printed $BaTiO_3$/ABS and ABS composites at 16 GHz, and described them as resonance effects induced by the composites with the strip-like geometry, where these perturbation effects become less significant with decreasing width of the $BaTiO_3$/ABS strips in the composites[31].

ε_{eff} measurements were conducted at room temperature and 77 K, and both sample and waveguide materials experience thermal contraction in the cooling process to 77 K. This could cause the YBCO/ABS composite samples to shrink in the brass sample holder.

Since the temperature expansion coefficient, α, of ABS ($\alpha_{ABS} = 60 - 130 \times 10^{-6}/K$)[32] is higher than the brass sample holder ($\alpha_{Brass} = 19 \times 10^{-6}/K$[33]), the shrinkage or movement of the sample would create gaps between the sample and the sample holder, which can cause 'microwave signal leakage', leading to errors in ε_{eff} and μ_{eff} measurements at 77 K. However, I have shown in the microwave measurements on pure epoxy ($\alpha_{epoxy} = 48 - 85 \times 10^{-6}/K$[32]) in Chapter 6, Figure 6.5, that ε_{eff} and μ_{eff} values drop less than 5.0% between room temperature and 77 K consistent with the reported uncertainty in this kind of measurement by Barry[17]. This suggests that leakage effects did not seriously compromise the measurement to 77 K. It is important to print the YBCO/ABS samples with the shape that can fit tightly inside a section of the waveguide sample holder to minimise movement of the sample during cooling to 77 K. The size of the section inside the sample holder (15.8 mm x 7.9 mm x 1 mm) was used to design and print the YBCO/ABS samples by 3-D printing. However, based on the size of the print nozzles (0.8 mm for coarse YBCO/ABS composite, and 0.7 mm for fine YBCO/ABS composite), YBCO/ABS samples were printed slightly bigger than the size intended. A post-print polishing process was conducted to give a smooth surface finish, as well as to fit the YBCO/ABS composite samples tightly into the waveguide holder at room temperature to minimise any leakage effects at 77 K.

9.4.3 3-D Printed Split-Ring Resonator Structures (SRRs)

Previous sections have shown that the fabrication of 3-D structures of YBCO/ABS composites with controlled ε_{eff} and μ_{eff} values are feasible using the 3-D printer. In addition to simple block structures, I have printed a simple split-ring resonator (SRR) structure using the same 20 vol% fine YBCO/ABS filaments. An array of SRR structures can form the resonant building blocks of metamaterials with the potential for antenna and microwave frequency applications[34].

A unit cell SRR interacts with electromagnetic wave propagation, allowing interaction with a perpendicular magnetic field (Figure 9.34). Magnetic flux enclosed by the metallic rings creates an inductance in the SRR[35]. The induced current flows in the rings and enables coupling from one ring to another through a distributed capacitance controlled by the gap spacing[34]. This enables the SRR to be effectively characterised by it resonant frequency at microwave frequencies at millimetre wavelengths[36].

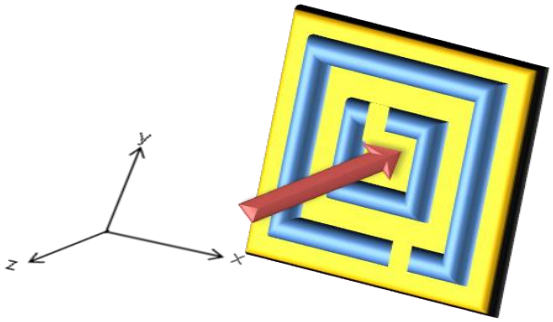


Figure 9.34 A unit cell of split-ring resonators (SRR) with magnetic field interaction along the z-axis. Figure adapted from Iyer *et al.*[37] with permission by John Wiley and Sons, Inc.

9.4.3.1 Resonant properties of SRR

A resonant frequency measurement was performed to measure the resonant properties of individual SRR. The transmission coefficient (S_{21}) was measured as a function of frequency over the frequency range 30 KHz to 6 GHz, and results displayed in dB.

The experimental stage consisted of a sample holder and two receive-transmit loop antenna holders aligned on optical board to reduce noise from the experimental apparatus (Figure 9.35). A single SRR was fixed in a clear acrylic cassette that was carefully positioned between these loop antennas held at a distance 2 cm from the cassette surface.

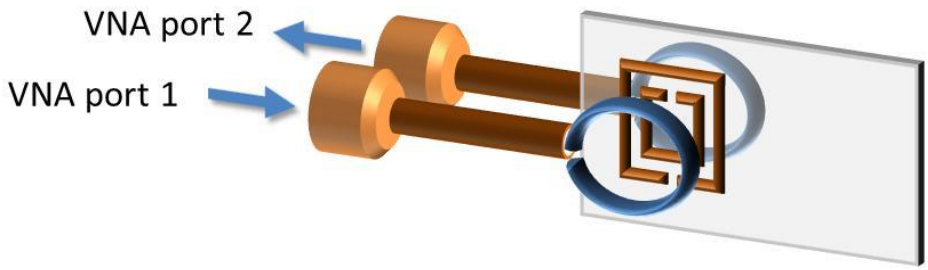
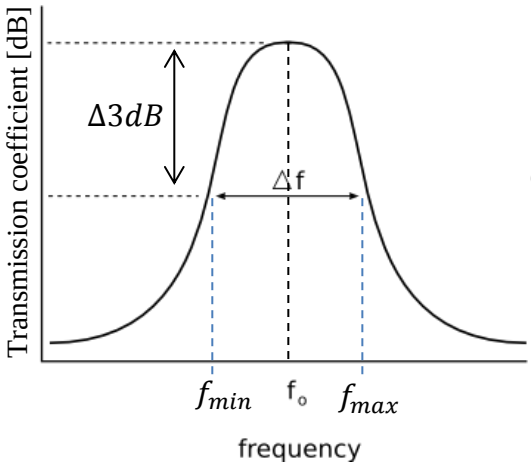


Figure 9.35 SRR sample position in between loop antennas (courtesy of Dr. E. Edwards, University of Oxford).

The efficiency of the SRR structure can be characterised by its quality factor (Q-factor). The Q-factor is defined by the sharpness of the resonant peak, with high Q-factor SRRs having narrow resonant peaks and low loss, whereas low Q-factor SRRs have broad resonant peaks and higher loss (Figure 9.36). Several methods have been introduced to measure the Q-factor[38], but the 3 dB method is one of the simplest[39]. The method involves measuring the scattering parameter (S-parameter) S_{21} as a function of frequency. The scattering parameter S_{21} is a measurement of transmitted waves in a linear two port system. The magnitude of S_{21} is altered by the response of the SRR, and is given by, $|S_{21}| = \sqrt{(ReS_{21})^2 + (ImS_{21})^2}$. The two frequencies, f_{min} and f_{max} are determined at half-power points, below the resonant peak, f_0, and the bandwidth, $\Delta f_{3\,dB}$ of those frequency values are calculated (refer to equation in Figure 9.36)[38].



$$Q = \frac{f_0}{\Delta f_{3dB}} = \frac{f_0}{f_{max} - f_{min}}$$

Figure 9.36 Schematic of resonant frequency and the Q-factor equation.

9.4.3.2 SRR fabrication by 3-D printing

Since the characteristic resonant frequency depends on both the constituent materials and the dimensions of the SRR structures[40,41], printed SRR unit cells were designed based on SRRs fabricated on PCB material, (Figure 9.37 (left image)), with parameters such as base dimension metallic strip dimension, inter ring spacing, strip thickness, strip width and gap width Figure 9.37 (right image). This will provides analytical comparisons for the quality of resonant frequencies. For the 3-D printing work, the SRR model was designed by Dr. F. Castles using the built-in software of the 3-D printer. 0.7 mm nozzles were used for printing both ABS and YBCO/ABS filaments.

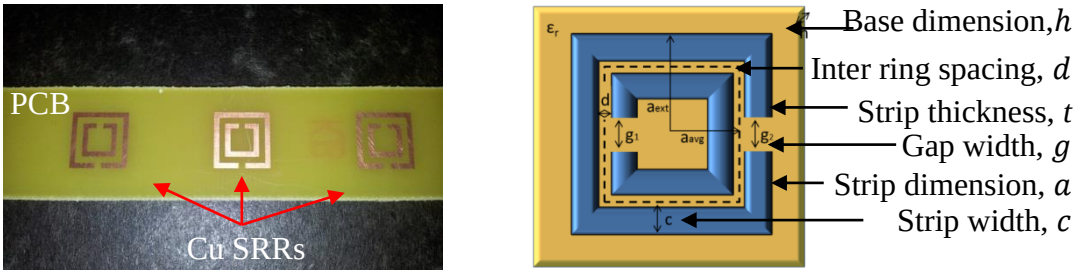


Figure 9.37 SRR structures on PCB board (left image) and design of SRR unit cell (right image). Figure adapted from Saha *et al.*[34]. Copyright © 2011, IEEE.

Table 9.5 Printed SRR dimensions

Types of printed SRR	***h* [mm]**	***a* [mm]**	***d* [mm]**	***c* [mm]**	***g* [mm]**	***t* [µm]**
Cu/PCB	15x15x1	10x10	1	1	2	18
Printed Cu/ABS	15x15x1	10x10	1	1	2	-
Large printed YBCO/ABS	15x15x1	14x14	1	1	2	1000
Small printed YBCO/ABS	15x15x1	10x10	1	1	2	500

Figure 9.38 shows several samples of printed SRR structures on a pure ABS base using the 3-D printer. The dimensions of the printed SRRs are summarised in Table 9.5. The large SRRs can be printed with sharp lines and a well-defined structure of the YBCO/ABS composite printed on an ABS base structure. However, the small SRRs are

rather poorly defined with holes between structures, indicating that the printing resolution for these 3-D SRR structures is limited by the size of available nozzles. This shows that the printing resolution is important in defining which complex geometrical structures can be attempted by 3-D fabrication with my customised YBCO/ABS filaments. In order to study the characteristics of the resonant frequency of these 3-D printed YBCO/ABS SRR structures, printed Cu SRRs on ABS structures were also prepared by Dr. D. Isakov.

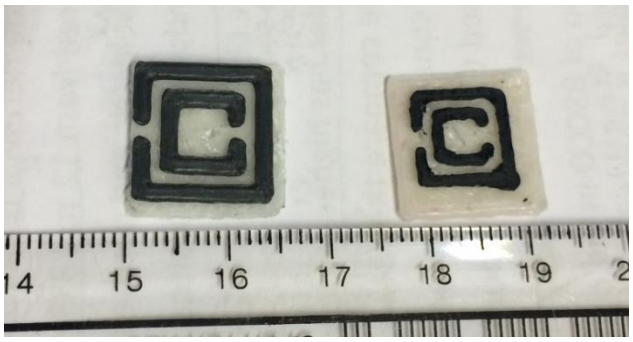


Figure 9.38 3-D printed SRR structures using ABS and YBCO/ABS filaments.

9.4.3.3 Characterisation of SRR

In close collaboration with Dr. E. Edwards, the printed SRRs were measured for resonant frequency using a loop antenna arrangement set up for the Cu SRRs (Figure 9.37). The samples were placed between receiver-transmitter loop antennas to measure S_{21} values over the frequency range 30 KHz to 6 GHz using the VNA (Figure 9.39).

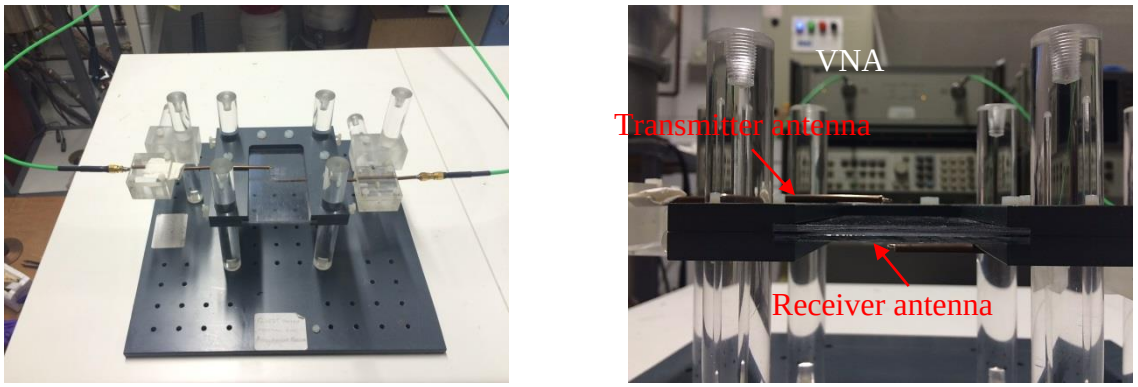


Figure 9.39 Experimental set up for SRR measurements using the VNA. The SRR unit cell is arranged between the transmitter and receiver antennas.

Figure 9.40 shows the resonant frequency for Cu SRRs on PCB, printed Cu SRRs with the Cu buried in the ABS and printed YBCO/ABS composite on ABS structures. This measurement was only attempted at room temperature, and no clear resonant response was observed in the YBCO/ABS SRR devices. This is due to low volume fraction of YBCO in the loaded ABS filament, resulting in a low conductivity.

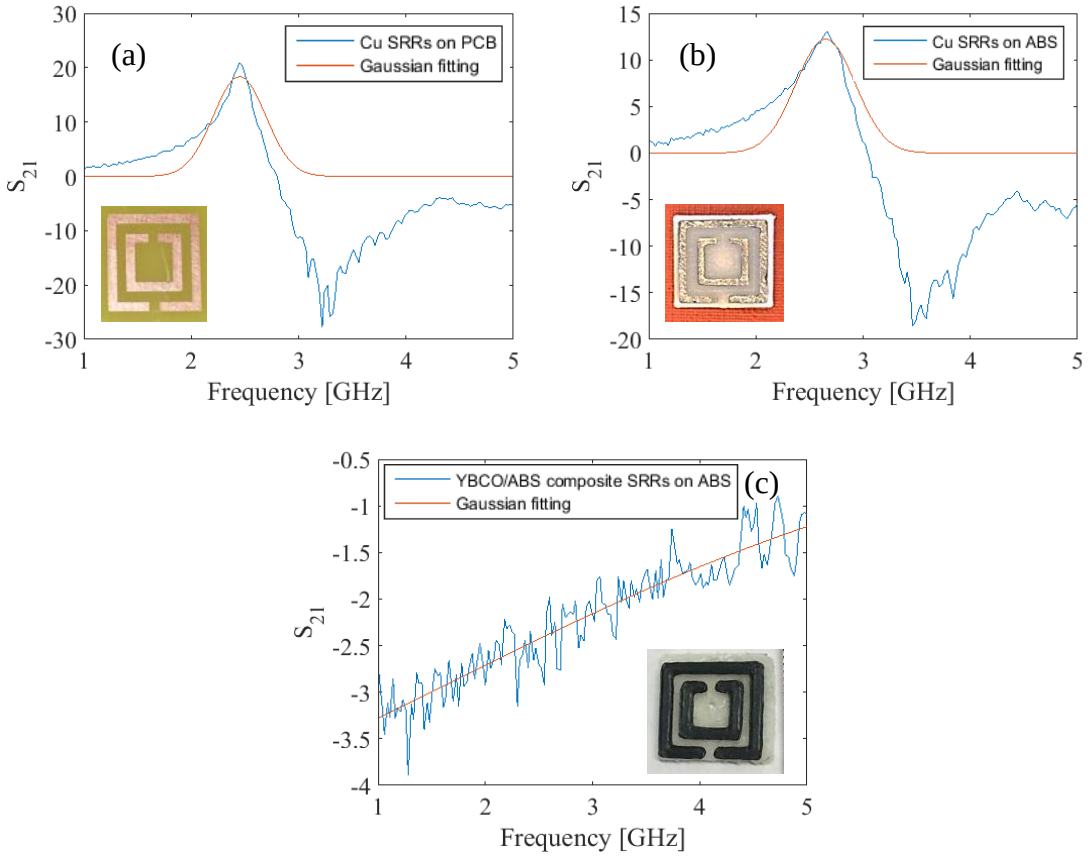


Figure 9.40 Resonant peaks of SRRs at room temperature (a) Cu SRRs on PCB, (b) printed Cu SRRs on ABS and (c) printed YBCO/ABS composite SRR on ABS.

At room temperature, Cu SRR on PCB and ABS samples were observed to have sharp peaks at 2.5 GHz and 2.7 GHz, with quality factors of 20 and 9 respectively. The sharpness of these peaks is due to the conductivity of Cu, resulting in reasonable Q-factor values. The increase in thickness and width of the Cu strips lowers the resistances, and, thus increases the sharpness of the peak. This is in agreement with the resistivity of Cu SRRs on the PCB, which is $2.2 \times 10^{-8}\ \Omega - m$. The resistivity of Cu

SRR on ABS sample was estimated two orders of magnitude higher than the Cu SRR on PCB sample, which explains the low Q-factor value. As expected no resistivity was measured from the printed YBCO/ABS SRR on ABS structures, due to no continuous path between YBCO grains in the SRR structure.

9.5 Discussion and Conclusions

The preliminary results above show that HTS composites can be fabricated using YBCO loaded ABS composite filaments by 3-D printing. Figure 9.1 has shown that the extrusion temperature and die size can affect the tolerance of the dimension of the feedstock filaments. The extrusion process has been optimised to produce YBCO/ABS filaments with close to the required diameter of 1.75±0.05 mm, by considering YBCO particle sizes and die swelling. The optimised extrusion conditions have been shown to produce YBCO/ABS filaments with a uniform particle distribution for both coarse and fine YBCO powder in Figure 9.6 and Figure 9.9, indicating good control of the extrusion process.

YBCO loaded ABS filaments were used as a feedstock filament in the 3-D printer. The size of nozzle used for the 3-D printing process has been optimised considering the size of YBCO powder loaded in the ABS filament. As expected, the size of the nozzle required to print YBCO/ABS composites with the coarse YBCO powder was bigger than the nozzle used for the fine powder. The resolution of 3-D printing can be adjusted by choosing the quality condition of the printing process, which is a pre-set parameter in the printer software. Unfortunately, this setting could not easily be changed by a user. The only way to adjust the resolution is by optimising the quality condition that best suits the size of the nozzle. The effect of nozzle size and setting quality can be observed from the 3-D structures in Figure 9.16. A post-polishing process is required to remove debris and fit the sample into the sample holder.

SEM microscopy has shown that the YBCO/ABS composites fabricated by the 3-D printer tend to have YBCO powder dispersed homogenously in the ABS matrix, however with small holes. The area fraction of YBCO/ABS composite of a coarse YBCO powder has been shown to be in a good agreement with the nominal volume fraction of YBCO/ABS starting material. This proves a well-controlled fabrication process of YBCO/ABS composite by 3-D printing.

The ε_{eff} and μ_{eff} values of 20 vol% coarse YBCO/ABS samples have been shown to be in a good agreement with the ε_{eff} and μ_{eff} values of cast YBCO/Epoxy sample with area fraction of 21±3%. This is as expected since both the size and area fraction of YBCO filler used in both composites are approximately the same. However the μ_{eff} values of the YBCO/ABS composite with finer YBCO powder have shown less decrease in μ_{eff} on cooling to 77 K. The weak magnetic properties of YBCO/ABS samples can be due to the decreased in particle size and the low content of superconducting phase in the YBCO filler. Further control over the effect of YBCO filler on the properties of YBCO/ABS composites by 3-D printing might have been developed by a more detailed study of the relationships between the size and volume fractions of YBCO filler.

In conclusion, studies on the 3-D printing technique have proved that YBCO loaded ABS filament with good control of area fraction and particle size of YBCO powder can be extruded and printed. The YBCO/ABS samples have been shown to have the expected superconducting and electromagnetic properties at 20 vol%, showing that the 3-D superconducting metamaterial structures could be reliably fabricated by this technique.

References

1 Ehrenberg, I. M., Sarma, S. E. & Wu, B.-I. A three-dimensional self-supporting low loss microwave lens with a negative refractive index. *Journal of Applied Physics* **112**, 073114 (2012).

2 Garcia, C. R. *et al.* 3D Printing Of Anisotropic Metamaterials. *Progress In Electromagnetics Research Letters* **34**, 75-82 (2012).

3 Deffenbaugh, P. I., Rumpf, R. C. & Church, K. H. Broadband Microwave Frequency Characterization of 3-D Printed Materials. *Components, Packaging and Manufacturing Technology, IEEE Transactions on* **3**, 2147-2155 (2013).

4 Grant, P. S. *et al.* Manufacture of electrical and magnetic graded and anisotropic materials for novel manipulations of microwaves. *Phil. Trans. R. Soc. A* **373**, 20140353 (2015).

5 Makerbot.com. *MakerBot The Replicator Setup Guide*, <https://images.makerbot.com/support/production/mt524.pdf> (2012).

6 Noztek.com. *Noztek Pro User Manual*, <http://www.noztek.com/wp-content/uploads/2013/11/User-manual-Nov-161.pdf> (2013).

7 Majumdar, A., Das, A., Alagirusamy, R. & Kothari, V. K. *Process Control in Textile Manufacturing*. pp. 114-116 (Elsevier Science, 2012).

8 Giles, H. F., Mount, E. M. & Wagner, J. R. *Extrusion: The Definitive Processing Guide and Handbook*. pp. 115 (Elsevier Science, 2004).

9 Huang, T., Hilmas, G. E., Fahrenholtz, W. G. & Leu, M. C. Dispersion of Zirconium Diboride in an Aqueous, High-Solids Paste. *International Journal of Applied Ceramic Technology* **4**, 470-479 (2007).

10 Dinger, T. R., Worthington, T. K., Gallagher, W. J. & Sandstrom, R. L. Direct observation of electronic anisotropy in single-crystal $Y_1Ba_2Cu_3O_{7-x}$. *Physical Review Letters* **58**, 2687-2690 (1987).

11 Larbalestier, D., Gurevich, A., Feldmann, D. M. & Polyanskii, A. High-Tc superconducting materials for electric power applications. *Nature* **414**, 368-377 (2001).

12 Bakar, N., Alkahari, M. & Boejang, H. Analysis on fused deposition modelling performance. *Journal of Zhejiang University SCIENCE A* **11**, 972-977 (2010).

13 Gibson, I., Rosen, D. W. & Stucker, B. *Additive Manufacturing Technologies: Rapid Prototyping to Direct Digital Manufacturing*. pp. 147-163 (Springer US, 2009).

14 Makerbot.com. *MakerBot Replicator 2X*, <https://images.makerbot.com/support/production/mt719.pdf> (2012).

15 Turner, B. N. & Gold, S. A. A review of melt extrusion additive manufacturing processes: II. Materials, dimensional accuracy, and surface roughness. *Rapid Prototyping Journal* **21**, 250-261 (2015).

16 Lee, C. S., Kim, S. G., Kim, H. J. & Ahn, S. H. Measurement of anisotropic compressive strength of rapid prototyping parts. *Journal of Materials Processing Technology* **187**, 627-630 (2007).

17 Barry, W. A Broad-Band, Automated, Stripline Technique for the Simultaneous Measurement of Complex Permittivity and Permeability. *IEEE Transactions on Microwave Theory and Techniques* **34**, 80-84 (1986).

18 Mazierska, J., Krupka, J., Jacob, M. V. & Ledenyov, D. Complex permittivity measurements at variable temperatures of low loss dielectric substrates

employing split post and single post dielectric resonators. *In Microwave Symposium Digest, 2004 IEEE MTT-S International* **3**, 1825-1828 (2004).

19 Jerzy, K. *Split Post Dielectric Resonator- User Guide*. (QWED, 2003).

20 Krupka, J., Mazierska, J. E., Jacob, M. V., Hartnett, J. G. & Tobar, M. E. Recent advances in measurements of permitivity and dielectric losses at microwave frequencies. *In Microwave and Optical Technology 2003, International Society for Optics and Photonics* **5445**, 311-317 (2004).

21 Lei, Q. *All-dielectric composites for metamaterial applications*, Thesis (D.Phil.)--University of Oxford, (2016).

22 Harshavardhan, K. S. *et al.* Low-loss $YBa_2Cu_3O_7$ films on flexible, polycrystalline-yttria-stabilized zirconia tapes for cryoelectronic applications. *Applied Physics Letters* **78**, 1888-1890 (2001).

23 Jerzy, K., Krzysztof, D., Bill, R. & James, B.-J. A dielectric resonator for measurements of complex permittivity of low loss dielectric materials as a function of temperature. *Measurement Science and Technology* **9**, 1751 (1998).

24 Mazierska, J. *et al.* Measurements of loss tangent and relative permittivity of LTCC ceramics at varying temperatures and frequencies. *Journal of the European Ceramic Society* **23**, 2611-2615 (2003).

25 Leong, K. & Mazierska, J. Precise measurements of the Q-factor of transmission mode dielectric resonators: accounting for noise, crosstalk, coupling loss and reactance, and uncalibrated transmission lines. *IEEE Transactions on Microwave Theory and Techniques* **50**, 2115-2127 (2002).

26 Udupa, G., Rao, S. S. & Gangadharan, K. V. Functionally Graded Composite Materials: An Overview. *Procedia Materials Science* **5**, 1291-1299 (2014).

27 Sihvola, A. Mixing rules with complex dielectric coefficients. *Subsurface Sensing Technologies and Applications* **1**, 393-415 (2000).

28 Sihvola, A. H. *Electromagnetic mixing formulas and applications*. pp. 20-200 (Institution of Electrical Engineers, 1999).

29 Grimvall, G. *Thermophysical Properties of Materials*. Chapter 17, 289-315 (Elsevier Science, 1999).

30 Daniel, L. & Corcolle, R. A note on the effective magnetic permeability of polycrystals. *Magnetics, IEEE Transactions on* **43**, 3153-3158 (2007).

31 Isakov, D. V. *et al.* 3D printed anisotropic dielectric composite with meta-material features. *Materials & Design* **93**, 423-430 (2016).

32 Domone, P. & Illston, J. *Construction Materials: Their Nature and Behaviour, Fourth Edition*. pp 309 (CRC Press, 2010).

33 Ekin, J. *Experimental Techniques for Low-Temperature Measurements: Cryostat Design, Material Properties and Superconductor Critical-Current Testing*. pp. 93 (Oxford University Press 2006).

34 Saha, C., Siddiqui, J. Y. & Antar, Y. M. M. Square split ring resonator backed coplanar waveguide for filter applications. *General Assembly and Scientific Symposium, 2011 XXXth URSI*, pp. 1-4 (2011).

35 Sauviac, B., Simovski, C. R. & Tretyakov, S. A. Double Split-Ring Resonators: Analytical Modeling and Numerical Simulations. *Electromagnetics* **24**, 317-338 (2004).

36 Capolino, F. & Wiltshire, M. C. K. *Theory and Phenomena of Metamaterials: RF Metamaterials*. pp. 14-1 to 14-7 (CRC Press, 2009).

37 Iyer, A. K. & Eleftheriades, G. V. *Negative-Refractive-Index Transmission-Line Metamaterials*. pp. 7 (John Wiley and Sons, 2005).

38 Petersan, P. J. & Anlage, S. M. Measurement of resonant frequency and quality factor of microwave resonators: Comparison of methods. *Journal of Applied Physics* **84**, 3392-3402 (1998).

39 Kajfez, D. & Hwan, E. J. Q-Factor Measurement with Network Analyzer. *Microwave Theory and Techniques, IEEE Transactions on* **32**, 666-670 (1984).

40 Aydin, K. *et al.* Investigation of magnetic resonances for different split-ring resonator parameters and designs. *New Journal of Physics* **7**, 168 (2005).

41 Guo, H. *et al.* Thickness dependence of the optical properties of split-ring resonator metamaterials. *physica status solidi (b)* **244**, 1256-1261 (2007).

Chapter 10 Conclusions and Suggestions for Further Work

The main aim of this thesis has been to study the fabrication of HTS composites and to investigate their microwave and superconducting properties. HTS composites have been fabricated by both casting and 3-D printing methods. The effects of the size and type of HTS filler and its volume fractions on these fabrication processes led to optimisation studies in producing reliable HTS composites.

Powder processing was studied as a preliminary step in the production of HTS composites for both casting and 3-D printing. BSCCO and YBCO were considered for the production of HTS composites due to their T_c exceeding 77 K. Even after an extended period of annealing in air (168 hours) the precursor BSCCO powder, the highest T_c value that could be achieved was 84 K. Due to the fact that fully reacted BSCCO powder is not available commercially, YBCO powder was then selected to produce HTS composites. Two types of YBCO powder were studied; commercial (CM) and melt-grown (MG) YBCO. Melt-grown YBCO powder was processed from the off-cut edges of top seeded melt-growth (TSMG) YBCO bulks. A simple magnetic levitation test was conducted to select good quality material of YBCO powder preparation. In order to control particle sizes, grinding and sieving process are required to produce MG YBCO powder from MG YBCO bulks.

It has been found that both CM and MG YBCO powders have T_c values of 93 K. However, the MG YBCO powder has an order of magnitude higher magnetisation performance than the CM YBCO powder. SQUID studies showed that the MG YBCO powder had irreversible components in the magnetisation at 77 K, caused by flux

pinning, which is a desirable property for both HTS powder and its corresponding composites. Based on Campbell's prediction in the literature of the particle size effect on magnetisation performance[1], the particle size of YBCO powder has been optimised to maximise the superconducting properties. It is likely that the performance could be further improved by a more precise control over the size range of YBCO particles. Moreover, the use of a MG YBCO processed in-house resulted in better control over the size distribution of the YBCO powder, and for this reason, it is generally considered to be a suitable source powder to fabricate HTS composites.

Cast MG HTS composites have been fabricated by mixing MG YBCO powder in epoxy and curing the mixture in a custom-made PTFE jig at room temperature. The size and volume fraction of YBCO fillers have been found to affect the casting process of the HTS composites. SEM images of the HTS composite proved that small YBCO particles ($d_{50} = 4.5\ \mu m$) have more tendencies to agglomerate in the epoxy matrix compared to larger counterparts. It was also proven that increased volume fractions induce agglomeration of YBCO fillers. Holes formed by air gaps were detected in the epoxy, which is attributed to entrapped air during the mixing and curing process. These air gaps can however be eliminated by slowly stirring the HTS mixture. It has also been demonstrated that the use of a PTFE jig resulted in the simplification of the process of fabricating HTS composites and minimised the consumption of materials. However, close control of the jig assembly was needed in order to avoid leakage of the epoxy, which can affect the distribution of YBCO particles in the HTS composites, and consequently the microwave and superconducting properties. It is unclear whether the microstructural effects such as agglomerates and holes seen in the HTS/Epoxy can significantly affect HTS composite properties. More detailed work focussing on these effects would therefore be prudent.

In studying the effect of the HTS filler on microwave properties, 35 vol% MG HTS composites were determined to possess better superconducting, magnetic, and microwave properties compared to the CM HTS composites with similar volume fraction. The magnetic levitation test has demonstrated magnet floatation on the surface of the HTS composite samples indicating a strong diamagnetic effect, which agrees with the irreversibility component of the hysteresis loop reported by the SQUID study. The diamagnetic effect of the MG HTS composites resulted in the effective magnetic permeability (μ_{eff}) decreasing by 41% at 77 K. No significant effect can be seen on the dielectric properties (ε_{eff}) of the MG HTS composites at the same low temperature. However, the ε_{eff} value of the 35 vol% HTS composites exceeds that of the pure epoxy at room temperature and 77 K due to polarisation of both the HTS filler and epoxy. The decrease of μ_{eff}, switched the refractive index (n) from 4.6 at room temperature to 3.5 at 77 K, a significant tuning effect.

It has also been demonstrated that the volume fractions of the MG HTS filler can affect the microwave properties of the HTS composites. The ε_{eff} values of the HTS composites increased with increasing volume fractions at both room temperature and 77 K, while the μ_{eff} values of the MG HTS composites decreased with volume fractions at 77 K, controlling the n values at room temperature and 77 K. The temperature dependence of n indicates that the microwave properties of the HTS composites can be controlled by tuning the HTS filler size and volume fractions. The microwave properties of the HTS composites can thus be controlled for potential microwave device applications.

The susceptibility study on the HTS composites samples has shown that size (d_{50}) of YBCO particles, volume fraction of superconducting phase (V_{123}) in YBCO particles

and thickness of a non-superconducting layer (d) on YBCO particles can significantly affect the superconducting properties of the HTS composites. It has been demonstrated that the susceptibility values of my MG HTS composites fitted the predicted static magnetic theory of a granular superconductor as described by Campbell et. al.[1], with $r = 52.9\ \mu m$, V_{123} =77% and $d = 0\ \mu m$. This is a particularly important observation if YBCO particles are used as a filler in HTS composites. It is not only the particle size that affects the superconducting properties, but the quality of YBCO filler as well, such as the magnetisation properties and the volume fraction of the particle that is superconducting (YBCO-123 phase).

In studying the potential of fabricating HTS composites using 3-D printing, HTS/ABS composites have been fabricated. 3-D printing has enabled the fabrication of HTS composites in various shapes and with complex structures, which would be difficult to fabricate via the casting technique. Prior to 3-D printing, HTS composite filaments must be prepared by the extrusion process. Despite the fact that it has been found from the cast HTS/Epoxy composites that high HTS loading gain larger changes in ε_{eff} and μ_{eff} values at room temperature and 77 K, these high HTS loadings render the filaments difficult to make in the extrusion process, so unfortunately, these requirements are in conflict, and have to be balanced when choosing a composite formulation for 3-D printing. Thus, in this preliminary work, the volume fraction of 20 vol% HTS loaded ABS composite were chosen for the fabrication of HTS composite filaments.

MG YBCO powder was mixed with ABS pellets in acetone to form a paste, and the mixture was dried and ground into YBCO/ABS particles. These YBCO/ABS particles were extruded to produce the feedstock filaments for 3-D printing. It was found that the size of the YBCO powder particles can affect the extrusion and 3-D printing process. The size of the feedstock filament needs to be 1.7±0.1 mm, in order for it to fit in the 3-

D printer. Optimisation studies on sizes of YBCO powder have indicated that a 1.5 mm die size is suitable for extruding both fine ($d_{50} = 20.3\,\mu m$) and coarse ($d_{50} = 59.2\,\mu m$) YBCO/ABS filaments. 0.7 mm and 0.82 mm nozzle sizes were used to 3-D print the fine and coarse YBCO/ABS samples respectively.

The cross section image of the printed 20 vol% coarse YBCO/ABS composite has shown 21±3% area fraction of homogeneous YBCO particles distribution. The microwave and superconducting properties of the printed YBCO/ABS samples seemed consistent with the cast YBCO/Epoxy samples with a similar area fraction. This is a particularly important finding pertaining to printing YBCO/ABS, implying that the microwave and superconducting properties of the resulting composite can be controlled. Air gaps were detected in the matrix, which likely originated from moisture during the extrusion process, or improper drying of the YBCO/ABS paste, however, it did not seem to significantly affect the microwave properties. A more detailed experimental approach would therefore be needed to further clarify these features.

The 3-D printing technique has also enable the study of loss tangent of the HTS composites using the split-post dielectric resonator method. The split-post method requires a maximum thickness of the sample to be 0.6 mm, which can be difficult to realise with casting. Split-post dielectric studies have indicated that the loss tangent values of both fine and coarse YBCO/ABS samples are higher by one order of magnitude than pure ABS samples at room temperature. The loss tangent values of the HTS composites from the split-post dielectrics have been shown to differ by more than 40% from the loss tangent values measured by the waveguide, suggesting that the waveguide measurement is not sufficiently accurate for loss properties, as indicated by Barry[2]. This might suggest a strategy for the YBCO/ABS loss measurement at low temperature with proper low temperature experimental set up. This is an area that

should be explored, as it will significantly add to the body of knowledge on fundamental materials properties necessary to consider future microwave applications.

In an attempt to print anisotropic structures, the use of coarse YBCO/ABS composite filaments appears to result in problems in printing alternating pure ABS and YBCO/ABS layers. The alternating structures tend to break during the printing process due to the brittle texture of the coarse YBCO/ABS layers. The use of fine YBCO/ABS filaments has enabled the fabrication of horizontally-and-vertically arranged layer structures with directions parallel and perpendicular to the measurement electric and magnetic field respectively. It has been found that ε_{eff} values of these structures showed an anisotropic effect ($\varepsilon_{eff,\parallel} = 3.51$ and $\varepsilon_{eff,\perp} = 2.89$) at room temperature and ($\varepsilon_{eff,\parallel} = 3.48$ and $\varepsilon_{eff,\perp} = 2.87$) at 77 K, which agrees with the predicted values. However, the anisotropic properties of μ_{eff} at 77 K are unlikely to be observed due to the insignificant change of $\mu_{eff,\parallel} = 0.904$ and $\mu_{eff,\perp} = 0.901$ as predicted by the Wiener model equation. The anisotropic effects μ_{eff} can be significantly improved if higher volume fraction YBCO/ABS composites were used instead, but the practical problems with their filaments have been discussed above.

The fine YBCO/ABS composites have also been used to print 3-D SRR structures on ABS layers. However, no resonant frequency can be observed from the YBCO/ABS SRR devices due to the low conductivity of YBCO/ABS SRR structures. A higher volume fraction of YBCO/ABS composites could in the future be used to improve these properties. Furthermore, a proper experimental kit for low temperature measurement of YBCO/ABS SRR devices is required in order to achieve accurate measurements at low temperatures. This could be further examined in the context of metamaterials applications.

It is therefore possible to postulate that the microwave properties of the 3-D printing structures could be improved by optimising the size, quality and volume fraction of YBCO filler in the YBCO/ABS composite, which would allow the fabrication of HTS composites with excellent microwave and superconducting performance. Although the 3-D printing for YBCO/ABS composites has not been fully optimised, printed 20 vol% YBCO/ABS materials with $\varepsilon_{eff} = 5.1$ and μ_{eff} values dropping to 0.8 at 77 K and 15 GHz have been produced in this preliminary study. The fabrication of HTS composites via 3-D printing has demonstrated the potential for microwave device or metamaterials fabrication, since optimising the extrusion and printing parameters for a specific size and volume fraction of MG HTS YBCO filler could result in homogenous particle distribution in the HTS composites with good control of microwave and superconducting performance.

References

1 Campbell, A., Blunt, F., Johnson, J. & Freeman, P. Quantitative determination of percentage superconductor in a new compound. *Cryogenics* **31**, 732-737 (1991).

2 Barry, W. A Broad-Band, Automated, Stripline Technique for the Simultaneous Measurement of Complex Permittivity and Permeability. *IEEE Transactions on Microwave Theory and Techniques* **34**, 80-84 (1986).

Appendix

A. Measurement of susceptibility

In general the magnetisation, M of a material is measured by the magnetic moment μ and divided by its volume, V, which can also be defined by its susceptibility, $M = \chi H$ [1]. The susceptibility for an ideal superconducting material with a uniform distribution of superconducting phase, and penetration depth larger than the sample size is -1. However, this condition is limited to superconducting materials with currents flow across the sample; leading to local fields dependent on size and shape of the sample. In general the field experienced by the materials in the sample, H can be given as,

$$H = H_o - nM \tag{A.1}$$

where H_o is an applied field, and n is a demagnetisation factor, which depends on the geometrical pattern of a sample and its position within the applied field. By substituting equation (A.1) in the $M = \chi H$, M and H can be given by,

$$M = \frac{\chi H_o}{1+n\chi} \tag{A.2}$$

$$H = \frac{H_o}{1+n\chi} \tag{A.3}$$

In this case, the effective susceptibility, χ_{eff} of superconducting materials in the sample can be measured using equation (A.2) into $M_o = \chi_{eff} H_o$, where M_o is a total magnetisation of the sample which includes both local and macroscopic currents. The χ_{eff} of superconducting materials can be given by,

$$\chi_{eff} = \frac{\chi}{1+n\chi} \tag{A.4}$$

Campbell *et al.* reported that the microscopic shape of a sample is essential to be considered in the calculation of magnetisation of superconducting materials[1]. By assuming that the shape of superconducting particle is a sphere with demagnetisation factor, $n = 1/3$, based on the equation (A.4), the susceptibility of a sphere particle, χ_p can be given by,

$$\chi_p = \frac{\chi}{1+\frac{\chi}{3}} \tag{A.5}$$

Using above equation, the magnetisation of the particle can be measured as, $M_p = \chi_p H_i$, where H_i is the local field experienced by the particle. In addition to the local field, the particle also experiences a Lorentz field, $\frac{M}{3}$, thus, $H_i = H_o - nM + \frac{M}{3}$. For a superconducting particle with volume fraction f, of 100% superconducting phase and a penetration depth smaller than the size of the particle ($\lambda < r$), by substituting equation (A.5), the magnetisation of the sample can be given by,

$$M = fM_p = fH_o\chi\left[\frac{1}{1+\frac{\chi}{3}(1+3fn-f)}\right] \tag{A.6}$$

By considering that these particles are well-dispersed and embedded in a non-superconducting material, the susceptibility of the composite materials. $\chi_{composite}$ can be given by,

$$\chi_{composite} = \frac{M}{H_o} = f\chi\left[\frac{1}{1+\frac{\chi}{3}(1+3fn-f)}\right] \tag{A.7}$$

The above equations assume that on the size of the YBCO particle is larger than the penetration depth ($r > \lambda$), where the effect of λ can negligible. However, for the inverse condition ($r < \lambda$), the size of the particle can affect the magnetisation property of the superconducting sample and λ needs to be considered in the equation. The relationship of $r$and λ is given in relation to the magnetic moment, μ of sphere in equation A.8.

$$\mu = -\left(\frac{H_o r^3}{2}\right) P\left(\frac{r}{\lambda}\right) \tag{A.8}$$

where $P\left(\frac{r}{\lambda}\right)$ is a magnetic suppression factor which arises from the penetration depth effect, if the size of the particle is of the same order of magnitude as the penetration depth[2]. The equation is referred to Clem et al.[2] which can be written as,

$$P\left(\frac{r}{\lambda}\right) = \left[1 - \frac{3\lambda}{r} coth\left(\frac{r}{\lambda}\right) + 3\left(\frac{\lambda}{r}\right)^2\right] \quad \text{(A.9)}$$

By multiplying equation (A.9) into equation (A.7) the $\chi_{composite}$ of the superconducting composites is given as,

$$\chi_{composite} = f\chi P\left(\frac{r}{\lambda}\right)\left[\frac{1}{1+\frac{\chi}{3}(1+3fn-f)P\left(\frac{r}{\lambda}\right)}\right] \quad \text{(A.10)}$$

The above equations assume a volume fraction of 100% superconducting phase in the particle, which is an ideal condition of the superconducting particle with $\chi_{ideal} = -1$. For a particle containing a mixture of superconducting and non-superconducting phase, the volume fraction of superconducting phase YBCO-123, V_{123} is considered as,

$$\chi_{particle} \sim V_{123}\chi_{ideal} = -V_{123} \quad \text{(A.11)}$$

By substituting $-V_{123}$ with χ in the equation (A.10), $\chi_{composite}$ can be written as,

$$\chi_{composite} = -fV_{123}P\left(\frac{r}{\lambda}\right)\left[\frac{1}{1-\frac{V_{123}}{3}(1+3fn-f)P\left(\frac{r}{\lambda}\right)}\right] \quad \text{(A.12)}$$

An impurity layer of a non-superconducting material coated on the surface of YBCO particles is also another factor that can affect the volume fraction of superconducting phase in the superconducting particle. This impurity can be a layer of a non-superconducting material from environmental exposure or extended storage of YBCO filler. Based on the particle image in Figure A.1, the volume fraction of particle with radius size, R is decreased due to the non-superconducting material coated on the surface of the particle with thickness d, giving $r = R - d$. The reduced size of particle has an effect on the $P\left(\frac{r}{\lambda}\right)$ function, thus, $P\left(\frac{R-d}{\lambda}\right)$.

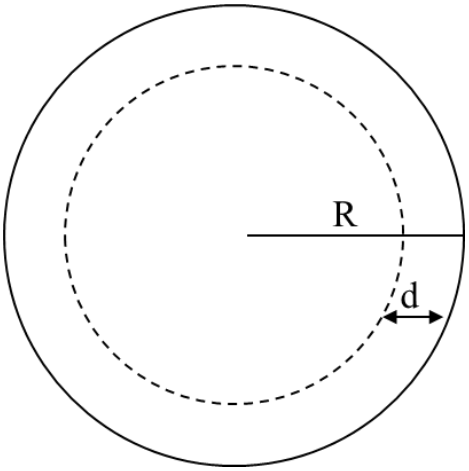


Figure A.1. A schematic image shows a non-superconducting layer with thickness d on the surface of the superconducting particle with radius size, R.

By considering the volume fraction of the non-superconducting layer, $4\pi R^2 d$, the volume fraction of an inner sphere that is superconducting in the particle can be written as,

$$Volume\ fraction\ of\ an\ inner\ sphere\ that\ is\ superconducting = \frac{\frac{4}{3}\pi R^3 - 4\pi R^2 d}{\frac{4}{3}\pi R^3} \quad \text{(A.13)}$$

$$= \frac{R-3d}{R} \quad \text{(A.14)}$$

By considering the non-superconducting layer of thickness, d on the spherical particle with radius, $r = R - d$, and the volume fraction of an inner sphere that is superconducting in the superconducting particle, $\chi_{composite}$ can now be written,

$$\chi_{composite} = -fV_{123}\left[\frac{R-3d}{R}\right]P\left(\frac{R-d}{\lambda}\right)\left[\frac{1}{1-\frac{V_{123}}{3}\left[\frac{R-3d}{R}\right]P\left(\frac{R-d}{\lambda}\right)(1+3fn-f)}\right] \quad \text{(A.15)}$$

References

1 Campbell, A., Blunt, F., Johnson, J. & Freeman, P. Quantitative determination of percentage superconductor in a new compound. *Cryogenics* 31, 732-737 (1991).

2 Clem, J. R. & Kogan, V. G. Theory of the Magnetization of Granular Superconductors: Application to High-Tc Superconductors. *Japanese Journal of Applied Physics* 26, 1161 (1987).